The impact of Aeolus wind observations in the tropics

Zur Erlangung des akademischen Grades eines
DOKTORS DER NATURWISSENSCHAFTEN (Dr. rer. nat.)
von der KIT-Fakultät für Physik des
Karlsruher Instituts für Technologie (KIT)

genehmigte

DISSERTATION

von

M. Sc. Maurus Borne
aus Freiburg im Breisgau

Tag der mündlichen Prüfung:	21.07.2023
Referent:	Prof. Dr. Peter Knippertz
Korreferent:	Prof. Dr. Martin Weissmann

Karlsruher Institut für Technologie

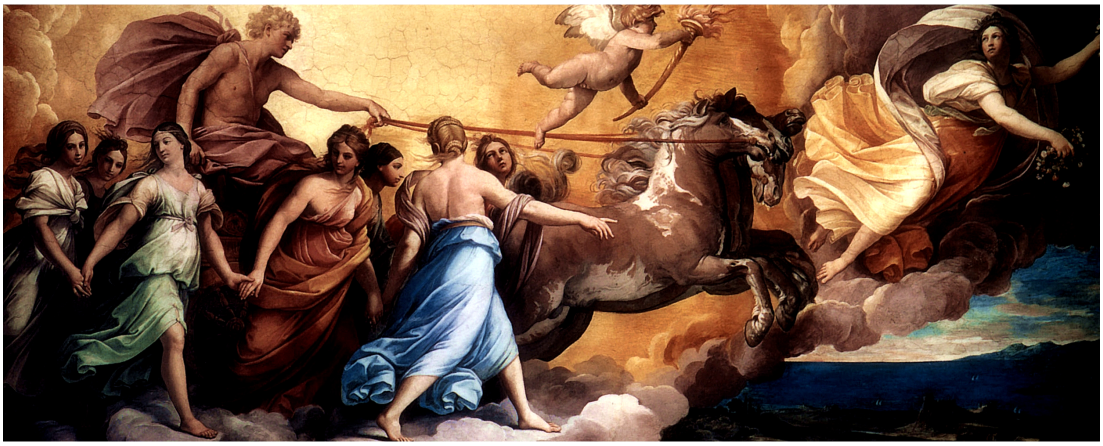

Figure 1: *Aeolus and Aurora* painted in 1614 by the Italian Baroque artist Guido Reni. The painting shows Aeolus, the "keeper of the wind" on the right, surrounded by clouds, followed by Aurora, the goddess of dawn, who brings daylight. The dynamic composition of light and shadow, sun and clouds shows a contrast of opposing forces, which Aeolus helps to balance with the wind. This balance between the elements shaping daily weather is necessary for a society to live in harmony.

Abstract

Aeolus is the first satellite mission to use a space-based Doppler Wind Lidar (DWL) for observing vertical wind profiles on a global scale. The instrument uniquely combines Rayleigh-clear (molecular) and Mie-cloudy (aerosol) backscatter measurements in clear and cloudy atmospheric conditions. This is particularly important in the tropics, where the large gap in wind observations in the Global Observing System (GOS) has posed significant challenges for Numerical Weather Prediction (NWP). By filling this gap, Aeolus offered a unique opportunity to significantly improve the representation of the tropical circulation in NWP models.

To ensure reliable data for NWP models, the sources of error in the Aeolus wind product measurements must be identified and understood. To this end, the quality of Aeolus Level 2B (L2B) wind product is assessed over the tropical Atlantic using radiosondes launched from the islands of Sal, Saint Croix and Puerto Rico during August-September 2021 as part of the Joint Aeolus Tropical Atlantic Campaign (JATAC). During this period, Aeolus sampled within a complex environment with a variety of cloud types in the vicinity of the Intertropical Convergence Zone (ITCZ) and aerosol particles from Saharan dust outbreaks. The results show that the presence of clouds or dust can affect the quality of Rayleigh-clear measurements, when the useful signal is significantly reduced, thus leading to an underestimation of the Error Estimate (EE). However, gross outliers with large deviations from the radiosonde reference but low EEs account for less than 5% of the data. These seem to affect measurements at all altitudes and under all environmental conditions, and, their root-cause remains unknown. Finally, we show the presence of an orbital-dependent bias of up to 2.5 ms^{-1} observed with both radiosondes and European Centre for Medium-Range Weather Forecasts (ECMWF) model equivalents.

Subsequent to the quality assessment of the Aeolus wind measurements, the impact of the L2B dataset on the ECMWF and the Deutscher Wetterdienst (DWD) analyses and forecasts over the adjacent West African Monsoon (WAM) during boreal summers of 2019 and 2020 is assessed. The WAM is notoriously challenging to forecast and is characterized by prominent and robust large-scale circulation features such as the African Easterly Jet North (AEJ-North) and the Tropical Easterly Jet (TEJ). Assimilating Aeolus generally improves the prediction of zonal winds in both forecasting systems, especially for lead times above 24 hours. These improvements are related to systematic

differences in the representation of the two jets, with the AEJ-North weakened at its southern flank in the western Sahel in the ECMWF analysis, while no obvious systematic differences are seen in the DWD analysis. In addition, the TEJ core is weakened in the ECMWF analysis and strengthened on its southern edge in the DWD analysis. The regions where the influence of Aeolus on the analysis is greatest correspond to the ITCZ region for ECMWF and generally the upper troposphere for DWD. In addition, we confirm the presence of an altitude and orbit dependent bias in the Rayleigh-clear channel, as already identified with radiosondes, over the entire WAM region, which causes the zonal winds to accelerate in the morning and slow down in the evening. Applying a temperature-dependant bias correction to this channel contributes to a better representation of the diurnal cycle and improved predictions of the WAM winds.

Ultimately, the NWP impact of Aeolus on large-scale tropical phenomena such as Equatorial Waves (EWs) and associated mechanisms contributing to the improvements are examined in both ECMWF and DWD systems. More specifically, EWs are isolated in analysis and forecast fields using two complementary methods. Large impacts of Aeolus on EWs identified in zonal wind forecasts can be found for most wave types, EWs identification methodologies and forecasting systems. Improvements in the upper levels are more pronounced, while the impact in the DWD system is significantly larger compared to the ECMWF system. EWs isolated in rainfall fields, also exhibit large positive impact in the DWD system compared to ECMWF. In the former, the positive impact appears to stem from improvements in zonal wind forecasts over the Pacific Ocean during the El Niño-Southern Oscillation (ENSO) phase change from neutral to La Niña phase. Especially during that period, relative improvements of more than 50 % are reached in this observation sparse area. Aeolus improves the DWD model first-guess by up to 5 ms^{-1}, which leads to improvements of zonal wind forecasts up to lead times of 96 hours. These improvements are not related to important changes in temperature, but rather to a better representation of vertical wind shear.

In conclusion, the Aeolus mission has now completed its 5 year mission in space, exceeding expectations with technological and scientific achievements. We demonstrated the positive impact of Aeolus, particularly in the Upper Troposphere and Lower Stratosphere (UTLS) region where clear skies and low observational availability predominate, with improvements seemingly related to better representation of vertical wind shear. The qualify of Aeolus has played a crucial role in the observed improvements, although further improvements are required to better characterizing the Rayleigh-clear error, particularly in cloud and aerosol-loaded regions. Moreover, addressing error assignment of the wind observations in NWP models can also lead to improvements. Future research should address the underlying relationship between improvements in EWs and precipitation forecasts, as well as the impact of Aeolus on longer time scales. The success of Aeolus has motivated the development of its successor, Aeolus-2, which aims to further improve space-based wind observation technology for meteorological applications.

Kurzfassung

Aeolus ist die erste Satellitenmission, bei der ein weltraumbasiertes Doppler Wind Lidar (DWL) zur Beobachtung von vertikalen Windprofilen auf globaler Ebene eingesetzt wird. Das Instrument kombiniert in einzigartiger Weise Rayleigh-clear (molekular) und Mie-cloudy (Aerosol) bei klarer und bewölkter Atmosphäre. Dies ist besonders in den Tropen wichtig, wo die große Datenlücke bei den Windmessungen im Global Observing System (GOS) das Numerical Weather Prediction (NWP) vor große Herausforderungen stellt. Durch die Schließung dieser Lücke bot Aeolus die einzigartige Möglichkeit, die Darstellung der tropischen Zirkulation in NWP-Modellen erheblich zu verbessern.

Um zuverlässige Daten für NWP-Modelle zu gewährleisten, müssen die Fehlerquellen in den Aeolus-Windproduktmessungen identifiziert und verstanden werden. Zu diesem Zweck wird die Qualität des Aeolus Level 2B (L2B)-Windprodukts über dem tropischen Atlantik mit Hilfe von Radiosonden bewertet, die im Rahmen des Joint Aeolus Tropical Atlantic Campaign (JATAC) im August-September 2021 von den Inseln Sal, Saint Croix und Puerto Rico gestartet wurden. Während dieses Zeitraums sammelte Aeolus Daten in einer komplexen Umgebung mit einer Vielzahl von Wolkentypen in der Nähe des Intertropical Convergence Zone (ITCZ) und Aerosolteilchen von Staubausbrüchen aus der Sahara. Die Ergebnisse zeigen, dass das Vorhandensein von Wolken oder Staub die Qualität von Rayleigh-Clear-Messungen beeinträchtigen kann, wenn das useful signal erheblich reduziert wird, was zu einer Unterschätzung des Error Estimate (EE) führt. Allerdings machen grobe Ausreißer mit großen Abweichungen von der Radiosondenreferenz, aber niedrigen EEs, weniger als 5% der Daten aus. Diese scheinen die Messungen in allen Höhen und unter allen atmosphärischen Bedingungen zu beeinflussen, und ihre Ursache bleibt unbekannt. Schließlich zeigen wir das Vorhandensein einer orbitalabhängigen Bias von bis zu 2,5 ms^{-1}, die sowohl mit Radiosonden als auch mit European Centre for Medium-Range Weather Forecasts (ECMWF)-Modelläquivalenten beobachtet wurde.

Im Anschluss an die Qualitätsbewertung der Aeolus-Windmessungen werden die Auswirkungen des L2B-Datensatzes auf die ECMWF- und Deutscher Wetterdienst (DWD)-Analysen und -Vorhersagen über dem anliegenden West African Monsoon (WAM) in den borealen Sommern 2019 und 2020 bewertet. Der WAM ist bekanntermaßen schwierig vorherzusagen und zeichnet sich durch markante und robuste großräumige Zirkulationsstrukturen wie den African Easterly Jet North (AEJ-North) und den Tropical Easterly

Jet (TEJ) aus. Die Assimilierung von Aeolus verbessert im Allgemeinen die Vorhersage der zonalen Winde in beiden Vorhersagesystemen, insbesondere bei Vorhersagezeiten über 24 Stunden. Diese Verbesserungen hängen mit systematischen Unterschieden in der Darstellung der beiden Jets zusammen, wobei der AEJ-North an seiner südlichen Flanke in der westlichen Sahelzone in der ECMWF-Analyse geschwächt ist, während in der DWD-Analyse keine offensichtlichen systematischen Unterschiede zu erkennen sind. Darüber hinaus ist der TEJ-Zentrum in der ECMWF-Analyse geschwächt und in der DWD-Analyse an seinem südlichen Rand verstärkt. Die Regionen, in denen der Einfluss von Aeolus auf die Analyse am größten ist, entsprechen bei ECMWF der ITCZ-Region und bei DWD im Allgemeinen der oberen Troposphäre. Darüber hinaus bestätigen wir das Vorhandensein einer höhen- und orbitabhängigen Bias im Rayleigh-Clear-Kanal, wie sie bereits mit Radiosonden identifiziert wurde, über der gesamten WAM-Region, die dazu führt, dass die zonalen Winde am Morgen beschleunigt und am Abend verlangsamt werden. Die Anwendung einer temperaturabhängigen Biaskorrektur auf diesen Kanal trägt zu einer genaueren Darstellung des Tageszyklus und einer verbesserten Vorhersage der WAM-Winde bei.

Letztendlich werden die Auswirkungen von Aeolus auf großräumige tropische Phänomene wie Equatorial Waves (EWs) und die damit verbundenen Mechanismen, die zu den Verbesserungen beitragen, sowohl in ECMWF- als auch in DWD-Systemen untersucht. Genauer gesagt werden EWs in Analyse- und Vorhersagefeldern mit zwei sich ergänzenden Methoden isoliert, darunter eine Raum-Zeit-Spektralanalyse mit Fast Fourier Transform (FFT) und eine räumliche Projektionsmethode, die dynamische Felder auf theoretische Wellenmuster projiziert. Große Auswirkungen von Aeolus auf die in zonalen Windvorhersagen identifizierten EWs können für die meisten Wellentypen, EWs-Identifizierungsmethoden und Vorhersagesysteme festgestellt werden. Die Verbesserungen in den oberen Ebenen sind ausgeprägter, während die Auswirkungen im DWD-System im Vergleich zum ECMWF-System deutlich größer sind. EWs, die in Niederschlagsfeldern isoliert sind, zeigen im DWD-System ebenfalls große positive Auswirkungen im Vergleich zu ECMWF. Im erstgenannten System scheint die positive Auswirkung auf Verbesserungen der zonalen Windvorhersagen über dem Pazifik während des El Niño-Southern Oscillation (ENSO)-Phasenwechsels von der neutralen zur La Niña-Phase zurückzuführen zu sein. Insbesondere in diesem Zeitraum werden in diesem beobachtungsarmen Gebiet relative Verbesserungen von mehr als 50 % erreicht. Aeolus verbessert die erste Schätzung des DWD-Modells um bis zu 5 ms^{-1}, was zu Verbesserungen der zonalen Windvorhersagen bis zu Vorhersagezeit von 96 Stunden führt. Diese Verbesserungen sind nicht auf wesentliche Änderungen der Temperatur zurückzuführen, sondern vielmehr auf eine bessere Darstellung der vertikalen Windscherung.

Zusammenfassend lässt sich feststellen, dass die Aeolus-Mission ihre fünfjährige Mission im Weltraum abgeschlossen hat und die Erwartungen hinsichtlich der technologischen und wissenschaftlichen Leistungen übertroffen hat. Wir haben die positiven Auswirkungen von Aeolus aufgezeigt, insbesondere in der Upper Troposphere and

Lower Stratosphere (UTLS)-Region, wo klare Wettebedingungenund geringe Anzahl von Beobachtungen vorherrschen, wobei die Verbesserungen offenbar mit einer besseren Darstellung der vertikalen Windscherung zusammenhängen. Die Qualifizierung von Aeolus hat eine entscheidende Rolle bei den beobachteten Verbesserungen gespielt, obwohl weitere Verbesserungen erforderlich sind, um den Rayleigh-clear-Fehler besser zu charakterisieren, insbesondere in wolken- und aerosolbelasteten Regionen. Darüber hinaus kann die Behandlung der Fehlerzuweisung in NWP-Modellen ebenfalls zu Verbesserungen führen. Künftige Forschungsarbeiten sollten sich mit der zugrunde liegenden Beziehung zwischen Verbesserungen bei EWs und Niederschlagsvorhersagen sowie mit den Auswirkungen von Aeolus auf längeren Zeitskalen befassen. Der Erfolg von Aeolus hat die Entwicklung seines Nachfolgers, Aeolus-2, motiviert, der die weltraumgestützte Windbeobachtungstechnologie für meteorologische Anwendungen weiter verbessern soll.

Preface

The PhD candidate confirms that the research presented in this thesis contains significant scientific contributions by himself. This thesis reuses material from the following publications:

> Borne, M., Knippertz, P., Weissmann, M., Martin, A., Rennie, M., and Cress, A. (2023): Impact of Aeolus wind lidar observations on the representation of the West African monsoon circulation in the ECMWF and DWD forecasting systems. *Quarterly Journal of the Royal Meteorological Society.*, 933-958, doi: 10.1002/qj.4442
>
> Borne, M., Knippertz, P., Weissmann, M., Witschas, B., Flamant, C., Rios-Berrios, R., and Veals, P. (2024): Validation of Aeolus L2B products over the tropical Atlantic using radiosondes. *Atmospheric Measurement Techniques.*, 561–581, doi: 10.5194/amt-17-561-2024
>
> Flamant, C., Chaboureau, J-P., C., Delanoe, J., Gaetani, M., Jamet, C., Lavaysse, C., Bock, O., Borne, M., Cazenave, Q., Coutris, P., Cuesta, J., Menut, L., Aubry, C., Benedetti, A., Bosser, P., Bounissou, S., Caudoux, C., Collomb , H., Donal, T., Febvre, G., Fehr, t., Fink, A., Formenti, P., Araujo, N., Knipertz, P., Lecuyer, E., Neves Andrade, M., Ngoungue-langue, C., Jonville, T., Schwarzenboeck, A., Takeishi, A. (2024). Cyclogenesis in the tropical Atlantic: First scientific highlights from the Clouds-Atmospheric Dynamics-Dust Interactions in West Africa (CADDIWA) field campaign. *Bulletin of the American Meteorological Society.*, E387–E417, doi:10.1175/BAMS-D-23-0230.1

Chapters 1, 2, 3, 4, 5 and 8 reuse material from Borne et al. (2024). Chapters 1, 2, 3, 4, 6 and 8 reuse material from Borne et al. (2023). Chapters 2, 4, and 5 integrate material originally prepared for Flamant et al. (2024) and are planned for use in a forthcoming publication.

The results leading to the results was accomplished in the framework of the project B6 of the Transregional Col-laborative Research Center SFB/TRR 165 Waves to Weather (W2W) funded by the German Research Foundation (DFG). The research proposal for this project was authored by Peter Knippertz, Corinna Hoose, and Tijana Janjic. The observing system experiments used in Chapters 6 and 7 were conducted at ECMWF by Michael Rennie and at DWD by Alexander Cress. The analyses in Borne et al. (2023) and Borne et al. (2024) were solely performed by the candidate, who also wrote the manuscripts with advice from Prof. Dr. Peter Knippertz and Prof. Dr. Martin Weissmann. The analysis and text regarding equatorial waves in Flamant et al. (2024) were also performed solely by the candidate.

The candidate confirms that appropriate credit has been given within the thesis where reference has been made to the work of others. This copy has been supplied on the understanding that this is copyright material and that no quotation from the thesis may be published without proper acknowledgment.

Contents

1. Introduction

Wind is the most critical atmospheric variable lacking in the current Global Observing System (GOS) (Baker et al., 2014). Especially in the tropics, where the lack of geostrophic balance requires simultaneous measurements of wind and mass information, Numerical Weather Prediction (NWP) models require additional wind observations with sufficient coverage in time and space to identify key atmospheric dynamics (Stoffelen et al., 2005; Straume et al., 2020). Prior the advent of Aeolus, satellite wind observations in these regions were only available for a limited number of tropospheric layers and are mainly provided by Atmospheric Motion Vectors (AMVs) estimated from tracking cloud and water vapour features (Bormann et al., 2003; Folger and Weissmann, 2014), or by scatterometer measurements of surface winds (Naderi et al., 1991; Portabella and Stoffelen, 2009). In particular, AMVs suffer from errors in height assignment, resulting in substantial systematic and correlated errors (Bormann et al., 2003; Velden and Bedka, 2009; Folger and Weissmann, 2014). In recent years, more satellite observations (e.g. passive microwave sensors and Global Navigation Satellite Systems (GNSS) radio occultation) have complemented the conventional observing network, but those observations mainly provide mass information and no direct measurements of wind profiles. In situ measurements derived from aircraft reports, ground stations or radiosondes are not globally distributed, leaving a significant data gap in the tropics. Several impact studies have demonstrated the urgent need of additional wind profile measurements to reduce uncertainties in initial conditions for NWP systems, especially over regions with a lack of direct wind observations (Marseille and Stoffelen, 2003; Stoffelen et al., 2005, 2006; Žagar et al., 2008; Baker et al., 2014; Weissmann and Cardinali, 2007; Weissmann et al., 2012; Žagar, 2004).

To address these deficiencies, the European Space Agency (ESA) deployed the Aeolus mission in 2018 (Figure 1.1), the first satellite capable of measuring atmospheric winds around the globe from space with a homogeneous space-time coverage and altitude-resolved profiles up to 30 km height (Reitebuch, 2012). The instrument carries a direct detection Doppler wind lidar called Atmospheric LAser Doppler INstrument (ALADIN) that can detect the Doppler shift of the narrowband particle backscatter signal (Mie channel; cloud droplets and aerosols or ice crystals), and of the Rayleigh-Brillouin backscatter spectrum (Rayleigh channel; air molecules). The processing algorithm also distinguishes between retrievals originating from "cloudy" or "clear" atmospheric

Figure 1.1: The Aeolus satellite measures wind from space using a Doppler Wind Lidar (DWL) called ALADIN. Aeolus emits a laser pulses into the Earth's atmosphere with two different wind detection channels. The Rayleigh channel measures wind from the scattering of air molecules, while the Mie channel captures wind from the backscattering of clouds and aerosol particles, allowing for wind measurements in different atmospheric conditions. **Image credit: ESA**.

conditions, resulting in Rayleigh-clear and Mie-cloudy observation types. The two channels partially complement each other, as Mie-cloudy winds can compensate for gaps in Rayleigh-clear measurements, providing information in cloudy and aerosol-loaded regions. Various NWP centres have demonstrated the added value of assimilating Aeolus winds through significant improvements in model fields and model background information, especially in tropical regions, the upper tropical troposphere and the lower stratosphere (Rennie and Isaksen, 2020; Rennie et al., 2021; George et al., 2021; Garrett et al., 2022; Laroche and St-James, 2022; Pourret et al., 2022; Martin et al., 2023).

For an optimal use of the Aeolus wind observations in NWP models, an assessment of the data quality is essential. To achieve this, several scientific and technical studies are carried out in the framework of Calibration/Validation (Cal/Val) activities organised by ESA. For wind validation, several reference products have been used such as ground-based remote sensing observations (Belova et al., 2021; Guo et al., 2021; Iwai et al., 2021; Abril-Gago et al., 2022), in situ measurements (Baars et al., 2020; Chen et al., 2021; Ratynski et al., 2022), airborne measurements (Lux et al., 2020; Witschas et al., 2020; Bedka et al., 2021; Witschas et al., 2022b) or NWP model equivalents (Martin et al., 2021; Zuo et al., 2022). Several errors in the Aeolus data have already been detected and improvements in the processing chain and the instrument have been made accordingly. These include the implementation of a bias correction in both channels related to the seasonal temperature variations of ALADIN's M1 mirror (Weiler et al., 2021a) and the correction of "hot pixels" (Weiler et al., 2021b), which reduced the systematic and random errors in the Rayleigh channel. Although the largest source of errors could be explained, some remaining – not yet fully understood – systematic errors are still expected to be present. One phenomenon that still needs to be explored is the sensitivity of Aeolus wind quality to the presence of aerosols and clouds, potentially affecting key parameters used to calculate the Line Of Sight (LOS) winds and the associated Error Estimate (EE). The tropical Atlantic during the boreal summer, spanning from West Africa to the Caribbean, is the ideal place to explore these dependencies, with a wide range of atmospheric aerosols (Saharan dust aerosols, sea salt aerosols, biomass combustion aerosols) and convective cloud types associated with the West African Monsoon (WAM) circulation and the Intertropical Convergence Zone (ITCZ). For this purpose, ESA organized the Joint Aeolus Tropical Atlantic Campaign (JATAC) in the period July to September 2021, which deployed high-quality airborne lidar instruments over Cabo Verde and the Virgin Islands but also ground-based instruments such as radiosondes and Doppler lidar systems. In the first part of this study, we validate Aeolus wind products using radiosondes launched from western Puerto Rico, northern St. Croix and Sal airport on Cabo Verde. The semi-arid island of Sal is located over the tropical East Atlantic off the West African coast, near the northern boundary of the WAM. Rain events are relatively sporadic there, and most tropical cyclones propagate south of the island. The region is exposed to mineral dust plumes emanating from Saharan dust outbreaks. In contrast, the islands of St. Croix and Puerto Rico are located in the formation areas of hurricanes and tropical cyclones and are frequently hit by them. The contribution of the radiosondes in JATAC is complementary to other instruments as they provide accurate wind measurements throughout the troposphere up to the lower stratosphere.

Having assessed the quality of Aeolus in such complex atmospheric environment, it is essential to explore the impact of Aeolus data on representing the WAM during its peak from June to September in the NWP systems of the European Centre for Medium-Range Weather Forecasts (ECMWF) and the Deutscher Wetterdienst (DWD). The WAM was chosen as a study region for the following three reasons: (a) Sparse observations: The conventional station network in tropical Africa is sparse, in particular with respect to radiosondes (Parker et al., 2008; Knippertz et al., 2017), and even existing data are sometimes not transferred to the Global Telecommunication System (GTS) in time for assimilation in global forecasting systems. Moreover, reports from commercial air traffic is very limited over tropical Africa, leading to relatively few aircraft reports. (b) Low predictability: NWP models are known to have a poor ability to predict rainfall over West Africa (Fink et al., 2011), barely outperforming ensemble predictions based on climatology (Vogel et al., 2018, 2021; Walz et al., 2021). One reason for this appears to be the great importance of highly organized Mesoscale Convective Systems (MCSs), which contribute up to 80% of the annual rainfall (Bayo Omotosho, 1985; Mathon et al., 2002; Fink et al., 2006). It is computationally challenging to achieve km-scale horizontal resolution that would be required for representing these systems explicitly over a large enough model domain (Pante and Knippertz, 2019; Senior et al., 2021) but some improvements in the ECMWF system have recently been achieved through a more sophisticated convective parametrization (Becker et al., 2021). (c) Socio-economic impact: The West African population is highly reliant on rainfed agricultural and thus vulnerable to weather extremes, threatening local health, food security and socioeconomic development (Krishnamurthy et al., 2014). An improvement in rainfall forecasts may therefore prove beneficial not only for agriculture but also for energy production, water supply and disease prevention.

A comprehensive understanding of the impact of Aeolus on NWP systems can be gained by examining tropical weather patterns, which are mainly driven by Equatorial Waves (EWs). EWs are east- and westward propagating disturbances trapped near the equator. When coupled with convection, these systems, known as convectively coupled EWs, can substantially control precipitation and its variability in the tropics. EWs are theoretically described by the shallow water equations (Matsuno, 1966), and evidence of EWs can be provided by the wavenumber-frequency power spectrum of tropical cloudiness data, which display spectral peaks consistent with the theoretical dispersion curves (Wheeler and Kiladis, 1999). Many techniques have been developed to isolate equatorial waves in space and time by exploiting their unique propagation and structure characteristics (Knippertz et al., 2022). EWs are assumed to be a major source of predictability in the tropics (Ying and Zhang, 2017; Li and Stechmann, 2020; Judt, 2018, 2020), but are not well captured in global models and are subjected to errors in phase velocity and amplitude (Lin et al., 2006; Straub et al., 2010; Benedict et al., 2013; Hung et al., 2013; Ferrett et al., 2020; Yang et al., 2021). Improving the representation of EWs in global models is crucial to improve the prediction of EWs and associated precipitation events. By providing accurate information on wind and it's vertical shear, Aeolus has the potential to improve the representation of the dynamical structure of EWs and thus improve practical predictability in the tropics.

Thesis structure

This thesis is organized as follows: **Chapter 2** provides the theoretical background on the importance and need for wind observations in the tropics, followed by an overview of the measurement principle and main objectives of the Aeolus mission and lastly a description of the data assimilation systems implemented at ECMWF and DWD. **Chapter 3** provides the different research questions that motivates this thesis. **Chapter 4** gives an overview of the analysed data, the applied verification strategies and details the quality control and co-location criteria used for the validation study. This chapter also provides a description of the different Observing System Experiment (OSE)s and the Horizontal Line of Sight (HLOS) wind observation error modelling and settings. Finally a description of the the different equatorial wave identification methodologies used in this study is presented. **Chapter 5** is the first result chapter on the validation of Aeolus L2B wind product in tropical Atlantic. This chapter deals with the quantification of errors, their dependency on temporal and spatial distance between the compared observations as well as on the presence of clouds and dust. Furthermore, the chapter includes a case study illustrating the different behaviour of Rayleigh-clear and Mie-cloudy winds under different environmental conditions. In **Chapter 6**, we discuss the impact of Aeolus on the representation of the WAM in the ECMWF and DWD operational systems. This includes a description of the various atmospheric components and observed circulation features that Aeolus captures and the related error structure. This chapter also contains a description of the influence of Aeolus on the African Easterly Jet North (AEJ-North) and Tropical Easterly Jet (TEJ) (Lemburg et al., 2019), with a thorough evaluation of the orbital and channel contributions to the observed influence using background departure diagnostics. The forecast impact of Aeolus on the WAM winds, using background verification against radiosondes and forecast comparisons of zonal wind against ERA5 reanalysis is also presented. **Chapter 7** presents the impact of Aeolus on the representation of tropical waves on wind and precipitation forecasts as well as scenarios that can explain the observed improvements. Finally, **Chapter 8** provides the conclusions and **Chapter 9** an outlook on future work.

2. Theoretical background

This chapter provides the essential theoretical background necessary to comprehend the research undertaken in this thesis. First, we examine the key aspects of tropical meteorology, including equatorial waves, which play a major role in determining atmospheric variability in the tropics, and the West African Monsoon (WAM) system, which is characterised by it's complex meteorology and low observational coverage. We also discuss the concept of predictability and explore the potential for improvements in practical predictability in the tropics. We then explore the need for global wind measurements, in the context of the problems posed by the lack of geostrophic balance in the tropics and the lack of wind observations in the Global Observing System (GOS). Secondly, we focus on the Aeolus mission, its motivation and measurement principle. We will also give an overview of the Aeolus products. Finally, we examine the data assimilation frameworks used by European Centre for Medium-Range Weather Forecasts (ECMWF) and Deutscher Wetterdienst (DWD) in which the Aeolus data are assimilated. A full understanding of the characteristics of the Aeolus measurements, their assimilation into the ECMWF and DWD systems, together with an introduction to tropical meteorology, are essential foundations for understanding the research presented in this thesis.

2.1 Tropical meteorology and predictability

Wind is a critical component of the Earth's weather and climate system, regulating temperature and precipitation patterns worldwide. Wind can manifest in particularly violent wind phenomena such as hurricanes or tornadoes, which can cause significant damage to people and infrastructure. Especially in the tropics, accurate weather forecast is critical for agriculture, energy production, water supply and disease prevention. The development of supercomputers, the advancement of prediction models and data assimilation systems as well as the increasing observational coverage have enabled meteorologists to significantly improve the accuracy of Numerical Weather Prediction (NWP) forecasts in recent years (Bauer et al., 2015). However, weather forecasting in the tropics remains challenging, as it involves complex atmospheric processes with rapidly changing weather conditions and limited data availability. Increasing the number of observations have the potential to address these challenges and improve the accuracy of NWP forecasts in the tropics. On repeated occasions, the World Meteorological Organisation (WMO) has highlighted that three-dimensional global wind fields are “essential for operational weather forecasting on all scales and at all latitudes" (WMO, 1996; Jarraud, 2008).

2.1.1 Atmospheric circulation

Global wind circulation

Wind plays a vital role in the Earth atmosphere by transporting heat and moisture around the planet. It is primarily driven by the uneven distribution of solar radiation across Earth’s surface, creating temperature differences between the equator and the poles. The rotation of the Earth also affects the movement of air masses with the Coriolis force causing air to deflect in a curved path. In the extratropics, where the stronger Coriolis force balances the horizontal pressure gradient forces, geostrophic winds can occur, where the wind is directed parallel to isobar. Geostrophic adjustment occurs when the winds are not in balance with the pressure pattern. The jet stream, a high-altitude fast-moving westerly wind in the mid-latitudes, can steer storms, resulting in changes in precipitation patterns and intensity. The interaction between pressure systems, the jet stream, and the Coriolis force can generate relatively predictable weather patterns in the extratropics. In contrast to higher latitudes, the Coriolis force is weaker in the tropics. As a result, its influence on the atmospheric circulation is smaller, as the ageostrophic winds flow rapidly between the pressure centres neutralising each other. The tropical atmosphere is consequently more barotropic, with tropical pressure maps lacking the distinct structure found at higher latitudes. Moisture content and solar heating play a significant role in the formation of convective clouds and precipitation in the tropics. These are influenced by the diurnal cycle of convection, which in turn affects atmospheric pressure. However, the absence of a strong Coriolis force means that pressure systems in the tropics are more dependent on smaller-scale processes, such as clouds and rain. The rapid growth of uncertainty in convection makes it challenging to predict rainfall and other weather systems accurately in tropical regions. However, convective processes in the tropics can result in self-sustaining, organized Mesoscale Convective Systems (MCSs) that persist for a few hours to several days and cover large geographical areas (Mapes and Houze Jr, 1993). Scientific studies suggest that these convective systems are induced and sustained by the passage of Equatorial Waves (EWs) in the atmosphere, providing an untapped source of predictability in the tropics.

Equatorial waves

EWs play a crucial role in determining synoptic and intraseasonal variability in the tropical atmosphere. EWs are theoretically solutions of the Shallow Water (SW) equations that propagate in the zonal direction and are trapped near the equator. These equations describe the motion of a rotating, inviscid fluid layer with constant density and vertical stability. In the tropics, where the beta-plane approximation can be applied, the linearized form of the equations about a motionless base state can be expressed as follows

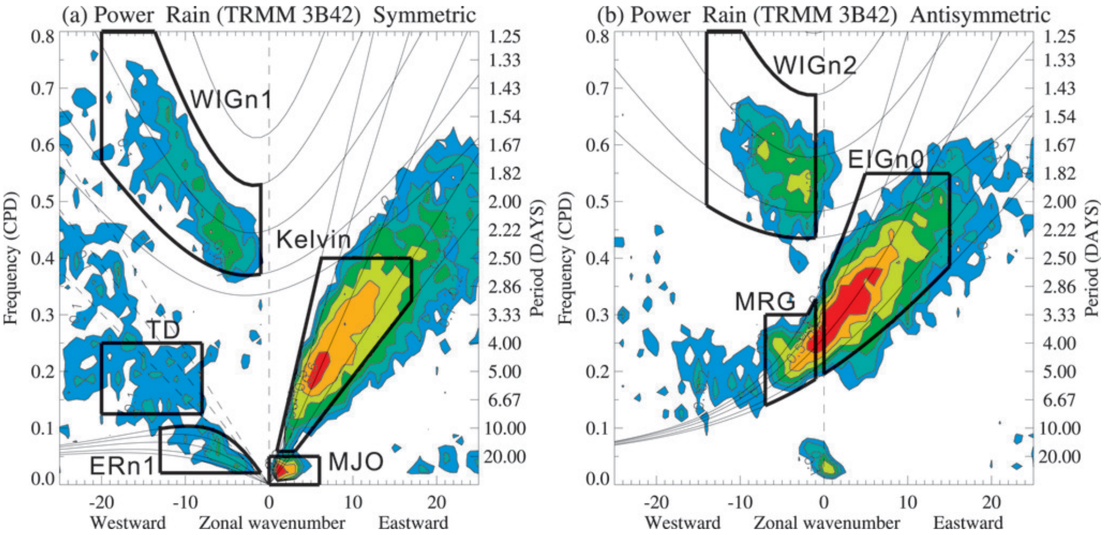

Figure 2.1: Signal strength of (a) symmetric and (b) antisymmetric components of precipitation (Tropical Rainfall Measurement Mission (TRMM)-3B42) over the latitudes of 15°S–15°N. Shading interval is 0.1 with first level at 0.1. Positive and negative wavenumbers correspond to eastward and westward propagation, respectively. Dispersion curves are also plotted for Kelvin, n = 1 equatorial Rossby (ERn1), n = 1 and n = 2 westward inertia–gravity (WIGn1, WIGn2), n = 0 eastward inertia–gravity (EIGn0), and mixed Rossby–gravity (MRG) waves, with equivalent depths of 8, 12, 25, 50, and 90 m. In (a) three diagonal dashed lines for the symmetric components indicate constant phase speeds of 7.0, 9.0, and 11.0 ms^{-1}. The regions enclosed with thick solid lines represent filters for the isolation of each wave activity. **From Yasunaga and Mapes (2012b). © American Meteorological Society. Used with permission.**

$$
\begin{aligned}
&\frac{\partial u'}{\partial t} - \beta y v' + \frac{\partial \phi'}{\partial x} = 0 \\
&\frac{\partial v'}{\partial t} + \beta y u' + \frac{\partial \phi'}{\partial x} = 0 \\
&\frac{\partial \phi'}{\partial t} + c^2 \left(\frac{\partial u'}{\partial x} + \frac{\partial v'}{\partial y} \right) = 0
\end{aligned}
\tag{2.1}
$$

where f is the Coriolis parameter $f = \beta y$, and c the gravity wave phase speed $c = \sqrt{g h_e}$, with h_e the equivalent depth and g the gravitational acceleration. The variables u', v' and ϕ' represent the linearized form of zonal wind, meridional wind and geopotential height with respect to the motionless basic state. Assuming a wave-like solution in the zonal direction and allowing for arbitrary meridional structure, the solutions can be expressed as

$$
\begin{pmatrix} u'(x,y,z) \\ v'(x,y,z) \\ \phi'(x,y,z) \end{pmatrix} = \begin{pmatrix} \hat{u}(y) \\ \hat{v}(y) \\ \hat{\phi}(y) \end{pmatrix} e^{(kx - wt)} \tag{2.2}
$$

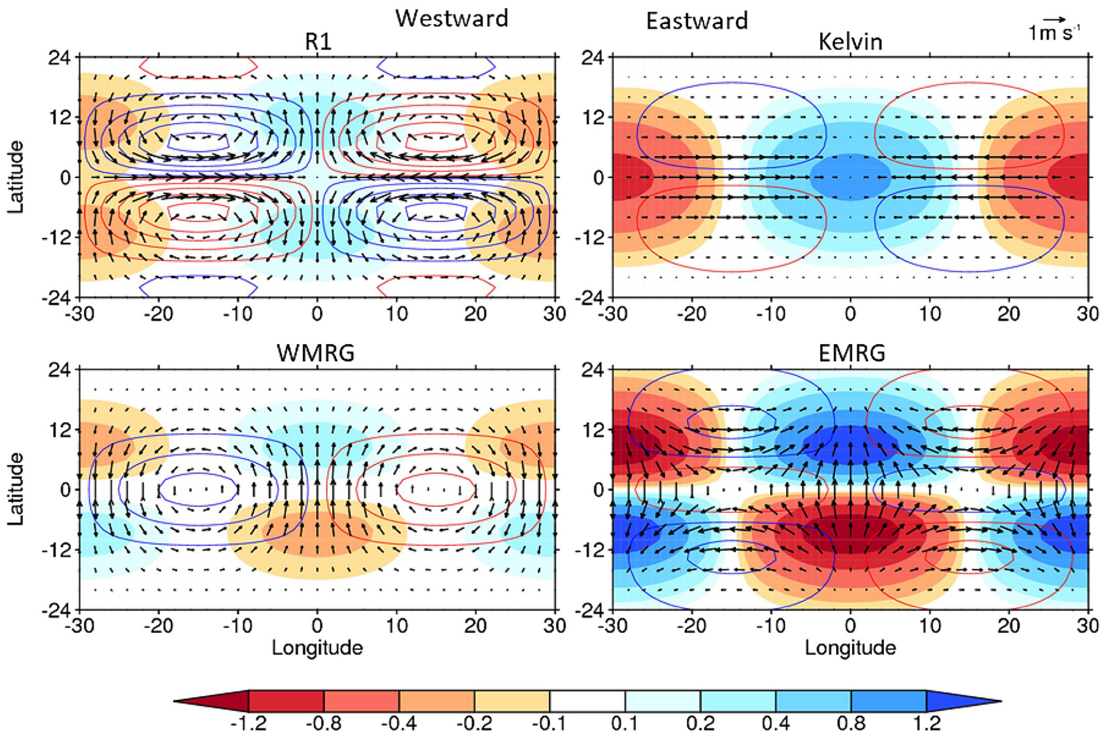

Figure 2.2: The theoretical horizontal structures of some of the gravest equatorial wave modes in the resting atmosphere. The Kelvin wave, the $n = 0$ westward-moving mixed Rossby-gravity (WMRG) and the eastward-moving mixed Rossby-gravity (EMRG), the $n = 1$ westward-moving Rossby (R1) waves. The meridional trapping scale y_0 has been taken to be 6° and the zonal wave number $k = 6$. Vectors indicate horizontal wind. Filled contours indicate divergence ($10^{-6}\ s^{-1}$) with convergence set to be positive. Color contour lines represent vorticity ($10^{-6}\ s^{-1}$) with blue lines for positive vorticity and red lines for negative vorticity; the contour interval is 0.6 starting from ±0.2. The maximum zonal wind for the Kelvin wave and the maximum meridional wind for the $n = 0$ MRG are set to be 1 m/s, and the maximum meridional wind for the $n = 1$ Rossby (R1) wave is set to be ~0.86 m/s. **From Ferrett et al. (2020) under the Creative Commons Attribution 4.0 International License (CC BY 4.0)**.

with k the zonal wave number and w the frequency. By substituting the solution into the previous equation set, we can derive the dispersion relation

$$\frac{c}{\beta}\left(\frac{w^2}{c^2} - k^2 + \frac{k}{w}\beta\right) = 2n + 1 \tag{2.3}$$

where n is the meridional wave number. The resulting dispersion curves (Matsuno, 1966; Gill, 1980; Wheeler and Kiladis, 1999) provide essential information about each wave mode, such as its wave numbers, periods, and specific horizontal structures. Fig.2.1 display the dispersion curves for different EWs modes, including Kelvin waves, Equatorial Rossby waves (ER), Mixed Rossby gravity waves (MRG), Westward Inertio-Gravity waves (WIG) and Eastward Inertio-Gravity waves (EIG) for different equivalent depths. When coupled with deep convection, EWs can modulate tropical convection and precipitation and can be referred to as convectively coupled EWs. Early studies of Takayabu (1994) and Wheeler and Kiladis (1999) provided initial evidence of their existence. For example,

As illustrated by Yasunaga and Mapes (2012a,c), rainfall and brightness temperature, which can be used to detect clouds, show similar patterns in the frequency-wavenumber power spectrum, with most of the signal found in the higher frequency and more divergent wave types. Fig.2.1 depicts the power spectrum of TRMM satellite precipitation, serving as an indicator of convection in the equatorial region (15°S-15°N). The spectrum provides observational evidence for the existence of these waves, which are symmetric (a) and antisymmetric (b) about the equator. The spectral peaks from observations are remarkably aligned along the dispersion curves of the linear theory for different equivalent depths. Additionally, a spectral peak not described by the SW equations is visible for periods of 30-60 days and wavenumbers of 1-3, which corresponds to the Madden-Julian Oscillation (MJO). The MJO (Madden and Julian, 1971) is a planetary-scale structure that propagates slowly eastward (5 ms^{-1}) with a large region of enhanced rainfall and convective activity. Tropical Disturbances (TDs) are another important type of wave observed in the tropics that are not predicted by the SW theory. In the framework of this thesis, these waves are also included in the definition of EWs. The EWs solutions also feature specific spatial structure, with more divergent waves such as Kelvin waves, and rotational types of waves such as ER, MRG, WIG and EIG. Fig.2.2 illustrates the theoretical structures of different equatorial wave modes, which are labeled according to the EWs naming nomenclature proposed by Yang et al. (2003).

The West African Monsoon

The West African Monsoon (WAM) is a complex system characterized by prominent and robust large-scale circulation features such as the midlevel African Easterly Jet North (AEJ-North) and the upper-tropospheric Tropical Easterly Jet (TEJ) (Lemburg et al., 2019). The latter is commonly described as the southern part of the upper-level Asian monsoon anticyclone and extends from the Indian Ocean to the tropical Atlantic. The AEJ-North is characterised by an easterly wind of about 10-15 ms^{-1} and peaks at 700–600 hPa (Burpee, 1972; Thorncroft and Blackburn, 1999; Nicholson and Grist, 2003; Parker et al., 2005b) and is generated by the temperature gradient between the hot Saharan air and the relatively cool monsoon air from the Gulf of Guinea (Charney and Stern, 1962; Cook, 1999). The AEJ-North is closely linked to the synoptic variability of precipitation, since it supports the formation and propagation of African Easterly Waves (AEWs) (Burpee, 1972), which in turn modify moisture transport, stability and vertical wind shear and thus convective organization (Mohr and Thorncroft, 2006; Janiga and Thorncroft, 2016; Schlueter et al., 2019b,a). The representation of the AEJ-North in the ECMWF model has undergone significant changes in response to model updates and improvements, which have modified the structure and intensity of the jet (Kamga et al., 2000; Tompkins et al., 2005a). The assimilation of additional observations taken in the framework of field campaigns has unveiled remaining issues, e.g. that the AEJ-North is too weak in the ECMWF model over the eastern Sahel (Tompkins et al., 2005b; Agustí-Panareda et al., 2010).

AEWs typically correspond to the TD wave type (see previous section) and have a significant impact on precipitation patterns, modulating precipitation on a 2-6 day period with wavelengths ranging from 2000-5000 km. During boreal summer, AEWs are the dominant weather feature in West Africa, with approximately 60% of organized squall lines associated with them (Fink and Reiner, 2003). Especially moisture, 70% of which lies below 700 hPa, is strongly modulated by AEWs, which result primarily from a strong meridional temperature and moisture gradient, carrying moisture zonally out of the Sahel (Poan et al., 2015). Below the zonal modulation of moisture, near-surface southwesterly monsoon flow also transport moisture from the western Atlantic Ocean across the Guinea coast to the Sahel (Lélé and Leslie, 2016).

According to several studies (Kamsu-Tamo et al., 2014; Schlueter et al., 2019a,b), EWs are the most important modulator of convection over West Africa. Specifically, TDs and Kelvin waves are responsible for most of the rainfall variability (30%) on short time scales (3 hours to 3 days), while MJO and ER dominate on longer time scales (40% for 7-20 days). Due to the close vicinity of TDs and MRG waves in wavenumber-frequency space, various interactions have been reported. While "hybrid" waves have been observed over Africa (Cheng et al., 2019), transition from MRG into off-equatorial TDs waves has also been documented over the Pacific Ocean (Takayabu and Nitta, 1993; Zhou and Wang, 2007). However, more research is needed to further clarify the nature of the relationship and the involved mechanisms between the two types of waves over the regions where they both occur.

2.1.2 Predictability

Intrinsic predictability

Intrinsic predictability describes the inherent finite limit up to which predictions are possible given nearly perfect forecast model and initial conditions (Lorenz, 1969; Zhang et al., 2003, 2007; Sun and Zhang, 2016). Lorenz (1969) first demonstrated its existence using the concept of the butterfly effect which describes the rapid upscale grow of error and multi-scale interaction caused by the chaotic nature of the atmosphere leads to a finite range of predictability Lorenz (1969). Estimating predictability is challenging, especially in the tropics, where moist convection cannot be resolved properly. Therefore, various simplified and idealised models were used to investigate intrinsic predictability, such as simple spectral turbulence models (Lorenz, 1969), global storm-resolving ideal twin experiments (Judt, 2018), a stochastic convection scheme (Selz, 2019) or storm-resolving aqua-planet simulations (Mapes et al., 2008). Although it remains somewhat unclear whether these idealised models reflect the actual atmosphere well enough, it is generally accepted that they can represent the inherent predictability in our atmosphere (Palmer et al., 2014). Lorenz used a simple spectral turbulence model and derived the

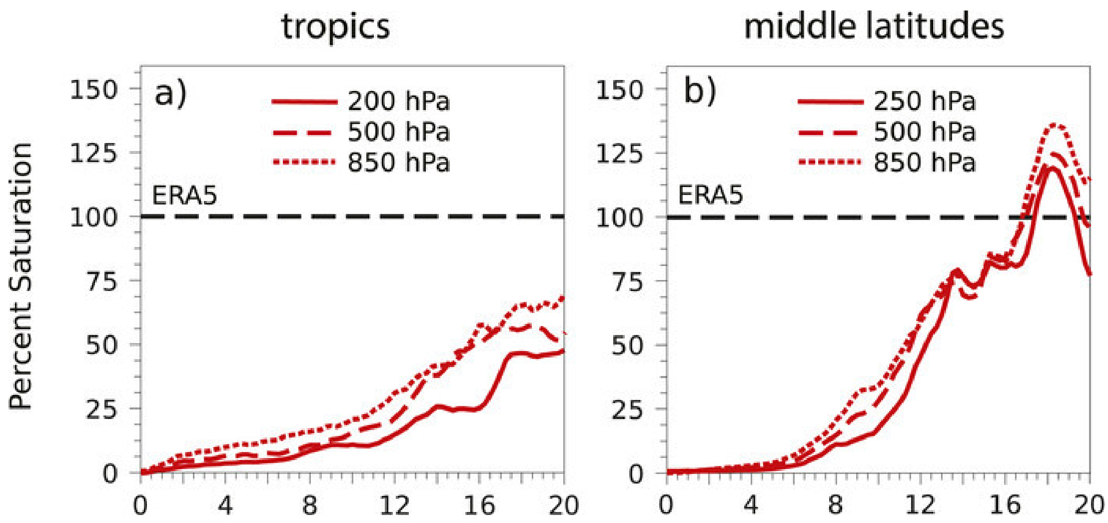

Figure 2.3: Time series of horizontal averaged Difference Kinetic Energy (DKE) for the (a) tropics, (b) middle latitudes at three levels: upper troposphere (solid lines), middle troposphere (dashed lines), and lower troposphere (dotted lines). Black lines denote the saturation limits computed from ERA5 (dashed). The DKE time series are normalized by the respective saturation limits. **From Judt (2020). © American Meteorological Society. Used with permission.**

Kinetic Energy (KE) spectrum of the unperturbed flow, to describe the KE contained at each wavenumber. In global mean, he showed that the predictability for spectral slopes lower than -3 has a finite limit, with error growth scale- and time-dependent leading to an upscale error spreading (Lorenz, 1969; Rotunno and Snyder, 2008; Morss et al., 2009). For steeper spectral slopes than -3, unlimited predictability can be achieved. Using an identical-twin predictability experiment using perturbed simulations, Judt (2018) showed that each latitudinal zone has distinct error growth characteristics depending on the underlying dynamics. The tropical atmosphere seems to be predictable on average beyond 20 days, which is longer compared to the extratropics (see Figure 2.3). In particular, the spectral slope in the extratropics is -3 at synoptic scales (>600 km) and -5/3 at mesoscale scales (<100 km), while it is quasi-uniformly shallower at -5/3 in the tropics. For mesoscale flows, the predictability is shorter in the tropics (5-7 days) than in the extratropics (10-12 days). One hypothesis for the low predictability of mesoscale flows in the tropics is that they depend on convective processes and are less constrained by synoptic-scale forcing compared to the extratropics. For synoptic scales of around 1000 km the predictability is similar, around 10 days, while for larger scales (> 5000 km) the extratropics reach a predictability limit of 15-17 days, which corresponds to 60% of the saturation of the error in the tropics, which is set at twice the climatological variance. It is assumed that the longer predictability on large scales in the tropics compared to the extratropics is related to the propagation of EWs, as various studies revealed that EWs have a long limit of predictability (Ying and Zhang, 2017; Li and Stechmann, 2020; Judt, 2020). Other studies suggest that the shape of the spectral slope of the background kinetic energy is key to understanding scale-dependant error growth and thus predictability (Lilly, 1972; Rotunno and Snyder, 2008).

Practical predictability

Practical predictability describes the current limit of predictability that can be reached by NWP "given realistic uncertainties in both the forecast model and initial and boundary conditions" (Lorenz, 1969; Zhang et al., 2003, 2007). Since the introduction of NWP, weather forecasting capabilities have been gradually improving, with forecast skill for lead times of 3 to 10 days increasing on average by one day per decade (Bauer et al., 2015). This has been achieved by the increasing computational power, the improvement of model physics and the higher model resolution. But the sophistication of Data Assimilation (DA) techniques and the increasing quality and quantity of observations have also contributed to this progress. The improvement is true for forecast skills, mainly in the extratropics in the Northern Hemisphere. Despite longer instrinsic predictability in the tropics as we discussed earlier, Zhu et al. (2014) showed that practical predictability in the tropics is limited to a day to a week. Especially over West Africa, there is a very poor ability to predict rainfall (Fink et al., 2011) with predictions barely outperforming ensemble predictions based on climatology, despite the use of state-of-the-art statistical post-processing methods (Gneiting et al., 2005; Vogel et al., 2018, 2021; Walz et al., 2021). The large gap between practical and intrinsic predictabilities in the tropics can be understood in a number of ways. First, convective precipitation is the largest cause of error in weather forecasts (Reynolds et al., 2020; Vogel et al., 2018, 2021; Walz et al., 2021), but moist convective processes are parameterised in most operational global models. Different weather service centers implement their own convection parameterization scheme. Due to the convective nature of the tropics, modeling atmospheric phenomena in the tropics is highly sensitive to the choice of convection parameterization, such as the MJO (Wang and Schlesinger, 1999; Maloney and Hartmann, 2001) or the Intertropical Convergence Zone (ITCZ) (Song and Zhang, 2018). Amongst the various atmospheric phenomena in the tropics, an accurate representation of EWs is arguably crucial for practical predictability (Ying and Zhang, 2017; Judt, 2018; Ferrett et al., 2020), but weather and climate models often struggle to capture them realistically, with biases and errors in the phase velocity, amplitude and structure of the waves (Lin et al., 2006; Straub et al., 2010; Benedict et al., 2013; Hung et al., 2013; Ferrett et al., 2020; Yang et al., 2021). For example, the propagation velocity of convectively coupled Kelvin waves in atmospheric models is often too high, which affects the representation of the associated high impact weather system (Ferrett et al., 2020; Yang et al., 2021). Convection-permitting models are thought to be a cure to represent convectively coupled EWs better in models. However, these models require finer model resolution, which is computationally challenging in a sufficiently large model domain (Pante and Knippertz, 2019; Senior et al., 2021). Furthermore, a convection-permitting simulation does not always guarantee better capturing convectively coupled EWs compared to its counterpart with parameterized convection (Jung and Knippertz, 2023). This indicates

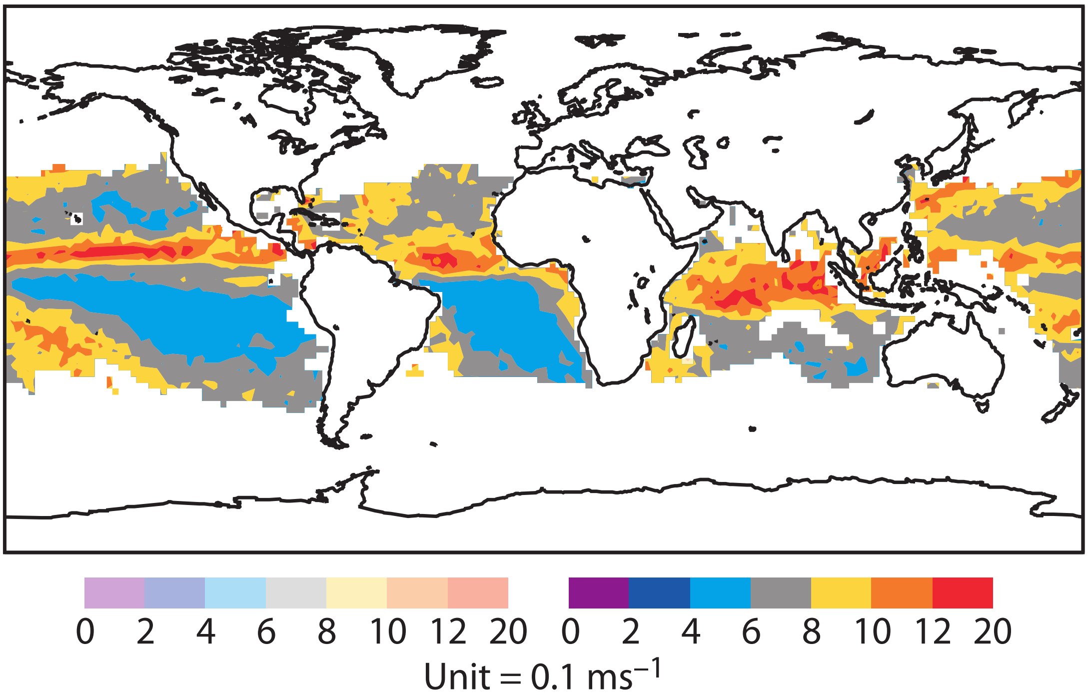

Figure 2.4: Standard deviation of wind speed analysis increments at 1000hPa for October–December 2011. Statistical significance at the 95% level is denoted by intense colours, pale colours are employed otherwise. **From Bechtold et al. (2013) under the Creative Commons Attribution-NonCommercial-NoDerivatives 4.0 International License (CC BY-NC-ND 4.0).**

that the development of convection parameterization, which alleviates coupling between convection and large-scale circulations, is still necessary to capture tropical phenomena (Becker et al., 2021), ultimately associated with skillful rainfall prediction in the tropics. Finally, a major problem in improving the representation of tropical circulations is the lack of satellite and in situ observation coverage, especially over the oceans and tropical Africa. In these regions, moist convection leads to extensive cloud layers that are generally opaque to observations. Despite the sophistication of modern DA methods, these regions have large analysis and short-range forecast uncertainties (Park et al., 2008; Žagar, 2017), as the influence of observations depends mainly on their density and quality. This phenomenon is illustrated in Figure 2.4, which shows the seasonal standard deviation of the ECMWF wind speed analysis increment at 1000 hPa, with high values up to 1 ms^{-1} following the ITCZ. Improvement of the tropical analysis can be achieved by better formulating the background forecast error (Bonavita et al., 2012) or by reducing the assigned observation error by improving the observational network. Amongst the others, wind is the most important meteorological observation type that has to be obtained to accurately capture atmospheric circulation in global models (Baker et al., 2014).

2.1.3 The need of global wind measurements

Geostrophic balance

Geostrophic balance (Blumen, 1972) occurs when the Coriolis force and the pressure gradient force in the atmosphere are in geostrophic equilibrium. The geostrophic balance relationship is commonly used to derive large-scale winds from indirect mass field information. However, this approximation can only be used at higher latitudes than the tropics, where EWs play the main role in the dynamics (Žagar, 2004). Direct wind information is therefore essential in the tropics and can be employed to better characterise the structure and intensity of various tropical weather systems such as tropical cyclones, EWs and monsoon circulations. The geostrophic balance relationship is particularly useful in non-equatorial regions where pressure information is available to estimate wind information. However, in regions where mass field information is lacking, indirect wind cannot be estimated and direct wind measurements are required. Additionally, the theory is only valid for atmospheric motion systems that have certain horizontal and vertical scales. The Rossby radius of deformation, can help to identify those scales, by providing the horizontal length scale on which the pressure gradient force is balanced by the Coriolis force. The Rossby radius of deformation R is defined as:

$$R = \frac{\sqrt{gH}}{f} = \frac{\sqrt{gH}}{2\Omega sin\Theta} \tag{2.4}$$

where the numerator describes the mass field with g the gravitational acceleration and H the depth of the vertical atmospheric system under consideration and the denominator is the expression for the Coriolis parameter f, which depends on the latitude Θ and the Earth rotation rate Ω. At higher latitudes, the geostrophic balance relationship is thus applicable to large-scale atmospheric systems (L»R) with shallow vertical structure (H«L), and can be used to better define mid-latitude circulation patterns including atmospheric fronts and polar lows. However, for deep vertical structures (H»L) and horizontal scales smaller than the Rossby radius of deformation (L«R) such as tornadoes, thunderstorms or tropical cyclones, the theory breaks down. Since the theory neglects non-geostrophic effects such as friction or buoyancy, it may not be applicable in mountainous and coastal regions where boundary layer turbulence and gravity waves prevail.

Deficiencies in the current Global Observing System (GOS)

Global geophysical observations are essential for monitoring and understanding Earth's system, providing key information about the atmosphere, ocean, land and cryosphere. The GOS, coordinated by the WMO, was developed for this purpose, by collecting, processing and disseminating Earth's geophysical observations for weather forecast models world-wide. The GOS thus supports a wide range of applications extending from day-to-day decision making, through weather forecasting, disaster preparedness and air quality monitoring to long-term adaptation strategies related to climate change. The

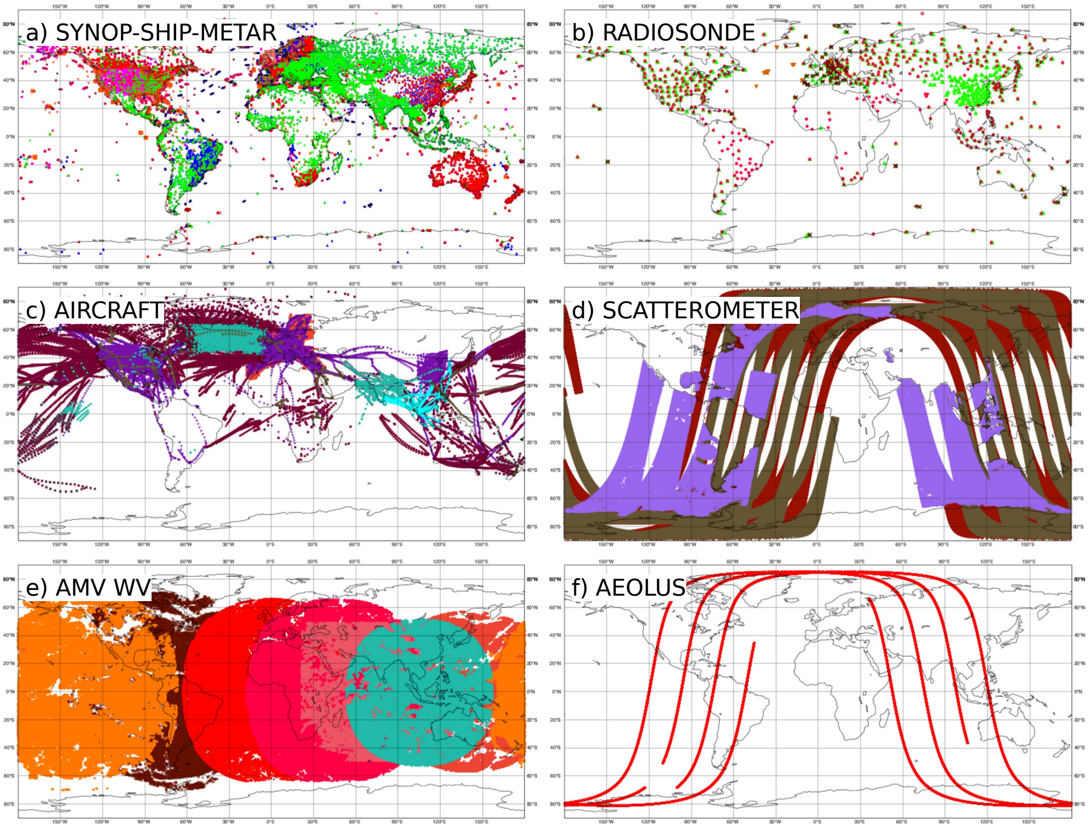

Figure 2.5: Geographic coverage on the 2023-04-05 of the different wind observation types assimilated at ECMWF, including SYNOP-SHIP-METAR (a), radiosonde (b), aircraft reports (c), polar-orbiting scatterometer (d), geostationary satellite Atmospheric Motion Vectors (AMVs), water vapour winds (e) and polar-orbiting Aeolus (d). Each color represents the coverage of a single satellite or data type. **Adapted from ECMWF Geographical coverage charts (`https://charts.ECMWF.int/catalogue/packages/monitoring/products/dcover?`).**

GOS gathers a variety of weather data, with different spatio-temporal coverage, vertical resolution and accuracy. In situ measurements derived from ground stations (Fig.2.5a), radiosondes (Fig.2.5b) or aircraft reports (Fig.2.5c) are generally more accurate, but not globally distributed, and are mainly located over land in the Northern Hemisphere. Satellite data cover larger areas and provide a comprehensive overview of global weather patterns, but are generally less accurate and vertically less resolved. It is widely recognised that the GOS has deficiencies in wind observations, with the observing network heavily biased towards mass observation type and a particular lack of wind observations in the Southern Hemisphere (SH), over the oceans and in regions close to the equator. Although temperature soundings can be used to derive wind information for large-scale wind fields in the extratropics, they are not a substitute for direct wind observations (Stoffelen et al., 2005; Straume et al., 2020). Most satellite-based wind observations in these regions are limited in vertical coverage. AMVs (Fig.2.5e) estimated from tracking cloud and water vapour features (Bormann et al., 2003; Velden and Bedka, 2009; Folger and Weissmann, 2014) are mostly limited to the lower and middle atmospheric layers in regions where clouds are present but exhibit systematic and correlated errors due to inaccuracies of their height assignment. Scatterometer measurements (Fig.2.5d) only provide information on surface winds (Naderi et al., 1991; Portabella and Stoffelen, 2009). Ultimately, Aeolus (Fig.2.5f) is the world's first space-based Doppler Wind Lidar (DWL) that measures direct wind information worldwide with high vertical coverage and high accuracy, partially closing the gap in the GOS.

2.2 The Aeolus wind mission

2.2.1 Motivation, objectives and achievements

Motivation

The Aeolus wind mission is motivated by the WMO's recognition that global wind measurements are necessary for understanding and improving weather forecasts and climate models (Baker et al., 2014). This led to the first investigations in the 1970s into the possibility of measuring wind profiles from space using lidar technologies. The first basic technique for measuring atmospheric wind was the Laser Atmospheric Wind Sounder (LAWS, Beranek et al. (1989)) developed by the National Aeronautics and Space Administration (NASA). However, it turned out that building this instrument and launching it into space would be extremely complex and expensive, putting its development on hold. In parallel, alternative and more effective approaches using atmospheric DWL were developed by European Space Agency (ESA), leading to the first concept for Aeolus in 1989 with the Atmospheric LAser Doppler INstrument (ALADIN) (Betout et al., 1989; Reitebuch et al., 2009). The Aeolus mission (ESA, 1999; Stoffelen et al., 2005; Reitebuch, 2012; Straume et al., 2020) was finally accepted in 1999 and selected as the fifth Earth Explorer Mission and as a core project of the Living Planet Program. Many pre-launch studies highlighted the potential of global wind profiles in NWP with the largest benefits found in the oceans, tropics and southern hemisphere (Tan et al., 2007; Marseille et al., 2008; Horányi et al., 2015). In particular in the tropics, DWL winds can improve quality of tropical analyses (Žagar, 2004; Žagar et al., 2008) and short range forecasts (Masutani et al., 2010), thus improving the representation of tropical phenomena such as monsoonal circulations and tropical cyclones (George and Gray, 1976; Holland, 1983; Andersson et al., 1998; Pu et al., 2010). Improvement in the tropics can also have an upstream effect through teleconnection effects (Raicich et al., 2003; Magnusson, 2017) and improve mid-latitude weather forecasting (Bielli et al., 2010; Gaetani et al., 2011; Pante and Knippertz, 2019). In the mid-latitudes, various studies have also demonstrated that assimilating wind observations have a significant positive impact on analyses and predictions of the DWD and ECMWF forecast system (Cress and Wergen, 2001; Weissmann and Cardinali, 2007; Weissmann et al., 2012).

Objectives

The main objective of Aeolus is to demonstrate DWL technology as a proof of concept for measuring wind profiles from space. This includes providing global wind profiles suitable for assimilation into NWP models to improve analyses and forecasts of 3D wind fields over a minimum period of three years. The secondary objective of the mission is to address some of the key concerns of the World Climate Research Programme (WCRP) and to support objectives of the Global Climate Observing System (GCOS). This includes providing datasets suitable for evaluating and improving climate models to achieve a better understanding of climate variability.

Overall, the main objectives of the Aeolus mission can be summarized as following (Ingmann and Straume, 2016)

- Improve medium range forecast in the extratropics with a better definition of planetary-scale waves
- Improve short-range forecasts of intense storm developments though the measurement of vertical wind shear of small-scale features
- Improve the analysis of tropical circulation systems through provisions of direct wind measurements
- Improve understanding of stratospheric mixing processes and dynamics
- Provide data on atmospheric optical properties (aerosols and clouds) to improve knowledge of atmospheric state and composition
- Provide data to evaluate climate models

Achievements

Eventually, Aeolus was launched in 2018 in the European spaceport in Kourou and became the first satellite to provide global atmospheric wind profiles along the Horizontal Line of Sight (HLOS) from the surface up to 30 km altitude. The winds are obtained from short pulses of ultraviolet light emitted by ALADIN that are scattered by air molecules (Rayleigh channel) and tiny particles (Mie channel) in the atmosphere before being reflected back to the satellite telescope. The European Centre for Medium-Range Weather Forecasts (ECMWF), the Royal Netherlands Meteorological Institute (KNMI) and German Aerospace Center (DLR) were mainly involved in the planning and support of the mission. For instance, they developed the Level 2B (L2B) processing chain that produces the HLOS winds suitable for DA (de Kloe et al., 2020; Rennie et al., 2020). Aeolus was shown to have a positive impact in many global institutions, including ECMWF, the National Oceanic and Atmospheric Administration (NOAA), the German Weather Service (DWD), Météo-France, the UK Met Office, the Canadian Global Deterministic Prediction System and many others (Rennie and Isaksen, 2020; Rennie et al., 2021; George et al., 2021; Martin et al., 2023; Garrett et al., 2022; Laroche and St-James, 2022; Pourret et al., 2022). Significant improvements were observed in particular in model fields and model background information, especially in tropical regions, the Upper Troposphere and Lower Stratosphere (UTLS) and the polar troposphere. The assimilation of Aeolus also had a positive effect on analyses and predictions of improving wind and mass variables up to 1–2 % in the lower stratosphere in the medium forecast range (Rennie et al., 2021), through background error covariances providing the flow dependence in the wind-mass balance (Song et al., 2017). On the short-range forecasts at ECMWF, Aeolus had a positive impact of up to 5 % using the Forecast Sensitivity to Observation Impact (FSOI) during the period July to October 2019, similar to the impact of the radiosonde network (Rennie, 2022). In addition, Aeolus showed positive benefits in the tropics by improving the prediction of tropical cyclone tracks (Garrett et al., 2022), influencing the representation of the El Niño-Southern Oscillation (ENSO) (Martin et al., 2023) and the representation of vertically propagating Kelvin waves (Žagar et al., 2021).

To ensure that the data provided by the Aeolus mission is reliable and suitable for assimilation into NWP models, the ESA coordinated numerous Calibration/Validation (Cal/Val). Cal/Val activities involve a range of instrumentation to validate wind, such as in situ measurements (Baars et al., 2020; Chen et al., 2021; Ratynski et al., 2022), ground-based remote sensing observations (Belova et al., 2021; Guo et al., 2021; Iwai et al., 2021; Abril-Gago et al., 2022), airborne measurements (Lux et al., 2020; Witschas et al., 2020; Bedka et al., 2021; Witschas et al., 2022b) or NWP model equivalents (Martin et al., 2021; Zuo et al., 2022). Different instrumental and algorithm related issues were detected during those activities, and were accounted for with adjustments in the processing chain. For example, several systematic and random sources of error – mainly affecting the Rayleigh-clear winds – were identified and corrected, such as biases related to uncorrected "hot pixels" (Weiler et al., 2020), decreasing laser energy and signal losses in the receiver path (Reitebuch et al., 2019) as well as seasonal temperature variations over the M1 mirror of the receiving telescope (a bias correction scheme was implemented in the operational processing chain in April 2020) (Weiler et al., 2021a; Rennie et al., 2021; Krisch et al., 2020; Martin et al., 2021) . A gradual degradation of the laser pulse energy during the mission also led to a degradation of the impact of Aeolus over time. This was most likely caused by laser-induced contamination on the mirror surface, which deteriorated the laser transmission through the instrument's optics.

Having finally outlived its three-years nominal lifetime, Aeolus has exceeded expectations in terms of technical performance and scientific achievements. Despite these successes, challenges remain that need to be addressed in order to realise the full potential of Aeolus and to prepare for the follow-up mission (Wernham et al., 2021). These include accounting for biases and errors that may arise from a number of factors, involving the instrument calibration, the data processing chain or the DA procedures.

2.2.2 Measurement technique

Doppler wind lidar principle

The DWL is a remote sensing instrument that enables the measurement of atmospheric spatially resolved wind speed and direction based on the Doppler effect. The DWL instrument first emits a laser signal that travels through the atmosphere and is scattered back to the instrument by atmospheric particles and molecules moving with the wind. During the scattering process, the frequency of the emitted laser beam is shifted with respect to the transmitted laser signal. Since the movement of the atmospheric components is mainly driven by the wind, there is a increase in the frequency (blue shift) when the wind is blowing towards the lidar and a decrease in the frequency (red shift) when it is blowing away from the lidar. The wind velocity LOS_{AEOLUS} along the laser beam of wavelength λ is thus directly proportional to the frequency Doppler shift Δf, through the Doppler equation

$$LOS_{AEOLUS} = \frac{\lambda}{2}\Delta f \tag{2.5}$$

Depending on the characteristics of the scattering body, the scattering process can lead to changes in the spectral properties and the intensity of the backscattered signal. By operating in the ultraviolet range, DWL can achieve molecular scattering (or Rayleigh scattering), which is most effective for molecules whose size is much smaller than the wavelength of the incident light. Because the velocity of air molecules is not constant, but varies due to the Brownian motion, which is a function of both pressure and temperature, the spectrum of the scattered light is broadened in frequency. The broadening of the backscatter spectrum is nearly Gaussian but must be corrected for temperature and pressure before the Doppler shift and the wind speed can be estimated. For Mie, scattering occurs for aerosol and cloud particles whose size is larger or similar to the wavelength of the incident light. The backscattered light has a relatively narrow frequency spectrum, which makes it easier to measure the Doppler shift accurately. The intensity of the backscattering depends on the concentration of the molecules and particles in the atmosphere. Thus, the Mie signal depends on the attenuated backscattering of the clouds (Marseille and Stoffelen, 2003) and the density of the aerosols, which varies greatly geographically, with most intensity occurring at the top of the optically thick clouds. Furthermore, high relative humidity leads to a swelling of hygroscopic aerosol particles and therefore an increase in backscatter intensity (Weissmann et al., 2005b). The scattering ratio γ is often used to quantify the amount of aerosols in the atmosphere, and represents the ratio between the total (molecular γ_{Mol} and particulate γ_A) and the molecular backscatter coefficients.

$$\gamma = \frac{\gamma_A + \gamma_{Mol}}{\gamma_{Mol}} \tag{2.6}$$

It is strictly equal to or greater than one and describes the contribution of the particles to the backscattered signal.

The ALADIN instrument

The Atmospheric Laser Doppler Instrument (ALADIN Schillinger et al., 2003) is a direct-detection high-spectral-resolution wind lidar with a Nd:YAG laser transmitter that operates at an ultraviolet wavelength of $\lambda = 354.8$ nm. The instrument emits laser pulses of around 60 mJ at a frequency of 50.5 Hz through its 1.5 m diameter Cassegrain telescope into the atmosphere. The ALADIN instrument consists of a two-channel receiver that allows the simultaneous measurement of wind speed from molecular (Rayleigh channel) and particulate (Mie channel) return signal (Fig.2.6), thus allowing wind retrieval in clear atmospheres and aerosol loaded regions (Stoffelen et al., 2005; Reitebuch, 2012).

The Rayleigh channel relies on the double-edge technique (Chanin et al., 1989; Garnier and Chanin, 1992; Flesia and Korb, 1999; Kovacic et al., 2000) which uses a sequential Fabry-Perot Interferometers (FPI) to measure wind speed by detecting molecular scattered light. After the backscattered laser signal has returned to the instrument, the interference between the emitted and the returned laser signal creates two sets of interference fringes, symmetrical to the emitted laser frequency. The intensity of the fringe depends on the phase difference between the two beams, which relies on the Doppler shift and the distances between the FPI mirrors. Two filters A and B are then used in sequence to isolate the two peaks with signal intensities $I_A(f)$ and $I_B(f)$ that lie on either side of the spectrum of the backscattered signal (Fig.2.7). Both filters have a certain spectral width and distance from each other to have a high transmittance for a certain wavelength range, allowing each peak to be isolated with high accuracy while blocking unwanted wavelengths. The interference fringes are detected with a Detection Front End Unit (DFU), which is then imaged by an Accumulation and Control and Calculation Device (ACCD) with a 16 x 16-pixel imaging zone and converted into a measurable signal. By comparing the intensities of the two filtered interference fringes, a differential measure of frequency change proportional to the speed of the scattering object can be calculated using the Rayleigh response (R_{Ray} Garnier and Chanin, 1992). The latter is defined as the frequency-dependent contrast ratio between the intensities transmitted through filters A and B

$$R_{Ray}(f) = \frac{I_A(f) - I_B(f)}{I_A(f) + I_B(f)} \tag{2.7}$$

With a Doppler shift to the right, the intensity $I_A(f)$ increases, resulting in a larger Rayleigh response $R_{Ray}(f)$. The Rayleigh contrast can thus finally be used to measure the wind along the Line Of Sight (LOS) using a suitable calibration and inversion mechanism (Tan et al., 2008; Dolfi-Bouteyre, 2008; Marksteiner et al., 2018). Since the FPI takes into account the total signal with the contributions of both Rayleigh and Mie signals, unwanted Mie signal can leak into the Rayleigh channel. This optical "cross-talk" can cause biases, especially in the case of strong Mie returns, as the Rayleigh-channel assumes pure molecular signal in the processing chain. For Mie winds, the Doppler

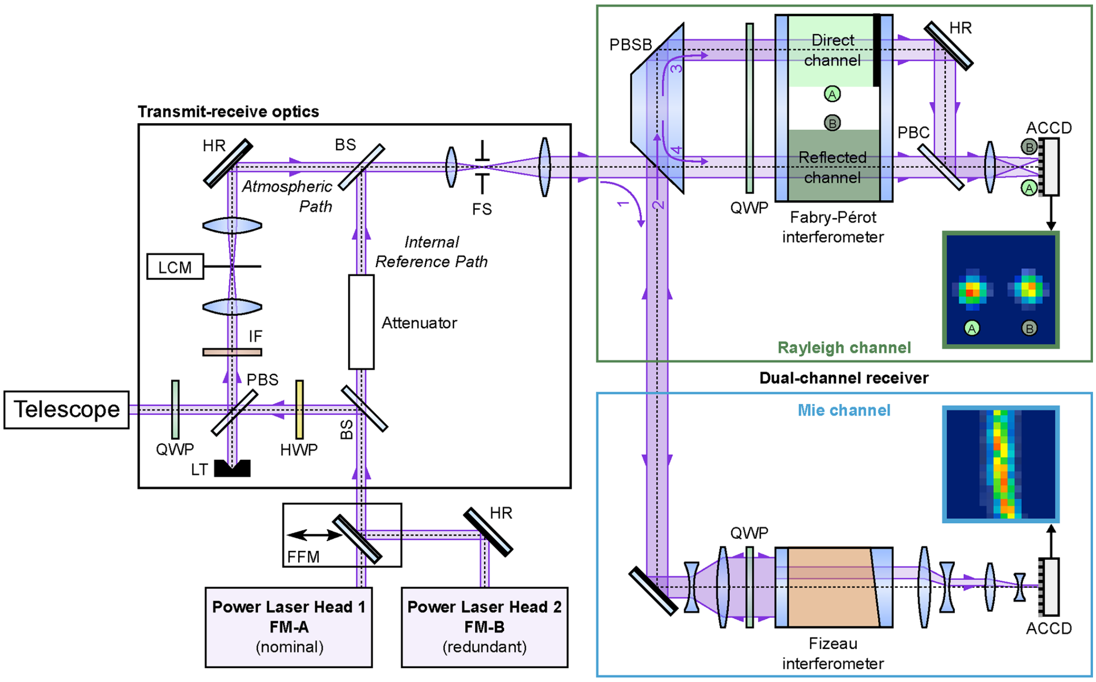

Figure 2.6: Sketch of the ALADIN optical receiver layout reproduced from Lux et al. (2021). QWP: quarter-wave plate; HWP: half-wave plate; PBS: polarizing beam splitter; PBSB: polarizing beam splitter block; PBC: polarizing beam combiner; FFM: flip-flop mechanism; BS: beam splitter; HR: high-reflectance mirror; LCM: laser chopper mechanism; FS: field stop; IF: interference filter; LT: light trap; ACCD: accumulation charge-coupled device. **From Witschas et al. (2022a) under the Creative Commons Attribution 4.0 International License (CC BY 4.0).**

shift is determined based on a fringe-imaging technique (McKay, 2002) using a the Fizeau interferometer. The latter consist of two plates slightly titled with respect to each other, with the emitted and returned light forming interferences fringes at distinct lateral positions along the plate. The lateral displacement of the interference fringe is approximately linearly depends with the frequency of the incident light, and vertically imaged onto a ACCD detector. The peak position referred to as the Mie response can then used to calculate the Doppler frequency shift, using a Nelder-Mead downward simplex algorithm (Nelder and Mead, 1965), which optimises the fit of the signal distribution using a Lorentzian function (Reitebuch et al., 2006; Rennie et al., 2020). The Mie response $R_{Mie}(f)$ can thus be written as

$$R_{Mie}(f) = x_0 + k \times \Delta f \tag{2.8}$$

with x_0, the Mie fringe centroid position of the transmitted pulse, and k the proportionality factor between the Doppler shift Δf and the Mie fringe shift (Lux et al., 2018). It should also be mentioned that the useful signal is defined as the total returned signal level per observation and includes corrections for solar background, dark current and Detection Front Offset (DCO).

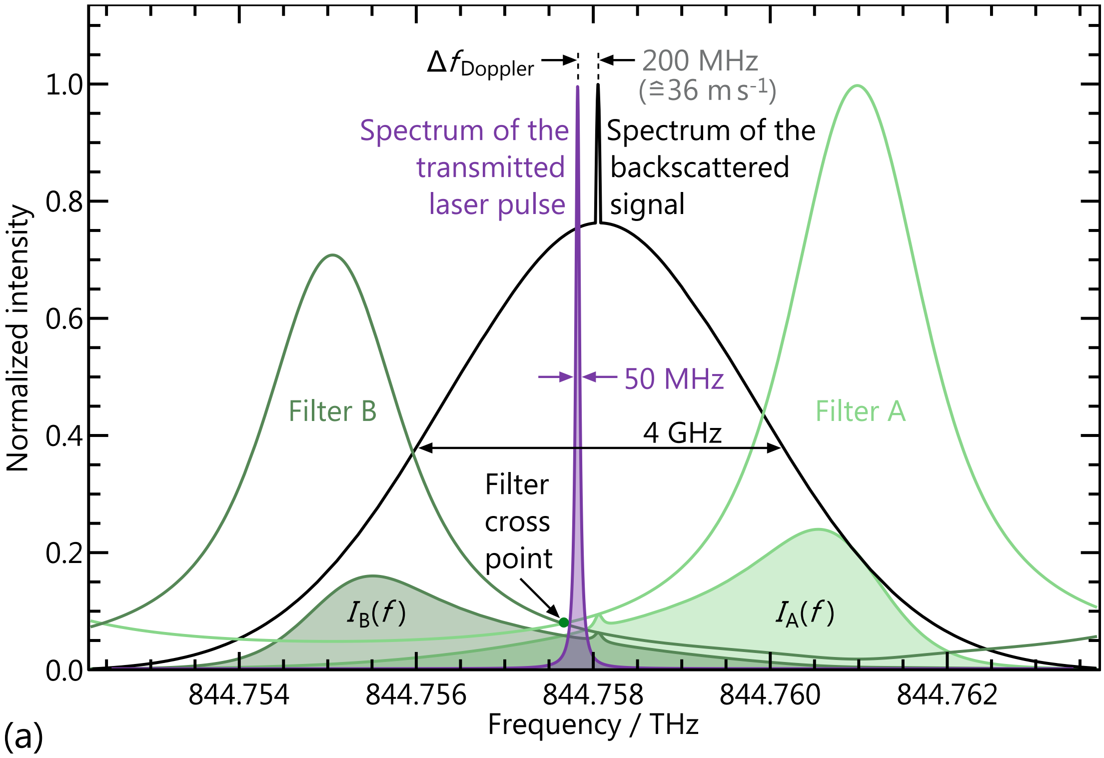

Figure 2.7: Spectral distribution of the transmitted laser pulse (purple) and the backscattered signal (black), which is composed of the narrowband Mie and the broadband Rayleigh component. The transmission spectra of the two FPI filters of the Rayleigh channel are shown in green, while the filled areas illustrate the respective intensities $I_A(f)$ and $I_B(f)$ transmitted through the filters A and B for determining the Doppler shift. **From Lux et al. (2018) under the Creative Commons Attribution 4.0 International License (CC BY 4.0).**

.

Error Estimates

The Error Estimates of the Rayleigh EE_{Ray} and Mie EE_{Mie} channels are quantifications of the measurements uncertainties that are provided by the Aeolus L2B processor (ATBD, 2020; Rennie and Isaksen, 2020; Lux et al., 2022a). The Rayleigh channel Error Estimate EE_{Ray} is based on the uncertainty of the Signal-to-Noise Ratio (SNR) of the spectrometer response R_{Ray} and takes into account error propagation arising from the sensitivity of the FPI, Poisson noise in the useful signal and the solar background. The Rayleigh response error σ_{Ray} is thereby given as

$$\sigma_{Ray} = \frac{2}{(I_A + I_B)^2}\sqrt{I_B^2\sigma_A^2 + I_A^2\sigma_B^2} \tag{2.9}$$

with

$$\sigma_A = \frac{I_A}{SNR_A} \propto \sqrt{I_A} \quad \text{and} \quad \sigma_B = \frac{I_B}{SNR_B} \propto \sqrt{I_B} \tag{2.10}$$

the noise terms of the two FPI filters with SNR_A and SNR_B the respective SNR values of filters A and B. Taking into account errors in the projection onto the Rayleigh HLOS and assuming that $I_A(f) = I_B(f)$, EE_{Ray} can be simplified as follows

$$EE_{Ray} \propto \frac{\sigma_A}{I_A} \propto \frac{1}{\sqrt{I_A}} \tag{2.11}$$

As a result, EE_{Ray} is proportional to the inverse squared root of the useful signal on the detector. Future baseline versions will include additional noise terms, such as noise related to atmospheric temperature and pressure, or cross-talk contamination, which influence the Rayleigh response (Dabas et al., 2008).

In contrary, the error in the Mie response σ_{Mie} is determined from the accuracy of the fringe peak position using the solution covariance of the Lorentzian fitting algorithm based on four characteristics of the signal shape, i.e the peak position, height, width and offset. It can be converted to the following Mie error estimate EE_{Mie}

$$EE_{Mie} = \frac{\lambda}{2\, R_{Mie}\, sin\theta}\, \sigma_{Mie} \tag{2.12}$$

with θ the projection angle with the horizontal axis. Thus, EE_{Mie} is mainly characterized by the accuracy of the Lorentzian fitting algorithm of the signal distribution, while EE_{Ray} is more related to the signal levels.

2.2.3 Orbit geometry

Aeolus was taken into orbit by ESA on 22th August 2018 from the Kourou spaceport in French Guinana. The launch was carried by Arianespace, using a Vega rocket which lifted off at 21:30 UTC. The ALADIN instrument is the main component mounted on the Aeolus satellite platform. The longevity of Aeolus depends primarily on the performance of ALADIN and the amount of propellant needed to prevent orbital drifting, resulting in a nominal lifetime of 3 years. The satellite flies in a sun-synchronous dawn-dusk orbit with an inclination of 96.97°, covering almost the entire globe and crossing the equatorial latitudes at 06:00 local mean solar time for the descending orbit and 18:00 for the ascending orbit. This allows Aeolus to sample at sunset and sunrise, when there is less convective activity and thus less cloud obstruction, as well as consistent temperature and lighting conditions. Aeolus is a low orbit satellite at an altitude of about 320 km to achieve sufficient accuracy and resolution in the wind measurements. The LOS points at 35° from the nadir to ensure best instrument performance and 90 ° from the satellite's ground track, eliminating the Doppler frequency shift caused by satellite velocity (Fig.2.8). To avoid the contribution of solar background radiation and reduce noise, the instrument is pointed in the opposite direction of the Sun toward the night side of the Earth (ESA, 1999). Aeolus mainly measures along the zonal wind direction for the tropical and mid-latitude parts of the track, at an angle of about 10° to the zonal direction, which allows better detection of the vertical wind shear that dominates in the zonal direction (Stoffelen and Marseille, 1998). At the poles, however, meridional wind information predominates. The satellite orbits the Earth at a speed of

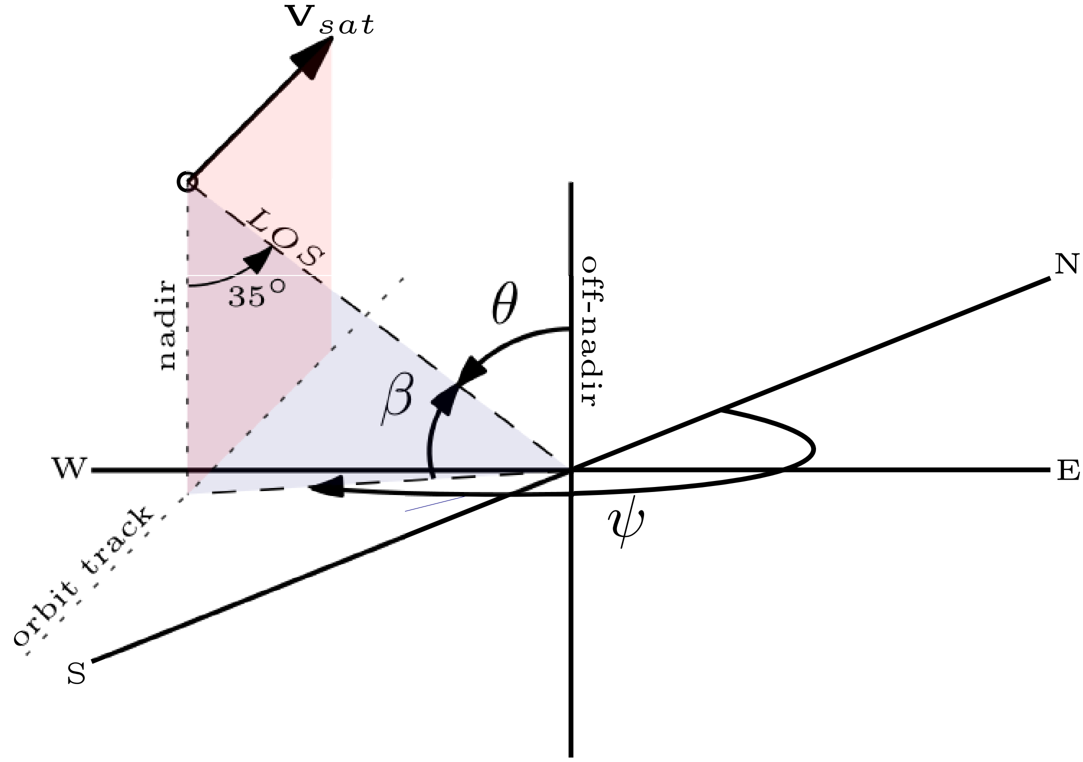

Figure 2.8: Geometry for the HLOS wind observation during the ascending orbit phase. **Courtesy Steven Albertema**.

about 7.5 kms^{-1} and completes about 15 revolutions per day with an orbital period of 90 minutes. This means that the satellite orbits the entire globe every 7 days, which corresponds to 111 orbits.

The horizontal projection of the LOS wind observation is referred to as the HLOS wind component $HLOS_{AEOLUS}$ can be retrieved by dividing the LOS wind observation LOS_{AEOLUS} with the sinus of the local incidence angle θ

$$HLOS_{AEOLUS} = \frac{LOS_{AEOLUS}}{sin\theta} \tag{2.13}$$

The HLOS wind vector can be further decomposed into zonal u and meridional v wind components

$$HLOS_{AEOLUS} = -u\, sin\psi - v\, cos\psi \tag{2.14}$$

with the azimuth angle ψ, which is the angle clockwise between the LOS pointing direction and geographical north, and is approximately ~260° for ascending and ~100° for descending orbits. Although a single line-of-sight observation cannot provide the full wind vector, Lorenc et al. (1992) has demonstrated that it can be assimilated into the ECMWF model and improve weather forecasting. In particular Horányi et al. (2015) has shown that the ECMWF model is able to derive 75% of the full wind vector information from a single line-of-sight wind observation, especially for medium-range forecasts. Finally, it should be mentionned that the sign convention of the HLOS wind is defined to be negative (positive) when the wind is measured towards (away) the instrument.

2.2.4 Measurement resolution

To ensure a sufficient SNR of the signal accumulation of the return signal, the wind measurements are averaged vertically and horizontally into single observations. The atmospheric return from individual laser pulses are accumulated on the detectors on board the spacecraft.

Horizontal resolution

Horizontally, the measurements are defined by the average of 20 accumulated laser pulses, corresponding to a minimum sample-length of 3 km. The sequence of 30 consecutive measurements define a Basic Repeat Cycle (BRC). The BRC profiles are subsequently processed into observations with 87 km nominal horizontal averaging length, performed on-ground for the Level 1B (L1B) products. The distance between two consecutive observations is 200 km, which corresponds to the typical spatial error correlation length of the wind patterns, providing independent observations to the Global Circulation Models (GCMs). The BRC can contain multiple wind profiles, with flexible horizontal averaging from the measurement scale to the observation scale, on the basis of the grouping algorithm in the L2B processor (Rennie et al., 2021). Rayleigh measurements are typically averaged over 87 km, owing to the larger shot noise, while Mie measurements are averaged between 10 and 15 km to achieve a good compromise between spatial resolution and SNR.

Vertical resolution

Vertical sampling is performed within 24 vertical elevation bins with a resolution that can vary from 0.25 km at lower elevations to 2 km at higher elevations, from the surface up to the lower stratosphere at 25km, sometimes up to 30 km. Thicker bins are generally used at higher altitudes, to accumulate enough signal due to the lower density of air molecules. They are defined by the Range Bin Settings (RBS) and can be adjusted up to eight times for one orbit, depending geographically on the under-laying topography or climate zone and between the respective detection channel (Rayleigh and Mie). In particular, RBS can be configured to meet the specific needs of scientific applications, with six primary settings: tropical, extratropical, Quasi-Biennial Oscillation (QBO), polar, eastern Mediterranean and Chile. For example, the tropical setting covers the entire tropics from 30°S to 30°N (Fig.2.9), with increased resolution between 12 and 15 km to accurately measure gravity waves and vertical mass fluxes. In contrast, the Extratropical settings are lower compared to the tropics, reaching a maximum height of about 17.5 km, with increased vertical resolution in the lower troposphere between 5 km and 10 km for a better sampling of the jet stream.

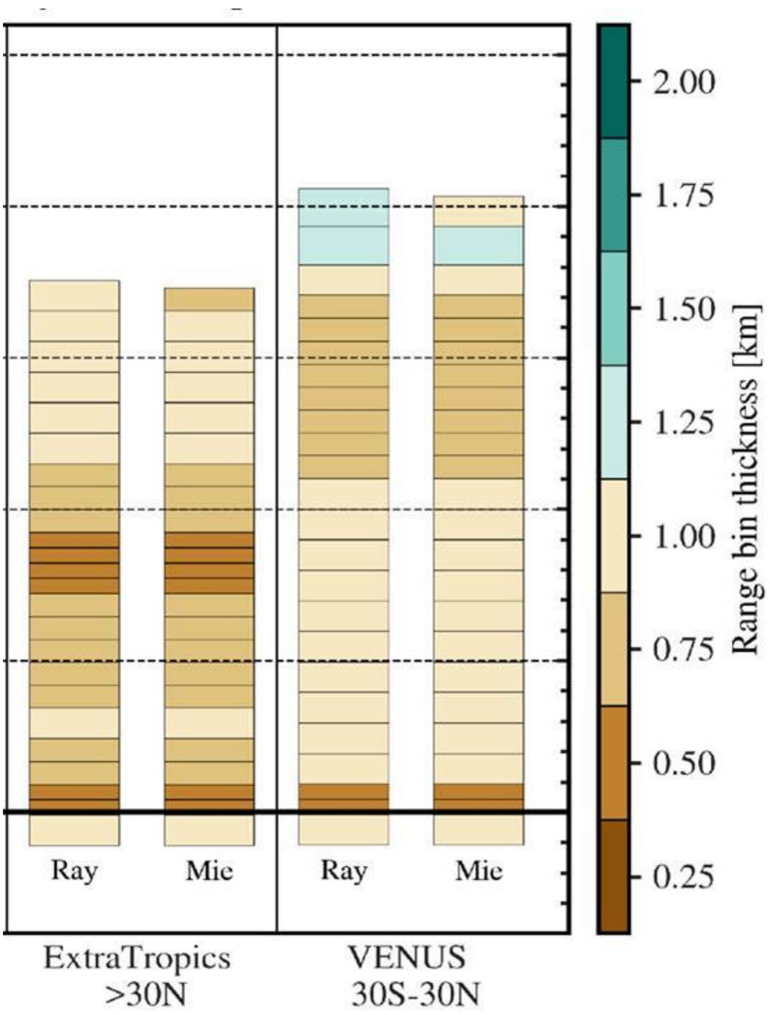

Figure 2.9: Tropical and Extratropical range bin thickness (km). Dotted lines represent vertical intervals of 5 km. **Courtesy Alexander Geiss and Sebastian Bley**.

2.2.5 Aeolus products overview

The data products are processed through a multi-stage processing chain generated by the Aeolus Payload Data Ground Segment (PDGS), with each level containing different information (Tan et al., 2008; Reitebuch et al., 2018; ATBD, 2020). In the first phase, the collected Aeolus data are forwarded to a ground station in Svalbard, where they are referred to as Annotated Instrument Source Packets (AISP). The data is then transferred to the Aeolus Processing Facility (APF) in Tromsø, Norway, where it is processed into Level 0 (L0) and Level 1A (L1A) products. In L1B, the data is cleaned, geolocated and projected onto the HLOS winds. The data are calibrated in terms of instrument offsets, atmospheric backgrounds, satellite orientation information and instrument responses using the Harmonic Bias Estimator. Further processing takes place at the Aeolus Calibration and Monitoring Facility (ACMF) in ESA-European Space Research Institute (ESRIN), where the Level 2A (L2A) and L2B products are generated. The L2A product is mainly designed to obtain information on atmospheric

Table 2.1: Overview of the Aeolus data products and product levels.

Level	Data product	Description
Level 0	Raw data	Raw data as measured by the Aeolus satellite
Level 1A	Geo-located unprocessed observational data	Intermediate level between Level-0 and Level 1B.
Level 1B	Geo-located calibrated observational data	Near-real time product. Measurement-scale data with preliminary HLOS wind profiles with basic calibration.
Level 2A	Aerosol and cloud layer optical properties	Off-line product. Aerosol (extinction, backscatter profiles, optical depth) and cloud (layer, coverage, top heights) information along the satellite's orbit.
Level 2B	Meteorologically representative HLOS winds observations	Near-real time product. Fully processed profiles of HLOS winds at ECMWF suitable for assimilation. Temperature and pressure correction using ECMWF model data. Contains group measurements and scene classification
Level 2C	Aeolus-assisted wind vectors	Supplementary product based on L2B product. Contains vertical, zonal and meridional wind profiles, using ECMWF model output after assimilation.

clouds and aerosols from the raw measurements and optical properties of the L1B product. The L2B is the primary data products from Aeolus. The L2B wind retrieval software is developed by ECMWF and the KNMI and provides HLOS wind observations and uncertainty estimates suitable for NWP and research purposes (Rennie et al., 2021). It contains the final horizontal projection of the LOS wind speed profiles of the Rayleigh and Mie channels, where all necessary calibration and instrument corrections have been performed (Dabas et al., 2008). Among the various steps within the L2B processor (ATBD, 2020), the software corrects for the effect of atmospheric temperature and pressure broadening on the Rayleigh-clear winds to avoid systematic biases (Dabas et al., 2008). Since Aeolus does not measure temperature and pressure, the L2B processor utilizes short-range forecasts from ECMWF's Integrated Forecasting System (IFS). The L2B product also provides scene classification based upon the backscatter ratio corresponding to the wind originating from a 'cloudy' or 'clear' atmospheric region, resulting in Rayleigh-clear, Rayleigh-cloudy, Mie-clear and Mie-cloudy observation types. Most of the wind data originate from the Rayleigh channel, which is related to the scattering by air molecules. Level 2C (L2C) is generated in the final processing stage, also conducted at ECMWF. It combines assimilated Aeolus data with model fields to reconstruct the horizontal and vertical 3D wind components. An overview of the Aeolus data and products can be found in Table 2.1. Throughout the processing chain, the L1B and L2B processors are continuously updated into different baseline versions to account for revisions and identified problems. The processor development and product reprocessing are carried out through a collaborative effort between the Aeolus Data Science and Innovation Cluster (DISC) and the Aeolus PDGS. This leads to different HLOS wind observations and quality in different time periods.

2.3 Data assimilation

DA is a technique that aims to combine collected observations and NWP "prior knowledge", usually a short-range forecast (sometimes called background or first guess), to obtain an "analysis" that is the best estimate of the true state of the system (Nychka and Anderson, 2010). DA is used in a variety of applications in the geosciences and engineering, but originated in the field of meteorology with the development of weather forecasting. As computers became more powerful, NWP models were able to approximate global atmospheric flows by integrating nonlinear partial differential equations that could be used to predict future weather. Nevertheless, the high non-linearity of the simulated primitive equations, makes it difficult to propagate initial condition uncertainties and can lead to large uncertainties in model predictions. For the purpose of weather forecasting, those numerical models require real atmospheric observations to have accurate initial conditions. However, observations are unevenly distributed geographically and temporally and are subject to a wide range of uncertainties that do not match the spatial and temporal resolution of the NWP models. The purpose of DA is to combine these observations with model predictions that take into account the corresponding observational and model errors. The analysis is usually a weighted average of observations and model forecasts, with the weighting determined by the uncertainties in the observations and model forecasts. DA can also provide indirect information about variables that are not measured directly, through error covariances spreading the information in space and across variables. These covariances can be estimated with statistical methods taking into account model and observation uncertainties, using empirical techniques based on climatology or based on an ensemble of forecasts. However, the high dimensionality of the model state results in a large number of unknowns that have to be estimated, which can be computationally challenging. There are several DA approaches to estimate the true state of the atmosphere given the nonlinear evolution operator and the large dimensionality of the observations. Variational DA and ensemble DA approaches are highly popular in the DA community, both methods offering advantages and limitations given the nature of the problem to be solved. Variational methods iteratively minimise a cost function using a gradient-based approach, while ensemble methods use error estimates from an ensemble. Hybrid approaches, such as those used by ECMWF and DWD, combine elements of both variational and ensemble methods. Here we will provide an overview of the different DA algorithms that are used in operational settings in the ECMWF and DWD DA systems.

2.3.1 The Ensemble Kalman Filter (EnKF)

The Ensemble Kalman Filter (EnKF) is a DA technique, part of the Kalman filter family, suitable for high-dimensional problems. The EnKF operates on an ensemble of the model state vector which is updated with observational data to produce the best estimate of the true state. Here we provide a description of the stochastic EnKF, which is used in combination with 4D-Var in the ECMWF system, as well as the Local Ensemble Transform Kalman Filter (LETKF) used in the DWD system.

The stochastic Ensemble Kalman Filter (EnKF)

The stochastic EnKF is a data assimilation technique that uses an ensemble approach to represent forecast uncertainty within a Kalman filter framework which updates the analysis using the available observations. The stochastic EnKF can employ stochastic perturbations in both the background and the observations to account for model and observational errors. Suppose the state of the atmosphere is represented by an ensemble of model states $\mathbf{x}_k$ that approximates the state distribution

$$\mathbf{x}_k, \quad k = \{1, \ldots, N\} \tag{2.15}$$

with k the ensemble member of an ensemble size of N. We denote $\mathbf{x}_k^a$, the analysis ensemble state that was used as initial conditions at time $t-1$ to generated the background ensemble state $\mathbf{x}_k^b$ at time t. The background perturbation matrix $\mathbf{X}^b$ is a matrix where the k-th column contains the departures between each background ensemble state and background ensemble mean $\overline{\mathbf{x}}^b$. The background covariance matrix can be estimated by

$$\mathbf{B} = (N-1)^{-1}\mathbf{X}^b(\mathbf{X}^b)^T \tag{2.16}$$

In the analysis step, the observations are assimilated into the ensemble of analyses, with the analysis of each ensemble member given by

$$\mathbf{x}_k^a = \mathbf{x}_k^b + \mathbf{K}(\mathbf{y}^o + \mathbf{r}_k - \mathbf{H}\mathbf{x}_k^b) \tag{2.17}$$

where $\mathbf{H}$ is the observation relation operator, $\mathbf{y}^o$ the observation vector, $\mathbf{r}_k$ the random noise vector for the observations and $\mathbf{K}$ the Kalman gain. The latter can be expressed as

$$\mathbf{K} = \mathbf{B}\mathbf{H}^T\left(\mathbf{H}\mathbf{B}\mathbf{H}^T + \mathbf{R}\right)^{-1} \tag{2.18}$$

where $\mathbf{R}$ is the observation error covariance matrix. A deterministic optimal estimate can be additionally derived from the mean of the ensemble of forecasts, such as

$$\mathbf{x}^a = \overline{\mathbf{x}}^b + \mathbf{K}\left(\mathbf{y}^o - \mathbf{H}\overline{\mathbf{x}}^b\right) \tag{2.19}$$

with no noise term. Finally, the analysis error covariance matrix can be expressed as following

$$\mathbf{A} = \mathbf{I} - \mathbf{KHBI} - \mathbf{KH}^T + \mathbf{KRK}^T \tag{2.20}$$

The obtained ensemble and deterministic analysis is then used as the prior state in the next assimilation cycle, which is then iteratively repeated to produce a sequence of analyses and corresponding uncertainty estimates.

The Local Ensemble Transform Kalman Filter (LETKF)

In this section, we introduce the LETKF and its main equations. For a detailed derivation of the LETKF equations, see Hunt et al. (2007). Similar to the stochastic EnKF, the background covariance matrix can be estimated by

$$\mathbf{B} = (N-1)^{-1}\mathbf{X}^b(\mathbf{X}^b)^T \tag{2.21}$$

The latter is mapped from the model grid point space into the observation space by use of the observation relation operator $\mathbf{H}$, such as $\mathbf{y}_k^b = \mathbf{H}(\mathbf{x}_k^b)$. The corresponding background perturbation matrix in observation space is denoted as $\mathbf{Y}^b$. The analysis is therefore given by

$$\overline{\mathbf{x}}^a = \overline{\mathbf{x}}^b + \mathbf{X}^b\overline{\mathbf{w}} \tag{2.22}$$

where $\overline{\mathbf{w}}$ is the mean weighting vector computed as

$$\overline{\mathbf{w}} = \widetilde{\mathbf{A}}(\mathbf{Y}^b)^T\mathbf{R}^{-1}(\mathbf{y}^o - \overline{\mathbf{y}}^b) \tag{2.23}$$

with $\widetilde{\mathbf{A}}$ is the analysis error covariance matrix in ensemble space. The latter can be expressed as

$$\widetilde{\mathbf{A}} = \left[(\mathbf{Y}^b)^T\mathbf{R}^{-1}(\mathbf{Y}^b) + (N-1)\mathbf{I}\right]^{-1} \tag{2.24}$$

with $\mathbf{I}$ the identity matrix. Finally, the ensemble perturbation of the analysis field is determined by

$$\mathbf{X}^a = \mathbf{X}^b\left[(N-1)\tilde{\mathbf{A}}\right]^{1/2} \tag{2.25}$$

The latter provides an estimate of the analysis uncertainty, which can be used to construct an analysis ensemble $\mathbf{x}_k^a$ by perturbing the analysis ensemble mean $\overline{\mathbf{x}}^a$. An important component of the LETKF is localisation. During the analysis step, only observations within a certain distance from the respective grid points are assimilated and the respective observation error is increased according to their distance by a localisation weight. This localisation weight is usually described by Gaussian-like rational functions (Gaspari and Cohn, 1999; Miyoshi and Yamane, 2007), decaying from 1 to 0 with the distance.

2.3.2 Variational data assimilation

Variational DA methods were first introduced in the early 1950s (Sasaki, 1955, 1958) and became very popular in the 1990s, especially in the meteorology community (Parrish and Derber, 1992; Courtier et al., 1998; Andersson et al., 1998). The method can treat a problem globally by finding an optimal solution that minimizes a global cost function considering model and observation constraints. The two most widely used variational approaches in NWP centers are presented here, namely the Three-Dimensional Variational assimilation (3D-Var) and the Four-Dimensional Variational assimilation (4D-Var) methods. The former considers the three-dimensional space at a specific point in time, while the latter also considers the temporal evolution of the model state.

Three-dimensional variational assimilation (3D-Var)

The three-dimensional variational assimilation (3D-Var) consists of minimising the cost function J to find the optimal analysis $\mathbf{x}^a$. The 3D-Var cost function is given by

$$J(\mathbf{x}) = \frac{1}{2}(\mathbf{x} - \mathbf{x}^b)^T \mathbf{B}^{-1}(\mathbf{x} - \mathbf{x}^b) + \frac{1}{2}(\mathbf{y}^o - \mathcal{H}(\mathbf{x}))^T \mathbf{R}^{-1}(\mathbf{y}^o - \mathcal{H}(\mathbf{x})) \tag{2.26}$$

where $\mathbf{x}_b$ is the background state, $\mathbf{y}_o$ are the observations, $\mathcal{H}(\mathbf{x})$ is the nonlinear observation operator, $\mathbf{B}$ is the background error covariance matrix, and $\mathbf{R}$ is the observation error covariance matrix. There are numerous methods for performing this minimization, which depend on the optimisation problem, i.e. the structure of the cost function and the form of the observation operator, which can be either linear or non-linear. Minimisation is usually performed numerically in an iterative process. The optimal analysis can be derived by iteratively adjusting the model state in the direction of the negative gradient until convergence, with

$$\nabla_x J(\mathbf{x}) = \mathbf{B}^{-1}(\mathbf{x} - \mathbf{x}^b) - \mathbf{H}^T \mathbf{R}^{-1}(\mathbf{y}^o - \mathcal{H}(\mathbf{x})) \tag{2.27}$$

where $\mathbf{H}$ is the Jacobian matrix, i.e the tangent linear of the observation operator $\mathcal{H}$ ($\mathbf{H}^T$ is the corresponding adjoint operator).

Four-dimensional variational assimilation (4D-Var)

Four-dimensional variational assimilation (4D-Var) is a temporal extension of 3D-Var, in which the optimisation is not fixed to a specific point in time, but aims for the optimal distance between the model trajectory and the observations in a specific time window . The distribution of observations is thus taken into account both spatially and temporally in the minimization process. The standard formulation of the cost function (Le Dimet and Talagrand, 1986) is given by

$$J(\mathbf{x}_0) = \frac{1}{2}(\mathbf{x}_0 - \mathbf{x}^b)^T \mathbf{B}_0^{-1}(\mathbf{x}_0 - \mathbf{x}^b) + \frac{1}{2}\sum_{i=1}^{\tau}[\mathbf{y}_i^o - \mathcal{H}(\mathbf{x}_i)]^T \mathbf{R}_i^{-1}[\mathbf{y}_i^o - \mathcal{H}(\mathbf{x}_i)] \tag{2.28}$$

where $\mathbf{x}_0$ is the model state at time t_0 and $\mathbf{x}_i$ the model state at time t_i. The propagation of the model state from time t_i to t_{i+1} can be carried out by means of the nonlinear NWP model $M_{i+1,i}$ such as

$$\mathbf{x}_{i+1} = M_{i+1,i}(\mathbf{x}_i) \tag{2.29}$$

Considering an atmospheric perturbation, the model can be linearised in the vicinity of $\mathbf{x}_i$ as following

$$\delta\mathbf{x}_{i+1} = \mathbf{M}_{i+1,i}(\mathbf{x}_i)\delta\mathbf{x}_i \tag{2.30}$$

with $\mathbf{M}_{i+1,i}$ the tangential linear model. The analysis can again be determined by iteratively adjusting the model state in the direction of the negative gradient until convergence.

$$\nabla_{x_0} J(\mathbf{x_0}) = \mathbf{B}^{-1}(\mathbf{x_0} - \mathbf{x}^b) - \sum_{i=1}^{\mathcal{T}} \mathbf{M}_{i,0}^T \mathbf{H}_i^T \mathbf{R}_i^{-1}(\mathcal{H}_i(\mathbf{x}_i) - \mathbf{y}_i^o) \tag{2.31}$$

$\mathbf{M}_{i,0}^T$ is the adjoint model and is computed from the tangent linear model as a backward integration from time t_i to t_0 with

$$\mathbf{M}_{i,0}^T = \mathbf{M}_{1,0}^T \mathbf{M}_{2,1}^T ... \mathbf{M}_{i,i-1}^T \tag{2.32}$$

However, the backward integration of the adjoint model can be very computationally expensive with slow convergence due to non-linearities. To reduce the computational cost, an approximation of the 4D-Var of was proposed by (Courtier et al., 1994), namely the incremental approach. The incremental algorithm for minimising the cost function uses forward integration of the tangential linear model with reduced model resolution.

2.3.3 Error modeling

Representing the error covariances correctly is essential in both variational (Fisher, 2003) and ensemble (Sénégas et al., 2001) DA algorithms. The structure of the error covariances describes how the errors are correlated in space and time and between variables, so that e.g. wind field observations can be used to retrieve mass field information. The observation and background error covariance matrices are defined as

$$\mathbf{B} = \mathbf{Cov}(\epsilon^b, \epsilon^b) \tag{2.33}$$

$$\mathbf{R} = \mathbf{Cov}(\epsilon^o, \epsilon^o) \tag{2.34}$$

where

$$\epsilon^b = \mathbf{x}^b - \mathbf{x} \tag{2.35}$$

$$\epsilon^o = \mathcal{H}(\mathbf{x}) - \mathbf{y}^o \tag{2.36}$$

denote the background and observation errors, respectively. To simplify the probability distribution of the uncertainties, errors are generally assumed to be uncorrelated and zero-mean Gaussian distributed

$$\epsilon^b \approx \mathcal{N}(0, \mathbf{B}) \tag{2.37}$$

$$\epsilon^o \approx \mathcal{N}(0, \mathbf{R}) \tag{2.38}$$

However, both **R** and **B** are difficult to construct empirically because of the unknown statistical relationship to the true state and the high dimensionality of the problem. The performance of the DA depends on the quality of both model and observation errors. The latter usually depend on the various sources of uncertainty associated with the measurement process (***instrumentation error***) or within the DA process, such as errors in the representation of the model state by the observations (***representativeness errors***) and errors arising from the interpolation of model fields into the observation space (***operator error***). Background errors, in contrast, are uncertainties in the model state that are related to the limitations in the representation of physical processes as well as errors of the preceding analysis that was used to initialize the forecasts. The ensemble estimates of the background error also includes **sampling errors** due to limited ensemble size. A proper description of the correlation between variables and different scales is essential to improve the accuracy of the DA process.

2.3.4 Operational data assimilation configurations

This section provides an overview of the data assimilation systems used operationally at ECMWF and DWD.

ECMWF

The operational system of ECMWF is based on the state-of-the-art operational weather prediction system IFS that provides four forecast runs per day (00/06/12/18 UTC) with a horizontal resolution of about 9 km and 137 vertical model layers globally. ECMWF operates a hybrid system known as Ensemble Data Assimilation (EDA), which combines the ensemble 4D-Var approach at the lower resolution of 18 km with a deterministic 4D-Var analysis at the full model resolution of 9 km. In the EDA system, an ensemble of 50 independent 4D-Var analyses is performed, which allows the quantification of forecast uncertainties obtained from observations and model perturbations (e.g. sea surface temperature (SST)). The deterministic 4D-Var analysis is then performed, combining the climatological background and the ensemble-derived background error covariance matrices from the EDA. The observations are assimilated following a two-step analysis process, starting with an early data analysis cycle with a short time window of 6 hours, used for the High-RESolution forecasts (HRES) at 00 and 12 UTC. This is followed by a Long-Window Data Assimilation (LWDA) analysis with a 12-hour assimilation window, which allows late-arriving observations to be incorporated into the final analysis. For example, for the 00 UTC (12 UTC) assimilation window, the LWDA cycle starts at 18 UTC (06 UTC) on the previous (current) day and ends at 06 UTC (18 UTC) on the current day. The LWDA analysis is then used as the initial condition for the short-range forecast used in the next DA and LWDA analyses. By combining the ensemble and deterministic approaches, the EDA system assimilates about 40 million observations per day to provide accurate initial conditions for reliable weather forecasts.

DWD

The DWD uses the global Icosahedral Nonhydrostatico (ICON) model to produce deterministic forecasts worldwide with a native resolution of 13 km and 90 atmospheric levels. The assimilation system is based on a hybrid approach combining an LETKF and 3D-Var. The LETKF (Hunt et al., 2007; Schraff et al., 2016) algorithm is used to dynamically generate the background error covariance matrix, which is combined with a climatological static background error covariance matrix, that has the advantage of smaller sampling errors. By combining both approaches linearly, the Hybrid Variational Ensemble Kalman Filter (VarEnKF) can generate a hybrid background error covariance matrix with 70% of the weight given to the LETKF and 30% to the 3D-Var components. This allows the incorporation of temporal evolution which enables a more comprehensive use of the observational data. The LETKF ensemble forecasts are composed of 40 members at a 40 km coarse resolution, combined with a 3-hourly cycled 3D-Var to provide the initial conditions for the ICON forecasts. The 3D-Var algorithm finally solves the large-scale problem to achieve a deterministic analysis. Prior to assimilation, observations also undergo a Variational Quality Check (VarQC) to handle outliers and verify for realistic probability density functions of the observation errors. As a title of comparison, ECMWF assimilates about ten times more data than DWD, with a significant proportion of this coming from satellite radiation measurements.

3. Research questions

The broad objective of this thesis is to investigate the impact of Aeolus wind observations in the tropics. Since Aeolus is a research and demonstration mission, Cal/Val activities and NWP impact studies are essential to evaluate Aeolus wind products and fully exploit the benefits of this technology for the purpose of weather forecasting.

Research questions 1

First, the quality of the Aeolus products in the tropics must be assessed to ensure that the data are accurate and can be used effectively for NWP purposes. To this end, radiosondes have been launched over the tropical Atlantic region, extending from the Caribbean to the Cabo Verde Islands, as part of the Joint Aeolus Tropical Atlantic Campaign (JATAC) during August-September 2021. Especially during boreal summer, the atmospheric conditions in this region are characterized by a variety of tropical features with mineral dust and convective cloud types that can interfere with Aeolus measurements. Radiosondes, which provide very accurate wind profiles of the lower 25 km of the atmosphere, were used to identify biases and random errors in both the Rayleigh-clear and Mie-cloudy measurement channels. The first research focus concerns the validation of Aeolus wind observations with radiosondes over the tropical Atlantic. This addresses the following research questions:

RQ 1.1 What is the quality of Aeolus L2B wind products in the tropics in terms of systematic and random errors?
RQ 1.2 What are the error dependencies of Rayleigh-clear in terms of co-location features and the presence of clouds and dust?
RQ 1.3 What are the error dependencies of Mie-cloudy in terms of co-location features and the presence of clouds and dust?

Research questions 2

Having assessed the quality of Aeolus in this region, sufficient understanding of its performance is provided for an assessment of the NWP impacts of Aeolus. It is particularly important to demonstrate the impact of Aeolus in the adjacent region where the Cal/Val was conducted, namely the WAM during the boreal summer of 2019 and 2020. This is accomplished using Observing System Experiment (OSE)s that were conducted in the operational systems of ECMWF and DWD. This region is of particular importance because of its low predictability, sparse observational network, and socioeconomic significance. Assessing the impact of Aeolus on key features of the atmospheric wind circulation, such as the AEJ-North and TEJ, in both the analysis and forecast fields, can provide substantial insight into the impact of Aeolus in the tropics. The second research focus consequently addresses the impact of Aeolus wind observations on the representation of the WAM circulation in the operational systems of ECMWF and DWD. The corresponding research questions can be formulated as follows:

RQ 2.1 Which atmospheric features of the WAM can Aeolus effectively sample?
RQ 2.2 What is the influence of Aeolus on wind analysis in the WAM in the ECMWF and DWD operational systems?
RQ 2.3 What is the impact of Aeolus on wind forecasts in the WAM in the ECMWF and DWD operational systems?

Research questions 3

Having investigated the impact of Aeolus on a specific tropical region, it is critical to understand the effect of Aeolus on the representation of large-scale tropical dynamics, such as EWs in both operational systems. EWs are critical in the tropics as they modulate much of the tropical weather and are a source of untapped predictability that Aeolus can potentially leverage. Additionally, it is important to isolate particular high NWP impact events on wind predictions to investigate the underlying mechanism that contribute to the observed improvements. The third research interest focuses on the impact of Aeolus wind observations on the representation of EWs. This addresses the following research questions.

RQ 3.1 What is the impact of Aeolus on EWs predictions in the tropics?
RQ 3.2 How does Aeolus affect the modulation of tropical rainfall associated with EWs?
RQ 3.3 What are the dynamical mechanisms that contribute to the observed improvements?

4. Data and methods

4.1 Observational Data

4.1.1 Aeolus wind products

For the validation study of Aeolus using radiosondes, data from the near-real-time version Baseline product 12 (L2bP 3.50) are used. We evaluate all observation types and corresponding Error Estimates (EEs) of the Level 2B (L2B) product except Mie-clear, which should not be detectable in clear sky conditions. Additionally, two Level 1B (L1B) products are used, namely the Scattering Ratio (SR) and the useful signal. Note that the SRs of the L2B products are not used, as some SRs were manually set to one during the processor baseline to eliminate a cross-talk correction, which had detrimental effects on the wind quality. The useful signal represents the returned signal levels per observation and comprises corrections for the solar background, the dark current and the Detection Front Offset (DCO). Here we apply an additional range correction and signal normalization that takes into account the different range bin thickness and distances between the instruments and the height bins.

For the Numerical Weather Prediction (NWP) impact studies, both the reprocessed Aeolus L2B product and the European Space Agency (ESA) Payload Data Ground Segment (PDGS) Near-Real Time (NRT) operational products with PDGS baslines 2B10 are used, where a bias correction for M1 mirror temperature variations and additional instrumental drift biases are included. In addition, we use feedback files from the Meteorological Archival and Retrieval System (MARS), which are generated at the end of each assimilation cycle at European Centre for Medium-Range Weather Forecasts (ECMWF). These reports contain information on the assimilated observations, the assimilation system and the forecast model. In this study, the short-range forecast or "background" equivalents of Aeolus observations are used as an additional reference to validate Aeolus Horizontal Line of Sight (HLOS) winds.

4.1.2 Radiosondes

The radiosondes were launched from three different locations over the tropical Atlantic and coordinated by different research components of Joint Aeolus Tropical Atlantic Campaign (JATAC). Between the 7 and 28th of September 2021, a total of 37 radiosondes

Table 4.1: Overview of Aeolus overflights and associated radiosonde profiles. **From Borne et al. (2024) under the Creative Commons Attribution 4.0 International License (CC BY 4.0).**

	Week day	Start and stop time	Orbit node	Co-location radius	Number of profiles
Sal	Tuesday	07:28 – 07:29 UTC	Descending	50 km	3
	Thursday	19:23 – 19:24 UTC	Ascending	180 km	3
	Friday	19:36 – 19:37 UTC	Ascending	280 km	3
Saint Croix	Monday	10:17 - 10:18 UTC	Descending	90 km	3
	Wednesday	22:12 – 22:13 UTC	Ascending	160 km	3
	Thursday	22:25 – 22:26 UTC	Ascending	340 km	1
Puerto Rico	Tuesday	10:29 – 10:30 UTC	Descending	160 km	2
	Thursday	22:25 – 22:26 UTC	Ascending	100 km	2

were launched from Sal airport in Cape Verde, 9 of them corresponding to Aeolus overflights. The launches were coordinated by the Karlsruhe Institute of Technology (KIT) with local support from the JATAC team. This was accomplished using the DFM-09 (GRAW) light weather radiosondes, which measure air pressure, air temperature, relative humidity, wind speed and wind direction. The vertical resolution depends on the ascent speed, which varies with the amount of helium in the balloon, but can generally be estimated at about 5 ms^{-1}. Most of the radiosondes launched at Sal were ingested into the Global Telecommunication System (GTS).

The radiosondes launched on the Virgin Islands were organised by National Aeronautics and Space Administration (NASA)'s Convective Processes Experiment-Aerosols and Wind campaign (CPEX-AW) component of JATAC, with the University of Utah conducting the launches on Saint Croix and the University of Oklahoma conducting the launches from Puerto Rico. On Saint Croix, launches were conducted from Carambola between 19 August 2021 and 14 September 2021. Altogether 73 launches were conducted, of which a total of seven radiosondes were used to validate Aeolus in this study. As for Sal, these measurements were performed with the radiosonde instrument DFM-09 (GRAW). Lastly, 32 launches were conducted from the University of University of Puerto Rico at Mayagüez (UPRM) campus between 26 August and 14 September 2021, 7 of which could be used for the validation of Aeolus. All launches were performed with iMet-4 radiosondes from the International Met System. As with DFM-09, the iMet-4 radiosondes provide measurements of wind speed, wind direction, temperature, humidity and air pressure. The radiosonde data also underwent a quality control check using the Atmospheric Sounding Processing Environment (ASPEN) software (Martin and Suhr, 2021) developed by the National Center for Atmospheric Research (NCAR). A summary of the radiosonde launches and weather events sampled at UPRM was provided by Rios-Berrios et al. (2023).

The total number of radiosonde profiles corresponding to Aeolus overpasses thus amounts to 20, of which 12 correspond to ascending and 8 to descending orbits of Aeolus. An overview of the launches from the different sites can be found in Table 4.1, along with other co-location parameters fully discussed in Section 4.4.2.

4.1.3 Satellite-based observations

EUMETSAT SAFNWC Cloud type product

The Satellite Application Facility for supporting NoWCasting and very short range forecasting (SAFNWC) (Alonso Lasheras et al., 2005) developed a number of satellite-based meteorological products distributed by the European Organisation for the Exploitation of Meteorological Satellites (EUMETSAT). Among others, they provide the Cloud Type (CT) product (Derrien and Le Gléau, 2005), which is a detailed scenery classification of clouds based on different main classes.

The baseline data originate from the Spinning Enhanced Visible and Infrared Imager (SEVIRI) operated onboard the second generation METEOSAT geostationary satellites (MSG). Multispectral thresholding techniques (Saunders and Kriebel, 1988; Derrien et al., 1993; Stowe et al., 1999) are subsequently applied in the SAFNWC software to process the SEVIRI/MSG images into the various NWC products. The product is available with a temporal resolution of 15 minutes and a nadir spatial resolution of 3 km, compared to 11 km at the edge of the field of view.

In this thesis, CT is used to identify the cloud type and cloud cover along the Aeolus tracks and to assess the quality of the Aeolus wind products relative to the presence of clouds. More specifically, we identify the pixels closest to each track of Aeolus and determine the average percentage of cloud cover at each altitude based on a cloud classification. According to this classification, a measurement bin is considered as cloudy, if it is situated within or below a cloud. This refers to following classes for altitudes above 16 km (very high clouds), between 7 and 16 km (very high and high cloud types), between 3 and 7 km (very high, high, mid-level, low and fractional cloud types) and finally below 3 km (very high, high, mid-level, low, very low and fractional cloud types).

GPM IMERG

For precipitation, we use the globally gridded rainfall product Integrated Multi-Satellite Retrievals for Global Precipitation Measurement (IMERG) (Huffman et al., 2015), which is estimated using information from the Global Precipitation Mission (GPM) satellite constellation. The precipitation data was aggregated to 12-hourly on a horizontal grid of 1°.

4.2 Model data

ERA5 reanalysis

For the NWP impact studies, forecasts are verified against the ERA5 reanalysis (Hersbach et al., 2020), which is a robust and relatively independent reference as Aeolus is not assimilated in this dataset. The ERA5 product is constructed using an older version of the Integrated Forecasting System (IFS) Four-Dimensional Variational assimilation (4D-Var), namely CY41R2 with a resolution of 31 km. Output is provided on 37 interpolated pressure levels.

CAMS Dust products

The fourth generation of ECMWF Global Atmospheric Composition Reanalysis (EAC4) (Inness et al., 2019) is produced by Copernicus Atmosphere Monitoring Service (CAMS) global atmospheric composition and prediction (Benedetti et al., 2009; Morcrette et al., 2009), with the main objective of global aerosol monitoring. EAC4 relies on ECMWF's IFS, which has been extended to predict and assimilate aerosols (Rémy et al., 2019), trace gases (Flemming et al., 2015; Huijnen et al., 2019) and greenhouse gases. The IFS meteorological and atmospheric composition models are combined with data assimilation from satellite products using the 4D-Var data assimilation scheme in CY42R1. In particular, CAMS assimilates the Aerosol Optical Depth (AOD) at 550 nm derived from MODIS and the Polar Multi-Sensor Aerosol Optical Properties (PMAp). Reanalysis outputs are provided on three-dimensional time-consistent fields interpolated on 25 pressure levels, a horizontal resolution of about 80 km and a sub-daily time resolution of 6 hours.

For the validation study using radiosonde, the dust-aerosol mixing ratio is averaged along each track and projected onto Rayleigh-clear and Mie-cloudy measurement bins to obtain an estimate of the dust concentration for each observation.

4.3 Observing system experiments (OSEs)

An Observing System Experiment (OSE) is a well-established method frequently conducted at NWP centres to study the added value of a given observation type (Bouttier and Kelly, 2001; Kelly et al., 2004). OSEs are for example used to assess data from field campaigns (Agustí-Panareda et al., 2010; van der Linden et al., 2020; Harnisch et al., 2011; Schindler et al., 2020; Weissmann et al., 2011), groups of observations (Cress and Wergen, 2001) and to estimate the benefit of various observation groups (Zapotocny et al., 2002). In an OSE, two parallel assimilation and forecast experiments are performed, one with and one without the assimilation of the observations of interest. The impact of the added data in an OSE is assessed by comparing the accuracy of the forecasts. It is usually expected to have a negative impact when denying a given observation type. In the current study, four OSEs were conducted to evaluate the impact of Aeolus L2B data in the Deutscher Wetterdienst (DWD) Icosahedral Nonhydrostatico (ICON) and the ECMWF IFS covering the boreal summers of 2019 and 2020. The two 2019 OSEs are based on the reprocessed L2B product, while the two 2020 OSEs use the PDG NRT product (see Table 4.2). The DWD OSE was performed using the operational version of the global ICON model global ICON model (Zängl et al., 2015) with a horizontal grid spacing of 13 km (R3B07 grid), 90 vertical levels and a six-hourly output at 00,

Table 4.2: Overview of the four OSEs used in this study. **From Borne et al. (2023) under the Creative Commons Attribution 4.0 International License (CC BY 4.0).**

OSE Name	Period	L2B data source	PDGS baseline	Data assimilation system	Bias correction
ECMWF2019 hil4 (Ctrl), hil5 (Exp)	July-September 2019	Reprocessed	2B10	IFS Cycle: 46R1.2. TCO399 ($\Delta x \approx 29km$)	
ECMWF2019BC hil4 (Ctrl), hldz (Exp)	July-September 2019	Reprocessed	2B10	IFS Cycle: 46R1.2. TCO399 ($\Delta x \approx 29km$)	Rayleigh-clear temperature-dependant
ECMWF2020 hel1 (Ctrl), hel4 (Exp)	July-September 2020	PDGS NRT dataset	2B10	IFS Cycle: 47R1.1. TCO399 ($\Delta x \approx 29km$)	
DWD2020 610 (Ctrl), 600 (Exp)	July-September 2020	PDGS NRT dataset	2B10	ICON deterministic R3B07 ($\Delta x \approx 13km$)	Rayleigh-clear vertically dependant

06, 12 and 18 UTC. Additionally to the operationally implemented M1 temperature dependent bias correction scheme at DWD, a vertical-latitude dependant correction based on the previous seven days was applied to the Rayleigh-clear observations before the assimilation.

Three ECMWF OSEs were conducted using the IFS cycles 46R1.2 and 47R1.1 for the 2019 and 2020 OSEs, respectively, with a 4D outer loop resolution of TCO399 corresponding to a grid spacing of 29 km with 137 vertical layers. In contrast to the DWD OSEs and the operational ECMWF system, only the deterministic analysis was conducted for the OSEs, while the model error estimates were taken from the operational ensemble of data assimilation. The ECMWF2019 OSE, was rerun with an additional bias correction for Rayleigh-clear data as a function of atmospheric temperature from the ECMWF IFS model, while the two other ECMWF OSEs do not include any bias-correction (2019 and 2020). Further description of the ECMWF2019 and ECMWF2020 OSEs can be found in Rennie et al. (2021). The systematic comparison between all four OSEs thus allows evaluating the effects of different bias correction methods in the two different models.

Generally, the weight given to an observation in data assimilation is based on the uncertainty associated with its measurement and representativity. Observation minus background Observation minus Background (O-B) statistics and Desroziers diagnostics (Rennie et al., 2021; Desroziers et al., 2005) were mainly used to determine the assigned observation errors in the ECMWF and DWD OSEs. The ECMWF OSEs used the following assigned HLOS wind observation error modelling:

$$\sigma_{ass} = \sqrt{(\alpha^2 \sigma_{instr}^2 + \sigma_{repr}^2)} \tag{4.1}$$

with α the L2B processor instrument error estimate scaling factor, which accounts for important noise terms that are missing in the L2B estimated error, σ_{instr} L2B processor reported instrument error standard deviation, which has the advantage of capturing drifting signal levels in the range-bin thickness and σ_{repr} the representativeness error standard deviation. In contrary, the assigned observation error in the DWD OSE is

Table 4.3: Summary of the observation error parameters and error thresholds of the OSEs used in this study. The listed assigned observation error of DWD is given for the following pressure levels (in hPa): 1000, 850, 700, 500, 400, 300, 250, 200, 150, 100, 70, 50, 30, 20, 10. **From Borne et al. (2023) under the Creative Commons Attribution 4.0 International License (CC BY 4.0).**

NWP Center	Channel	Error Threshold (ms^{-1})	Assigned observation error (ms^{-1})
ECMWF	Rayleigh-clear	$8.5 > 200hPa$ $12 < 200hPa$ $0 > 850hPa$	$1.4\sigma_{instr}$
	Mie-cloudy	5	$\sqrt{(1.25^2\sigma_{instr}^2 + 2^2)}$
DWD	Rayleigh-clear	7	5.50; 5.00; 4.50; 4.50; 4.75; 5.00; 5.00; 5.25 5.25; 5.50; 6.00; 6.50; 7.00; 7.50; 8.00
	Mie-cloudy	5	3.50; 3.00; 3.50; 4.00;4.50; 4.75; 5.00; 5.25 5.25; 5.50; 6.00; 6.00; 6.00; 6.00; 6.00

estimated using a look-up table for specific altitude levels and interpolation between levels. An important step in preprocessing the data is the quality control of the L2B product, which verifies the validity of the measurement and corresponding errors. Only Rayleigh-clear or Mie-cloudy winds with a valid confidence flag and below a specific error thresholds are assimilated. More information about the assigned observation error parameters and error thresholds can be found in Table 4.3.

4.4 Methods

4.4.1 First-guess departures

A common tool for assessing observation quality is the use of departures between observations (O) and short-range forecasts (B). They can be used to estimate systematic and random errors in the observation, background and analysis fields, and are an essential part of quality control in NWP centers (Hollingsworth et al., 1986). This procedure can also be applied to forecast ranges beyond 12 hours, which are considered sufficiently independent of the observation against which they are verified.

To assess the impact of Aeolus on the West African Monsoon (WAM) circulation features, we compute the standard Root Mean Square Error (RMSE) according to the following equation

$$RMSE = \sqrt{\frac{1}{M}\sum_{m=1}^{M}(x_m^f - x_m^r)^2} \tag{4.2}$$

with x^f the forecast value, x^r the reference value against which the forecast is verified, and M the number of data pairs. In both OSEs, the predictions are verified against the ERA5 reanalysis, which comprises additional satellite and in-situ observations that were not included in the OSEs. We calculate the RMSE for the zonal wind over West Africa for both the Aeolus and control experiments, and evaluate the improvement by calculating the relative difference in RMSE . To characterize the atmospheric constituents that influence the Aeolus measurements, cloud fraction from ERA5 and aerosol mixing ratio products from the CAMS global atmospheric composition and prediction (Benedetti et al., 2009; Morcrette et al., 2009) are used. The model employed for the CAMS prediction of global atmospheric composition is the IFS, which uses the CY47R2 4D-Var cycle corresponding to a horizontal resolution of 40 km with output on 25 pressure levels.

4.4.2 Co-location criteria

For the comparison of Aeolus against radiosonde profiles, several steps are required to fit the radiosonde wind measurements to the Aeolus measurement grid and to co-locate them in time and space.

To ensure vertical consistency, the high-resolution radiosonde measurements are vertically averaged within the 24 range bins as specified in the Aeolus L2B product. Subsequently, the radiosondes total horizontal wind speed V_{RS} and direction ϕ_{RS} are projected to the Aeolus HLOS ($HLOS_{RS}$) using the azimuth angle ϕ also specified in the L2B product, in accordance to

$$HLOS_{RS} = V_{RS} \times cos(\phi - \phi_{RS}) \tag{4.3}$$

Moreover, we have chosen co-location radii of up to 340 km, as we assume typical variations in zonal wind to be of a larger scale. In fact, during boreal summer, African Easterly Waves (AEWs) and tropical disturbances dominate the tropospheric zonal wind variability over the tropical Atlantic, which generally have a horizontal wavelength of 2000-5000 km with a periodicity of 2-7 days (Belanger et al., 2016). Section 5.3.1 discusses the error dependencies related to co-location aspects in more detail.

4.4.3 Statistical metrics

Different metrics were used to validate and estimate the systematic and random error of Aeolus wind products. The bin-to-bin wind speed difference between Aeolus and radiosonde along the HLOS is defined as

$$\Delta_{diff_{HLOS}} = (HLOS_{AEOLUS} - HLOS_{RS}) \tag{4.4}$$

Thus, the bias μ is defined as the total mean difference

$$\mu = \frac{1}{N}\sum_{i=1}^{N}\Delta_{diff_{HLOS}} \tag{4.5}$$

with the Mean Absolute Difference (MADI) yielding

$$MADI = \frac{1}{N}\sum_{i=1}^{N}|\Delta_{diff_{HLOS}}| \tag{4.6}$$

and N the total number of data points.

Additionally, we calculated the Standard Deviation (STD) of the difference

$$STD = \sqrt{\frac{1}{i-1}\sum_{i=1}^{N}(HLOS_{AEOLUS} - HLOS_{RS})^2} \tag{4.7}$$

and the Scaled Median Absolute Deviation (SMAD)

$$SMAD = 1.4826 \times median\left(\left|\Delta_{diff_{HLOS}} - median(\Delta_{diff_{HLOS}})\right|\right) \tag{4.8}$$

The SMAD is equivalent to the standard deviation for a normal distribution of errors, but is often used in Aeolus validation studies as it is less sensitive to individual outliers with very large differences than the standard deviation.

Since the number of data points varies greatly depending on the measurement channel and height, we define the uncertainty of the mean bias ϵ_μ as

$$\epsilon_\mu = \frac{SMAD}{\sqrt{N}} \tag{4.9}$$

4.4.4 Representativeness

The difference between Aeolus and radiosonde observations is the sum of the Aeolus observation error, the radiosonde observation error and the error arising from spatial and temporal displacement of the observations and different observation geometries. The latter is usually referred to as representativeness error (Weissmann et al., 2005a). As the three error components can be assumed to be uncorrelated, the standard deviation of the Aeolus HLOS winds observation error (σ_{Aeolus}) can therefore be calculated as

$$\sigma_{Aeolus} = \sqrt{\sigma_{tot}^2 - \sigma_{RS}^2 - \sigma_{rep}^2} \tag{4.10}$$

where σ_{tot} is the standard deviation of the total difference between Aeolus and radiosonde observations, σ_{RS} is the standard deviation of the radiosonde observation error and σ_{rep} is the standard deviation of the representativeness error. Martin et al. (2021) estimated that the representativeness error for the comparison of Aeolus and radiosonde observations in mit-latitudes is about 2.5 ms^{-1} based on high-resolution model simulations. As the wind fields in the area of the present validation study is comparably homogeneous, we estimate the representativeness error for our comparison to be in the range of 1.5 ms^{-1} to 2.5 ms^{-1}. The radiosonde observation error σ_{RS} is estimated to be 0.7 ms^{-1} based on Dirksen et al. (2014).

The representativeness and radiosonde observations errors also need to be considered when comparing the differences between Aeolus and radiosonde observations with the expected error provided in the Aeolus data product (EE_{Aeolus}). To account for this, we add the the radiosonde observation error and an estimated representativeness error of 2 ms^{-1} to achieve the total expected error for the comparison (EE_{tot}) as follows:

$$EE_{tot} = \sqrt{EE^2_{Aeolus} + \sigma^2_{RS} + \sigma^2_{rep}} \tag{4.11}$$

4.4.5 Quality control

Quality Control (QC) is an important step in the evaluation of Aeolus wind errors. The aim is to check for the validity of the measurements and discard nonphysical wind results from the analysis process. The QC we apply here is based on the existing quality control recommendations (Rennie and Isaksen, 2020) from the Aeolus Data Science and Innovation Cluster (DISC), and primarily rely on the HLOS wind Error Estimate (EE) in the L2B product and the validity flags.

The Rayleigh channel EE is based on the uncertainty of the Signal-to-Noise Ratio (SNR) spectrometer response and takes into account error propagation arising from the sensitivity of the Fabry-Perot interferometer, Poisson noise in the useful signal and the solar background. Ultimately, the Rayleigh EE is proportional to the inverse squared root of the useful signal on the detector. Future baseline versions will include additional noise terms, such as noise related to atmospheric temperature and pressure, or cross-talk contamination. In contrary, the Mie EE is determined from the accuracy of the fringe peak position using the solution covariance of the Lorentzian fitting algorithm based on four characteristics of the signal shape, i.e the peak position, height, width and offset.

Following the default QC flags, all Aeolus wind products with a validity flag of 0, EE above 8 ms^{-1} for Rayleigh and 4 ms^{-1} for Mie, are omitted. Nevertheless, the used QC might not be enough and the data algorithm may contain gross errors in the wind estimate that have not been flagged as invalid. These errors are usually due to non-Gaussian error sources, such as instrument/transmission failure, or to a misrepresentation of the measurements in space and time. Since the two aforementioned QC are not sufficient to remove these gross errors, an additional QC parameter is used, namely the modified Z-score (Lux et al., 2022a; Witschas et al., 2022b; Iglewicz and Hoaglin, 1993). The modified Z-score $Z_{m,i}$ is defined as

$$Z_{m,i} = \frac{\Delta_{diff_{HLOS}} - median(\Delta_{diff_{HLOS}})}{SMAD} \tag{4.12}$$

and describes the median deviations between each wind speed difference normalized with the SMAD. The modified Z-score significantly influences small data sets, such as those used in this study. Following literature recommendations (Lux et al., 2022a; Witschas et al., 2022b; Sandbhor and Chaphalkar, 2019; Tripathy et al., 2013), we discard wind observations with a modified Z-score greater than 3 as a final QC.

4.5 Equatorial wave identification methods

In recent decades, several methods have been developed to identify equatorial wave modes from observational data (Knippertz et al., 2022), most notably including space-time spectral analysis (Wheeler and Kiladis, 1999; Gehne and Kleeman, 2012; Roundy, 2018; Kikuchi et al., 2018) and spatial projection based approaches (Yang et al., 2003; Žagar et al., 2009; Castanheira and Marques, 2015). Here we introduce two of these methods that are used in this work. The first method was developed by Wheeler and Kiladis (1999) and isolates the Equatorial Waves (EWs) using the Fast Fourier Transform (FFT) in the wavenumber-frequency spectrum. The second method, developed by Yang et al. (2003), projects dynamic variables into the horizontal structure of the EWs modes.

4.5.1 Wavenumber–frequency filtering using fast Fourier transform

He we present the method described by Wheeler and Kiladis (1999); Kiladis et al. (2009) to isolate EWs using a space-time spectral analysis. The method consists of spectrally isolating the EWs in wavenumber and frequency domains for eastward and westward propagating signals according to the dispersion relations of Shallow Water (SW) theory. Generally, the employed data are filtered using a two-dimensional FFT and thus decomposed into zonally propagating waves, symmetrically and anti-symmetrically about the equator. In this study, five different wave modes are isolated using different wavenumber k, period p and equivalent depth h window selection. Those include more divergent waves such as Kelvin waves (k=1:14, p=2.5:20, h=8:90) and rotational types of waves such as ER (k=-10:-1, p=9:72, h=0.1:90) and Mixed Rossby gravity waves (MRG) (k=-10:-1, p=3:8, h=8:90). The method also allows the detection of two wave types that are not solutions of the SW equations such as the Madden-Julian Oscillation (MJO) (k=0:9, p=30:96) and Tropical Disturbances (TDs) (k=-20:-6, p=2.5:5) which includes AEWs.

Since we are interested in filtering waves in relatively narrow time periods of up to 3 months, we use the padded filtering approach developed by Janiga et al. (2018). In order to obtain a significantly large data range for filtering, the data of interest must be combined with consistent observations. In this study, the wind and geopotential fields of the ECMWF and DWD OSEs are merged with the ERA5 reanalysis, while precipitation is combined with GPM IMERG records. More specifically, the method consists of padding two years of observations with the three months of data of interest and adding zeros afterwards to get a total of four years of data. For the investigation of EWs over Cape Verde, only 2 years of the ERA5 and GPM IMERG data were merged with 2 years of zeros. Before filtering, the first four harmonics of the nonzero portion of the data are removed to obtain anomalies. Lastly, the four years of data are tapered with a split-cosine bell fit to reduce spectral leakage (Wheeler and Weickmann, 2001), and finally filtered with a twice daily resolution for the different wave signals.

4.5.2 2D Spatial Projection using Parabolic Cylinder Functions

This method was originally introduced by Yang et al. (2003) and mainly consists of a horizontal projection of the upper and lower tropospheric dynamical fields onto equatorial wave modes. Principally, this method assumes that the linear adiabatic theory for equatorial waves on a resting atmosphere is not directly applicable. It argues that the real tropical atmosphere is not at rest, leading to distortions in the theoretical dispersion curves, Doppler shifts in the case of a strong background zonal flow (Dias and Kiladis, 2014) and invalidity of the concept of equivalent depth due to variations in the vertical heating profiles. With this method, there are no restrictions on the dispersion relation and vertical structure, but only on the horizontal structure.

The method is applied to the two zonal and meridional horizontal-velocity (u, v) and geopotential-height (ϕ) fields at 850 hPa and 200 hPa simultaneously. The meridional structure of equatorial waves of latitude y are described using Parabolic Cylindrical Functions (PCFs), according to Gill (1980)

$$D_n\left(\frac{y}{y_0}\right) = \exp\left[-\frac{1}{4}\left(\frac{y}{y_0}\right)^2\right] P_n\left(\frac{y}{\sqrt{2}y_0}\right) \tag{4.13}$$

where P_n is a polynomial of degree n, and where y_0 is the latitudinal trapping scale of the modes. The later is set empirically to $y_0 = 6^\circ$ using a best fit to observational data. The equatorial wave solutions of the PCFs, are easily described using new dynamical variables $\{q, r, v\}$ that are expressed as following

$$q = (g/c)\phi + u \quad \text{and} \quad r = (g/c)\phi - u \tag{4.14}$$

where c is the gravity wave speed. The first step of this methodology is to spatially and temporally filter the new dynamic variables q, r and v into eastward and westward moving components. This is achieved using a FFT with a wide frequency (2 - 30 days) and wavenumber (2 - 40) range to remove stationary features. The resulting Fourier coefficients are then projected onto the different horizontal structures using the PCFs,

$$\{q, r, v\} = \sum_{n=0}^{\infty} \{q_n, v_n, r_n\} D_n \tag{4.15}$$

where n is the meridional mode number. Those structures corresponds to different wave solutions, e.g. the Kelvin waves, the Westward moving Mixed Rossby Gravity wave (WMRG), the Equatorial Rossby wave with meridional mode number 1 (R1) and 2 (R2). Because the projection is only applied to the theoretical modes, TDs and the MJO cannot be identified. Finally, the projected fields are transformed back into physical space to obtain the different equatorial wave modes. This approach can be implemented in real-time and has the advantage of being applicable to relatively short time series.

In this study, we apply this methodology to the dynamic fields of ECMWF and DWD OSEs that are no longer than 3 months with a 12 hourly resolution.

5. Validation of Aeolus wind observations over the tropical Atlantic using radiosondes

5.1 Equatorial wave activities during the campaign

In this section we examine the role of Equatorial Waves (EWs) in modulating moisture using Total Column Water Vapour (TCWV) from ERA5 and precipitation from Global Precipitation Mission (GPM) Integrated Multi-Satellite Retrievals for Global Precipitation Measurement (IMERG) over the tropical Atlantic Ocean in September 2021, with a particular focus on Sal Island (Cape Verde). Figure 5.1 shows a Hovmöller diagram of the ERA5 TCWV (Fig. 5.1a) and GPM IMERG precipitation (Fig. 5.1b) anomalies during September 2021, averaged in the latitude band 14°N–18°N, in which the Cape Verde Islands are located. The superposed colored lines represent the associated filtered tropical waves with contours at 3.5 mm for the TCWV and 2.5 $mm\ day^{-1}$ for the precipitation. The dotted vertical line at 22.5°W represent the location of Sal Island. As expected, the moisture field is dominated by westward propagating waves such as Mixed Rossby gravity waves (MRG) (green), Tropical Disturbances (TDs) (blue) and Equatorial Rossby waves (ER) (red), while the precipitation field also exhibits eastward propagating Kelvin waves (orange). The Madden-Julian Oscillation (MJO) does not appear to significantly modulate precipitation and moisture during September 2021. TCWV and precipitation anomalies as well as wave patterns have similar characteristics, but are not always correlated as the mechanism involved in the modulation of moisture and precipitation differs, the latter being generated in situ from moisture fluxes while the other involves dynamical transport.

In the precipitation field, one can identify the major African Easterly Waves (AEWs), tropical storms and hurricanes that occurred during September 2021, especially visible west of Cape Verde where they became more organized and intense. These events are often associated with a superposition of wave types that interact with each other on different time scales, thereby amplifying the precipitation events. This is the case for the Hurricane Larry (Category 3) that propagated from 25°W to 45°W between 2021-09-03 and 2021-09-08 where the locations of enhanced rainfall is associated with the superposition of high-frequency TD and MRG and low-frequency ER waves. Larry

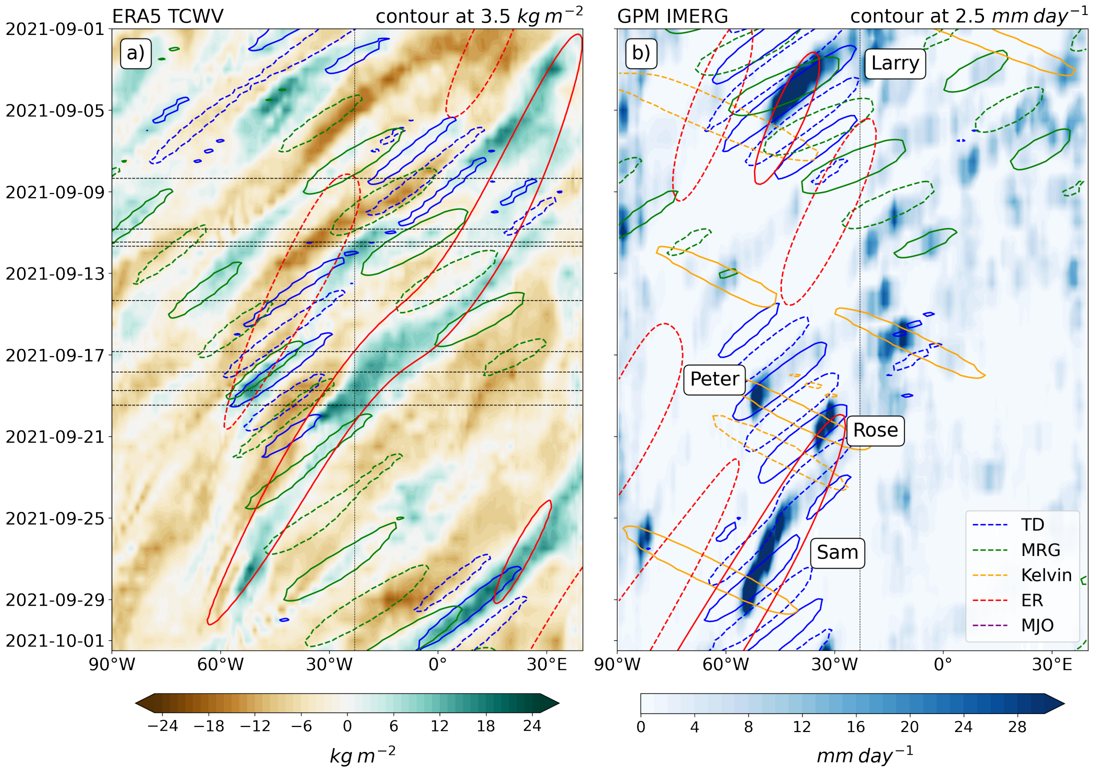

Figure 5.1: Hovmöller diagrams for ERA5 total column water vapour (a) and IMERG total precipitation (b), averaged from 14°N to 18°N for September 2021. The contour lines denote individual propagating tropical waves detected using the Wheeler-Kiladis space-time filter. The solid (dashed) lines represent positive (negative) wave anomalies at the interval of 3.5 *mm* and 2.5 $mm\,day^{-1}$, respectively. MRG, TD, MJO and ER stand for Mixed-Rossby Gravity waves, Tropical Disturbance, Madden-Julian Oscillation and Equatorial Rossby waves, respectively. The dotted black vertical line at 22.5°W represent the location of Sal Island and the dotted black horizontal lines represent the dates of the Falcon 20 flights during Clouds-Atmospheric Dynamics–Dust Interactions in West Africa (CADDIWA).

is also visible in the moisture field anomaly, but is not associated with prominent wave activity there. The period from 2021-09-17 to 2021-09-24 was an active Tropical Storm (TS) period, with the passage of e.g. Peter and Rose which are associated with the superposition of an westward TD wave packet and a Kelvin wave. Those TSs seems to be associated with TD and MRG wave activities in the moisture field. Finally, we note the propagation of Hurricane Sam (Category 4), which occurred between 24-09-2021 and 29-09-2021 and extended to 60°W. Sam appears to be mainly modulated by an ER acting like an envelope that sustains precipitation on a longer time scale, along with a fast-propagating TD. The ER signal modulating Sam is also very prominent in the TCWV field and seem to originate already from eastern Africa at the beginning of September 2021 (30°E).

Figure 5.1 shows time series of the TCWV anomaly and the corresponding sum of the five filtered wave types (Fig. 5.2a) alongside the contribution from each individual wave (Fig. 5.2b) in September 2021 near Sal Island (16.5°N; 22.5W). The Pearson correlation between the anomaly and each type of wave is indicated in the legend. We find that

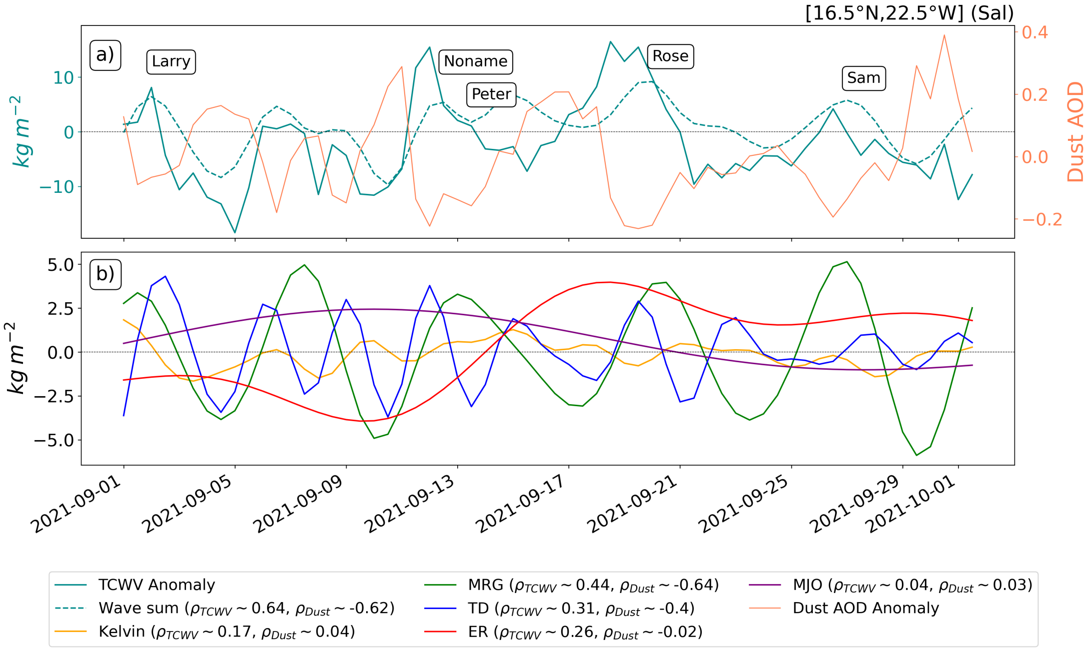

Figure 5.2: TCWV anomaly (solid, teal), Dust Aerosol Optical Depth (AOD) anomaly (solid, coral) and sum of tropical wave contribution (dashed, teal) (a) together with individual tropical wave contribution (b) filtered following the Wheeler-Kiladis approach during September 2021 near Sal Island [16.5°N;22.5°W]. The anomalies were computed on the period 2015-2021. The Pearson correlation ρ between the waves and the anomaly is given for each wave type in the legend. The names of the identified events crossing Sal are indicated in panel a).

the sum of tropical waves can explain most of the observed TCWV variability, with a correlation reaching 0.76. The most strongly correlated waves are MRG (0.60) followed by TDs (0.36), which, as anticipated, are rotational waves that accounts for most of the moisture transport in the region. They are followed by lower amplitude waves such as the higher frequency Kelvin wave (0.25) and the lower frequency ER and MJO (both 0.15). Different regions where the TCWV anomalies are positive could be identified as following chronological sequence of events: Larry (Hurricane, early phase), Noname (non identified event), Peter (TS), Rose (TS) and Sam (Hurricane, early phase). Most of these positive anomalies are in a phase with a positive signal from MRG, TD or a combination of both. This suggests that most of the TSs and AEWs that crossed Sal had a mixed flavor of MRG and TD, while other lower amplitude waves mainly modulated the TCWV background.

The marked contribution of MRG in the modulation of moisture in September 2021 over Cape Verde is also illustrated in the appendix, where the relative importance of the tropical wave signal for the different variables has been investigated. It can be concluded that moisture (TCWV) and clouds (OLR) are unusually strongly modulated by MRG waves with respect to the climatology (September 2000–2020), while they are almost absent in the precipitation field, as September 2021 was largely dry over the Cape Verde Islands.

5.2 Statistical comparison of Aeolus with radiosonde observations and model winds

In this section, the Level 2B (L2B) Horizontal Line of Sight (HLOS) winds (L2bP 3.50) from Aeolus are compared statistically with radiosonde observations and model winds. This includes a comparison with the European Centre for Medium-Range Weather Forecasts (ECMWF) model equivalents (subsection 5.2.1), an overview of systematic and random differences with respect to Calibration/Validation (Cal/Val) sites and orbital nodes (subsection 5.2.2), and finally the identification of an orbital- and altitude-dependent bias in the Rayleigh-clear channel (subsection 5.2.3). The present study relies on a total of 384 Rayleigh-clear and 59 Mie-cloudy bin pairs, of which $\sim 60\%$ and $\sim 53\%$ are from ascending orbits, respectively, with the majority of observations obtained from the Caribbean launch sites ($\sim 56\%$ for Rayleigh-clear and $\sim 64\%$ for Mie-cloudy). Rayleigh-cloudy bin pairs are also available, but only in a very small number (16 counts), which makes a statistical analysis difficult.

5.2.1 Comparative analysis with the ECMWF model equivalents

Figure 6.1 shows a scatter plot of the radiosonde HLOS ($HLOS_{RS}$) against Aeolus L2B ($HLOS_{AEOLUS}$) Rayleigh-clear (blue), Mie-cloudy (red) and Rayleigh-cloudy (orange) wind products (a) as well as against Aeolus ECMWF model equivalents ($HLOS_{ECMWF}$) (b). Since Rayleigh-cloudy wind observations are not assimilated at ECMWF, they are not displayed in Fig. 6.1b. The × symbol represent the gross errors rejected with a Z-score threshold of 3 ($\sim 3.5\%$, $\sim 4.8\%$ and $\sim 6.7\%$ of the total Rayleigh-clear, Mie-cloudy and Rayleigh-cloudy data points, respectively). The dashed lines represent the $\pm 10\ ms^{-1}$ and $\pm 20\ ms^{-1}$ difference between two measurements. The Aeolus model equivalent $HLOS_{ECMWF}$ for Rayleigh-clear shows a much better agreement with the radiosonde measurements $HLOS_{RS}$ with a Standard Deviation (STD) of 2.1 ms^{-1} (Fig. 6.1b) compared to the Aeolus $HLOS_{AEOLUS}$ Rayleigh-clear observations, which have a larger spread and a STD of 4.8 ms^{-1} (Fig. 6.1a). The systematic difference of the model equivalent is also smaller with a bias of $0.1 \pm 0.1\ ms^{-1}$ compared to $-0.5 \pm 0.2\ ms^{-1}$ for the Aeolus observations. In contrast, the Mie-cloudy winds of both Aeolus model equivalents and $HLOS_{AEOLUS}$ behave similarly with respect to the radiosonde measurements, with STD of 2.93 ms^{-1} and 2.9 ms^{-1}, respectively. Again, the systematic difference in the model equivalent is smaller than for Aeolus Mie-cloudy winds, with biases of $0.4 \pm 0.3\ ms^{-1}$ and $-0.9 \pm 0.3\ ms^{-1}$, respectively. For Rayleigh-cloudy, the STD is larger at 6.6 ms^{-1} with a bias of $1.0 \pm 1.4\ ms^{-1}$, but given the small statistical sample size, there is a risk of a large margin of error. The generally good agreement between radiosonde and model equivalent shows that the co-location parameters used in this study are reliable, as most of the systematic and random errors seem to be specific to the Aeolus Rayleigh-clear data. This stresses the need to identify the underlying potential error sources of Rayleigh-clear observations with respect to the presence of clouds and dust aerosols, which are frequent in the region of interest. It

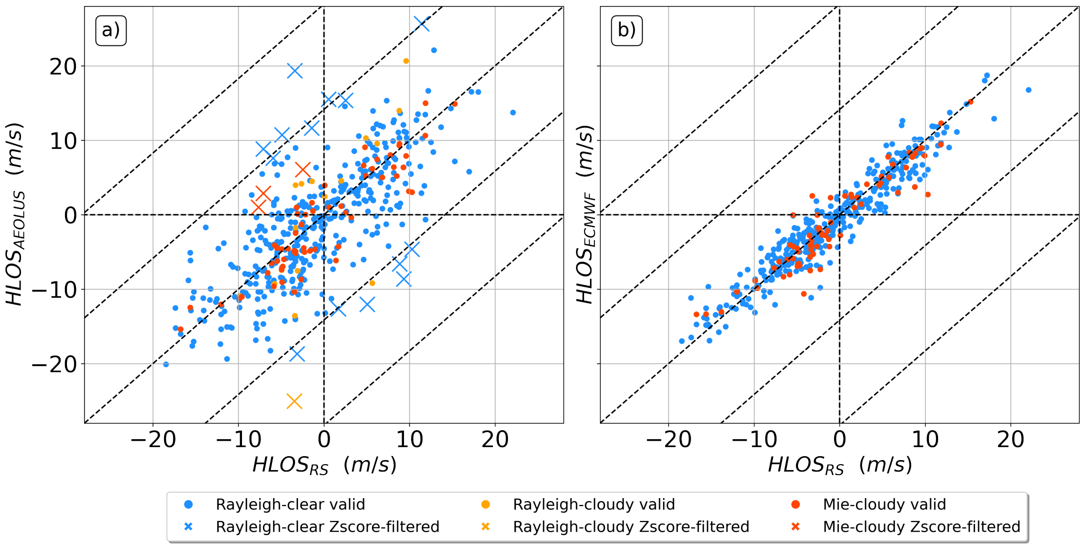

Figure 5.3: (a) Aeolus HLOS Rayleigh-clear (blue), Mie-cloudy (red) and Rayleigh-cloudy (orange) wind products plotted against radiosonde measurements projected along the HLOS for the 20 radiosonde profiles. The gross errors (crosses) are determined using the modified Z-score with a threshold of 3. (b) Aeolus HLOS model equivalents from the ECMWF feedback files plotted against radiosonde measurements. The dashed lines are located at the ±10 ms^{-1} and ±20 ms^{-1} wind speed difference between two measurements. **From Borne et al. (2024) under the Creative Commons Attribution 4.0 International License (CC BY 4.0).**

is also worth noting that this good agreement indicates that the model equivalent is a robust reference for validating the Aeolus winds in the tropical Atlantic.

5.2.2 Systematic and random errors using radiosondes

An overview of the bias and random differences of both channels can be found in Table 5.1. In terms of systematic errors, Rayleigh-clear shows a relatively small negative bias of $-0.5 \pm 0.2\ ms^{-1}$, on average, which is below European Space Agency (ESA)'s specification of 0.7 ms^{-1} (Ingmann and Straume, 2016). This bias is, however, the result of a large heterogeneity with respect to the Cal/Val sites and orbital nodes, with compensating biases of $-1.5 \pm 0.6\ ms^{-1}$ and $0.6 \pm 0.4\ ms^{-1}$ for the descending and ascending nodes on Sal, respectively, compared to negative biases of $-1.0 \pm 0.3\ ms^{-1}$ (ascending) and $-0.6 \pm 0.4\ ms^{-1}$ (descending) in the Virgin Island. As for random differences, Rayleigh-clear has an average STD of 4.8 ms^{-1}, which varies only marginally between the Cal/Val sites and orbital nodes, ranging from 4.1 ms^{-1} to 5.3 ms^{-1}. The overall Scaled Median Absolute Deviation (SMAD) is found to be slightly below at 4.3 ms^{-1}.

For comparison with the ESA recommendation for random errors, we derived the random errors for Aeolus observations considering also the representativeness errors for the comparison and radiosonde observation errors according to Eq. 4.10 (table 5.2). The random error at 2–16 km altitude of 3.8 – 4.3 ms^{-1} exceeds the threshold of 2.5 ms^{-1}, while at 16–20 km altitude it amounts to 4.3 – 4.8 ms^{-1}, also exceeding the ESA threshold

Table 5.1: Overview of the mean bias and uncertainty (μ, σ_μ; ms^{-1}), Standard deviation (STD; ms^{-1}), Scaled Median Absolute Deviation (SMAD; ms^{-1}) and counts (COUNT) for the Rayleigh-clear and Mie-cloudy channels, orbital nodes and the different radiosonde locations. Due to the small amount of available data, Rayleigh-cloudy is not shown here. **From Borne et al. (2024) under the Creative Commons Attribution 4.0 International License (CC BY 4.0).**

Region	Orbital node	Rayleigh-clear				Mie-cloudy			
		μ	STD	SMAD	COUNT	μ	STD	SMAD	COUNT
Sal	Ascending	0.6±0.4	4.9	4.4	112	-1±0.9	2.9	3.5	15
	Descending	-1.5±0.6	4.6	4.8	55	-1.6±0.8	2.2	2.1	6
	All	-0.1±0.3	4.9	4.5	167	-1.2±0.7	2.7	3.2	21
SCRX/PR	Ascending	-1.0±0.3	4.1	3.7	119	-0.6±0.7	2.9	3.7	16
	Descending	-0.6±0.4	5.3	4.3	98	-1.0±0.5	2.9	2.5	22
	All	-0.8±0.3	4.7	4.3	217	-0.8±0.4	2.9	2.5	38
Sal/SCRX/PR	Ascending	-0.2±0.3	4.6	4.2	231	-0.8±0.6	2.9	3.3	31
	Descending	-0.9±0.4	5.0	4.6	153	-1.1±0.4	2.8	2.2	28
	All	-0.5±0.2	4.8	4.3	384	-0.9±0.3	2.9	2.6	59

of 3 ms^{-1}. The quality of Rayleigh-clear measurements primarily depends on the signal accumulation, which can vary with the thickness of the Range Bin Settings (RBS) and the horizontal accumulation length as well as with the atmospheric path signal. The latter has been decreasing in recent years as a result of initial instrumental misalignment, laser-induced contamination, as well as the wavefront error of the 1.5 m telescope. The solar background noise, which varies along the orbit and sea

For Mie-cloudy, the systematic difference indicates a bias of -0.9 ± 0.3 ms^{-1}, which is within the uncertainty range of the ESA's specification and more uniform across regions and orbital nodes with a slightly larger bias in the descending orbits and over Sal. Concerning the random differences, the measurements exhibit a total random error of 1.1 – 2.3 ms^{-1}, which is below ESA's 2–16 km recommendation, as most Mie-cloudy measurements are located underneath 16 km altitude. As with the bias, the STD and SMAD of Mie-cloudy are also quite independent of orbital and regional dependence. The overall accuracy of Mie-cloudy depends on the signal accumulation, the classification algorithm and the quality of the calibration data. The accuracy of Mie-cloudy winds is higher than that of Rayleigh-clear winds as particle backscatter is usually stronger than that of clear air in addition to the fact that Mie backscatter is not subject to broadening induced by Rayleigh-Brillouin scattering (Witschas et al., 2012).

Comparing the results of different Cal/Val studies is tricky as the influence of geographical regions, atmospheric conditions, decreasing laser energy, product baseline and quality control procedures on the result can be significant and must be considered. In this analysis, comparisons are only made with statistics derived from Aeolus Validation Through Airborne Lidars in the Tropics (AVATAR-T) airborne-based measurements

Table 5.2: Overview of the total systematic (μ, σ_μ; ms^{-1}) and random (σ_{Aeolus}; ms^{-1}) errors derived according to Eq. 4.10 for Rayleigh-clear and Mie-cloudy winds for altitudes ranges 2–16km and 16–20km, as well as the corresponding ESA's error recommendations. The random error σ_{Aeolus} was computed for a representativeness error σ_{rep} ranging from 1.5 ms^{-1} to 2.5 ms^{-1}. For Mie-cloudy, only the altitude range 2–16km is shown for the random error, as Mie-cloudy does not sample sufficiently above 16km. **From Borne et al. (2024) under the Creative Commons Attribution 4.0 International License (CC BY 4.0).**

	Rayleigh-clear			Mie-cloudy	
	σ_{Aeolus} 2–16km	σ_{Aeolus} 16–20km	μ	σ_{Aeolus} 2–16km	μ
Ascending	3.4 – 3.9	4.0 – 4.4	-0.2±0.3	1.1 – 2.3	-0.8±0.6
Descending	4.3 – 4.7	4.4 – 4.9	-0.9±0.4	0.5 – 2.1	-1.1±0.4
All	3.8 – 4.3	4.3 – 4.8	-0.5±0.2	1.1 – 2.3	-0.9±0.3
ESA	2.5	3	0.7	2.5	0.7

(Witschas et al., 2022b; Lux et al., 2022a), as these were carried out in the framework of the same Joint Aeolus Tropical Atlantic Campaign (JATAC) campaign. The statistical analysis of AVATAR-T shows systematic errors of -0.1 ± 0.3 ms^{-1} for Rayleigh-clear and -0.7 ± 0.2 ms^{-1} for Mie-cloudy, which are slightly smaller than for radiosondes. However, the random error of 7.1 ± 0.3 ms^{-1} for Rayleigh-clear is significantly higher. The difference in results is caused by the different altitudes at which the data are sampled, as the aircraft only samples the lower 10 km portion of the troposphere, which is shown to be more noisy owing to the abundance of dust aerosols in this region. For Mie-cloudy, the random error gives 2.9 ± 0.3 ms^{-1}, which is similar to our radiosonde-based results as most Mie-cloudy scattering occurs at lower levels.

5.2.3 Orbital bias in the Rayleigh-clear channel

Figure 6.2 shows vertical profiles of the differences between Aeolus Rayleigh-clear observations and radiosonde measurements projected along HLOS (O-RS; solid lines), and the corresponding ECMWF model equivalents (O-B; dotted lines) for both ascending (red) and descending (blue) orbits over Sal (a), Puerto Rico (PR) and Saint CRoiX (SCRX) (b). The shading represents the bias uncertainty σ_μ. HLOS winds from the descending track are multiplied by -1 to conform with the sign convention of the model coordinate system. The vertical profiles illustrate the presence of an ascending/descending bias visible in both the Observation minus Background (O-B) and Observation minus RadioSonde (O-RS) profiles, reaching up to 2.5 ms^{-1} around 8 km altitude in both regions. The differences below 5 km altitude could be related to the greater amount of dust in Cabo Verde during this period, while above 17 km the differences could partly be related to the lack of descending orbit data over Sal (Fig. 6.2a). This altitude- and orbit-dependent bias is further described in Chapter 6 using first-guess departure statistics over West Africa.

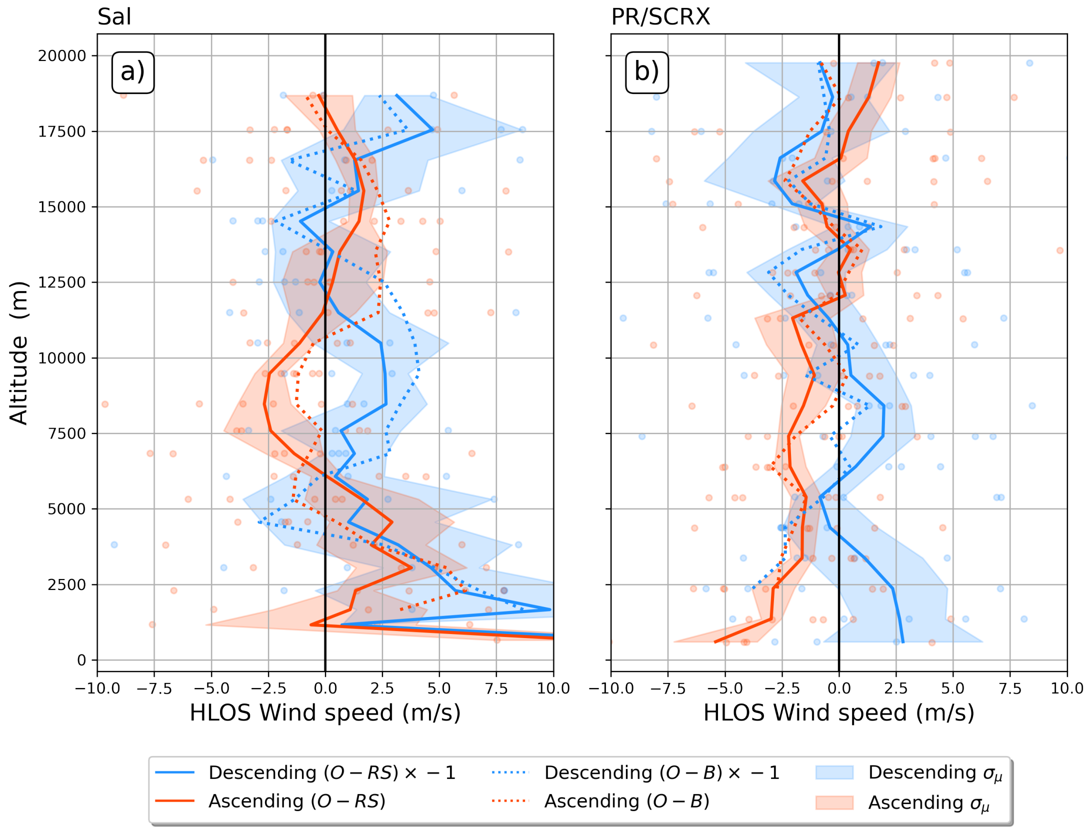

Figure 5.4: Differences (dots) and average differences (lines) between ascending (red) and descending (blue) winds between Aeolus observations (O) and radiosonde HLOS wind measurements (RS, solid line) along with ECMWF model equivalents (B, dotted line) over Sal (a) and Puerto Rico - Saint Croix (PR/SCRX, (b). The shadow represents the bias uncertainty σ_μ. To comply with the sign convention of the model coordinate system, the HLOS winds from the descending orbit are multiplied by -1. **From Borne et al. (2024) under the Creative Commons Attribution 4.0 International License (CC BY 4.0).**

This latitude consistent bias caused the zonal winds in the ECMWF analysis to accelerate in the morning and weaken in the evening, affecting the African Easterly Jet North (AEJ-North) and Tropical Easterly Jet (TEJ) in particular. Correcting this bias with a temperature-dependent approach helped to improve the representation of winds in the analysis and forecast fields (see Chapter 6). However, the cause of this bias remains unknown, as it has not been proven to be related to temperature, nor has any dependence on wind speed, Signal-to-Noise Ratio (SNR) or useful signal been found (not shown here). Here, as both the O-B and O-RS profiles are very close to each other, with deviations below 0.5 ms^{-1}, the existence of this bias can be confirmed observationally with radiosondes. As highlighted by Horányi et al. (2015), biases of the order of 1 ms^{-1} can already deteriorate forecast quality.

5.3 Error dependency

In this section we examine the error dependency and associated error sources of the different Aeolus wind products. Firstly, we investigate the error dependency as a function of co-location parameters, such as radius and time difference between two measurement points, to account for representativeness. Secondly, we explore the error dependency in relation to the presence of clouds and dust, as these supposedly influence the quality of Aeolus wind products.

5.3.1 Temporal and spatial co-location

Rayleigh-clear and Rayleigh-cloudy

Figure 6.3 shows the absolute difference between Aeolus and radiosonde measurement points $|\Delta_{diff_{HLOS}}|$ as a function of EE_{tot} (a), altitude (b), co-location radius (c) and co-location time (d) for the Rayleigh-clear (blue) and Rayleigh-cloudy (orange) observation types. The solid and dashed blue lines show the Rayleigh-clear Mean Absolute Difference (MADI) and SMAD, respectively, with each value calculated using a minimum sample size of 40 data points for panels a, b and d. Also shown are outliers (cross symbol +), that we define in this study as values with low Error Estimate (EE) ($< 5\ ms^{-1}$) and large absolute difference ($> 10\ ms^{-1}$), which are of particular interest as they contribute the most to the wind quality degradation. The Rayleigh-clear outliers account for 13 observations, i.e. $\sim 3.4\%$ of the data points. For Rayleigh-cloudy, no MADI and SMAD are computed due to the lack of data.

In general, the MADI and SMAD between Rayleigh-clear and radiosonde wind measurements appear to be proportional to the Aeolus EE_{tot} (Fig. 6.3a), with larger deviations associated with larger EE_{tot}s, as expected. However, on average, the mean EE_{tot} overestimates the MADI by 1 ms^{-1} for EE_{tot} values below 6 ms^{-1} (see grey line). This discrepancy can be attributed to the relatively small amount of data used in the study, as the EE is based on the Gaussian assumption of a large data set. For Rayleigh-cloudy measurements, it is difficult to establish a dependency although the absolute difference appears to be generally larger owing to the large STD of 6.6 ms^{-1} for this observation type. Considering the altitude error dependency of Rayleigh-clear (Fig. 6.3b), a general pattern emerges with MADI and SMAD reaching a minimum of 3 ms^{-1} and 2 ms^{-1} respectively on average in the middle troposphere at 10 km, while increasing above and below, with MADIs of $4 - 5\ ms^{-1}$ and SMADs of almost 6 ms^{-1} at 2.5 km and 19 km altitude. As we will see in the next subsection 5.3.2, this error pattern is inversely proportional to the Rayleigh backscattered useful signal, as it directly affects the SNR and thereby the quality of the measurement points. Rayleigh-clear outliers seem to occur at all altitudes and Rayleigh-cloudy measurements are primarily found in the lower troposphere, below 6 km.

In Fig. 6.3c we examine the error dependency with respect to the co-location radius, which extends up to 340 km, a distance that is large relative to the 100 km specified in ESA's recommendations. However, the MADI and SMAD for Rayleigh-clear do not increase with radius, but stagnate at an average of 3–4 ms^{-1} for radii above 100 km, while they are slightly higher below 100 km, reaching 4–5 ms^{-1}. Furthermore, outliers appear

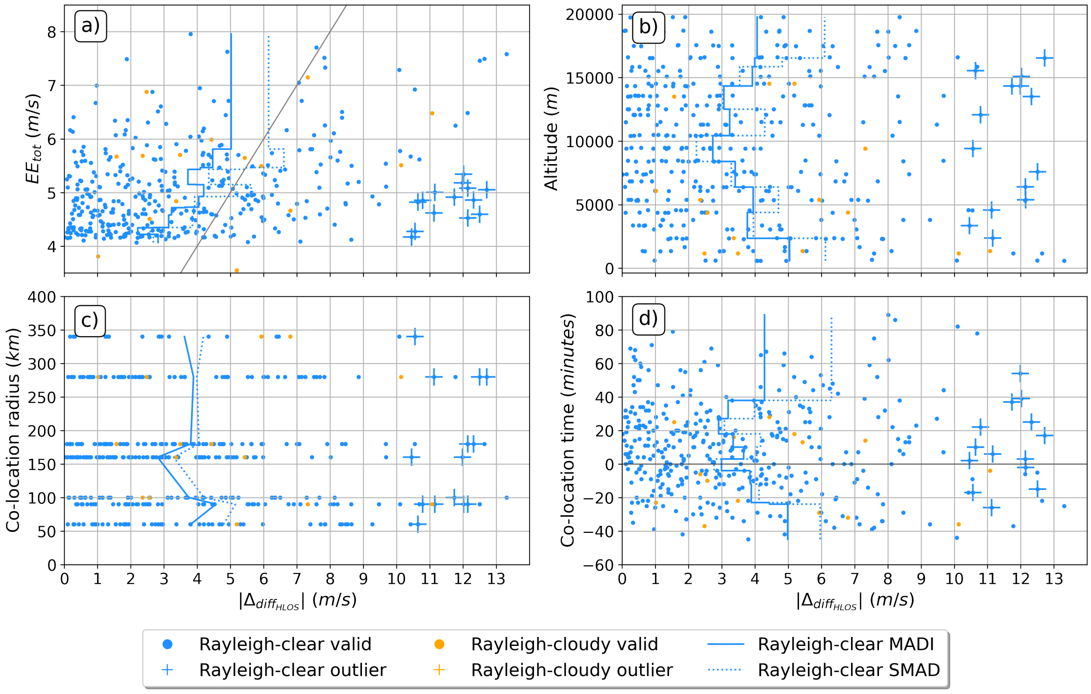

Figure 5.5: EE_{tot} (a), altitude (b), co-location radius (c) and co-location time quantities expressed as a function of the absolute difference between radiosonde HLOS winds ($HLOS_{RS}$) and Aeolus ($HLOS_{AEOLUS}$) Rayleigh-clear (blue) and Rayleigh-cloudy (orange) observations. Outliers are defined as values with an EE below 5 ms^{-1} and absolute difference larger than 10 ms^{-1} and are represented by the cross symbol +. The solid blue lines indicate the MADI while the dotted blue lines represent the SMAD of Rayleigh-clear and each value is computed using a minimum sample size of 40 data points. The grey line in panel a represents the diagonal at intercept 0 with slope 1. Due to the limited amount of data, no MADI and SMAD are shown for Rayleigh-cloudy. **From Borne et al. (2024) under the Creative Commons Attribution 4.0 International License (CC BY 4.0).**

across all co-location radii. This indicates that the use of a co-location distance up to 340 km is acceptable for the statistical comparison. Exploring the error dependency with respect to the time difference between the observations (Fig. 6.3d), there is indication for increasing difference for larger time-differences, going from 3–4 ms^{-1} at 0 minutes to 4–6 ms^{-1} above 30 minutes. There is also an asymmetry of the error dependence, with a larger error magnitude for radiosonde observations preceding the Aeolus passage. Since most radiosondes were launched with the objective of reaching the mid-troposphere during the satellite's passage, the measurements preceding/following Aeolus of more than 30 minutes correspond mainly to measurements at lower/higher altitudes. The larger MADI and SMAD values for these time differences could hence be an indirect effect of the larger errors found at those altitudes (Fig. 3b). Again, no error dependency is observed for outliers, with most occurring below ±40 minutes time differences.

Mie-cloudy

Figure 6.4 shows the same error dependencies as in Fig. 6.3, but for the Mie-cloudy observation type. For Mie-cloudy, we define outliers as values exceeding an absolute

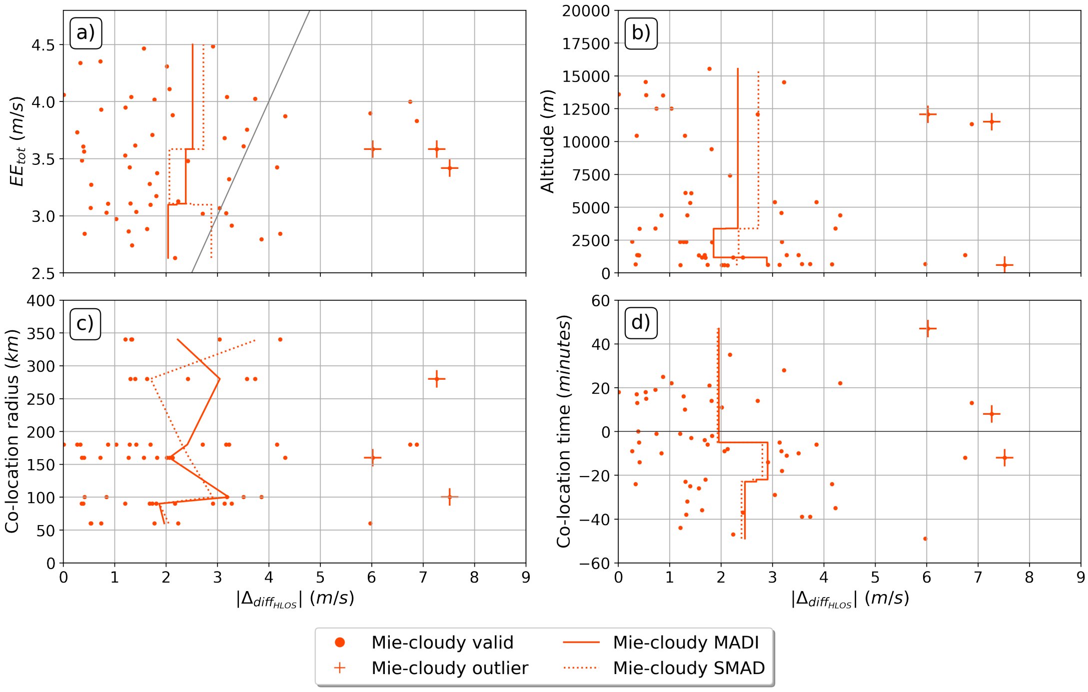

Figure 5.6: Same as for Fig. 6.3, but for Mie-cloudy. For Mie-cloudy (red), outliers are defined as values having an absolute error above 6 ms^{-1} and an EE inferior to 3 ms^{-1}. The MADI and the SMAD values are computed using a minimum sample size of 15 data points. **From Borne et al. (2024) under the Creative Commons Attribution 4.0 International License (CC BY 4.0).**

error of 6 ms^{-1} along with EEs inferior to 3 ms^{-1}. With a total of 3 data points, they account for $\sim$ 5% of the total Mie-cloudy observations. In panels a, b and d, each MADI and SMAD value is calculated using a minimum sample size of 15 data points.

As shown in Fig. 6.4a, the absolute differences for Mie-cloudy measurements are generally smaller than for Rayleigh-clear, with the largest deviations around 7–8 ms^{-1}, while attaining 13–14 ms^{-1} for Rayleigh-clear. The MADI and SMAD remain between 2 and 3 ms^{-1}, indicating an overestimation of the EE_{tot}, especially for increasing EE_{tot}. Regarding the altitude error dependency (Fig. 6.4b), most of the data are found within the 10-15 km layer, which is probably related to the presence of high-level clouds, and below 7 km, where low- and mid-level clouds and dust layers are found. Due to the sparseness of Mie-cloudy data, both MADI and SMAD do not show a specific vertical error trend. While MADI and SMAD remain between 2.3 and 2.7 ms^{-1}, respectively, they decrease to 1.8 and 2.3 between 1.5 and 3 km altitude before increasing to almost 3 ms^{-1} in the lowest 1 km. Fig. 6.4c shows that similarly to Rayleigh-clear, Mie-cloudy reveals no error dependency with respect to co-location radii, with the mean absolute error and SMAD mainly ranging from 1.7 to 3.2 ms^{-1}, and outliers found at all radii. Regarding the error dependence on time difference (Fig. 6.4d), we find that most of the measurement differences occur at time intervals of less than ±40 minutes. MADIs and SMADs are generally higher for negative co-location times, corresponding to cases where radiosonde observations are sampled before those from Aeolus. Nevertheless, we do not notice a strong relationship between co-location time and errors.

5.3.2 Cloud type and dust

As already mentioned, the accuracy of Rayleigh-clear and, to a lesser extent, Mie-cloudy depends on the signal level and SNR. In general, the signal level depends on the range bin thickness, the horizontal accumulation length, the atmospheric path signal and the overall signal background level. In addition, Rayleigh-clear winds are sensitive to signal attenuation due to atmospheric conditions, with weaker signal return under optically thick clouds and dust-aerosol layers. Mie-cloudy is less concerned as backscatter from particles is stronger, although it is sensitive to weak backscatter, e.g. from dust layers. Because of its strong sensitivity on signal levels, the EE of Rayleigh-clear only considers Poisson noise and is therefore inversely proportional to the squared root of the useful signal. For Mie-cloudy, this rule of thumb is not true. In this context, we aim to investigate the quality of the Rayleigh-clear and Mie-cloudy winds and the reliability of the corresponding EE with respect to the presence of clouds and dust.

Rayleigh-clear

Table 5.3 describes the error dependency of the Rayleigh-clear observations with respect to the presence of clouds and dust, with cases below 50%, above 50% and above 75% of cloudiness, as well as sub-categories distinguishing the dust mixing ratio above ($Dust$) and below ($Dust_{NO}$) 10^{-8} $kgkg^{-1}$. Note that SMAD is not used for this analysis as this reliably removes outliers, which ought to be quantified here. We note that the MADI, the STD, and the EE_{tot} all increase with the amount of clouds and dust along the track, presumably due to the reduced return signal. In non-dusty conditions ($Dust_{NO}$), we observe that for low cloud cover (<50%), the MADI (3.3 ± 0.2 ms^{-1}) is significantly lower than the EE_{tot} (4.8 ms^{-1}) with a difference of 1.5 ms^{-1}, while for higher cloud cover, the difference between MADI and EE_{tot} is much smaller (1.1 ms^{-1} and 1.0 ms^{-1} for above 50% and 75% of cloudiness, respectively). This phenomenon is further enhanced at higher dust concentrations, with the MADI reaching even higher values (5.7 ± 0.8 ms^{-1}) than the EE_{tot} (5.8 ms^{-1}) for cloud cover above 75%. This highlights how the EE_{tot} in clear sky conditions is well calibrated, while it is becoming gradually too low with the increasing presence of clouds and dust. The larger STD with increasing cloudiness and dust concentration suggests an increasingly perturbed pattern of Rayleigh-clear measurements,possibly owing to the lower signal levels or to a cross-talk.

Figure 6.5 puts this phenomenon into perspective, by showing the altitude-dependent absolute difference $|\Delta_{diff_{HLOS}}|$ (a,e), the EE_{tot} (b,f), the normalized useful signal (c,g) and the SR (d,h), where the colouring depends on the percentage of SAFNWC clouds (upper row) and the CAMS dust mixing ratio (lower row) along the track. For reference, the values that did not pass the Quality Control (QC) are shown transparently. In

Table 5.3: Overview of the total Error Estimate (EE_{tot}; ms^{-1}), mean absolute difference and uncertainty (MADI, σ_μ; ms^{-1}), Standard deviation (STD; ms^{-1}) and counts (COUNT) for the Rayleigh-clear measurements under different cloud and dust conditions. This includes three categories of cloud cover ($<$ 25 %, $>$ 50 %, $>$ 75 %) for dust mixing ratios above ($Dust$) and below ($Dust_{NO}$) 10^9 $kgkg^{-1}$ along the track. **From Borne et al. (2024) under the Creative Commons Attribution 4.0 International License (CC BY 4.0).**

	Cloud < 50 %		Cloud > 50 %		Cloud > 75 %	
	$Dust_{NO}$	Dust	$Dust_{NO}$	Dust	$Dust_{NO}$	Dust
EE_{tot}	4.8	5.4	5.0	5.6	5.3	5.8
MADI	3.3±0.2	4.4±0.6	3.9±0.5	5.0±0.5	4.3±0.7	5.7±0.8
STD	4.3	5.0	5.1	5.9	5.6	6.4
COUNT	234	28	64	52	38	24

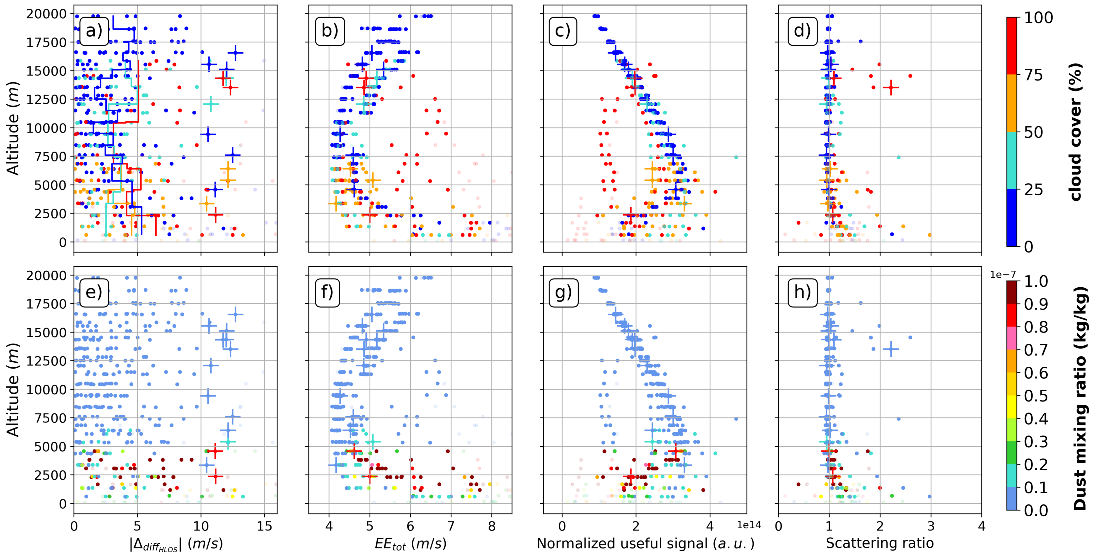

Figure 5.7: Altitude as a function of Rayleigh-clear absolute difference $|\Delta_{diff_{HLOS}}|$ (a,e), EE_{tot} (b,f), normalized useful signal (c,g) and Scattering Ratio (SR) (d,h), where the colouring is dependent on the percentage of Satellite Application Facility for supporting NoWCasting and very short range forecasting (SAFNWC) clouds (upper row) and Copernicus Atmosphere Monitoring Service (CAMS) dust mixing ratio (lower row) along the track. The cross symbol + stands for outliers and defines values with an EE below 5 ms^{-1} and an absolute difference of more than 10 ms^{-1}. Panel (a) includes the MADI for each cloud cover percentage, with a minimum sample size of 10 data points used to compute each value. **From Borne et al. (2024) under the Creative Commons Attribution 4.0 International License (CC BY 4.0).**

addition, panel 6.5a includes the MADI of four cloud cover percentage categories, where each MADI is computed with a minimum sample size of 10 values. The colourings in Fig. 6.5 are illustrative of the results summarised in Table 5.3, with measurements showing generally greater MADI under high cloud cover (red, orange, Fig. 6.5a) than under lower cloud cover (blue, blue-green). Measurements in the lower troposphere are naturally more strongly affected by cloud cover compared to higher levels. The same applies to dust (Fig. 6.5e), which also occurs mainly in the lower 5 km of the troposphere.

As we have already shown in Fig. 6.3b, the absolute error is higher in the upper and lower troposphere and minimised in the middle troposphere around 10 km altitude. This trend is well reflected in the EE_{tot} in Fig. 6.5b, which is an indication of the generally good consistency between the EE_{tot} and the absolute differences. As expected, this tendency fits inversely with the normalized useful signal shown in Fig. 6.5c, with lower signal in the upper and lower troposphere. Indeed, in the higher troposphere the air is less dense and the thickness of the RB's is not sufficient to compensate for the decrease in air molecule density. In the lower troposphere, the return signal is lower due to strong attenuation under clouds and dust layers. Interestingly, the values with high EE_{tot} and smaller useful signal in the mid-troposphere between 5 and 12.5 km in red likely correspond to measurements sampled under thick clouds, resulting in a strongly attenuated signal. They account for most of the measurements with cloud cover greater than 75 % in this altitude range, while the cloud tops appear to be located between 12.5 and 15 km, as they exhibit a larger normalized useful signal and a SR greater than 1 (Fig. 6.5d,h). Finally, outliers are found under all types of cloud and dust conditions and affect different altitude ranges. They also occur for regular normalized useful signals, with most SRs lying around 1, which rules out a cause related to atmospheric particles.

Mie-cloudy

Table 5.4 shows the same as Table 5.3, but for Mie-cloudy. Due to the limited amount of data for Mie-cloudy winds, the interpretation of the results should be treated with caution. We find that, in contrast to Rayleigh-clear, the EE, MADI and STD decrease with the percentage of cloud cover along the path. This is understandable as clouds provide the strongest backscatter signal required for high quality Mie-cloudy measurements. However, the presence of dust for cloud cover below 50 % leads to a decrease in EE_{tot}, MADI and STD, while conversely there is an increase of these quantities in more dense cloudy conditions (>50 %, >75 %). A possible explanation is that in clear-sky conditions, the backscatter from dust layers is strong enough to obtain high quality measurements, whereas in cloudy conditions, the attenuation by clouds weakens the backscatter return from the dust.

Figure 6.6 depicts the same as Fig. 6.5, but for Mie-cloudy. As mentioned in the previous section when discussing in Fig. 6.4b, most backscatter occurs in two layers, i.e. within 10–15 km and below 7 km altitude. The majority of measurements have normalized useful signals above $5e^{13}$ a.u. (Fig. 6.6c,g), which is overall above the normalized useful signal of the rejected measurements shown in transparent. Furthermore, the SRs are generally above 1 (Fig. 6.6d,h), which is characteristic of Mie-cloudy measurements. More specifically, measurements sampled above 12.5 km have a cloud cover of more than 75 % along the track and probably correspond to cloud tops, as they have stronger SRs between 1.5 and 3 (Fig. 6.6d,h). They exhibit good quality as well, with an

Table 5.4: Same as table 5.3, but for Mie-cloudy. **From Borne et al. (2024) under the Creative Commons Attribution 4.0 International License (CC BY 4.0).**

	Cloud < 50 %		Cloud > 50 %		Cloud > 75 %	
	Dust$_{NO}$	Dust	Dust$_{NO}$	Dust	Dust$_{NO}$	Dust
EE$_{tot}$	3.7	3.6	3.4	3.5	3.2	3.4
MADI	2.8±0.5	2.4±0.2	1.8±0.3	2.5±0.4	1.6±0.3	2.6±0.6
STD	2.96	1.53	1.89	2.95	1.68	3.18
COUNT	11	9	16	23	8	13

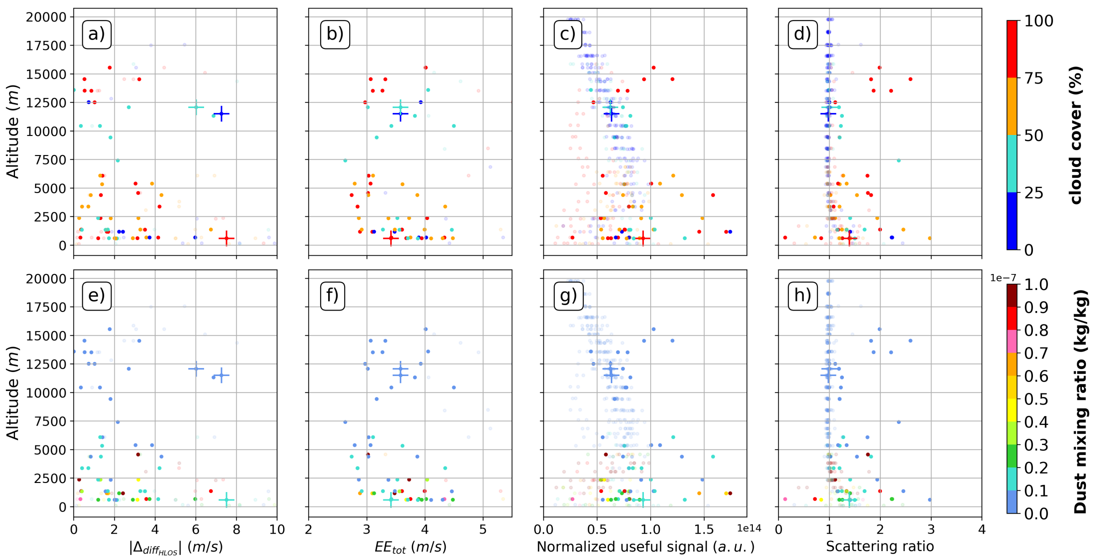

Figure 5.8: Same as Fig. 6.5 but for Mie-cloudy. Here the cross symbol + defines values with an EE below 3 ms^{-1} and an absolute difference above 6 ms^{-1}. **From Borne et al. (2024) under the Creative Commons Attribution 4.0 International License (CC BY 4.0).**

average MADI of 1.5 ms^{-1} (Fig. 6.4b). Between 7.5 and 12.5 km altitude, most of the measurements occur with cloud cover less than 50 %, with SRs falling below 1.3. In this altitude range, there are also 2 outliers, which interestingly have SRs around 1 and a normalized useful signal in the same order of magnitude as the discarded ones. Their presence is unusual, as Mie-cloudy measurements are only obtainable for SRs above 1. Finally, below 7.5 km, the cloud cover is mainly above 50 %, while the dust concentration is mainly below 5×10^{-8} $kgkg^{-1}$, showing that most of the Mie-cloudy backscatter results from clouds and not from dust. As can be seen in Fig. 6.6g, measurements with high dust concentration (brown) are discarded (transparent) with normalized useful signals below $5e^{13}$ a.u. Surprisingly, measurements sampled at the lower 1 km have the lowest normalized useful signals, mostly below $5e^{13}$ a.u. and are not discarded. These, however, tend to have larger SRs between 1 and 2, which can compensate for the low normalized useful signal in the calculation of the EE. They also correspond to the largest MADI scaling up to 4 ms^{-1} on average (i.e. Fig. 6.4d) in addition to relatively high EE_{tot}s (i.e. Fig. 6.6b,f). Two measurements also show negative SRs, which is an artifact, due to insufficient background signal corrections. The third outlier in the lower 1 km does not have abnormal characteristics compared to other measurements at this altitude.

5.3.3 Case studies

To further investigate the properties of the Aeolus wind errors, this section presents three case studies comparing Aeolus and radiosonde wind measurements under three different atmospheric conditions, namely clear sky, high cloud cover and high dust concentration.

The first case-study illustrated in Fig. 6.7 presents a comparison between Aeolus and radiosonde wind measurements collected under clear sky conditions. The radiosonde was launched over Sal Airport at 18:45 UTC on 9 September 2021, and Aeolus passed over on an ascending orbit between 19:23:56 UTC and 19:24:31 UTC within a co-location radius of 180 km around the launch site. Figure 6.7a depicts the corresponding sampled radiosonde HLOS wind profile (black lines) as well as Rayleigh-clear (blue) wind measurement points with associated EE_{tot} shown as error bars and ECMWF model equivalents shown as stepped lines. The corresponding Rayleigh-clear EE_{tot}, normalized useful signal and CAMS dust mixing ratio profiles are shown in blue in Figs. 6.7b, 6.7c and 6.7d, respectively, along with all other profiles in grey and the average of all profiles in black. Figure 6.7e shows the SAFNWC Cloud Type (CT) over the Cape Verde region at 19:00 UTC. In the latter panel, it can be seen that conditions were predominantly cloud-free along the Aeolus track (red solid line) and within the co-location radius (white solid line), while some low clouds can be found in the surrounding area. In these clear-sky conditions, it is not surprising to find that most of the measurements are of the Rayleigh-clear observation type, with no Mie-cloudy and Rayleigh-cloudy measurements (Fig. 7a). Throughout the atmosphere above 2.5 km, the quality of Rayleigh-clear is very good, with most error bars overlapping with radiosonde measurements and ECMWF model equivalents. In general, we found that the EE_{tot} estimate (Fig. 6.7b) is below average throughout the atmosphere, with a minimum of 3.5 ms^{-1} at 8 km altitude and a maximum above 5 ms^{-1} at 17.5 km and 2.5 km altitude. This is consistent with to a normalized useful signal (Fig. 6.7c) close to the average, except between 2.5 and 12.5 km, where it is higher, most likely due to the absence of cloud attenuation. In general, EE_{tot} and normalized useful signal decrease below 5 km, which is accompanied by an increase in the dust mixing ratio. This increase reaches 1.2 $kgkg^{-1}$ at about 2 km altitude, below which no measurements are found, presumably filtered out during the QC procedure.

Figure 6.8 shows the same as Fig. 6.7, but for cloudy conditions. In this case study, the radiosonde was also launched from Sal airport, this time at 07:00 UTC on 14 September 2021, with a co-location radius of 60 km. Aeolus passed across the co-location region between 07:28:32 UTC and 07:28:55 UTC, i.e. during the descending node. As can

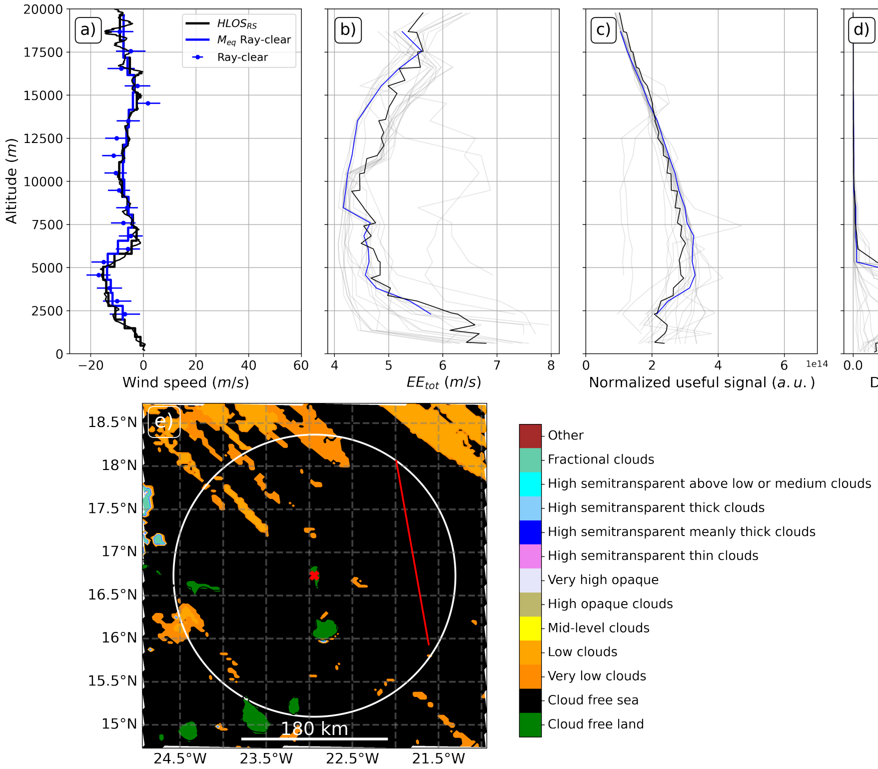

Figure 5.9: Overview of the cloud-free case study for a radiosonde launched from Sal airport on 9th September 2021 at 18:45 UTC and the ascending orbit of Aeolus between 19:23:56-19:24:31 UTC for a co-location radius of 180km. (a) Vertical radiosonde HLOS wind profile (black solid line) and projected onto Rayleigh-clear RBS (black stepped line), as well as averaged Rayleigh-clear observations (blue dots), corresponding EE (error bars) and ECMWF model equivalents (M_{eq}, stepped lines). (b) Vertical profile of the Rayleigh-clear EE_{tot} (blue line), together with the EE_{tot} of all profiles (grey solid lines) and their average (black solid line). (c), (d) Same as (b), but for normalised useful signal and CAMS dust mixing ratio, respectively. (e) Horizontal map showing the SAFNWC CTat 19:00 UTC and the co-location perimeter (white solid line), the Aeolus track (red solid line) and the radiosonde launch site (red cross). **From Borne et al. (2024) under the Creative Commons Attribution 4.0 International License (CC BY 4.0).**

been seen in panel 6.8e, which corresponds to SAFNWC CT at 07:30 UTC, Aeolus overpasses a variety of high clouds, mainly high semitransparent clouds. These high-clouds appear to be located between 13 km and 16 km altitude, as three Mie-cloudy (red) and two Rayleigh-cloudy (orange) measurements are found in this range, and where the normalized useful signal is found to have a maximum. In this altitude range, all Rayleigh-clear, Rayleigh-cloudy and Mie-cloudy measurements exhibit good quality, with radiosonde measurements generally within the error bars. Above this cloud cover at 16 km, we only find Rayleigh-clear measurements that also perform well, with an EE_{tot} (Fig. 6.8b) and normalized useful signal (Fig. 6.8c) close to average. Beneath the cloud base at 13 km altitude, however, it appears that the Rayleigh-clear measurements follow an irregular pattern, with most of the measurements and error bars not matching the radiosonde observations, reaching deviations higher than 10 ms^{-1}. Accordingly, we

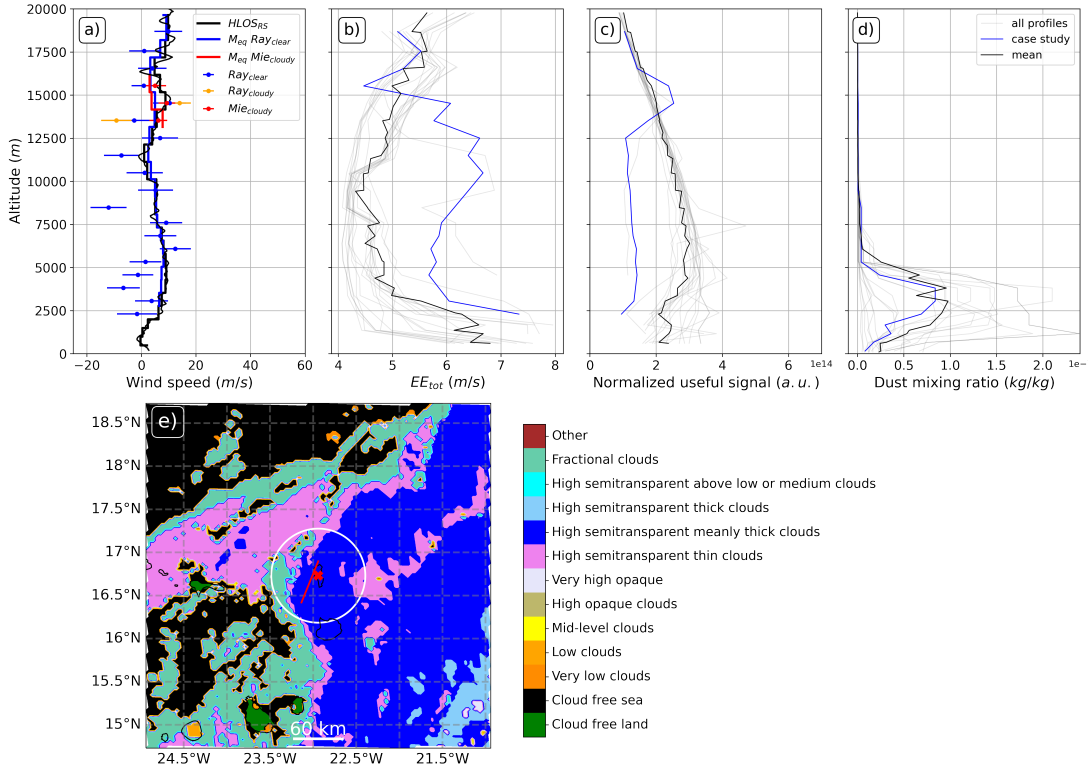

Figure 5.10: Same as Fig. 6.7, but for the case study with high cloud cover. Here, the radiosonde was launched from the Sal airport at 07:00 UTC on the 14th September 2021, while Aeolus overpassed the co-location area, with radius of 60km, on a descending node between 07:28:32 and 07:28:55 UTC. In panel a, the red and orange colours represent the averaged Mie-cloudy and Rayleigh-cloudy observations (points), respectively, with the corresponding EE shown as error bars and ECMWF model equivalents (M_{eq}) shown as stepped lines. The SAFNWC CT shown in (e) corresponds to 07:30 UTC. **From Borne et al. (2024) under the Creative Commons Attribution 4.0 International License (CC BY 4.0).**

find that the EE_{tot} (Fig. 6.8b) is larger in this altitude range mainly varying between 5 and 6 ms^{-1}, which also corresponds to a sharp decrease of the normalized useful signal well below the average (Fig. 6.8c). Nonetheless, the ECMWF model-equivalents in Fig. 6.8a remain fairly accurate relative to the radiosonde measurements. This result mirrors the findings presented in the previous section, namely that the Rayleigh-clear EE_{tot} is systematically underestimated when the normalized useful signal is strongly attenuated. It appears that the normalized useful signal further decreases below 2.5 km, presumably as a result of the increasing dust concentration at this height (Fig. 6.8d), which most likely leads to a QC rejection of the Rayleigh-clear measurements.

Lastly, Fig. 6.9 examines the influence of dust on the quality of Aeolus. In this case, the radiosonde was launched on 21 September 2021 at 06:50 UTC for a descending orbit of Aeolus, which passed over a co-location perimeter with a radius of 60 km between 07:28:44 UTC and 07:29:07 UTC. As can be seen in Fig. 6.9e, the atmospheric conditions in the co-location area were completely cloud free at 07:30, with some low level cloud further south of the island. The radiosonde profile shown in Fig. 6.9a

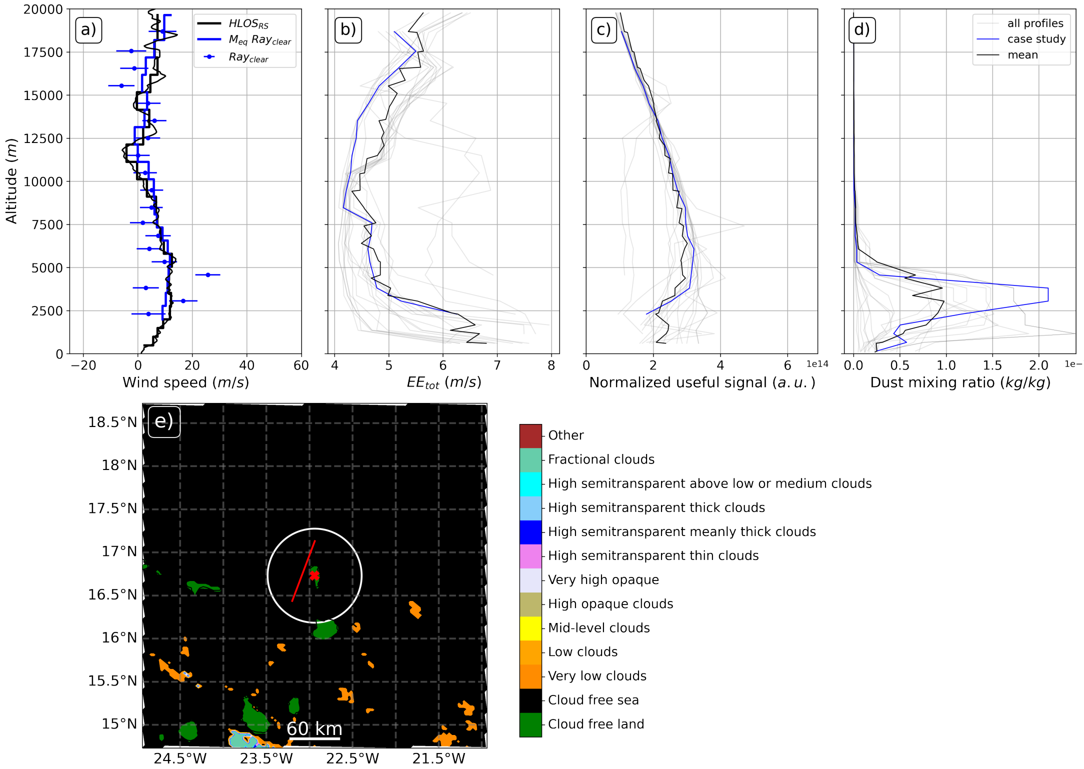

Figure 5.11: Same as Figs. 6.7 and 6.8 but for the case study with dust. Here, the radiosonde was launched from the Sal airport at 06:50 UTC on the 21th September 2021, while Aeolus overpassed the co-location area, with radius of 60km, on a descending node between 07:28:44 UTC and 07:29:07 UTC. The SAFNWC CT shown in (e) corresponds to 07:30 UTC. **From Borne et al. (2024) under the Creative Commons Attribution 4.0 International License (CC BY 4.0).**

indicates that Aeolus primarily measured in the Rayleigh channel along this orbital segment. Rayleigh-clear measurements appear to be consistent with radiosonde wind measurements throughout the mid-troposphere between 5 km and 15 km altitude, while outliers with EEs of less than 5 ms^{-1} (Fig. 6.9b) can be spotted above 15km and below 5km. This error structure is surprising, as both the normalized useful signal and error estimation curves are similar to the one of the cloud-free case study in Fig. 6.7b and 6.7c. However, in panel 6.9c, we see that the Rayleigh-clear error pattern coincides with a strong peak in dust mixing ratio, reaching more than 2 10^{-7} $kgkg^{-1}$ around 3.5 km altitude. The presence of dust seems to affect the quality of Rayleigh-clear measurements without influencing the normalized useful signal and thus leading to an underestimation of the EE. Reason could be linked to a cross-talk.

5.4 Concluding remarks

In this study, we conducted a cross-Atlantic validation of Aeolus wind observations using radiosondes in the scope of the JATAC. Of the total 20 radiosonde profiles included in this work, 11 were launched from Puerto Rico and St. Croix in the Caribbean and 9 from Sal Airport on Cape Verde between August and September 2021. The advantage of radiosondes is that they provide good vertical coverage, providing 384 Rayleigh-clear bin-to-bin comparisons from the surface to an altitude of 20 km and 59 Mie-cloudy comparisons, mainly restricted to the presence of clouds and aerosols. After having applied several QC and adaptation grid procedures, we quantified the quality of Rayleigh-clear, Mie-cloudy and to a lesser extent Rayleigh-cloudy observation types, with respect to co-location aspects as well as atmospheric conditions such as cloud cover and dust concentration.

According to our statistical analysis, the total systematic error of Rayleigh-clear is $-0.5 \pm 0.2\ ms^{-1}$, which is in agreement with the ESA recommendation of 0.7 ms^{-1}. The random error was calculated from the standard deviation of the difference between radiosonde and Aeolus measurements, accounting for radiosonde observation errors estimated at $0.7 \pm 0.28\ ms^{-1}$ and representativeness errors ranging from 1.5 to 2.5 ms^{-1}. In the altitude range of 2–16 km and 16–20 km, the random error is 3.8 – 4.3 ms^{-1} and 4.3 – 4.8 ms^{-1}, respectively, which is above the ESA-specified values of 2.5 ms^{-1} and 3 ms^{-1}, respectively. In general, Rayleigh-clear shows no error dependency with respect to co-location radius, even for distances reaching 340 km, whilst being more sensitive to co-location time, especially if the radiosonde measurement is ahead of Aeolus' overflight time, which presumably corresponds to low altitude measurements. In addition, the systematic and random errors are height-dependent, with larger errors occurring in the upper troposphere, mainly caused by the reduction in signal return from decreasing air density, and in lower levels, most likely caused by the signal attenuation by clouds and dust. The error estimate likewise follows a similar form to the observed height error dependency, as it is inversely proportional to the squared root of the normalized useful signal. In cases where the normalized useful signal is strongly attenuated by clouds or dust, the error estimate is generally underestimated, with measurements exhibiting non physical features and departures from radiosonde winds larger than the error estimate. A redefinition of the Rayleigh-clear error estimate could account for this underestimation by including other sources of noise, such as detector noise or readout noise, which increase for reduced signal levels. Furthermore, a cross-talk, i.e. the leakage of the Mie signal into the Rayleigh receiver, could also explain this underestimation, especially in the case of strong Mie returns. However, this supposition was not investigated in the context of this study. Outliers, defined as measurements with small error estimate and large absolute differences, are found under all conditions, i.e. for all co-location radii, co-location times, altitudes as well as cloud and dust cover. Their origin does not appear to be correlated with low signal levels but seem to be inherent to the statistical nature of the error distribution. Taking other terms into account when defining the error estimate, such as the influence of temperature, pressure or scattering ratio on the Rayleigh response, could certainly contribute to improving the error characterisation. The ECMWF model equivalents of Rayleigh-clear are found to have a significantly better agreement with the radiosonde wind measurements compared to the Rayleigh-clear observations. This is a further confirmation that the co-location parameters used for this validation study are appropriate and that the model equivalents provide a suitable reference for validating Aeolus. In addition, we demonstrate the existence of an orbital- and altitude-dependent bias in the Rayleigh-clear channel, which is visible with respect to both radiosondes and ECMWF model equivalents. This bias is documented in Chapter 6 in West Africa using model equivalents and is now confirmed observationally. The underlying cause for this bias, however, remains unknown. In addition, we find that Rayleigh-clear performs better compared to Rayleigh-cloudy, but due to the lack of Rayleigh-cloudy data we cannot draw any strong conclusions.

For Mie-cloudy, the statistical analysis yielded a systematic negative deviation of $-0.9 \pm 0.3\ ms^{-1}$ within ESA specifications when uncertainty is taken into account, and it is consistent across all orbital nodes and Cal/Val sites. The random error between 2–16 km is $1.1 - 2.3\ ms^{-1}$, which falls within the ESA recommendations. The general quality of Mie-cloudy winds does not depend on the co-location radius, while it is more sensitive to temporal differences. The errors appear to be larger at 5 km and about 1 km altitude, typically at the upper and lower limits of the Saharan Air Layer, where clouds frequently occur. According to Lux et al. (2022b), the Mie fringe of the Fizeau interferometer can be distorted in the case of strong backscatter gradients, e.g. at cloud edges. Interestingly, Mie-cloudy does not seem to sample within dust layers, as most bins with high dust concentrations are rejected by the QC. Furthermore, the systematic and random Mie errors decrease with the percentage of cloud cover, while they increase in the presence of dust. This may be attributed to the generally weak backscatter of dust, increasing the error of the Mie-cloudy winds. Similar to Rayleigh-clear, outliers with small error estimate and large absolute differences can be found for all co-location distance, co-location time, altitude, dust concentrations and cloud cover. An improvement of the Mie EE is expected from an optimisation of the Mie core algorithm, such as the fitting function or the classification algorithm.

6. Impact of Aeolus wind observations on the representation of the West African monsoon circulation

This section presents the main results of this study in three subsections. The first one (section 6.1) examines the distribution of observation in the Rayleigh-clear and Mie-cloudy channels, shows resulting climatologies and discusses the assigned observation and background errors in the different Observing System Experiment (OSE)s. Section 6.2 analyzes the impact of Aeolus data on 3D analyses fields with a special emphasis on the contributions from the two orbit phases and the two channels as well as the effect of the bias correction tested at European Centre for Medium-Range Weather Forecasts (ECMWF) for 2019. Finally, section 6.3 presents the impact of Aeolus data on 1–4 days forecasts with a special emphasis on the predictions of the African Easterly Jet North (AEJ-North) and Tropical Easterly Jet (TEJ). This analysis is supplemented by a verification of model background with radiosondes over Africa.

6.1 Observed atmospheric features

West Africa during boreal summer is characterized by many different types of aerosols and clouds that affect the Aeolus measurements. Figure 6.1 shows longitudinal averages between 30°E and 30°W of the number of counts for both Rayleigh-clear and Mie-cloudy channels from the ECMWF2019 OSE, as well as mixing ratios of different aerosol types from the CAMS and cloud fraction from ERA5 during the boreal summer of 2019. Irrespective of latitude the Rayleigh-clear counts (Fig. 6.1a) peak in the upper troposphere and lower stratosphere with values around 3000. Counts below 300 hPa are markedly reduced around the cloudy Intertropical Convergence Zone (ITCZ), which reaches its northernmost position in August at about 11°N and is often referred to as the African rainbelt (Nicholson, 2009). There are also indications for slightly reduced counts at midlevels towards the subtropical ends of the study domain in both hemispheres. Rayleigh-clear data below 850 hPa are rejected at ECMWF, as the impact found there was slightly negative. (see Table 4.3). The more complex Mie-cloudy signal (Fig. 6.1b) is shaped by the distribution of clouds and aerosols. There is a distinct maximum in the upper troposphere between 300 and 100 hPa over the African rainbelt around 10°N,

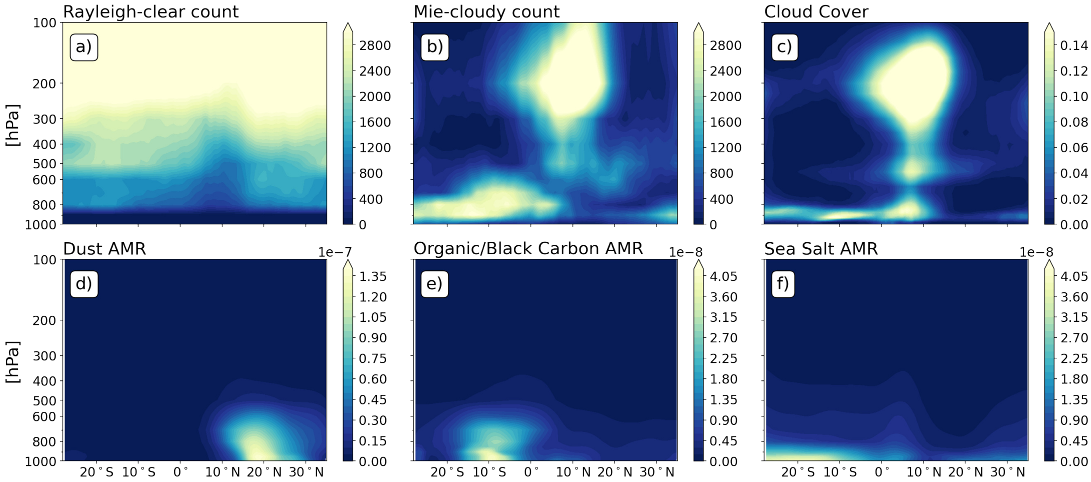

Figure 6.1: Latitude-height cross-sections of counts for Aeolus Rayleigh-clear (a) and Mie-cloudy (b) measurements, as well as ERA5 cloud cover (c), Copernicus Atmosphere Monitoring Service (CAMS) Dust Aerosol (0.03–20 μm) mixing ratio (d), CAMS Organic Matter and Black Carbon Aerosol mixing ratio (e) and CAMS Sea Salt Aerosol (0.03–20 μm) mixing ratio (f). AMR stands for Aerosol Mixing Ratio. The fields are averaged between 30°W and 30°E during July–September 2019 period. **From Borne et al. (2023) under the Creative Commons Attribution 4.0 International License (CC BY 4.0).**

corresponding to returns from cumulonimbus clouds, their associated anvils or from optically thick cirrus. The corresponding maximum in cloud fraction can be seen in Fig. 6.1c. In this area Rayleigh-clear and Mie-cloudy counts are of a similar magnitude exceeding 3000 counts (cf. Fig. 6.1a and b). During the ascending orbit at 18 UTC (not shown here), there is a higher number of Mie-cloudy counts over this location, caused by the stronger land convection occurring in the afternoon. Below the prominent high cloud maximum, two smaller peaks are evident in Fig. 6.1c, likely corresponding to early stages of cumulonimbus, cumulus congestus or altocumulus layers just below 500 hPa and boundary-layer clouds below 800 hPa (Johnson et al., 1999). These, however, are less prominent in Mie-cloudy counts (Fig. 6.1b) due to attenuation effects. Higher counts at midlevels extend northwards from the rainbelt region into the Sahara. These appear to be partly related to midlevel clouds (Fig. 6.1c) and to the high dust content of the dry and warm Saharan Air Layer (SAL) (Fig. 6.1d) (Dunion and Marron, 2008). The SAL is mainly sampled in its upper parts by Mie-cloudy scattering (Fig. 6.1b). To the south of the African rainbelt, a distinct low-level maximum is evident stretching from 30°S to 5°N (Fig. 6.1b). The southern part is restricted to levels below 700 hPa but around 8°S enhanced counts reach up to about 550 hPa. This maximum is likely due to a combination of sea salt aerosol in the shallow marine boundary layer (Fig. 6.1f, below 900 hPa), low mostly stratiform clouds at the top of the boundary layer (Fig. 6.1c, below 800 hPa) as described, for example, in Knippertz et al. (2011) and Schrage and Fink (2012), and a relatively deep plume of Biomass Burning (BB) aerosol, as indicated by enhanced levels of black carbon and organic matter (Fig. 6.1e, around 10°S) (Reid et al., 2005; Levin et al., 2010; Zuidema et al., 2016; Carter et al.,

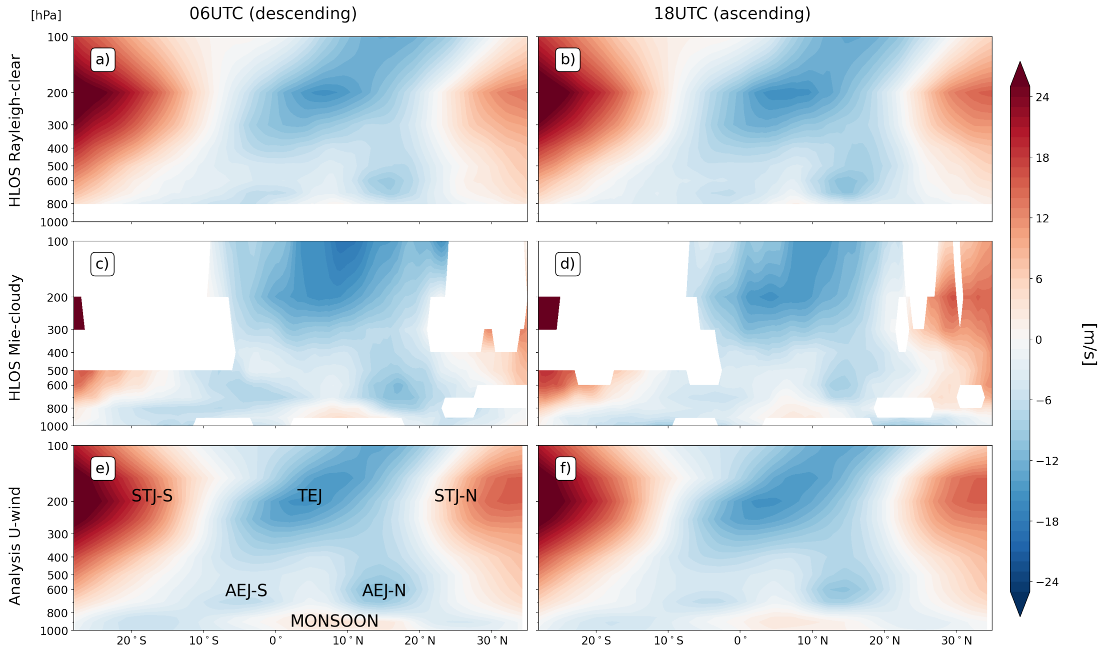

Figure 6.2: Latitude-height cross-sections of Aeolus measured Rayleigh-clear (a,b) and Mie-cloudy (c,d) Horizontal Line of Sight (HLOS) winds, as well as zonal wind from the ECMWF2019 analysis that includes Aeolus data (e,f). Shown are 06 UTC (left column) and 18 UTC (right column), corresponding to the descending and ascending orbits, respectively. The fields are averaged between 30°W and 30°E and smoothed using a latitudinal moving average of 2° grid size for the period July–September 2019. Regions for which no wind data were collected are shown in white. The major jet features AEJ-North and **AEJ!** (**AEJ!**)-South , Tropical Easterly Jet (TEJ), Subtropical Jet (STJ) North (STJ-N) and South (STJ-S) as well as the southwesterly Monsoon flow are labelled in panel e. HLOS winds from the descending track are multiplied by -1 to correspond with the sign convention of the model coordinate system. **From Borne et al. (2023) under the Creative Commons Attribution 4.0 International License (CC BY 4.0).**

2021). This plume originates from agricultural and forest burning (Barbosa et al., 1999; Haslett et al., 2019) with some parts getting thermally lifted above the low-level clouds. Taken Rayleigh-clear and Mie-cloudy signals together, most parts of the West African Monsoon (WAM) region show a satisfactory level of sampling such that the main circulation features should be captured by Aeolus measurements. Since the WAM region is located around the Greenwich meridian, the Aeolus descending and ascending observations are included in the 06 UTC and 18 UTC assimilation windows, respectively. Figure 6.2 compares the HLOS winds for ascending and descending orbits with the zonal wind of the analysis field of the ECMWF2019 OSE where Aeolus is assimilated. The Rayleigh-clear HLOS wind observations (Fig. 6.2a and b) can well represent all important wind features above 850 hPa, i.e. the TEJ around 5°N and the subtropical jets of both hemispheres in the upper troposphere, as well as the AEJ-North (10–15°N, between 700 and 500 hPa) and **AEJ!**-South (5°S, ~800 hPa) in the mid-troposphere (see labels in Fig. 6.2e). Rayleigh-clear winds are generally consistent between ascending (Fig. 6.2a) and descending (Fig. 6.2b) orbits, although some differences in the intensity of the TEJ and AEJ-North are visible, and can possibly be attributed to either diurnal cycle effects between dusk (18 UTC) and dawn (06 UTC) or orbital-dependant biases. The Mie-cloudy observations (Fig. 6.2c and d) have too few measurements in the usually cloud- and aerosol-free areas of the subtropical jets (see Fig. 6.1) but can capture the TEJ, the AEJ-North, partially the AEJ-South as well as the westerly component of the monsoon flow between 0 and 15°N at 900 hPa. Differences between the orbits are again noteworthy, with the intensity of the AEJ-North and the TEJ stronger near 100 hPa at 06 UTC (Fig. 6.2c) compared to 18 UTC (Fig. 6.2d). Furthermore, Mie-cloudy winds have a much larger TEJ jet core with respect to Rayleigh-clear winds. According to Lemburg et al. (2019), cloud-related processes such as convection and the change in diabatic heating/cooling due to radiation have an influence on the TEJ. In general, the TEJ is expected to strengthen a few hours after a large-scale convective event, mainly southwest of the convection, which is consistent with the stronger TEJ observed in Mie-cloudy winds. Finally, the HLOS Rayleigh-clear winds (Fig. 2a and b) seem to have the best agreement with the analysis field (Fig. 2e and f) in terms of the pattern and intensity of the different jets, while Mie-cloudy seems to have a stronger TEJ compared to the analysis. The largest impact of Aeolus data on analysis fields is expected in regions with high data density, low assigned observation errors and large background errors. Figure 6.3 shows both the Rayleigh-clear and Mie-cloudy assigned observation errors for the three OSEs without bias correction. The assigned observation error in the ECMWF OSEs is mainly derived from the instrument error estimate of the Level 2B (L2B) processor, while in the Deutscher Wetterdienst (DWD) OSE it is determined by a predefined look-up table (see Table 4.3). For ECMWF2019, the assigned Rayleigh-clear observation error has minima around 2.8 ms^{-1} in the free troposphere in the southern and northern parts of the study domain (Fig. 6.3a). Errors increase markedly in the area of the African rainbelt (around 10°N), where they exceed 5 ms^{-1} at lower levels. Here, the number of counts is reduced, as indicated by the grey line in Fig. 6.3a (see full field in Fig. 1c). The increase in error can be attributed to the lower signal-to-noise ratio in broken cloud scenes (see Fig. 1c). In addition, there is a general increase in the upper troposphere above 200-150 hPa, which is likely related to cirrus clouds, and below 600hPa in areas where clouds and aerosol are abundant (see Fig. 1c–f). The corresponding analysis for 2020 (Fig. 6.3b) shows some similarities in terms of the overall pattern but generally much higher values exceeding 5 ms^{-1} in large parts of the domain. This may be attributed to the decreasing atmospheric path signal and thinner range bin settings, increasing the Rayleigh-clear wind random error (Reitebuch et al., 2020). As indicated by the grey and black lines in Fig. 6.3b, this also leads to an overall reduced number of counts. The DWD experiment for 2020 (Fig. 6.3c) in contrast assumes a much smoother error pattern that reveals the height dependence of the assigned error. The error is generally lower and does not exceed 5 ms^{-1} anywhere in the domain. DWD does consider data from below 850 hPa but overall less observations than in ECMWF pass the initial quality control, as indicated by the grey and black lines

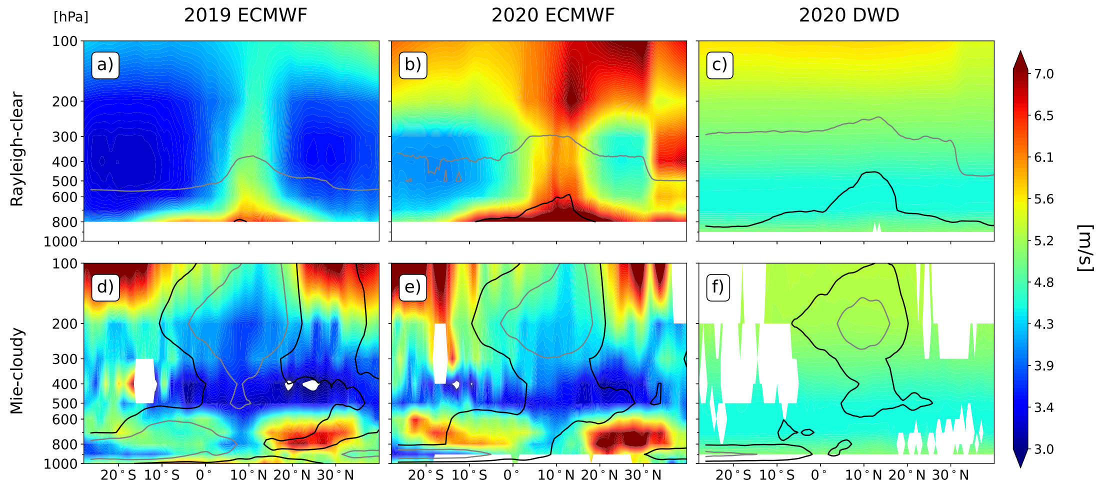

Figure 6.3: Latitude-height cross-sections of Rayleigh-clear (top row) and Mie-cloudy (middle row) assigned observation error for ECMWF2019 (left column), ECMWF2020 (middle column) and DWD2020 (right column), all for July–September. The fields are averaged between 30°W and 30°E and smoothed using a latitudinal moving average of 2° grid size for the period July-September 2019. Regions for which no wind data were collected are shown in white. The grey and black contours correspond to 1500 and 500 measurement counts, respectively. The lines in panels a and b here correspond to the shading in Fig. 1a and b. **From Borne et al. (2023) under the Creative Commons Attribution 4.0 International License (CC BY 4.0).**

in Fig. 6.3c. The corresponding observation errors for Mie-cloudy winds show a different and generally more noisy structure for both ECMWF experiments (Fig. 6.3d and e). Errors are larger in regions dominated by aerosols (i.e., BB and SAL) than in regions dominated by clouds (see Fig. 6.1c–f). Mie-cloudy backscatter from ice particles and cloud droplets generally has a stronger signal level, while backscatter from aerosol layers is weaker, thus increasing the wind errors. The representativeness error of Mie-cloudy winds may also depend on the spectral properties and concentration of the various atmospheric constituents. As for the Rayleigh signals, the assigned error for DWD and the number of counts used (Fig. 6.3f) are overall smaller than for ECMWF. The error is dominated by the height dependence, giving overall similar values for Mie-cloudy and Rayleigh-clear winds (cf. Fig. 3c and f).

6.2 Influence on analysis fields

6.2.1 Mean and root mean squared differences

To investigate the influence of Aeolus on the representation of WAM wind subsystems such as the AEJ-North and the TEJ in the analysis fields, Mean Differences (MD) and Root Mean Square Differences (RMSD) in the zonal wind component were computed for all four OSEs (see Table 1) with four-time daily data. Figure 6.4 shows these quantities as latitude-height cross-sections averaged between 30°W and 30°E, Fig. 6.5 shows corresponding horizontal maps at the levels characteristics of the AEJ-North (700 hPa) and TEJ (200 hPa). To locate the position of the jets, grey and black lines are drawn in

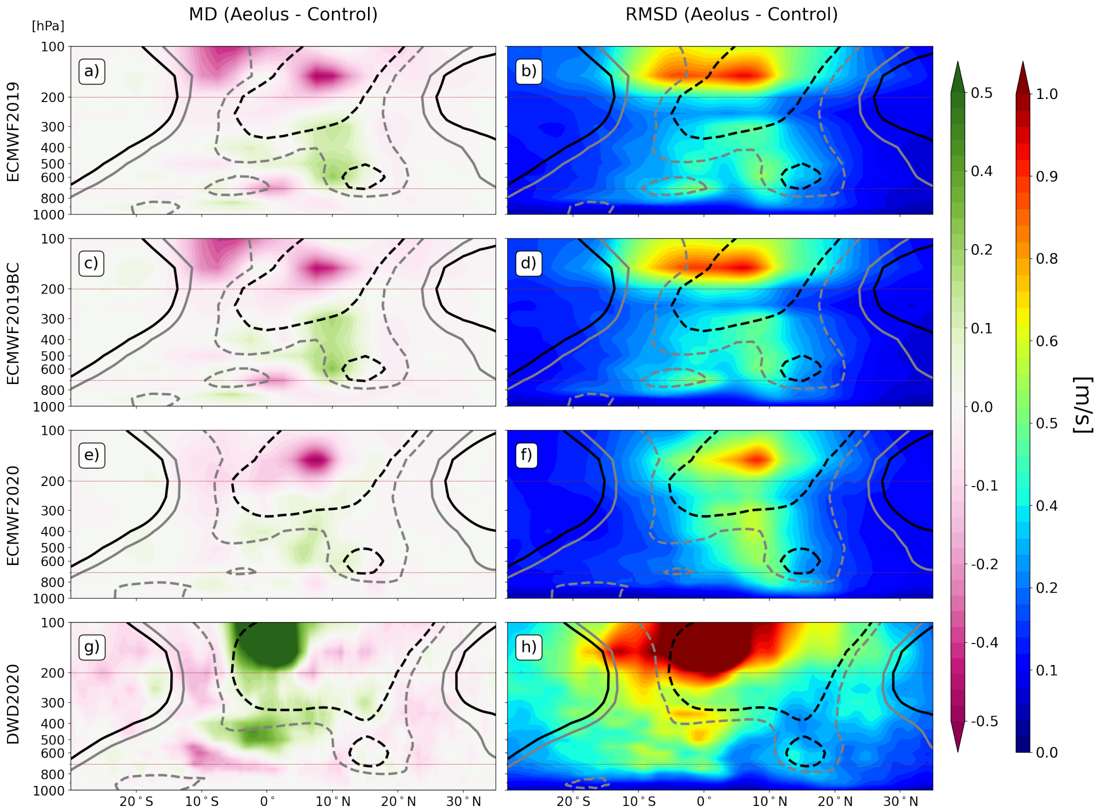

Figure 6.4: Latitude-height cross-sections of mean difference (MD, left column) and root mean square difference (RMSD, right column) between the analysis fields of the zonal wind component Aeolus minus Control for the four different OSEs (see Table 1). The fields are averaged between 30°W and 30°E during July–September. The grey and black contours correspond to zonal wind fields, taken from the OSE with Aeolus, of 6 and 9 ms^{-1}, respectively. Solid lines indicate westerlies, dashed ones easterlies. The brown lines mark the 200hPa and 700hPa levels. **From Borne et al. (2023) under the Creative Commons Attribution 4.0 International License (CC BY 4.0).**

both figures for zonal wind speeds of 6 and 9 ms^{-1}, respectively. For the ECMWF OSEs the largest MD and RMSD (top three rows in Fig 6.4) corresponds to the convective ITCZ and the cumulonimbus outflow region, where the background forecast error is largest (not shown), while for the DWD2020 OSE (bottom row in Fig 6.4) even more significant differences are present in the upper tropical troposphere centred on the equator south of the cumulonimbus outflow region. The ECMWF2019 OSE shows a strengthening of the central region of the TEJ (Fig. 6.4a, 6.5b) by up to 0.4 ms^{-1} and a weakening of the same magnitude south of the AEJ-North, corresponding to the region where Mie-cloudy captures congestus and altocumulus clouds (see Fig. 6.1b and c). These changes are accompanied by large random changes in wind (Fig. 6.4b) when Aeolus is assimilated. These features are also evident in Figure 5, with maximum weakening occurring south of the AEJ-North between 25°W and 15°E at 10°N, notwithstanding a strengthening of the AEJ-North towards the eastern part of the Sahel (~20°E) (Fig. 6.5a). The strengthening of the northern part of the **AEJ!**-South (Fig. 6.4a, 6.5a), associated with

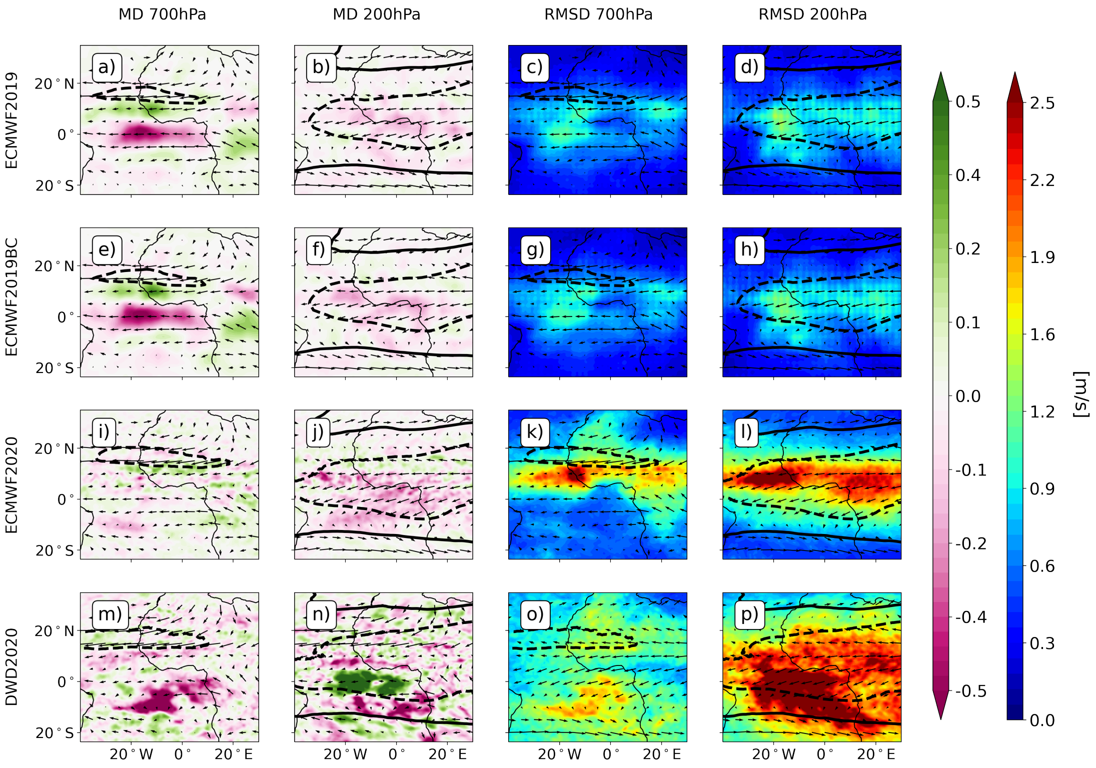

Figure 6.5: Horizontal maps of the July–September mean differences (MD, left two. columns) and root mean square differences (RMSD, right two columns) between the analysis fields of the zonal wind component Aeolus minus Control for the four different OSEs (see Table 1). The black contours show the $9ms^{-1}$ zonal wind isotach from the analysis with Aeolus. Solid lines indicate westerlies, dashed ones easterlies. The AEJ-North is evident at 700 hPa, while the TEJ and STJs are visible at 200 hPa. **From Borne et al. (2023) under the Creative Commons Attribution 4.0 International License (CC BY 4.0).**

a change in wind direction between the monsoon layer and the mean easterly winds, is also striking. For the TEJ, the strengthening is apparent across the entire jet (Fig. 6.5b). In comparison, the ECMWF2019BC OSE shows an almost identical influence of Aeolus on the analysis (Figs. 6.4a-d, 6.5a-h), implying that the temperature-dependent bias correction of the Rayleigh channel does not contribute noticeably to the analysis differences averaged over four times per day. The influence of Aeolus on the ECMWF2020 OSEs is similar to that of the ECMWF 2019 OSEs, with a comparable strengthening of the TEJ of ~0.4 ms^{-1} but a less pronounced weakening of the southern edge of the AEJ-North of only ~0.2 ms^{-1} and no obvious strengthening of the AEJ-North over the eastern Sahel (Figs. 6.4e, 6.5i-j). It is noteworthy that the maximum RMSD in the ECMWF 2019 OSEs affects the upper part of the TEJ between 200 and 100 hPa and between 700 and 300 hPa (Fig. 6.4b-d), while in the ECMWF2020 OSE it spans across the entire ITCZ region between 700 and 100 hPa (Fig. 6.4f), thus explaining the weaker RMSD at 200 hPa in 2019 (Fig. 6.5d-h) compared to 2020 (Fig. 6.5l). Moreover, the influence in the DWD2020 OSE is much larger, with a slowdown of the southern edge of the TEJ of more than 0.5 ms^{-1} and a less pronounced acceleration of ~0.2

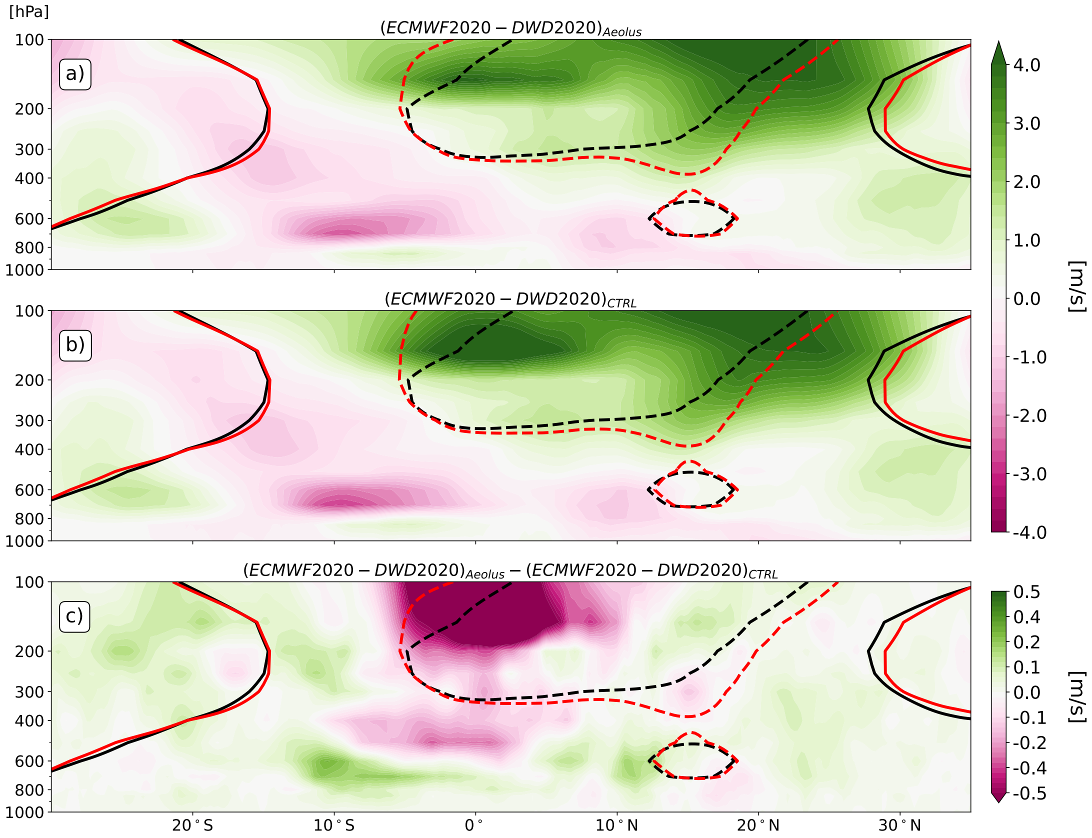

Figure 6.6: Latitude-height cross-sections of mean difference between the analysis fields of the zonal wind component of ECMWF2020 minus DWD2020 with (a) and without (b) Aeolus as well as the difference between both differences (c). The fields are averaged between 30°W and 30°E during July–September. The black and red contours correspond to zonal wind fields, taken from the OSE with Aeolus at 9 ms^{-1} for the ECMWF and DWD OSEs, respectively. Solid lines indicate westerlies, dashed ones easterlies. **From Borne et al. (2023) under the Creative Commons Attribution 4.0 International License (CC BY 4.0).**

ms^{-1} of the northern part of the TEJ (Figs. 6.4g, 6.5m-n). The strong deceleration is accompanied by more significant random changes in the zonal wind fields due to Aeolus compared to the ECMWF OSEs (Figs. 6.4h, 6.5o-p). Furthermore, the DWD2020 OSE does not show a significant change in the structure of AEJ-North, likely due to a relatively low background forecast error in the domain, which gives more weight to the background in the analysis. Finally, we assess to what extent Aeolus assimilation brings the analyses of ECMWF2020 and DWD2020 together. Figure 6.6a and b depict the difference between ECWMF2020 and DWD2020 analyses with and without Aeolus respectively, while Figure 6.6c shows the differences between Fig. 6.6a and b. The black and red lines represent the wind fields at 9 ms^{-1} in the ECMWF and DWD analysis with Aeolus, respectively. In general, the differences between ECMWF and DWD analyses are larger (Fig. 6.6a and b, up to 4 ms^{-1}) than the differences induced by the assimilation of Aeolus (Fig. 6.6c, up to 1.5 ms^{-1} exceeding the colorbar). The most significant differences between ECMWF and DWD model analyses are found over in the area of the TEJ, with DWD revealing a stronger TEJ up to 4 ms^{-1} compared to ECMWF. The AEJ-North, however, seems to be relatively consistent between the ECMWF and DWD. Figure 6.6c shows that the convective ITCZ above 600 hPa, culminating in the southern edge of the TEJ are the region where ECMWF and DWD converge most when Aeolus is assimilated. Elsewhere, especially in regions dominated by clear-sky conditions, the analyses diverge by up to 0.2 ms^{-1}. These differences appear to follow the Rayleigh-clear and Mie-cloudy measurement regions, with the Mie-cloudy observations in the convective ITCZ seemingly bringing the two model analyses closer together, while the Rayleigh-clear measurements pulls them apart. The additional vertical bias-correction included in the Rayleigh-clear channel in the DWD2020 OSE could explain the observed discrepancies in clear-sky regions.

6.2.2 Orbital phase and channel contributions

In this subsection we use statistics of observation minus background (Observation minus Background (O-B)) departures to disentangle the contributions of the HLOS Rayleigh-clear and Mie-cloudy wind observations on the analysis differences discussed in the previous subsection. Data corresponding to ascending and descending tracks will be examined separately to reveal the effects of the orbit phase. For the ECMWF2020 OSE, Fig. 6.7a and b shows the analysis differences Aeolus minus control at 06 UTC (descending orbit) and 18 UTC (ascending). These two panels can be compared directly to Fig. 6.4e and use the same shadings and lines. The comparison reveals that the total difference between the analyses with and without Aeolus data is dominated by 06 UTC, where the strengthening of the TEJ (plus a southward extension of negative differences) and the weakening of the southern edge of the AEJ-North are more pronounced. Signals in the northern hemispheric subtropics are generally small, while in the southern hemisphere, small-amplitude differences at 06 UTC and 18 UTC of opposite sign largely cancel each other out.

The subsequent panels of Fig. 6.7 (i.e., c–h) show background departures for the two Aeolus channels and their combination to examine where the diurnal differences in the Aeolus impact on the analysis fields come from. The O-B data of Rayleigh-clear and Mie-cloudy combined (Fig. 6.7c and d) have overall structures similar to their analysis counterparts but with amplitudes about 4–10 times larger, revealing considerable diurnal variations as already discussed in the context of Fig. 2. The magnitude of the influence on the analysis is a clear reflection of the assigned errors (see Fig. 3b, e and h). For example, the negative HLOS differences at upper-levels in the TEJ region, where background errors are assumed to be relatively large (Fig. 6.3h), translate into a strong signal in the analysis at 06 UTC (cf. Fig. 6.7a and c), while similar HLOS differences in the southern subtropics, where background errors are small, have very little impact.

Separating the Rayleigh-clear and Mie-cloudy contributions reveals that the combined O-B structures are dominated by the Rayleigh-clear signal (Fig. 6.7e and f), particularly in the upper levels. The results suggest an orbital- and vertical-dependent bias that is rather homogeneous with latitude, except maybe near the TEJ where both orbits

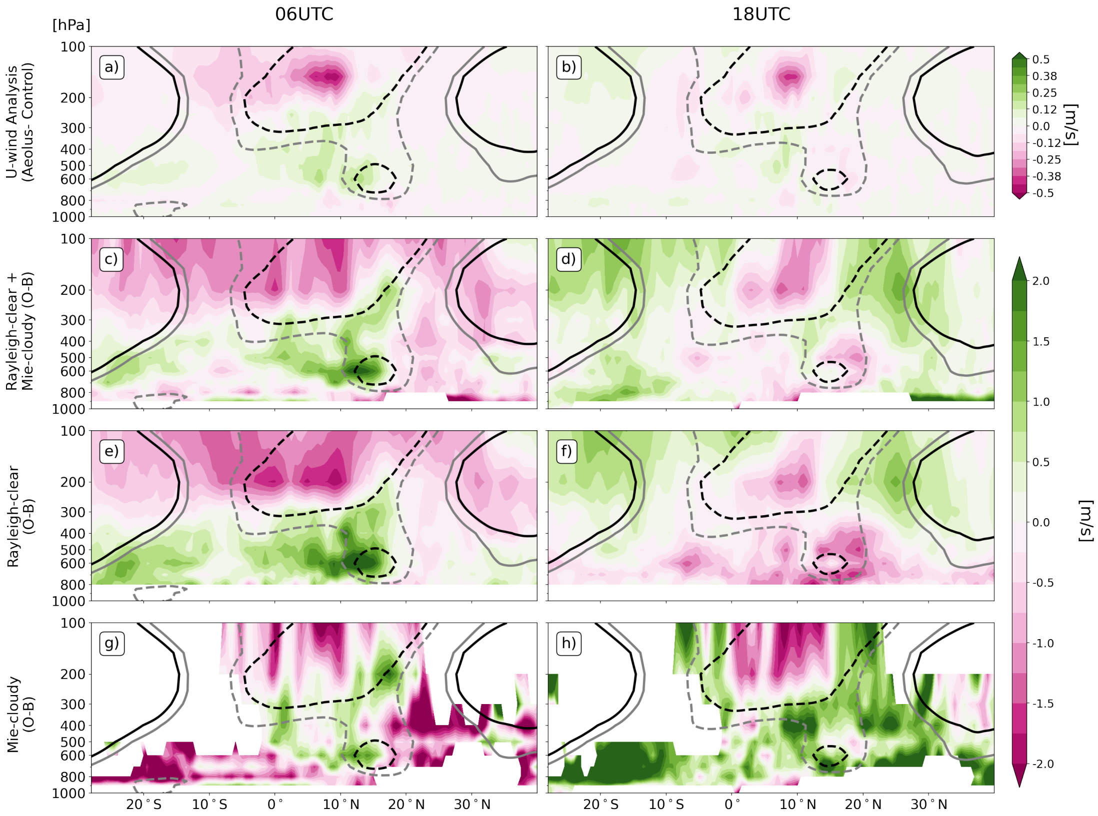

Figure 6.7: Latitude-height cross-sections showing July-September mean differences between the analysis fields of the zonal wind component Aeolus minus Control from the ECMWF2020 OSE at 06 UTC (a) and at 18 UTC (b). Subsequent panels show corresponding HLOS first guess-departures for Rayleigh-clear and Mie-cloudy combined (c,d), Rayleigh-clear (e,f) and Mie-cloudy (g,h). All fields are averaged between 30°W and 30°E. The grey and black contours correspond to zonal wind fields of 6 and 9 ms^{-1}, respectively, from the analysis with Aeolus. Solid lines indicate westerlies, dashed ones easterlies. HLOS winds from the descending track are multiplied by -1 to correspond with the sign convention of the model coordinate system. **From Borne et al. (2023) under the Creative Commons Attribution 4.0 International License (CC BY 4.0).**

show the same O-B sign. The Mie-cloudy signal (Fig. 6.7g and h), in contrast, is more consistent between ascending and descending tracks in the convectively active region, while the BB and SAL regions have opposite signs, which is also evident in the combined fields (Fig. 6.7c and d). The reason for this diurnal difference over the aerosol-loaded region is not fully understood and could be related to diurnal wind effects or instrumental factors associated with the presence of aerosols. It is worth noting that in the area of the TEJ all channels and orbits show the same-sign departure, which combined with the assumed low background error (Fig. 6.3h), leaves a strong imprint on the analysis. For the AEJ-North – and particularly its southern flank, the situation is considerably more complicated with positive differences in Rayleigh-clear at 06 UTC and Mie-cloudy at 18 UTC but negative differences in Rayleigh-clear at 18 UTC and mixed signals in Mie-cloudy at 06 UTC. For comparison, Fig. 6.8 shows the same analysis but for the DWD2020 OSE. In stark contrast to ECMWF2020 (Fig. 6.7), the

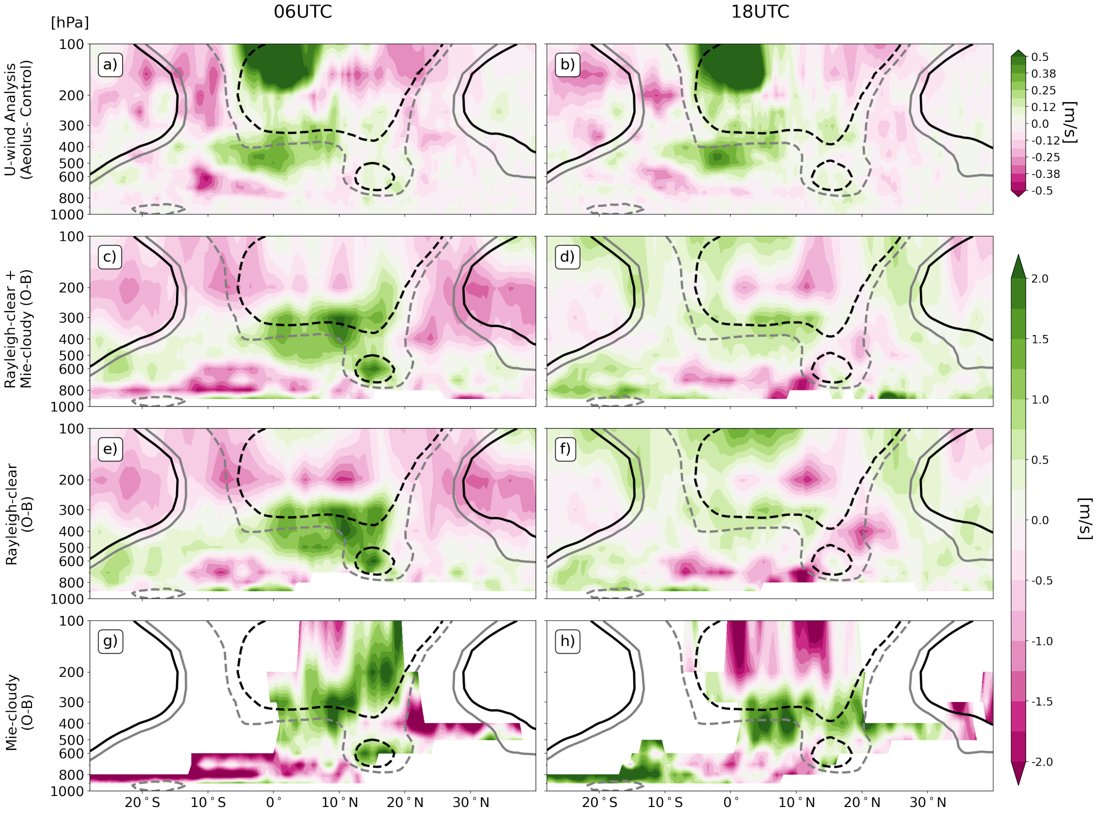

Figure 6.8: As Figure 6.7 but for the DWD2020 OSE.

mean analysis differences for morning and evening are almost identical (Fig. 6.8a and b) – and thus also closely agreeing with Fig. 6.4g. Somewhat surprisingly, however, the O-Bstatistics for Rayleigh-clear and Mie-cloudy combined (Fig. 6.8c and d) show a rather low agreement with the analysis differences. This is particularly true in the upper troposphere and lower stratosphere. The most striking example is the southern part of the TEJ region, where analysis differences are strongly positive, a signal not matched in O-B statistics, particularly not at 06 UTC. The exact reasons for this discrepancy are not fully understood, but could be related to the background error covariance in this region, which spreads the observational information in space, or through a non-linear dynamical response in the forecast model. Irrespective of this, the combined O-B data reveal marked diurnal differences that structurally resemble those seen for ECMWF (Fig. 6.7c and d), suggesting that the reason lies in the observations rather than the modelling systems. As for ECMWF, the combined HLOS signals are dominated by the Rayleigh-clear contribution (Fig. 6.8e and f) but for DWD the dominance is even clearer. Ascending and descending tracks are somewhat more consistent than for ECMWF, likely due to the vertical-dependent bias correction used in the DWD2020 OSE. The Mie-cloudy O-B statistics (Fig. 6.8g and h) structurally resemble those in the ECMWF2020 OSE, further supporting the conclusion that the O-B structures found in Fig. 6 and 7 are largely independent from the used modelling framework.

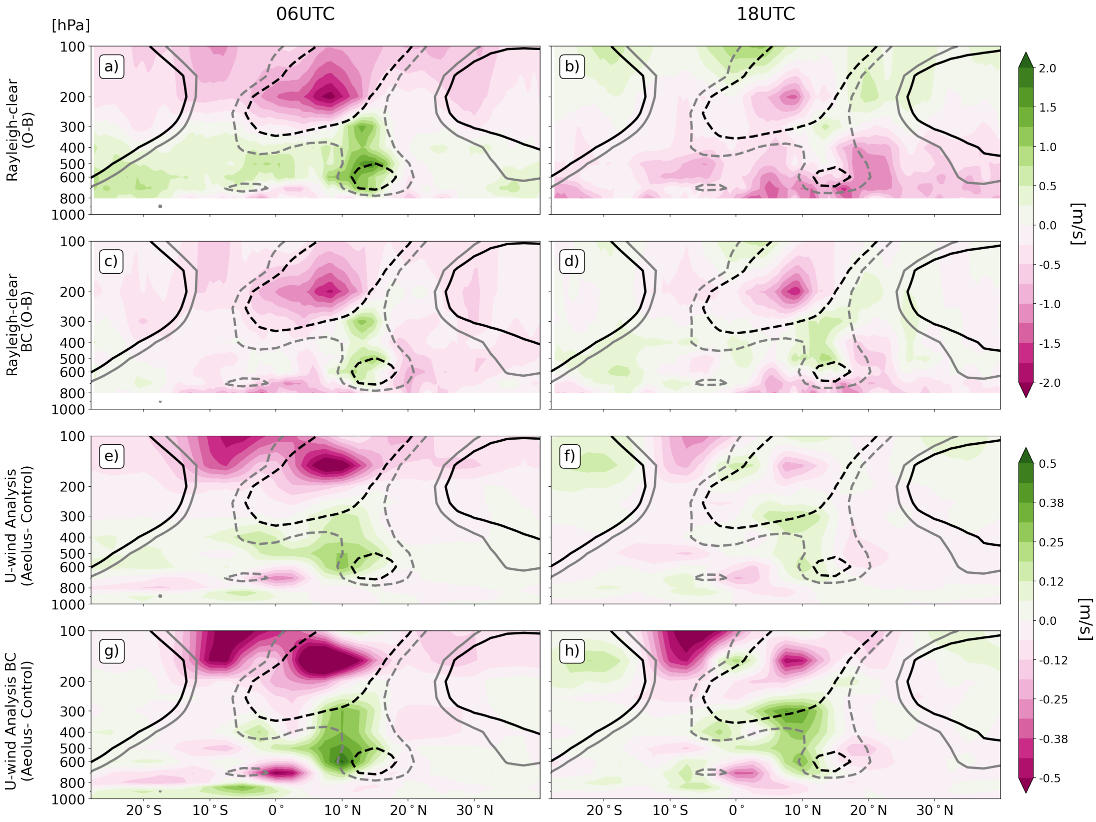

Figure 6.9: Latitude-height cross-sections showing July-September mean HLOS first guess-departures for Rayleigh-clear from the ECMWF2019 OSE with bias-correction (BC, top row) and without BC (second row) at 06 UTC (left column) and at 18 UTC (right column). These are analogous to Figs. 6e and f for the ECMWF2020 OSE. Corresponding differences between the analysis fields of the zonal wind component Aeolus minus Control are shown in the bottom two rows. These are analogous to Figs. 6a and b for the ECMWF2020 OSE. All fields are averaged between 30°W and 30°E. The grey and black contours correspond to zonal wind fields of 6 and 9 ms^{-1}, respectively, from the analysis with Aeolus. Solid lines indicate westerlies, dashed ones easterlies. HLOS winds from the descending track are multiplied by -1 to correspond with the sign convention of the model coordinate system. **From Borne et al. (2023) under the Creative Commons Attribution 4.0 International License (CC BY 4.0).**

Next we will explore to what extent a simple bias correction can cure some of the issues found in the ECMWF system for JAS 2020 (see discussion of Fig. 6.7). It was found that the atmospheric temperature is a good predictor for the Rayleigh-clear bias. Therefore, a temperature-dependent bias correction was tested in the ECMWF2019BC OSE (see Table 1). Figure 6.9 shows the O-B statistics for the Rayleigh-clear channel for the descending and ascending tracks without (ECMWF2019, Fig. 6.9a and b) and with (ECMWF2019BC, Fig. 6.9c and d) bias correction. These figures are analogous to Fig. 6.7e and f, indicating differences between the two years. Particularly for 06 UTC, the O-B structures are very similar, showing consistency despite the degradation of the instrument, while at 18 UTC positive differences are evident in the region of the southern STJ and to the south of the northern STJ in 2020, which are much weaker in 2019.

Comparing O-B statistics with and without bias correction (top vs. second row in Fig. 6.9) reveals an overall positive effect, reducing the magnitude of the differences almost everywhere. Some regions, mostly in the lower levels, even change sign, leading to a better agreement between the two tracks. The weaker TEJ signal at 18 UTC increases somewhat to better match that at 06 UTC. The temperature-dependent bias correction in the ECMWF2019BC OSE leads to diurnal differences of a similar magnitude as with the vertical-dependent bias correction applied in the DWD2020 OSE (cf. Fig. 6.9c and d with Fig. 6.8e and f).

Figure 6.9e-h show the corresponding analysis differences with and without bias correction in analogy to Fig. 6.7a and b for JAS. 2020. First comparing the two years with each other, we can see that the analysis impact is generally larger in 2019 than in 2020, particularly at 06 UTC. This is consistent with the assumed lower observational errors (shading in Fig. 6.3a, b, d and e) and the higher number of counts in 2019 (grey and black lines in the same panels). Comparing O-B statistics (Fig. 6.9a and b) with corresponding analysis differences (Fig. 6.9e and f), first both without bias correction, shows again some structural agreement but much lower amplitudes in the latter, broadly consistent with the results for 2020 (see Fig. 6.7). Applying the bias correction (Fig. 6.9g and h) clearly amplifies the impact of the Aeolus observations on the analysis for both tracks and particularly in and to the south of the TEJ and AEJ-North. This results in a much better agreement of the Aeolus effect between ascending and descending orbits, underlying the overall success of the bias correction.

Finally, in order to further investigate diurnal patterns in the different datasets analysed up to this point, we compare vertical profiles of the mean difference between 18 UTC and 06 UTC averaged horizontally over West Africa (10°S–20°N, 30°E–30°W) between the four OSEs (Table 1) and with ERA reanalysis data as a reference (Fig. 6.10). The chosen region is restricted to the low-latitude mean easterly wind features TEJ, AEJ-North and AEJ-South and excludes the two STJs but does include the low-level southwesterly Monsoon flow (see Fig. 2e for example). Nevertheless, since several wind features are averaged in this region, the diurnal patterns found may be the result of a mixture of different meteorological phenomena. The first row of Fig. 6.10 compares ERA5 reanalysis and OSE analysis fields with and without Aeolus data, all projected on the Aeolus HLOS. The most prominent feature in ERA5, with an amplitude of more than 1 ms^{-1}, occurs at 200 hPa, indicating the strengthening of upper-level easterlies at 18 UTC as also observed over northern India in the evening (Krishnamurti and Kishtawal, 2000; Mohan and Rao, 2016), which is related to the diurnal response of convective outflows to surface heating.

Between 800 and 700 hPa, an opposite but much weaker diurnal pattern is apparent, which likely reflects the decrease in wind speed in the AEJ-North (and possibly to a lesser

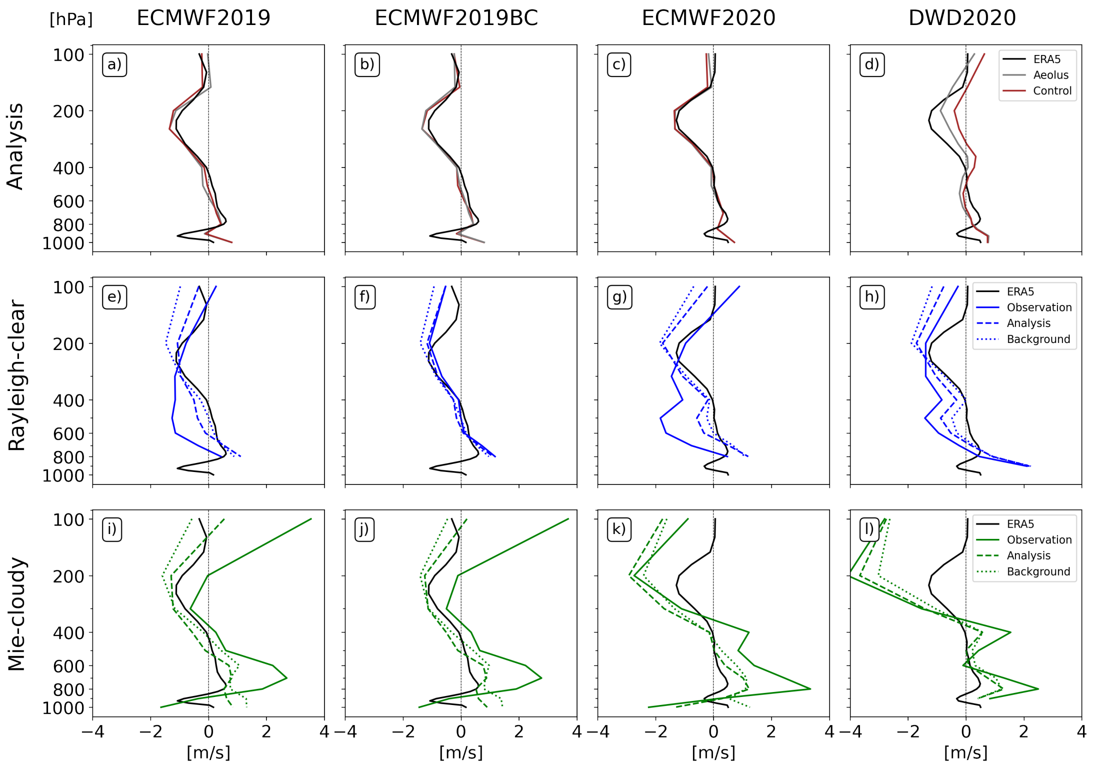

Figure 6.10: Vertical profiles of diurnal differences 18 UTC minus 06 UTC of HLOS winds for the four OSEs (Table 1; see column labels) averaged over West Africa (30°W–30°E, 10°S–20°N) during July-September. (a–d) Analysis fields, (e–h) Aeolus Rayleigh-clear and (i–l) Mie-cloudy observations with their analysis- and background-equivalents. Corresponding fields from the ERA5 reanalysis are plotted in all panels for reference. **From Borne et al. (2023) under the Creative Commons Attribution 4.0 International License (CC BY 4.0).**

extent EJ-South) during the afternoon, when the planetary boundary layer grows into the lower parts of the jet and slows it down through turbulent mixing (Agustí-Panareda et al., 2010). Finally, the low-amplitude negative signal around 900 hPa likely reflects the increase of monsoonal westerlies in the course of the night peaking shortly before sunrise at 06 UTC (Parker et al., 2005a,b; Kalapureddy et al., 2010; Kalthoff et al., 2018). The diurnal pattern at 1000 hPa should be regarded with some caution, as it will be under ground for larger parts of the averaging domain. In general, the ECMWF analysis fields with (grey solid lines in Fig. 6.10a–c) and without (red solid lines in Fig. 6.10a–c) Aeolus data reproduce the ERA5 pattern, except for the ECMWF2020 OSE in the lower troposphere (Fig. 6.10c), where the reanalysis and analysis show some discrepancy. An effect of Aeolus on the representation of the diurnal cycle in the analysis fields, however, is at best marginal. For the DWD2020 OSE (Fig. 6.10d) differences between the control analysis and ERA5 are substantially larger, with the former showing a less pronounced diurnal cycle throughout the troposphere. Assimilating Aeolus data has a relatively large influence and leads to a better agreement with ERA5, particularly in the TEJ region. This improvement is much more evident from Fig. 6.10 than from the vertical profiles shown in Fig. 6.8a and b.

The second row of Fig. 6.10 compares Rayleigh-clear HLOS observations with their background and analysis counterparts in HLOS space. The diurnal patterns in the background fields in all OSEs (Fig. 9e–h, blue dashed line) are similar to the ERA5 reanalysis below 200hPa, while above they display stronger easterly winds at 18UTC compared to 06UTC, suggesting that the Rayleigh-clear HLOS space may be representative of the regional diurnal cycle in the mid-troposphere. This is particularly true for the 2019 OSEs, while some inconsistencies around 600hPa are apparent for the 2020 OSEs. However, the corresponding HLOS observations without temperature bias correction (blue solid lines in Fig. 6.10e, g and h) does not follow the same diurnal cycle with a generally stronger easterly component in the mid-troposphere at 18 UTC compared to 06 UTC, reversing the sign of the expected diurnal cycle of the AEJ-North, while still having a realistic representation of the diurnal cycle of the TEJ. The analyses in HLOS space (blue dashed lines) are therefore shifted from the background equivalent towards the HLOS Rayleigh-clear data. When applying the temperature bias correction as seen in the ECMWF2019BC OSE (Fig. 6.10f), the Rayleigh-clear observation follows an almost identical diurnal cycle compared to the ERA5 reanalysis and background equivalent, especially below 200 hPa. Correcting for the temperature bias thus has a positive effect on the Rayleigh-clear winds and makes them more realistic in the mid-troposphere below 200 hPa.

Finally the bottom row of Fig. 6.10 shows a corresponding analysis for the Mie-cloudy channel. The background HLOS model equivalents in the all OSEs (Fig. 6.10i–l, red dotted lines) do not follow the ERA5 reanalysis closely, with a more pronounced diurnal cycle near the AEJ-North as well as a stronger TEJ diurnal cycle in 2020 compared to 2019. The magnitude of this discrepancy is generally larger than for Rayleigh-clear data (Fig. 6.10e–g) and related to the fact that the two channels do not measure the same wind properties with the same sampling density as discussed in the context of Fig. 6.3. The diurnal cycle of Mie-cloudy HLOS winds (red dotted lines) in the mid-troposphere is opposite to that for the Rayleigh-clear HLOS winds. At upper levels Mie-cloudy HLOS winds show large positive diurnal differences in 2019 and large positives ones in 2020, with little agreement with the Rayleigh-clear data. As expected, the bias correction applied in ECMWF2019BC has hardly any effect on the Mie-cloudy HLOS winds. The analysis counterparts (red dashed lines) are generally not driven in the direction of the Mie-cloudy observations – sometimes even in the opposite direction – indicating the dominant effect of the Rayleigh-clear data, also found in the analysis of Fig. 6.7. Despite the model differences between ECMWF and DWD, Rayleigh-clear (Fig. 9g-h) and Mie-cloudy (Fig. 9k and l) behave similarly, as do their model and analysis equivalents.

Exploring background departures of the Aeolus HLOS in the DWD and ECMWF assimilation systems enabled to assess the orbital and channel contribution to the influence on analysis between ascending and descending orbits. We showed the existence of a height- and orbital- dependant bias in the Rayleigh-clear channel that has the effect of accelerating and slowing down the AEJ-North and TEJ diurnally. This bias is a likely explanation for the earlier statement in section 6.2.1 that the Rayleigh-clear measurements pull the DWD2020 and ECWF2020 analyses apart. This is observed particularly outside the ITCZ region, where the Rayleigh-clear measurements predominate. It should also be noted that even small biases (of the order of 1 ms^{-1}) can lead to a deterioration of the forecast quality (Horányi et al., 2015). Correcting this bias, using a temperature-dependent bias corrections allows for better consistency of Rayleigh-clear winds between ascending and descending orbits. Finally, we showed that the assimilation of Aeolus brings the DWD analysis closer to both the ECMWF2020 analysis and the ERA5 reanalysis.

6.3 Influence on forecast fields

6.3.1 Background verification against radiosondes

As a first step to understand the impact of Aeolus data on forecast fields, this subsection evaluates the background fields from the three ECMWF OSEs with actively assimilated radiosondes measurements using O-B statistics (Fig. 6.11). Corresponding DWD statistics are not shown here as not enough radiosonde data were assimilated in the OSE to obtain meaningful statistics. In total 11 and 5 radiosonde stations in tropical Africa were used during July-September 2019 and 2020, respectively (Fig. 6.11i) with only two common stations (Accra in Ghana and Cabinda in Angola). Figure 6.11d and h show the number of reports assimilated in the different OSEs, which varies broadly between 500 and 1000 per level with generally more data in 2019 ($\sim$ 850) than in 2020 ($\sim$ 600). The number of reports are more variable within the lower troposphere. Figure 6.11a–c shows the mean O-B difference as well as the standard deviation from the ECMWF2020 OSE for absolute errors in zonal and meridional wind as well as the relative improvement for the total wind speed. The ECMWF first guess has a negative zonal wind bias in the upper troposphere peaking just above 200 hPa with about -1 ms^{-1} (Fig. 6.11a), which indicates a too weak TEJ, as we have shown previously. Aeolus reduces this bias to a small extent, in agreement with the analysis impact seen in Fig. 6.4e. There is also a smaller positive bias at midlevels, mostly above 700 hPa, which gets hardly improved when assimilating Aeolus data. The error standard deviation (solid lines in Fig. 6.11a) oscillates around 1.5 ms^{-1}. Assimilating Aeolus wind fields leads to some moderate reductions at upper levels. For meridional wind (Fig. 6.11b), the bias is small throughout the profile and changes little when Aeolus is assimilated. The random error has a similar magnitude as that for zonal wind and shows little sensitivity to the (mostly zonal) Aeolus measurements. Despite this, the assimilation of Aeolus leads to a mass-weighted vertical average random error reduction for the total wind component of 1.95%, which is vertically consistent (Fig. 6.11c).

Figure 6.11e–g shows the corresponding analysis for 2019 including both OSEs with and without bias correction. The overall patterns agree reasonably well with 2020 despite

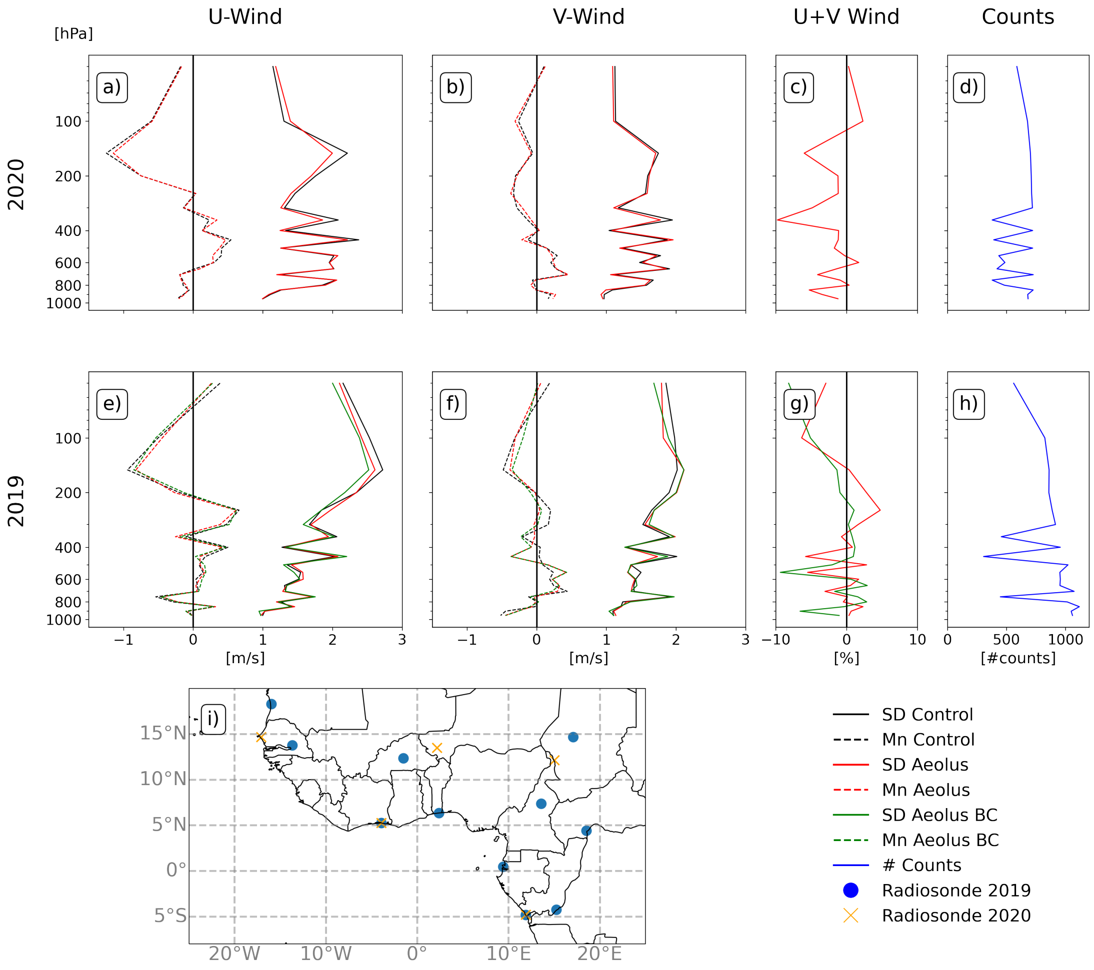

Figure 6.11: Vertical profiles showing July–September mean (Mn) and standard deviation (SD) of radiosonde background departures from the Aeolus and control experiments of the ECMWF2020 OSE for zonal (a) and meridional (b) winds, relative SD error reduction for the total wind component (c) and number of reports (d) used to generate the statistics. All fields are averaged over West Africa (20°W–20°E, 10°S–20°N. The second row shows corresponding fields for 2019 contrasting the OSEs with and without bias correction (BC). (j) Horizontal map showing the locations of the used radiosondes in 2019 (blue dots) and 2020 (orange crosses). **From Borne et al. (2023) under the Creative Commons Attribution 4.0 International License (CC BY 4.0).**

the large differences in radiosonde data coverage. The most interesting aspect is the effect of the bias correction in ECMWF2019BC. Overall improvements from that are moderate but some positive effects on the random error in zonal wind and the mean error in meridional wind at upper levels are evident. The vertically averaged relative improvement shown in Fig. 6.11g is overall smaller than in 2020 with only 0.45% in the ECMWF2019 OSE and 1.45% in ECMWF2019BC, demonstrating the additional benefit of correcting the Rayleigh-clear wind temperature-dependent bias. This is particular due to a reduction of the background deterioration with Aeolus around 200 hPa evident in ECMWF2019. Overall, a similar magnitude in the reduction of the background error, peaking in the upper troposphere, was observed in the DACCIWA radiosonde campaign in West Africa in June/July 2016 (van der Linden et al., 2020), suggesting that the assimilation of Aeolus has a comparable effect to a high-resolution radiosonde coverage over this region in the ECMWF model.

6.3.2 1-4 days forecast verification against ERA5 reanalysis

Finally, we will look at the improvements in longer-term forecasts verified with ERA5 over the entire tropical Africa domain. Figure 6.12 and Figure 6.13 show the relative reduction of the root mean square error (Root Mean Square Error (RMSE)) of the four OSEs (Table 4.1) as latitude-height cross-sections for forecast times of 1–4 days and as single levels at 200 hPa and 700 hPa at +48h forecast time, respectively. As before, isotachs at 6 ms^{-1} (grey) and 9 ms^{-1} (black) are included to identify the main jet features. In addition, Table 6.1 provides an overview of the relative improvement of the zonal wind RMSE at 200 hPa and 700 hPa for the whole tropical Africa domain and specifically for the AEJ-North and TEJ regions.

For all OSEs, we see a predominantly positive influence of Aeolus data for all forecast lead times. The reduction in RMSE is generally larger for forecasts lead times greater than 24 hours. In the 2019 ECMWF and DWD2020 OSEs (Fig. 6.12a,b and d), the largest decrease in RMSE at +24h are found in the lower stratosphere, before gradually vanishing at higher lead times, while in the ECMWF2020 OSE (Fig. 6.12c) the initial errors are more spurious, and seem to be preserved at longer lead times. One reason could be the generally poorer quality of the Aeolus Rayleigh-clear measurements (Fig. 6.3b) in 2020, when compared to 2019, caused by the aforementioned decreasing atmospheric path signal. In the ECMWF2019 OSEs with and without bias correction (Fig. 6.12a and b, Fig. 6.13e and f), the errors at +24h are found in the southern hemisphere at $\sim$ 700hPa between 20°S and 0°, which coincides with a change in wind direction between the monsoon layer and the midlevel easterlies. With a bin size of 1 km at this height, Aeolus data can not resolve large vertical gradients and thus may misrepresent the local dynamics. This region also corresponds to a strong increase in the analysis 700 hPa zonal wind of $\sim 0.5ms^1$ when Aeolus is assimilated (Fig. 6.5a and e at 0°). Nevertheless, this large RMSE is surprisingly not apparent at 700hPa in the ECMWF2020 and DWD2020 OSE (Fig. 6.13g and h).

Other errors over the SAL region at 20°N are also visible in all OSEs at +24h, in particular over the lower northern part of the AEJ-North around 800 hPa in the ECMWF OSEs (Fig. 6.12 a,b,c) and the whole northern AEJ-North region in the DWD2020 OSEs (Fig. 6.12 d). This includes the Intertropical Discontinuity (ITD), which is a confluence zone between the northeasterly dry and hot Harmattan winds and the southwesterly moist and cool monsoon flow. This pronounced meridional wind feature is challenging to resolve with an Aeolus Rayleigh-clear integration length of 87 km.

Furthermore, the AEJ-North is embedded in a dust-loaded region (Fig. 6.1d), which is subject to larger Mie-cloudy (Fig. 6.3d) and Rayleigh-clear assigned observation errors

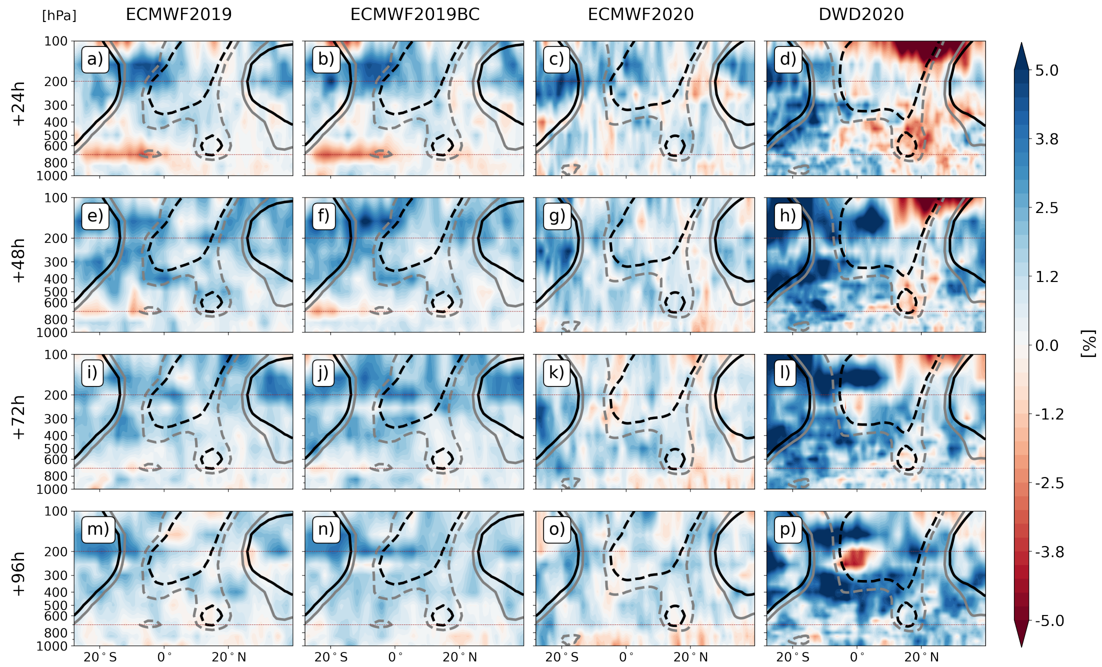

Figure 6.12: Latitude-height cross-sections showing the relative reduction of the RMSE of zonal wind (i.e. (RMSE(CONTROL)-RMSE(AEOLUS))/RMSE(CONTROL)×100) for the four OSEs (Table 4.1) for +24h to +96h lead-time forecasts against ERA5 reanalysis. Cold (warm) colours indicate improvement (degradation) when Aeolus is assimilated. All fields are averaged between 30°W and 30°E during July-September. The grey and black contours correspond to zonal wind fields of 6 and 9 ms^{-1}, respectively, from the analysis with Aeolus. Solid lines indicate westerlies, dashed ones easterlies. The brown lines mark the 200hPa and 700hPa levels. **From Borne et al. (2023) under the Creative Commons Attribution 4.0 International License (CC BY 4.0).**

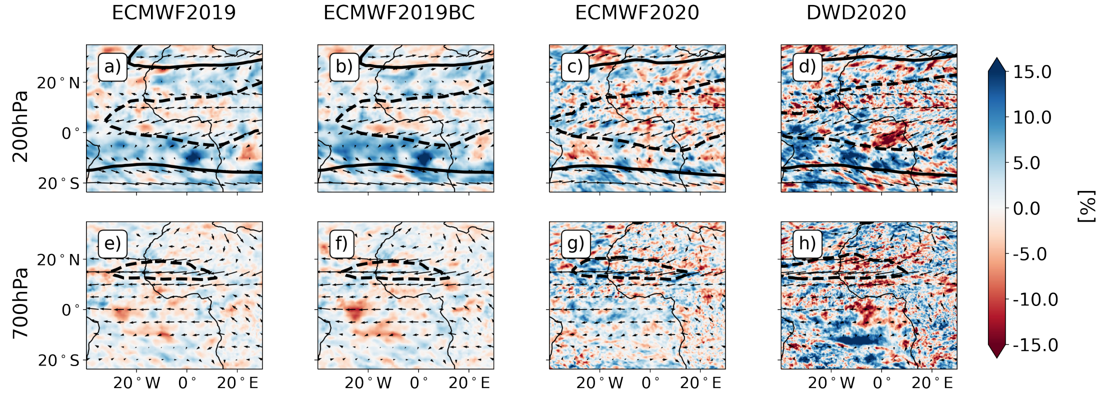

Figure 6.13: Horizontal maps at 200 hPa and 700 hPa showing relative reduction of the RMSE of zonal wind (i.e. (RMSE(CONTROL)-RMSE(AEOLUS))/RMSE(CONTROL)×100) for the four OSEs (Table 4.1) for +48 lead-time forecasts against ERA5 reanalysis. Cold (warm) colours indicate improvement (degradation) when Aeolus is assimilated. The fields are averaged over July-September. The grey and black contours correspond to zonal wind fields of 6 and 9 ms^{-1}, respectively, from the analysis with Aeolus. Solid lines indicate westerlies, dashed ones easterlies. **From Borne et al. (2023) under the Creative Commons Attribution 4.0 International License (CC BY 4.0).**

Table 6.1: Overview of the relative reduction of the zonal wind RMSE for the four OSEs (Table 1) in the AEJ-North and TEJ regions for +24h to 96h lead time forecasts verified against ERA5 reanalysis. The fields are averaged within [30°W–30°E; 10°S–20°N] for the TEJ at 200 hPa, [30°W–30°E; 8°N-.-22°N] for the AEJ-North at 700 hPa and [30°W–30°E; 30°S–30°N] for comparison at both levels. Blue (red) numbers indicate improvement (degradation) when Aeolus is assimilated. The values are expressed in percent. **From Borne et al. (2023) under the Creative Commons Attribution 4.0 International License (CC BY 4.0).**

	Lead time	ECMWF2019	ECMWF2019BC	ECMWF2020	DWD2020
200hPa (TEJ) [30°W-30°E;10°S-20°N]	+24h	+1.98	+2.45	+1.77	+0.74
	+48h	+1.67	+1.89	+1.07	+1.6
	+72h	+1.77	+2.35	-0.06	+0.89
	+96h	+1.81	+2.30	-0.10	+0.20
700hPa (AEJ-North) [30°W-30°E;8°N-22°N]	+24h	+0.1	+0.01	+0.80	-0.34
	+48h	+0.75	+0.24	+1.30	-0.74
	+72h	+0.37	+0.28	+1.03	-0.78
	+96h	+0.25	+0.42	+0.22	-0.83
200hPa [30°W-30°E;30°S-30°N]	+24h	+2.04	+2.39	+1.66	1.51
	+48h	+2.06	+2.42	+1.44	+2.52
	+72h	+1.97	+2.53	+0.96	+1.34
	+96h	+1.55	+2.35	+1.09	1.55
700hPa [30°W-30°E;30°S-30°N]	+24h	-1.4	-1.69	+0.34	-0.06
	+48h	-0.08	-0.44	+0.93	+0.83
	+72h	+0.09	+0.10	+0.86	1.31
	+96h	+0.20	+0.52	+0.80	+1.3

(Fig. 6.3a) due to reduced signal-to-noise ratio. These errors could also be insufficient to fully compensate for the large model errors related to the stochasticity of convection and the coupling between atmospheric dynamics and Mesoscale Convective Systems (MCSs). However, the general positive influence of Aeolus over the AEJ-North region for longer lead-times in the ECMWF OSEs (see Table 6.1) is promising for further studies exploring the impact of Aeolus on the propagation of African Easterly Waves (AEWs) and related precipitation.

As shown in Table 6.1, the upper troposphere shows a positive impact for all OSEs with an improvement of more than 2% for most lead times, especially in the southern and northern part of the TEJ (Fig. 6.12, Fig. 6.13), despite being more neutral for the ECMWF2020 OSE. The ECMWF2019BC OSE also shows a systematic improvement in the upper troposphere as well as in the TEJ region, indicating the added value of using a temperature-dependent bias correction for Rayleigh-clear winds. Those regions correspond to cloud-free outer branches of the Hadley cell, while the RMSE is more patchy within the TEJ convective outflow region. The general better forecast quality in the upper troposphere can possibly be related to the denser sampling together with the smaller measurement uncertainties.

Our findings are consistent with Rennie et al. (2021), who have highlighted the benefits of assimilating Aeolus wind observations in the tropics and the southern hemisphere with peak improvements in the tropical upper troposphere. In addition to wind, they also find improvement in other variables such as temperature or humidity. Žagar et al. (2021) also reported that the improvement observed in the upper troposphere can partly be attributed to the improvement of the representation of vertically propagating Kelvin waves in layers with a strong zonal wind shear forecast. Lastly, the improvements in the predictions are significant and consistent across the African region, despite the complex meteorology of the WAM and the assumed random errors and biases of the Aeolus measurements. Beyond this, it should be noted that the forecast improvement observed in Africa may depend on upstream areas where the influence of Aeolus on the analysis is more direct and propagates over time.

6.4 Concluding remarks

This study addresses the impact of Aeolus wind observations on the West African Monsoon (WAM) circulation in the Integrated Forecasting System (Integrated Forecasting System (IFS)) of the European Centre for Medium-Range Weather Forecasts (ECMWF) and in the global non-hydrostatic ICOsahedral Model (Icosahedral Nonhydrostatico (ICON)) of the German Weather Service (DWD). In particular, we investigated the crucial role of Aeolus in terms of its ability to complement the sparse conventional observing network and improve the low predictability in this region. The complementary wind observations in clear and cloudy atmospheric conditions are of great importance in a region with a broad range of cloud features and aerosol types. Accordingly, we assessed and compared the representation of the WAM wind subsystems in the analysis and forecast fields of four observing system experiments (OSEs) across both analysis and forecast fields during the 2019 and 2020 boreal summers. The main conclusions from these investigations are:

1. Aeolus Rayleigh-clear and Mie-cloudy channels complement each other well in a complex region like the WAM, which is characterised by many different cloud types and aerosols. Rayleigh-clear primarily samples in cloud-free regions surrounding the Intertropical Convergence Zone (ITCZ) and broken cloud scenes within it, while Mie-cloudy measures in the heart of the convective region across a range of different cloud types such as cumulonimbus, congestus or altocumulus clouds, as well as aerosols from biomass burning and within the Saharan Air Layer. These different atmospheric components are embedded in the main circulation features of the WAM and allow for a good representation of the mid-level AEJ-North and upper troposphere TEJ in both channels.
2. The assignment of observation errors for the HLOS wind measurements at ECMWF and DWD are determined using Observation minus background (O-B) statistics and Desroziers diagnostics but follow different formulations. While ECMWF

assumes values mainly based on the L2B processor instrument error combined with representativeness error estimates, the DWD assigned observation errors are based on a look-up table for different altitude levels. In the ECMWF OSEs, the assigned Rayleigh-clear observation error is largest within the convective active region and can be attributed to a larger signal-to-noise ratio in broken cloud scenes. In the ECMWF2020 OSE, the assigned observation error in the Rayleigh-clear channel is larger compared to 2019, and can be explained by the decreasing atmospheric path signal. For Mie-cloudy, the largest errors are visible in aerosol dominated regions (BB and SAL) compared to cloudy regions. The overall assigned error for DWD is smaller than for ECMWF, with a general height-dependent error yielding similar values for Mie-cloudy and Rayleigh-clear winds.

3. Throughout the different OSEs, Aeolus changes the representation of the main zonal wind features of the WAM. First, a weakening of the southern edge of the AEJ-North is apparent in all ECMWF OSE analyses. This weakening is accompanied by a strengthening of the AEJ-North towards the eastern part of the Sahel in the ECMWF 2019 OSEs. In the DWD OSE, the influence over the AEJ-North is less pronounced. Secondly, the assimilation of Aeolus data strengthens the TEJ core by about 0.4 ms^{-1} in the ECMWF analyses and, conversely, weakens the southern edge of the TEJ by more than 0.5 ms^{-1} in the DWD OSE analysis. This may imply the strengthening/weakening of the updraft in the convective region, leading to more/less divergence in the upper levels, which in turn would affect precipitation in the ECMWF or DWD models, respectively. This will be explored in future studies. Finally, the assimilation of Aeolus brings the ECMWF and DWD 2020 analyses closer together, in particular in the upper ITCZ and southern TEJ region, which is dominated by Mie-cloudy measurements and where the systematic differences between DWD and ECMWF zonal winds reach 4 m/s. In cloud-free regions, however, the analyses deviate slightly from each other, which may possibly be caused by the additional vertical-dependant bias correction present in the DWD OSE.

4. Background departures were analysed to assess the behaviour of the HLOS observations with respect to the model equivalents and to disentangle the orbital and channel contribution to the observed analysis differences. Primarily, the combined Rayleigh-clear and Mie-cloudy departures show a similar structure to the zonal wind analysis difference. This indicates the presence of a height- and orbital-dependent bias in the Rayleigh-clear channel, which causes the winds to speed up in the morning and slow down in the evening. However, correcting this bias using a temperature-dependent approach shows that the magnitude of this bias is too small to have a significant influence on the analysis and prediction fields. Although this influence is small, the temperature bias correction provides a better representation of the Rayleigh-clear diurnal winds. Despite the model differences

between ECMWF and DWD, both Rayleigh-clear and Mie-cloudy behave similarly with respect to their model equivalents.

5. The ECMWF and DWD zonal wind forecasts verified with ERA5 revealed that Aeolus has a positive influence on the WAM zonal winds. The positive impact is most notable in the upper troposphere because of denser observation sampling together with smaller measurement uncertainties. Cloud-free regions exhibit lower RMSE deterioration relative to cloudy regions, owing to the lower signal to noise ratio in broken-cloud scenes for Rayleigh-clear winds. Short forecast ranges of +24h show larger deterioration, possibly due to verification problems in data-sparse regions. Despite the presence of cumulonimbus clouds, the representation of the TEJ is positively impacted by Aeolus in most OSEs and lead-times. Although the AEJ-North also shows improvement, it is more modest compared to the TEJ and only apparent in the ECMWF OSEs.

6. The radiosonde verification in the ECMWF OSEs over West Africa showed that the vertically averaged total wind random errors in the 2019 and 2020 OSEs are reduced by 0.45% and 1.95%, respectively, with the effects peaking in the upper troposphere. The reduction of the latter would be comparable to a 1-2 year average reduction in the RMSE vector wind error (at 250 and 850 hPa) of the ECMWF +44h forecast verified against radiosondes in the tropics (Haiden et al. (2021), Fig. 17). The improvement is raised to 1.45% in the 2019 OSE, when a temperature-dependent bias correction in the Rayleigh-clear channel is applied, highlighting the usefulness of the correction.

7. Impact of Aeolus wind observations on the representation of equatorial waves

Equatorial Waves (EWs) are an important source of variability and predictability in the tropics. In this chapter we explore the benefits of Aeolus in improving the representation of EWs by examining the impact of Aeolus on both dynamical and precipitation fields in the two European Centre for Medium-Range Weather Forecasts (ECMWF) and Deutscher Wetterdienst (DWD) systems. We then investigate the dynamical mechanisms that contribute to these improvements by analysing a high-impact event in the DWD system observed over the Pacific associated with the El Niño-Southern Oscillation (ENSO) phase change from neutral to La Niña.

7.1 Influence of Aeolus on equatorial wave predictions

In this section, the impact of Aeolus on the representation of EWs in both ECMWF and DWD analyses and forecast fields is investigated. EWs are identified using the Wheeler and Kiladis (1999) (WK) and Yang et al. (2003) (YANG) methods (see section 4.5) for zonal wind fields in the upper and lower troposphere over the tropical belt (24°S-24°N) during July-September 2021. EWs were also identified from precipitation fields, which is only possible when using the WK method.

7.1.1 Impact in the ECMWF forecasting system

Figure 7.1 shows the relative error reduction in the zonal wind fields and related EW signals in both the ECMWF2020 OSE analysis and forecast fields relative to the ERA5 reanalysis. Interestingly, the raw and EWs analyses including Aeolus (EXP) are further apart from the ERA5 reanalysis when compared to the control (CTRL). This phenomenon may be the result of the lack of observational data in the tropics for direct comparison, which can can lead to a verification problem. Indeed, the absence of Aeolus in ERA5 brings CTRL closer to ERA5, as both assimilate a similar set of observations. In general, the greatest improvement occurs in the upper troposphere (200 hPa), with raw forecast fields showing an error reduction of up to 1% for a lead time of +72h. This improvement in prediction is related to forecast improvements in most

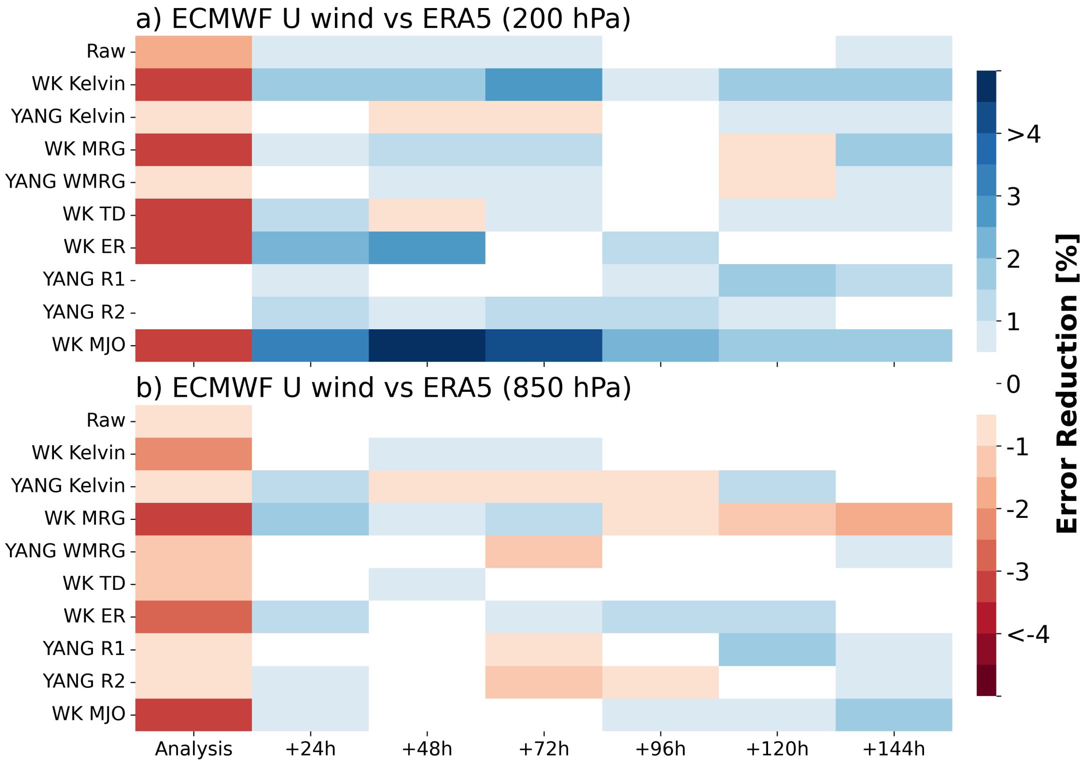

Figure 7.1: Relative reduction in Root Mean Square Error (RMSE) of zonal wind analysis and forecasts filtered for different EW types for the ECMWF2020 Observing System Experiment (OSE) compared to the ERA5 reanalysis at 200 hPa (a) and 850 hPa (b). The fields are averaged between 23°N and 23°S during the period July-September 2020. The EWs are identified using both Wheeler and Kiladis (1999) (WK) and Yang et al. (2003) (YANG) methods.

.

wave types using both WK and YANG methods. In particular, WK Kelvin and the slower wave types WK Equatorial Rossby waves (ER), YANG Equatorial Rossby wave with meridional mode number 1 (R1), and WK Madden-Julian Oscillation (MJO) show error reductions on longer lead times (up to +144h), while WK Mixed Rossby gravity waves (MRG) and WK TD result in error reductions on shorter time scales (up to +72h). Interestingly, Kelvin waves isolated with the YANG method show almost opposite skill changes to those identified with the WK method. The reason for these discrepancies is unknown, but may be due to the fundamentally different methods used to identify the waves. In particular, during the boreal summer, Kelvin wave propagation can be shifted off-equatorially, which can be a limitation for the YANG method. Indeed, the latter uses a spatial constraint when projecting the dynamical fields onto theoretical wave patterns, which restricts its ability to capture off-equatorial Kelvin wave propagation. Overall, the error reduction for meridional winds and related EWs is more modest than for zonal winds (not shown here). In the lower troposphere (850 hPa), the improvements are more mixed. The error reductions up to +72h in the wind fields are mostly related to WK ER and WK MRG. Again, discrepancies in the skill of similar wave types obtained by

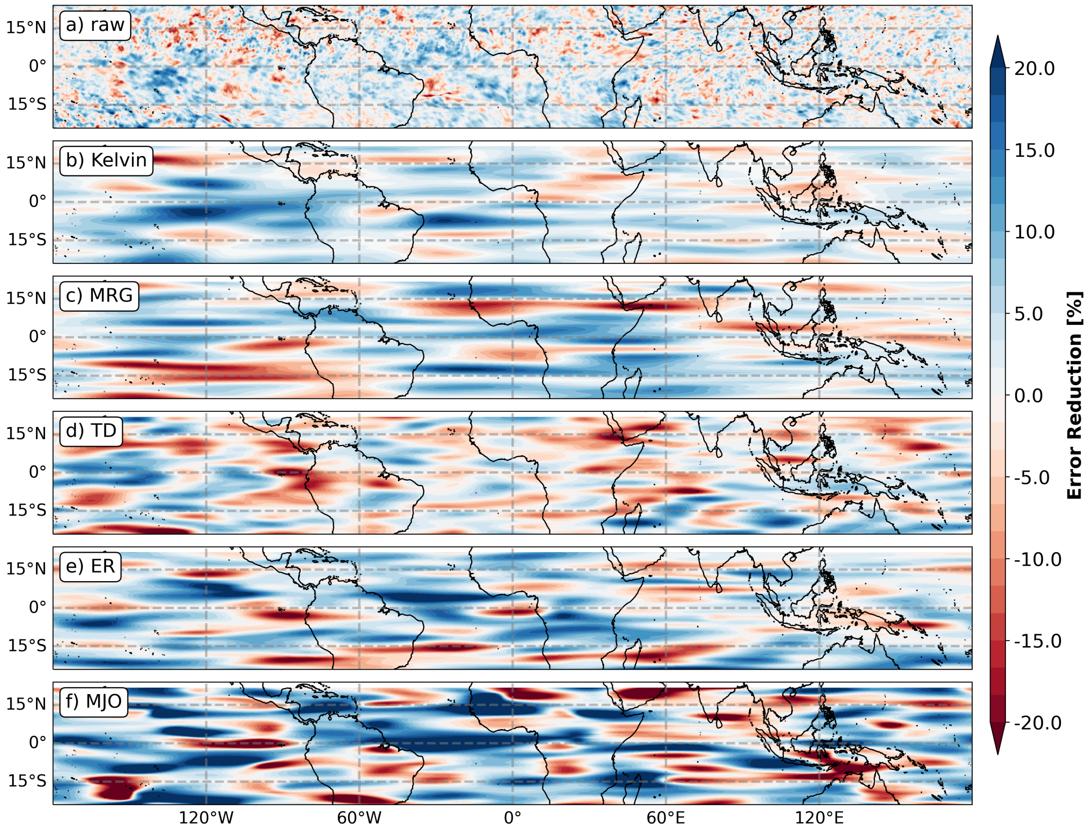

Figure 7.2: Relative reduction in RMSE of zonal wind (a) and associated EWs (b-f) at +48h forecast time for the ECMWF2020 OSE compared to the ERA5 reanalysis at 200 hPa. The EWs are identified using the WK methodology.

different methods may be related to the level of confidence in the results or to variations related to the methodology used.

To identify how the skill varies across different regions in the tropics, Fig. 7.2 shows the error reductions of the +48h zonal wind forecast for EWs as identified by the WK method. The skill change of the raw field is mixed across the tropics with small scale noise, especially over the Maritime Continent and Indian Ocean region. However, the Atlantic region, the South American continent and some parts of the Pacific Ocean show noticeable increases in the forecast skill of up to 15%. This enhancement is associated with error reductions in Kelvin waves, ER, MJO and MRG wave types. Although the MRG and ER are EWs, it should be noted that extratropical Rossby waves originating from mid-latitudes can interact and interfere with them, especially in the outer areas of the tropics. Slight degradation is noticeable for Tropical Disturbances (TDs), but this wave type usually does not play an important role in the dynamics of the upper troposphere.

Finally, we investigate the relationship between forecast improvements of EWs isolated using zonal wind fields with EWs identified from precipitation forecasts (see Fig. 7.3). First, somehwat disappointingly, we find that Aeolus improves the RMSE of precipitation forecasts by up to 0.1% on average for a forecast time of +24h, with no improvement

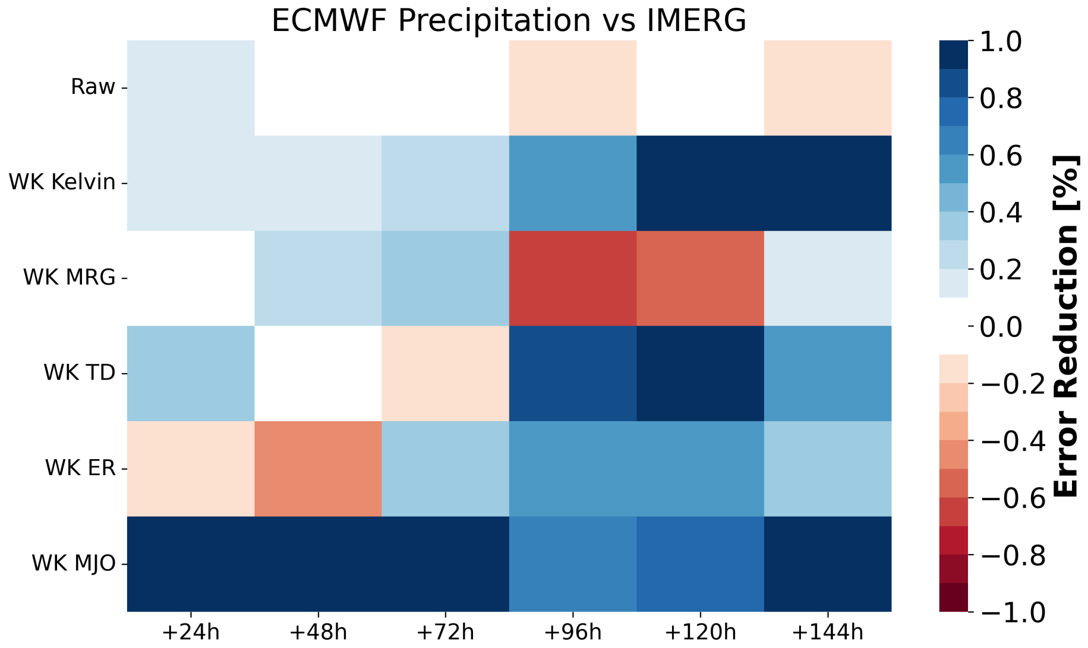

Figure 7.3: Relative reduction in RMSE of precipitation forecasts and associated EWs for various lead times of the ECMWF2020 OSE verified against Global Precipitation Mission (GPM) Integrated Multi-Satellite Retrievals for Global Precipitation Measurement (IMERG) precipitation product. The fields are evaluated over the tropical domain between 23°N and 23°S. The various EWs are determined using the WK method.

for longer forecast times. The RMSE, although often used as a verification metric, is not optimal for rainfall verification. Due to the skewed distribution of precipitation, small errors on non-event days can have a disproportionate effect on the overall error compared to larger precipitation events. Another problem is that when forecasting a shift of a feature with strong gradients, the forecast s penalised twice, for missing the feature in the correct location and for the false alarm in the wrong spot. Nevertheless, in this setup, the verification is performed on a 1° grid resolution, hence an improvement of the RMSE can still be considered a positive outcome in terms of averages reduction of the error magnitude. The RMSE of EWs derived from precipitation is less prone to such issues, since the rainfall fields are smoothed in time and space. Most notably, the largest and longest (up to +144h) error reduction are visible for the Kelvin wave type and the MJO, reaching up to 1% improvement. This observed improvement is coherent with the improvements observed for EWs identified from zonal wind forecasts, suggesting a good representations of the coupling between dynamics and convection for those wave types. Other improvements are visible for the MRG wave type, while TD and ER show some degradation on short-range predictions. This degradation may be the reason for the relatively short +24h lead time rainfall forecast performance.

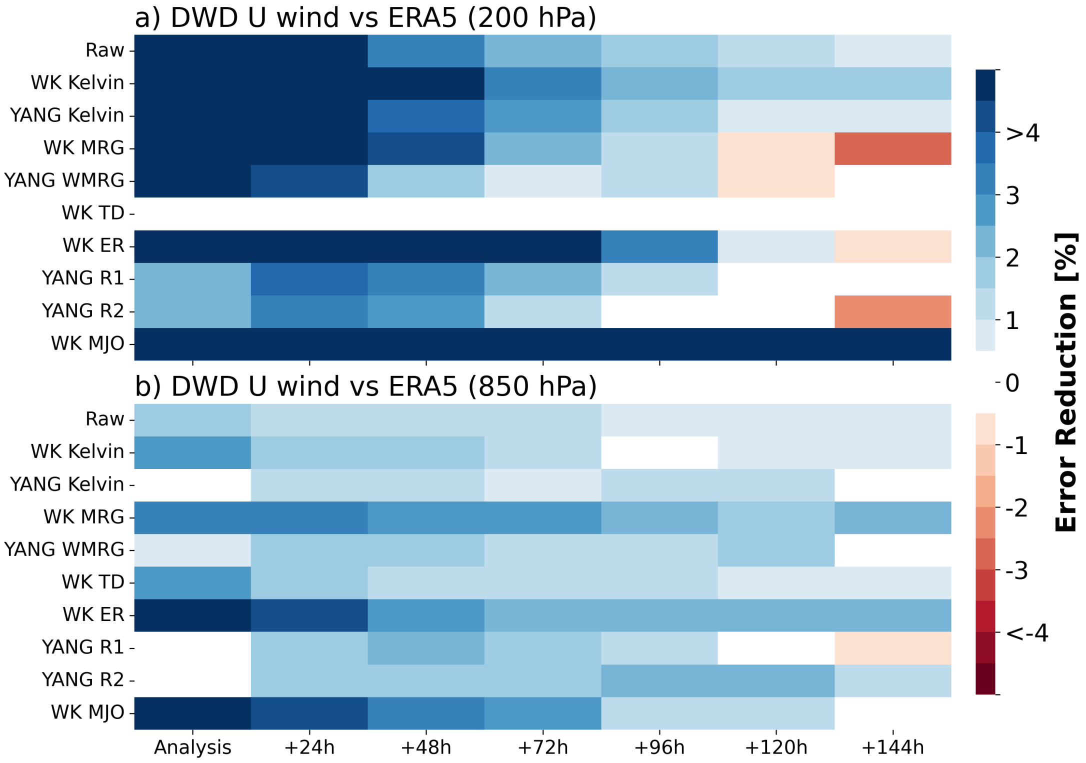

Figure 7.4: Same as Fig. 7.1, but for the DWD2020 OSE.

7.1.2 Impact in the DWD forecasting system

Now the impact of Aeolus on EW predictions in the DWD2020 OSE is explored. Fig. 7.4 shows the relative RMSE reduction of DWD zonal wind forecasts and related EWs in the tropics. The observed improvement in forecasts field is very large, when compared to the ECMWF2020 OSE (Fig. 7.1). At 200 hPa, the error reduction in the raw fields reaches more than 4% at +24h lead time before gradually decreasing to 1% improvement at +144h lead time. These improvements are related to error reduction in most EWs, regardless of the wave identification method used. The biggest improvements are in WK Kelvin, YANG Kelvin, WK ER and WK MJO, the latter achieving over 5% error reduction up to +144h. At shorter lead times, improvements are also observed in WK MRG and YANG Westward moving Mixed Rossby Gravity wave (WMRG), YANG R1. Curiously, the improvements in WK MRG and YANG WMRG have a similar magnitude in the case of DWD, while they exhibit a very different skill in the case of ECMWF. In the lower troposphere (850 hPa), we observe a consistent improvement in the raw zonal wind forecast between +24h and +144h forecast time of about 1% on average. The corresponding error reduction in the predictions of EWs is of similar magnitude and is consistent across wave types regardless of the method used. Finally, note that the analyses at both 200 and 850 hPa approach to the ERA5 reanalysis when Aeolus is assimilated. This behaviour is in contrast to what is observed for the ECMWF2020 OSE. The reasons for this are unknown, but could be related to the large model differences

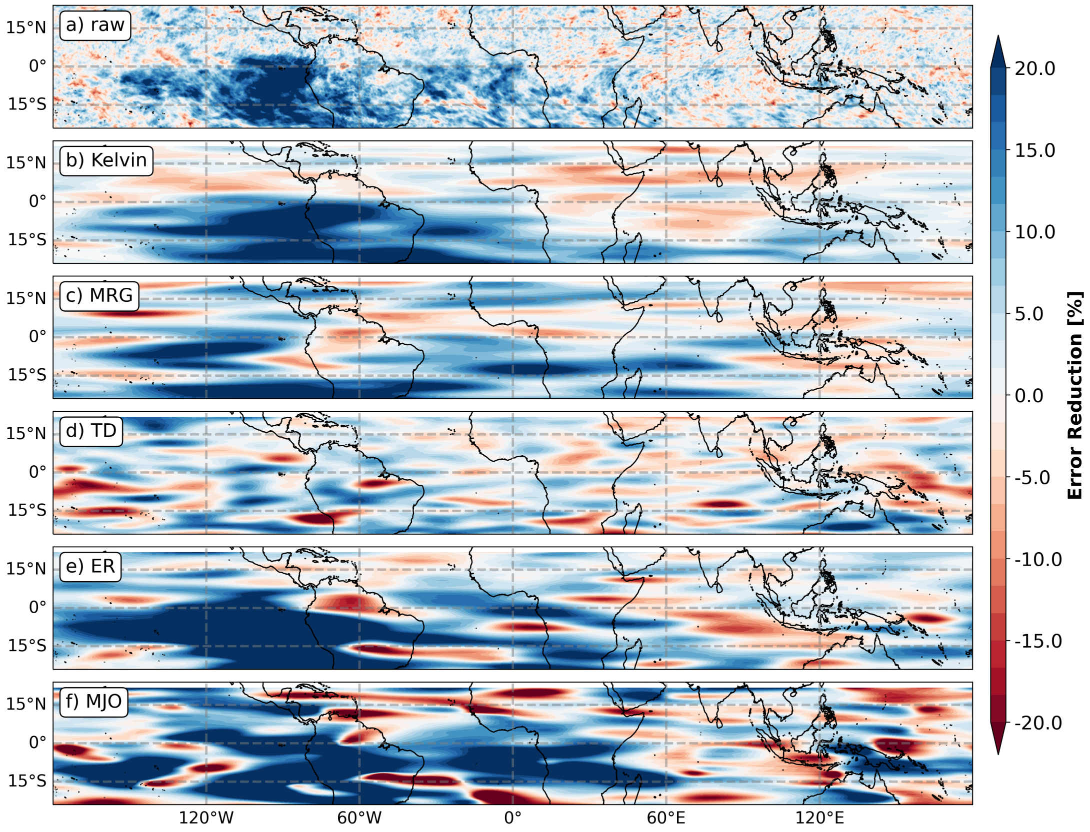

Figure 7.5: Same as in Fig. 7.2, but for the DWD2020 OSE.

.

between DWD and ERA5 as well as the different amount and nature of the assimilated data in each system.

Next, we examine the regional perspective on the impact of Aeolus in the DWD2020 OSE. Fig. 7.5 shows the horizontal impact of Aeolus on the zonal wind and associated EW forecasts at +48h and 200 hPa. In the raw zonal wind field (Fig. 7.5a), it is evident that the improvement varies region-wise. The largest improvements are observed over the Atlantic Ocean in the winter Hadley cell region and over the East Pacific and South American continents, exhibiting error reductions exceeding 20%. Interestingly, the improvements do not correspond to warm and humid regions, such as the Intertropical Convergence Zone (ITCZ) or the Maritime Continent Warm Pool. Improvements are more pronounced in drier and colder sea surface temperature (SST) regions such as the South Atlantic and Eastern Pacific. The region of maximum improvement occurs over the eastern Pacific and correspond exactly to the timing of the ENSO phase change between the neutral phase and the La Niña phase (Martin et al., 2023). The latter is associated with colder SST, making it the coldest region in the tropics. The improvement in the zonal wind forecast appears to be related to large improvements in the Kelvin and ER forecasts. Improvements associated with the MJO are also evident, but more noisy, while TD does not show any improvements, as expected, since this wave type does not affect the dynamics of the upper troposphere much. MRG also show improvements, but

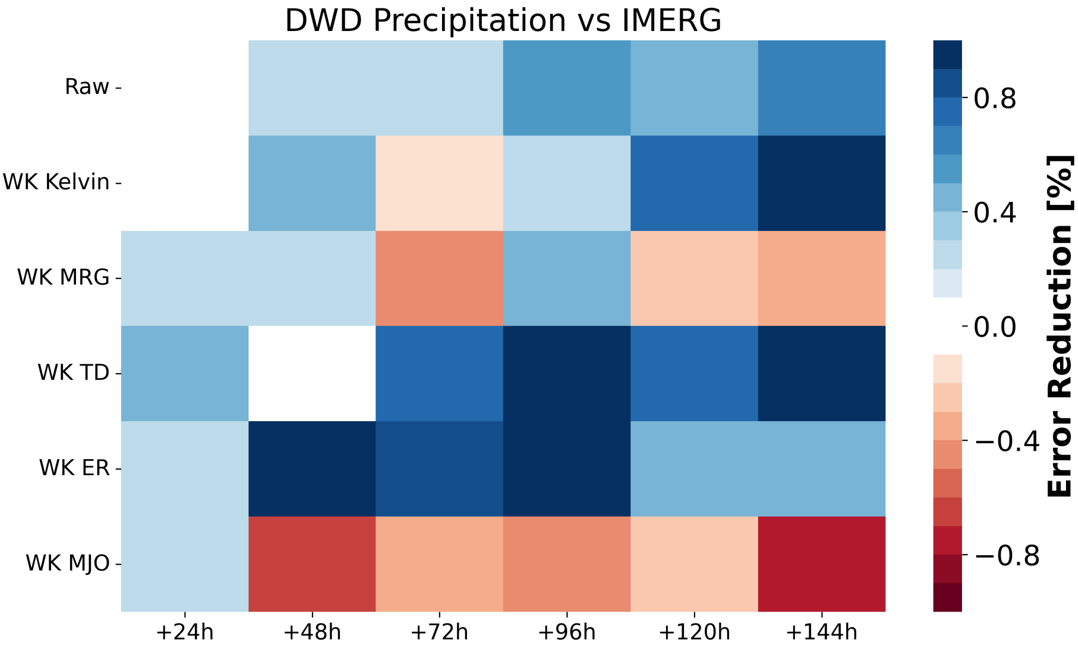

Figure 7.6: As in fig. 7.3, but for the DWD2020 OSE.

.

to a lesser degree. Again, note that MRG and ER can be influenced by non-tropical Rossby wave signals.

Finally, we examine the influence of Aeolus on rainfall and associated EW forecasts (Fig. 7.6). First, the raw precipitation forecasts show progressive improvement with lead time, ranging from 0% error reduction at +24h to 0.8% at +144h. The improvements are related to error reductions in Kelvin, TD, and ER wave types during longer lead times. While MRG waves show moderate forecast improvement, MJO reveals negative skill at all lead times except for the +24h forecast step. This deterioration in precipitation-filtered MJO forecasts accompanied by improvement in zonal wind-filtered MJO forecasts (Fig. 7.4) indicates that the coupling of the MJO with convection is not well represented in the DWD forecasting system. This point needs further investigation in the future.

7.2 Case study in the DWD forecasting system

Having identified the regions where the impact of Aeolus is particularly strong in the DWD2020 OSE, various underlying mechanisms contributing to the observed improvements are now being investigated. In particular, we study the strong impact observed over the Pacific Ocean, which occurs simultaneously with the ENSO phase change from neutral to La Niña.

7.2.1 Observed impact

Fig. 7.7 shows the temporal evolution of the vertical profile of zonal wind of ERA5 during July-September 2020 (a) together with the mean difference of EXP minus CTRL (b) and

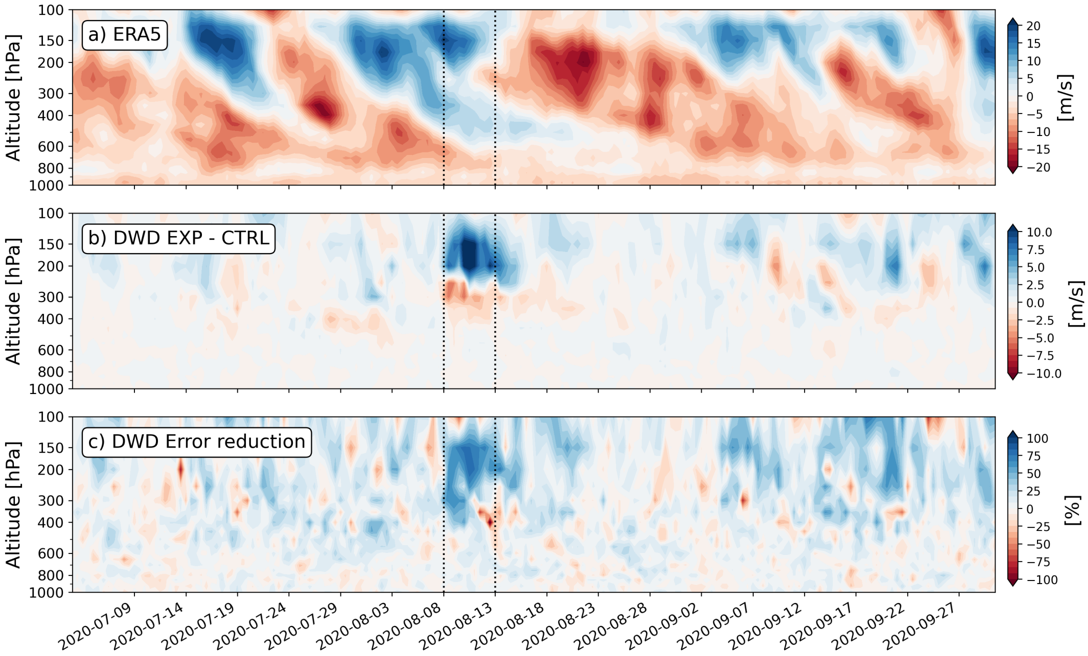

Figure 7.7: Time-altitude cross-section of zonal wind from ERA5 (a), mean difference Aeolus (EXP) - Control (CTRL) of +48h zonal wind forecast from the DWD2020 OSE and relative reduction in RMSE of the +48h zonal wind forecast verified against ERA5 zonal wind. The fields are averaged over the eastern Pacific region [0°-10°S,100°W-80°W]. The vertical dotted lines represent the period of maximum impact of Aoelus between 8 August 2020 and 13 August 2020.

the +48h forecast error reduction (c) over the eastern Pacific [0°-10°S, 100°W-80°W]. The zonal wind in the upper level shown in Fig. 7.7a reveals a weekly alternation between easterly and westerly winds, as opposed to the lower level where the wind direction is predominately easterly. This change in wind direction is primarily related to the focus region being in a crossover zone between the meridional upper branch of the Hadley cell and the westerly subtropical jet. In this in-between region, changes in the wind direction can be attributed to a combination of factors, such as atmospheric waves and teleconnection effects. The low-level easterlies are predominantly related to trade winds. Following Martin et al. (2023) the phase change to La Niña occurred around 8 August 2020, when the SST anomaly exceeded the -0.5 K threshold. At this time, large changes in vertical zonal wind shear are visible in the Upper Troposphere and Lower Stratosphere (UTLS) region (Fig. 7.7a, 400-150 hPa), with a dipole-like structure corresponding to the mean wind differences between the CTRL and EXP +48h zonal wind forecast, exceeding 10 ms^{-1} and lasting about a week. These observed differences are associated with a particularly high impact (Fig. 7.7c) in the same period and domain, nearing almost 100% error reduction. Before and after the ENSO-shift period, which occurred during 8 - 13 August 2020, some dipole-like changes are also apparent in the UTLS, concomitant with high error reductions, although less pronounced compared to the ENSO phase transition period.

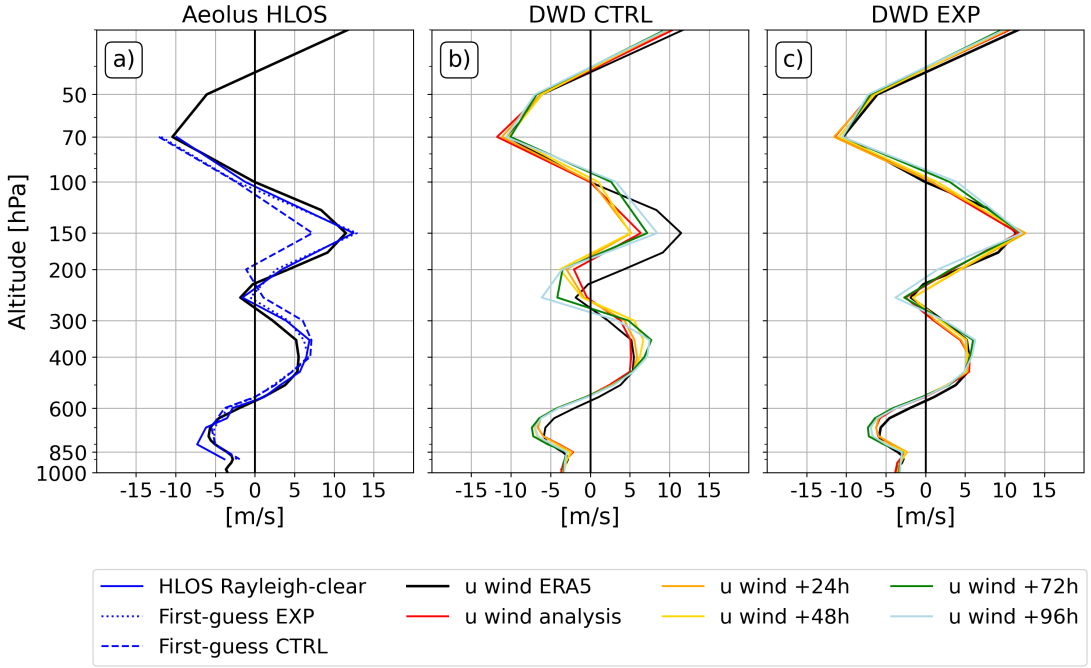

Figure 7.8: Vertical profile of the Aeolus Rayleigh Clear wind observation along the Horizontal Line of Sight (HLOS) (solid blue line) and corresponding model-equivalents of the EXP (blue dashed line) and CTRL (blue dashed line) experiments of the DWD2020 OSE (a); zonal wind predictions for different lead times of the CTRL (b) and EXP (c) experiments of the DWD2020 OSE. The black solid line represents the ERA5 zonal wind vertical profile. The fields are averaged over the eastern Pacific [0°-10°S, 100°W-80°W] during the period of greatest impact of Aeolus data between 8 and 13 August 2020.

Figure 7.8 specifically examines the area of highest impact occurring between 8 and 13 August, demarcated with dotted lines in Fig. 7.7. Fig. 7.8a shows the vertical zonal wind profile of ERA5 (black, continuous) together with the Aeolus Rayleigh-clear HLOS wind and the corresponding first-guesses of the run including Aeolus (EXP, blue dashed) and the control run (CTRL, blue dashed). The inspected region features pronounced vertical wind shear, with the zonal wind undergoing five changes in wind direction throughout the troposphere. Interestingly, the Aeolus and ERA5 wind fields are nearly identical, although the Rayleigh clear measurement slightly exceeds the 400 hPa ERA5 wind peak by about 2 ms^{-1}. The corresponding Mie-cloudy profile is not shown here as it is mainly sampling at the top of the boundary layer, indicating clear-sky conditions. The first-guess in EXP matches the Rayleigh-clear wind profile well, while the first-guess of CTRL shows large discrepancies with ERA5, especially between 400 and 100 hPa, where differences up to 5 ms^{-1} between both first-guesses can be found. The improvement of the first-guess with respect to ERA5 reanalysis can be attributed to the "cycling effect", which is an iterative improvement of the first-guess during each Data Assimilation (DA) cycle. Figures 7.8b and c shows the corresponding zonal wind analysis and forecasts for different lead times for the CTRL and EXP run, respectively. Generally, it appears that the improvement of the mean profile persists in the forecasts, as they follow the

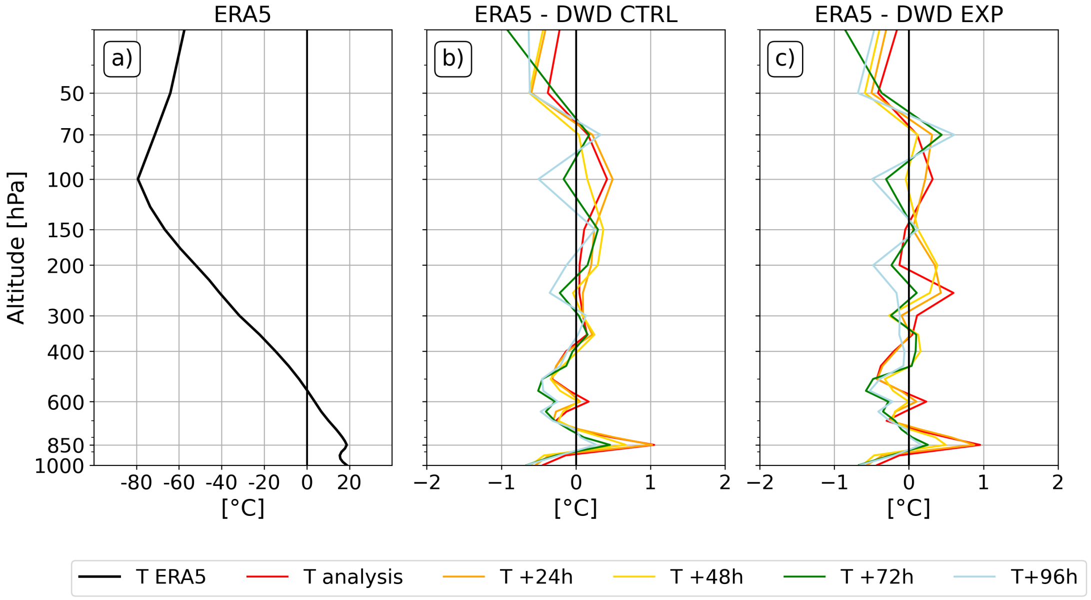

Figure 7.9: Vertical Temperature profile from ERA5 reanalysis (a), and differences between ERA5 and DWD analyses and forecasts up to +96h lead time for both CTRL (b) and EXP (c) runs.

shape of the first-guess closely. This leads to dramatic improvements in the 100 - 400 hPa altitude range in the EXP run.

7.2.2 Dynamical scenarios for the observed improvements

The aim of this section is to examine various hypothetical mechanisms that could be related to the observed improvements during the ENSO phase change from neutral to La Niña conditions in the eastern Pacific when Aeolus is assimilated into the DWD system. A plausible mechanism to explain larger errors during this period and time is that the cooling of the SST leads to a very stable atmosphere with enhanced subsidence and reduced convective activity. This enhanced stability renders the atmosphere highly sensitive to even small model errors. Especiallly in the UTLS region, radiative processes, including greenhouse gases and water vapour, play a crucial role in the temperature and energy balance. Small variations in temperature or radiative gases can trigger significant changes in radiative forcing, which is a particular challenge for models to accurately represent (de F. Forster and Shine, 1997; Forster and Shine, 2002; Zhang et al., 2004).

In addition to this sensitivity, the region of interest is in a remote and data-poor region of the eastern Pacific. In the absence of in situ observations and satellite measurements, the DA process can lead to heavy reliance on the model first-guess. Indeed, in situ wind observations are sparse and most satellite observations are derived from Atmospheric Motion Vectors (AMVs). The lack of convective activity during La Niña results in lower cloud cover and unstructured water vapour patterns, which limits the amount of AMVs measurements. Temperature observations are also available from satellite radiation measurements, but since there is no geostrophy in the tropics, assimilation of temperature data can generally not be used to derive wind information. Especially with the DWD DA system, the amount of assimilated satellite data is significantly lower compared to the ECMWF. Moreover, the difference between ECMWF Four-Dimensional Variational assimilation (4D-Var) and DWD Three-Dimensional Variational assimilation (3D-Var) DA, which is less effective in extracting wind information from mass observations, as well as the different model physics between the Integrated Forecasting System (IFS) and Icosahedral Nonhydrostatico (ICON) may contribute to the lower impact in ECMWF compared to DWD. Hence, Aeolus likely plays an important role as it is the only available wind information with vertical resolution in this region, in particular for the DWD.

Nevertheless, an insufficient representation of the temperature in the model first-guess can also lead to inaccuracies in the wind estimation. Figure 7.9a shows the vertical profile of the ERA5 temperature in the focus region. A relatively weak temperature gradient is evident, with a temperature inversion occurring near the tropopause at 100 hPa. The corresponding differences between ERA5 reanalysis and DWD2020 temperature analyses and forecasts are shown for both CTRL (Fig. 7.9b) and EXP (Fig. 7.9c) runs. First, there are no noticeable improvements nor strong departures in temperature predictions relative to ERA5 (Fig. 7.9b,c). However, around 250 hPa, we observe an increase in analysed temperature of 0.5°C of the EXP run with respect to ERA5 (Fig. 7.9c), which corresponds to the lower edge of the high impact region. However, this change is not related to forecast improvements in temperature in the EXP run (Fig. 7.9c). Thus, the inaccurate first estimate in the CTRL run seems to be mainly a result of the unavailability of wind observations in this region, which Aeolus can compensate for by improving the vertical wind shear.

7.3 Concluding remarks

In this chapter, we have investigated the impact of Aeolus data on the propagation of EWs in the ECMWF and DWD forecasting systems. The aim was to evaluate the improvements in zonal wind and precipitation forecasts associated with the variation of different wave types and lead times, and to explore the different mechanisms leading to the observed improvements.

In this context, we have used two different techniques to isolate EWs in space and time, namely the Wheeler and Kiladis (1999) (WK) and Yang et al. (2003) (YANG) methods. The EWs were identified from zonal wind field forecasts using both methods and verified against the ERA5 reanalysis. In general, the results showed that the impact was larger in the upper troposphere, with DWD demonstrating a more substantial positive impact compared to ECMWF. Most notably, at + 24 h forecast lead time, DWD achieved improvements of more than 4% for most wave types, compared to 1% for ECMWF. Furthermore, variations in forecast improvement also depend on wave type and lead time. For DWD, improvements that persist over longer lead times are mainly associated with the MJO, Kelvin and ER wave types, while for ECMWF they are mostly linked to the MJO and Kelvin wave types. In addition, for both forecasting systems, short-term improvements in the zonal wind forecast were found to be associated with the MRG and WMRG wave types. Generally the observed improvements vary geographically for both ECMWF and DWD forecasts, with ECMWF achieving error reductions up to 15% in the +48h 200 hPa zonal wind forecast over the Pacific Ocean, while DWD achieves up to +20% error reduction over the eastern Pacific. Furthermore, significant improvements were also identified over the Atlantic winter Hadley Cell region and the South America. It is interesting to note that while both the YANG and WK methods show similar performance for the same wave types for DWD, there is a lack of consistency between the two methods for ECMWF. This can possibly be the result of the inherent differences in the used methods and to limited statistical significance.

To explore the coupling between EWs and convection, we also identified EWs on rainfall predictions using the WK method that were validated against GPM IMERG rainfall product. The analysis revealed improvements in both ECMWF and DWD forecast, particularly in the DWD forecasting system. The DWD improvements were particularly notable in accurate predictions in Kelvin, TD and ER waves types, with error reductions up to 1 %. For ECMWF, the improvements are mostly visible in MJO and Kelvin wave types. Strikingly, although the MJO is well represented in the zonal wind fields, its performance deteriorates in the precipitation fields in the DWD system, while the opposite is true for ECMWF. This highlights the need to further examine the complex dynamics of the MJO and its coupling with convection and precipitation in the DWD system.

The study found that the most significant improvements were seen in cooler and drier regions of the tropics, especially in the DWD system. In particular, during the ENSO transition period between neutral and La Nina in the eastern Pacific in August 2020, the DWD system showed huge error reductions of more than 50%. The observed improvements were particularly pronounced in the UTLS region, which is characterised by high wind shear. Remarkably, Rayleigh-clear winds and ERA5 zonal wind in this region were closely aligned, leading to improvements in the first-guess of up to 5 ms^{-1} and forecasts at different lead times when Aeolus was assimilated. The limited number of observations in this remote area, and the limited availability of AMV satellite information due to low cloud cover and unstructured water vapour patterns, highlights the critical role of Aeolus in this region to compensate for the lack of conventional observations. This holds particularly true for DWD, which assimilates fewer satellite observations than ECMWF, resulting in a larger impact of Aeolus.

8. Conclusions

With the advent of Aeolus, a revolution in Numerical Weather Prediction (NWP) has taken place. Equipped with the first Doppler Wind Lidar (DWL) in space, Aeolus demonstrated excellent instrumentation and performance. In particular, Aeolus has addressed the long-standing shortage of wind observations in the tropics by providing unprecedented Horizontal Line of Sight (HLOS) wind profiles from space. Especially in this latitude band, wind cannot be inferred from mass information, giving Aeolus the potential to significantly improve the representation of the tropical circulation in NWP models. In this thesis, we provided a comprehensive analysis of the impact of Aeolus in the tropics.

First, we evaluated the quality of Aeolus data products by characterising the errors of both Rayleigh-clear and Mie-cloudy wind observation types in a complex tropical atmospheric environment. To achieve this, Aeolus wind observations were validated against radiosondes that were deployed as part of Joint Aeolus Tropical Atlantic Campaign (JATAC) across the tropical Atlantic ocean during the months of August-September 2021. During this period, the atmosphere in this region consists of a mixture of convective clouds associated with the Intertropical Convergence Zone (ITCZ) and the West African Monsoon (WAM), and dust aerosols within the Saharan Air Layer (SAL). This allows to investigate the error sensitivity of Aeolus wind observations with respect to mineral dust and cloud features.

RQ 1.1 What is the quality of Aeolus L2B wind products in the tropics in terms of systematic and random errors?

In terms of systematic error, Rayleigh-clear has a mean bias of $-0.5 \pm 0.2\ ms^{-1}$ and falls within the European Space Agency (ESA) recommendation of $0.7\ ms^{-1}$. An altitude and orbital-dependant bias in the Rayleigh-clear channel was also found with respect to both radiosondes and model equivalents. For Mie-cloudy, the systematic error lies on average at $-0.9 \pm 0.3\ ms^{-1}$ within the ESA specifications when the uncertainty of the bias is taken into account. For Rayleigh-clear, the random error is evaluated accounting for a range of representativeness errors and lies within 3.8 - 4.3 ms^{-1} and 4.3 - 4.8 ms^{-1} for the height ranges of 2 - 16 km and 16 - 20 km, respectively. In both cases the random errors do not meet the ESA recommendations of 2.5 ms^{-1} and 3 ms^{-1} respectively. For Mie-cloudy the random error between 2–16 km amounts to $1.1 - 2.3\ ms^{-1}$, which lies within the ESA specifications.

RQ 1.2 What are the error dependencies of Rayleigh-clear in terms of co-location features and the presence of clouds and dust?
In terms of co-location features, Rayleigh-clear and Mie-cloudy measurements do not indicate a strong error dependency on the co-location radius, while they are more sensitive to the co-location time. Both systematic and random errors are altitude dependent, with larger errors occurring in the lower troposphere, presumably due to signal attenuation by clouds and dust, and in the upper troposphere, related to lower air density that causes reduced signal return. The Error Estimate (EE), which is inversely proportional to the square root of the normalized useful signal, has a similar error structure. It was found that when the normalised useful signal is strongly attenuated by the presence of clouds and dust, Rayleigh-clear measurements exhibit large random errors, which exceed the EEs of Aeolus.

RQ 1.3 What are the error dependencies of Mie-cloudy in terms of co-location features and the presence of clouds and dust?
Mie-cloudy mainly samples from cloud tops, while most measurements within dust layers are rejected by the Quality Control (QC). As expected, Mie-cloudy measurements have a decreasing random error with increasing cloud cover, as most of the strong backscatter signal comes from cloud tops. However, the additional presence of dust in cloudy conditions increases Mie-cloudy errors, presumably due to the weak backscattering of dust, mainly below clouds, where the useful signal is attenuated. This increase in error is not well captured by the Mie-cloudy EE, as it is similar in magnitude in both dusty and non-dusty conditions.

Having carried out a comprehensive characterisation of Aeolus wind observation errors in the complex tropical atmosphere, we subsequently assessed the impact of these observations when assimilated into NWP models. More specifically, we investigated the impact of Aeolus wind observations on the atmospheric circulation of the WAM in the operational systems of European Centre for Medium-Range Weather Forecasts (ECMWF) and Deutscher Wetterdienst (DWD). This geographical area is of particular interest due to its very low predictability, its very sparse observational coverage and its socio-economic relevance.

RQ 2.1 Which atmospheric features of the WAM can Aeolus effectively sample?
Rayleigh-clear primarily samples the clear sky portion of the WAM away from the ITCZ, especially in the upper troposphere. It also samples the Tropical Easterly

Jet (TEJ) and to a lesser extent the African Easterly Jet North (AEJ-North), despite the presence of convective clouds. Mie-cloudy, on the other hand, captures the heart of the WAM convective systems across the full range of cloud types and aerosols. As a result, Mie-cloudy provides a good detection of the AEJ-North and TEJ. For ECMWF, the Rayleigh-clear assigned observation error is largest in the convectively active region, while for Mie-cloudy it is largest in the aerosol-rich layers. For the DWD the assigned observational error has comparable values for Rayleigh-clear and Mie-cloudy winds.

RQ 2.2 What is the influence of Aeolus on wind analysis in the WAM in the ECMWF and DWD operational systems?

Throughout the four Observing System Experiment (OSE)s, Aeolus brings significant changes in the representation of the main zonal circulation features of the WAM. While no significant effect on the AEJ-North is visible in the DWD, the ECMWF indicates a weakening of the southern edge of the AEJ-North. On the other hand, the TEJ core exhibits a strengthening of 0.4 ms^{-1} in the ECMWF analysis, while the southern edge of the TEJ is weakened by more than 0.5 ms^{-1} in the DWD analysis. Rayleigh-clear background departures show a height- and orbital-dependent bias causing the winds to accelerate and decelerate on half-day basis. Correcting for this bias using a temperature-based approach provides a more realistic representation of the diurnal cycle.

RQ 2.3 What is the impact of Aeolus on wind forecasts in the WAM in the ECMWF and DWD operational systems?

Both ECMWF and DWD zonal wind forecasts show a positive impact over the WAM region. In general, the impact is greatest in the upper troposphere and in cloud-free regions. In particular, the AEJ-North shows modest improvements in the ECMWF OSEs, while no positive effects are visible for the DWD. The TEJ, on the other hand, shows large improvements for most lead times, despite the presence of cumulonimbus clouds. Verification with radiosondes at ECMWF shows a reduction in the mean error of 0.45% and 1.95% in 2019 and 2020, respectively. It reaches 1.45% in 2019, when a temperature dependent bias correction in the Rayleigh-clear is introduced, highlighting the benefit of using such a bias correction.

To gain a more holistic understanding of the impact of Aeolus in the tropics, a further stage in the investigation was to examine the tropical large-scale dynamics, focusing in particular on Equatorial Waves (EWs). Specifically, we examine the impact of Aeolus on EWs predictions using two identification methods, namely the Wheeler and Kiladis (1999) (WK) and Yang et al. (2003) (YANG) methods applied to the ECMWF and DWD operational systems.

RQ 3.1 What is the impact of Aeolus on EWs predictions in the tropics?
In both the ECMWF and DWD forecasting systems, Aeolus contributes positively to EWs forecasts isolated from zonal wind fields, especially in the upper troposphere, with stronger improvements in the case of DWD. For DWD, the improvements, which persist over longer forecast lead times, are mainly related to the Madden-Julian Oscillation (MJO), Kelvin and Equatorial Rossby waves (ER) wave types, while for ECMWF they are mainly associated with the MJO and Kelvin waves. Forecast improvements in the ECMWF reach up to 15% error reduction in the +48h zonal wind forecast over the Pacific, while in the DWD system, the error is reduced by more than 20% in the eastern Pacific. Significant improvements are also observed over the Atlantic winter Hadley Cell region and the South American continent.

RQ 3.2 How does Aeolus affect the modulation of tropical rainfall associated with EWs?
Improvements in EWs identified in precipitation forecasts were found in both the DWD and ECMWF forecast systems, most notably in the DWD system. For the ECMWF, the improvements are mainly related to improvements in Kelvin waves and the MJO, while the DWD improvements are associated with accurate predictions of Kelvin, TD and ER wave types, in some cases reaching error reductions of 1%. Strikingly, the MJO shows a deterioration in performance in the DWD system, while being very well represented in the zonal wind fields. This discrepancy suggests the need to further investigate the coupling between the MJO and convection in the DWD forecast system, underlining the complex EW-dynamics at play in precipitation forecasting.

RQ 3.3 What are the dynamical mechanisms that contribute to the observed improvements?
Notably, the DWD improvements were mostly observed in cooler and drier regions of the tropics. In particular, the DWD system showed significant improvements during the El Niño-Southern Oscillation (ENSO) transition from neutral to La Niña conditions in the eastern Pacific during August 2020. During that time, error reductions of up to 100% were observed, covering the Upper Troposphere and Lower Stratosphere (UTLS) region where strong wind shear is found. Aeolus Rayleigh-clear and ERA5 zonal winds are in close agreement, improving the first guess by up to 5 ms^{-1} at 150 hPa and forecasts at different lead times over the UTLS. This large impact is likely related to the lack of observations in the area and the large model errors making DWD heavily reliant on Aeolus observations.

The presented results provide important new insights into the nature of Aeolus wind data and their influence in the ECMWF and DWD forecasting systems in the tropics. Firstly, Calibration/Validation (Cal/Val) activities revealed variations in the quality of Aeolus wind products with respect to tropical atmospheric constituents. While Mie-cloudy observations meet ESA's recommendations, the quality of Rayleigh-clear observations is affected by cloud attenuation, causing an underestimation of the corresponding EE. This holds particularly true for the WAM region, which is characterised by a range of convective cloud types and an abundance of aerosols. The observed degradation and EE miscalibration of Rayleigh-clear, combined with differing definitions of the assigned observation error across both ECMWF and DWD NWP systems, limits improvements in the representation of wind features in convective regions such as the mid-level AEJ-North. In particular, the DWD does not take into account the effect of clouds when defining the assigned observation error. The higher quality of the Mie-cloudy wind observations does not seem to be sufficient to compensate for this effect. Despite the sensitivity of Rayleigh-clear data to the presence of clouds and the existence of an altitude and orbit-dependent bias, significant improvements are observed in the tropics, particularly over the UTLS region over remote and data sparse regions where clear sky conditions prevail. These enhancements improve the representation of vertical wind shear, planetary-scale wave phenomena and associated precipitation forecasts, especially in the DWD forecasting system. Overall, Aeolus has transformed NWP by providing ground-breaking and unique wind observations from space, enabling unprecedented contributions to the understanding of tropical phenomena and assimilation of wind observations in the tropics.

9. Outlook

Aeolus, the groundbreaking wind mission launched in 2018, has now completed its five-year lifetime, exceeding expectations in terms of technological and scientific achievements. Over its lifetime, the Aeolus mission generated a substantial economic benefit, estimated at €2.5 billion, exceeding the cost of the mission estimated at €480 million (London Economics Space Team, 2022). Despite the challenges encountered during the mission, including complex biases and instrument-related noises, Aeolus achieved significant Numerical Weather Prediction (NWP) impacts, particularly in the tropics.

To realise the full potential of Aeolus, further refinements in processing algorithms and instrumentation should be addressed. For instance, a more comprehensive characterisation of the Rayleigh-clear error can be achieved by including additional noise terms such as detector and readout noise, and by considering more parameters such as temperature, pressure and scattering ratio in the definition of the Rayleigh response. Likewise, optimising the Mie core algorithm such as the fitting function or the classification algorithm can contribute to an improved Mie-cloudy error characterization. Further studies are needed to better characterise the contribution of the cross-talk effect in the quality of Rayleigh-clear measurements, particularly in dusty regions. Additionally, the underlying cause of the observed orbital-dependent bias in the Rayleigh-clear channel remains unidentified. More research is needed to better understand the factors contributing to this bias, as the relationship with temperature or wind speed has not been clearly established. Finally, a better consideration of the Aeolus errors in the processing chain and in models can be of advantage, especially in the convectively active or aerosol-loaded regions of the tropics. In particular for the Deutscher Wetterdienst (DWD), the error characterisation of Rayleigh-clear in clear and cloudy regions in the data assimilation process can be improved by including the Error Estimate (EE) in the definition of the assigned observation error.

In terms of NWP impact, further research is needed to investigate the impact of Aeolus on rainfall forecasts in convectively active regions and relationships with the propagation of planetary-scale Equatorial Waves (EWs). Especially over the West African Monsoon (WAM) region, the distinct influence of Aeolus on key circulation features such as the Tropical Easterly Jet (TEJ) and African Easterly Jet North (AEJ-North) can affect the propagation of African Easterly Waves (AEWs) and related Mesoscale Convective

Systems (MCSs). This could also potentially affect the forecast of tropical cyclones and hurricanes over the downstream Atlantic Ocean, which are closely related to AEWs (Brammer and Thorncroft, 2015). A positive impact of improving data assimilation in the WAM may also be observed remotely in the midlatitude Euro-Atlantic region (Bielli et al., 2010; Gaetani et al., 2011; Pante and Knippertz, 2019) and the Mediterranean basin (Raicich et al., 2003) through teleconnection effects. Investigating the impact of Aeolus data on long-term forecasts, from weekly to subseasonal scales, and their relationship with the propagation of EWs can also provide valuable information for understanding predictability in the tropics. Finally, the underlying mechanism for the large wind model errors observed in the DWD system during the El Niño-Southern Oscillation (ENSO) phase transition should be further clarified, whether these errors arise from data scarcity or from inherent model-related problems.

The success of Aeolus has now paved the way for its successor, Aeolus-2, which has already been approved by European Space Agency (ESA). Scheduled for launch in 2029, the Aeolus-2 wind mission aims to surpass the performance of its predecessor by achieving a more profound impact on global weather forecasting. With projections already indicating the potential to generate €7.1 billion over its planned lifetime (London Economics Space Team, 2022), the arrival of Aeolus-2 is very promising in terms of improving global weather forecasting and benefiting societies around the world. This PhD work has created a blueprint for analysis in the tropics that could and should be repeated with Aeolus-2.

Acronyms

3D-Var Three-Dimensional Variational assimilation

4D-Var Four-Dimensional Variational assimilation

ACCD Accumulation and Control and Calculation Device

ACMF Aeolus Calibration and Monitoring Facility

AEJ-North African Easterly Jet North

AEWs African Easterly Waves

AISP Annotated Instrument Source Packets

ALADIN Atmospheric LAser Doppler INstrument

AMVs Atmospheric Motion Vectors

AOD Aerosol Optical Depth

APF Aeolus Processing Facility

ASPEN Atmospheric Sounding Processing Environment

AVATAR-T Aeolus Validation Through Airborne Lidars in the Tropics

BRC Basic Repeat Cycle

BB Biomass Burning

BRC Basic Repeat Cycle

CADDIWA Clouds-Atmospheric Dynamics–Dust Interactions in West Africa

Cal/Val Calibration/Validation

CAMS Copernicus Atmosphere Monitoring Service

CPEX-AW Convective Processes Experiment-Aerosols and Wind campaign

CT Cloud Type

DA Data Assimilation

DCO Detection Front Offset

DFG German Research Foundation

DFU Detection Front End Unit

DLR German Aerospace Center

DISC Data Science and Innovation Cluster

DKE Difference Kinetic Energy

DWD Deutscher Wetterdienst

DWL Doppler Wind Lidar

ECMWF European Centre for Medium-Range Weather Forecasts

EE Error Estimate

EDA Ensemble Data Assimilation

EnKF Ensemble Kalman Filter

ENSO El Niño-Southern Oscillation

ER Equatorial Rossby waves

ESA European Space Agency

ESRIN European Space Research Institute

EVAA Experimental Validation and Assimilation of Aeolus observations

EWs Equatorial Waves

EIG Eastward Inertio-Gravity waves

EUMETSAT European Organisation for the Exploitation of Meteorological Satellites

FFT Fast Fourier Transform

FSOI Forecast Sensitivity to Observation Impact

FPI Fabry-Perot Interferometers

GCMs Global Circulation Models

GCOS Global Climate Observing System

GOS Global Observing System

GPM Global Precipitation Mission

GNSS Global Navigation Satellite Systems

GTS Global Telecommunication System

HLOS Horizontal Line of Sight

HRES High-RESolution forecasts

ICON Icosahedral Nonhydrostatico

IFS Integrated Forecasting System

IMERG Integrated Multi-Satellite Retrievals for Global Precipitation Measurement

ITCZ Intertropical Convergence Zone

ITD Intertropical Discontinuity

JATAC Joint Aeolus Tropical Atlantic Campaign

KE Kinetic Energy

KNMI Royal Netherlands Meteorological Institute

KIT Karlsruhe Institute of Technology

L0 Level 0

L1A Level 1A

L1B Level 1B

L2A Level 2A

L2B Level 2B

L2C Level 2C

LETKF Local Ensemble Transform Kalman Filter

LOS Line Of Sight

LWDA Long-Window Data Assimilation

MADI Mean Absolute Difference

MARS Meteorological Archival and Retrieval System

MCSs Mesoscale Convective Systems

MD Mean Differences

MJO Madden-Julian Oscillation

MRG Mixed Rossby gravity waves

MSG METEOSAT geostationary satellites

NRT Near-Real Time

NASA National Aeronautics and Space Administration

NCAR National Center for Atmospheric Research

NOAA National Oceanic and Atmospheric Administration

NWP Numerical Weather Prediction

OSE Observing System Experiment

O-B Observation minus Background

O-RS Observation minus RadioSonde

PR Puerto Rico

PCFs Parabolic Cylindrical Functions

PDGS Payload Data Ground Segment

QBO Quasi-Biennial Oscillation

QC Quality Control

RMSE Root Mean Square Error

R1 Equatorial Rossby wave with meridional mode number 1

R2 Equatorial Rossby wave with meridional mode number 2

RBS Range Bin Settings

RMSD Root Mean Square Differences

SAFNWC Satellite Application Facility for supporting NoWCasting and very short range forecasting

SAL Saharan Air Layer

SCRX Saint CRoiX

SEVIRI Spinning Enhanced Visible and Infrared Imager

SMAD Scaled Median Absolute Deviation

SNR Signal-to-Noise Ratio

SR Scattering Ratio

SST sea surface temperature

STD Standard Deviation

STJ Subtropical Jet

SW Shallow Water

TCWV Total Column Water Vapour

TDs Tropical Disturbances

TEJ Tropical Easterly Jet

TS Tropical Storm

TRMM Tropical Rainfall Measurement Mission

UPRM University of Puerto Rico at Mayagüez

UTLS Upper Troposphere and Lower Stratosphere

VarEnKF Hybrid Variational Ensemble Kalman Filter

VarQC Variational Quality Check

W2W Waves to Weather

WAM West African Monsoon

WMRG Westward moving Mixed Rossby Gravity wave

WCRP World Climate Research Programme

WIG Westward Inertio-Gravity waves

WMO World Meteorological Organisation

Symbols

R	Rossby radius of deformation
f	Coriolis parameter
g	Gravitational acceleration
H	Depth of the vertical atmospheric system
Ω	Earth rotation rate
Θ	Latitude
β	Rossby parameter
h_e	Equivalent depth
c	Gravity wave phase speed
w	Frequency
k	Zonal wave number
n	Meridional wave number
u	Zonal wind component
v	Meridional wind component
ϕ	Geopotential height
V_{LOS}	Wind velocity along the Line Of Sight (LOS)
λ	Laser wavelength
Δf	Frequency Doppler shift
γ	Scattering ratio
γ_A	Particulate backscatter coefficient
γ_{Mol}	Molecular backscatter coefficient
R_{Ray}	Rayleigh response
R_{Mie}	Mie response
I_A	Intensity transmitted through Fabry-Perot Interferometers (FPI) filter A
I_B	Intensity transmitted through FPI filter B
x_0	Mie fringe centroid position of the transmitted pulse
σ_{Ray}	Rayleigh response error
σ_{Mie}	Mie response error
σ_A	Noise term of FPI filter A
σ_B	Noise term of FPI filter B

EE_{Mie}	Mie error estimate
EE_{Ray}	Rayleigh error estimate
EE_{tot}	Total error estimate
EE_{Aeolus}	Error estimate provided by the Aeolus L2B product
θ	Local incidence angle
SNR_A	Signal-to-Noise Ratio (SNR) of FPI filter A
SNR_B	SNR of FPI filter B
$HLOS_{AEOLUS}$	Aeolus wind speed along the Horizontal Line of Sight (HLOS)
LOS_{AEOLUS}	Aeolus wind speed along the LOS
V_{RS}	Total horizontal wind speed measured by the radiosonde
ϕ_{RS}	Wind direction measured by the radiosonde
$HLOS_{RS}$	Wind speed measured by the radiosonde along the HLOS
ψ	Azimuth angle
σ_{ass}	European Centre for Medium-Range Weather Forecasts (ECMWF) assigned HLOS wind ob
σ_{instr}	Level 2B (L2B) processor reported instrument error standard deviation
σ_{tot}	Standard deviation of the total difference between Aeolus and radiosonde observations
σ_{RS}	Standard deviation of the radiosonde observation error
σ_{rep}	Standard deviation of the representativeness error
σ_{Aeolus}	Standard deviation of the Aeolus HLOS winds observation error
α	L2B processor instrument error estimate scaling factor
μ	Total mean difference
ϵ_{μ}	Uncertainty of the mean bias
$\Delta_{diff_{HLOS}}$	Bin-to-bin wind speed difference between Aeolus and radiosonde along the HLOS
$Z_{m,i}$	Modified Z-score
$J(\mathbf{x})$	Cost function
$\mathbf{B}$	Background error covariance matrix
$\mathbf{R}$	Observation error covariance matrix
$\mathcal{H}$	Observation operator
$\mathbf{H}$	Tangent linear of the observation operator
$\mathbf{I}$	Identity matrix
M	Model
$\mathbf{M}$	Tangent linear of the model
$\mathbf{K}$	Kalman gain
$\mathbf{x}^b$	Background state
$\mathbf{x}^a$	Analysis state
$\mathbf{y}^o$	Observation vector
$\bar{\mathbf{y}}^b$	Background state in observation space
$\mathbf{X}^a$	Analysis perturbation matrix
$\mathbf{X}^b$	Background perturbation matrix
$\mathbf{Y}^b$	Background perturbation matrix in observation space

$\mathbf{x}^b$	Background state
$\overline{\mathbf{x}}^a$	Analysis ensemble mean
$\overline{\mathbf{x}}^b$	Background ensemble mean
$\overline{\mathbf{w}}$	Mean weighting vector
$\mathbf{A}$	Analysis error covariance matrix
N	Ensemble size

Acknowledgements

I want to express my sincere gratitude to Peter and Martin for their guidance and continuous supervision. Peter, your knowledge and enthusiasm in tropical meteorology and your relaxed attitude have been truly inspiring. Your passion for tropical waves is remarkable, and I have always been curious to know if you secretly have a favorite wave type or if you just love them all equally. Martin, I am deeply grateful for introducing me to the world of wind measurements, with your valuable insights and contributions to my research, especially in the complex realm of data assimilation. Thank you both for the opportunity to learn from you and for being such influential figures in my academic life, empowering m(i)e to make a meaningful impact in the field of NWP.

A special thanks to the Waves to Weather (W2W) community, especially the members of B6, for their insightful discussions on data assimilation in the tropics. I am grateful to the Aeolus community, particularly Michael Rennie and Alexander Cress, for generously sharing their Observing System Experiment (OSE)s, engaging in valuable discussions, and providing guidance that had a profound impact on my work. I would also like to express my appreciation to Anne for our collaboration and data exchange. Additionally, I want to extend my gratitude to the Experimental Validation and Assimilation of Aeolus observations (EVAA) team for their fruitful exchanges, assistance, and engaging discussions on Aeolus. And last but not least, a big thank you to Benny for our collaborative efforts and countless meetings dedicated to unraveling the mysteries of Aeolus measurements among clouds and dust.

Thanks to the Joint Aeolus Tropical Atlantic Campaign (JATAC) community and Thorsten for organizing this successful international campaign in Cabo Verde. Special thanks to Azusa, Tanguy, and Cedric who willingly sacrificed their precious sleep to join me in the early morning ritual of launching radiosondes from the airport. Big thanks to Cyrille for the warm welcome into the Clouds-Atmospheric Dynamics–Dust Interactions in West Africa (CADDIWA) team, our fruitful scientific collaborations, navigating through the challenges of tropical disturbances, and the enjoyable beach bar sessions with the JATAC team amidst the palm trees and ocean breeze. My gratitude also goes to the German Aerospace Center (DLR) team for their assistance with radiosonde material transportation and their impressive handling of the Cabo Verde customs challenges. I would like to acknowledge the individuals involved in the radiosonde launches as part

of the Convective Processes Experiment-Aerosols and Wind campaign (CPEX-AW) campaign over Saint Croix and Puerto Rico.

I would also like to acknowledge my peers at IMK-TRO. Particularly I would also like to thank Hyunju and Athul, with whom I have embarked on this exciting journey full of challenging questions and memorable moments of confusion. I now look forward the day we can fulfill our master plan: starting a music band in Freiburg. I want to thank my office mates Raffi, Christoph, and Athul for their incredible talent in creating a working atmosphere that was...let's say, "unique." I also want to express my appreciation for their exceptional plant-care skills, as they miraculously managed to keep my plant alive during my absence. I would like to extend my gratitude to all those who have contributed to creating a wonderful atmosphere at the institute. Special thanks to individuals like Behrooz for adding to the enjoyable experiences in the bars.

I want to express my gratitude to my family for their support throughout my entire PhD journey. It is truly remarkable how the timing of my niece's birth aligned perfectly with the completion of my PhD, adding extra joy and celebration to our family. I am also grateful to my close friends in Freiburg with whom I have shared memorable times over the past years. A special thanks to my favorite Greek Malakas, Elpida and Vanessa, for countless unforgettable moments and their love for tiramisu and tomatoes. Sarah, your vibrant energy and introduction to accro yoga have been truly uplifting. Loukakos, my personal Bauhaus adviser. I extend my gratitude to Blume and Joanna for their delightful company and our shared love for Pferferminztee. And to Schen, my Taiwanese philosopher, thank you for the enlightening conversations. I would also like to thank Ipsa for our car-based friendship and our shared love for late-night McDrive runs, which we always end up regretting afterwards. Last but not least, Alejandro, your eternal Blick has left an indelible mark on me.

Merci Hugo, mon ami de tendre enfance, et à la toute-puissante quantique qui régit tout dans l'univers. Bien sûr, un grand merci à la Bourachos team, Hugo, Coco, Raph, Martin et Clément, j'espère sincèrement que nous pourrons bientôt nous retrouver à Berlin, pour visiter le zoo. Etienne, je tiens à te remercier pour tous tes précieux conseils et surtout pour ta maîtrise absolue des steaks. Merci à Baptiste, Louis et Erika, mes compagnons de longue date. Je dois enfin vous avouer un secret : c'est moi qui ai bu la bière.. je crois. Je tiens aussi à exprimer ma gratitude à Pierre-Yves et Martin, les hommes les plus classes du monde. Votre élégance, votre style impeccable et vos manières distinguées sont une source d'inspiration pour moi. Finalement, je tiens à exprimer ma gratitude à Charlou, copain d'enfance, à Paul qui se destine à devenir prêtre, et à Rémi le génie.

Bibliography

Abril-Gago, J., and Coauthors, 2022: Validation activities of aeolus wind products in the southeastern iberian peninsula. *Atmospheric Chemistry and Physics Discussions*, 1–32.

Agustí-Panareda, A., A. Beljaars, C. Cardinali, I. Genkova, and C. Thorncroft, 2010: Impacts of assimilating amma soundings on ecmwf analyses and forecasts. *Weather and Forecasting*, **25 (4)**, 1142–1160.

Alonso Lasheras, O., A. Sanz Diaz, and L. Lopez Cotin, 2005: The initial operations phase of the eumetsat's saf to support nowcasting (nwc saf) s. *ESA Special Publication*, **584**, 4.

Andersson, E., and Coauthors, 1998: The ecmwf implementation of three-dimensional variational assimilation (3d-var). iii: Experimental results. *Quarterly Journal of the Royal Meteorological Society*, **124 (550)**, 1831–1860.

ATBD, 2020: Aeolus level-2b algorithm theoretical basis document, ecmwf, available at: https://earth.esa.int/eogateway/documents/20142/37627/aeolus-l2b-algorithm-atbd.pdf. *Quarterly Journal of the Royal Meteorological Society: A journal of the atmospheric sciences, applied meteorology and physical oceanography.*

Baars, H., and Coauthors, 2020: Validation of aeolus wind products above the atlantic ocean. *Atmospheric Measurement Techniques*, **13 (11)**, 6007–6024.

Baker, W. E., and Coauthors, 2014: Lidar-measured wind profiles: The missing link in the global observing system. *Bulletin of the American Meteorological Society*, **95 (4)**, 543–564.

Barbosa, P. M., D. Stroppiana, J.-M. Grégoire, and J. M. Cardoso Pereira, 1999: An assessment of vegetation fire in africa (1981–1991): Burned areas, burned biomass, and atmospheric emissions. *Global Biogeochemical Cycles*, **13 (4)**, 933–950.

Bauer, P., A. Thorpe, and G. Brunet, 2015: The quiet revolution of numerical weather prediction. *Nature*, **525 (7567)**, 47–55.

Bayo Omotosho, J., 1985: The separate contributions of line squalls, thunderstorms and the monsoon to the total rainfall in nigeria. *Journal of climatology*, **5 (5)**, 543–552.

Bechtold, P., P. Bauer, J. Bidlot, C. Cardinali, L. Magnusson, F. Prates, and M. Rodwell, 2013: Uncertainty in tropical winds. *ECMWF Newsletter*, **(134)**, 33–37.

Becker, T., P. Bechtold, and I. Sandu, 2021: Characteristics of convective precipitation over tropical africa in storm-resolving global simulations. *Quarterly Journal of the Royal Meteorological Society*, **147 (741)**, 4388–4407.

Bedka, K. M., and Coauthors, 2021: Airborne lidar observations of wind, water vapor, and aerosol profiles during the nasa aeolus calibration and validation (cal/val) test flight campaign. *Atmospheric Measurement Techniques*, **14 (6)**, 4305–4334.

Belanger, J., M. Jelinek, and J. Curry, 2016: A climatology of easterly waves in the tropical western hemisphere. *Geoscience Data Journal*, **3 (2)**, 40–49.

Belova, E., S. Kirkwood, P. Voelger, S. Chatterjee, K. Satheesan, S. Hagelin, M. Lindskog, and H. Körnich, 2021: Validation of aeolus winds using ground-based radars in antarctica and in northern sweden. *Atmospheric Measurement Techniques*, **14 (8)**, 5415–5428.

Benedetti, A., and Coauthors, 2009: Aerosol analysis and forecast in the european centre for medium-range weather forecasts integrated forecast system: 2. data assimilation. *Journal of Geophysical Research: Atmospheres*, **114 (D13)**.

Benedict, J. J., E. D. Maloney, A. H. Sobel, D. M. Frierson, and L. J. Donner, 2013: Tropical intraseasonal variability in version 3 of the gfdl atmosphere model. *Journal of Climate*, **26 (2)**, 426–449.

Beranek, R., J. Bilbro, D. Fitzjarrald, W. Jones, V. Keller, and B. Perrine, 1989: Laser atmospheric wind sounder (laws). *Laser Applications in Meteorology and Earth and Atmospheric Remote Sensing*, SPIE, Vol. 1062, 234–248.

Betout, P., D. Burridge, and C. Werner, 1989: Aladin: Atmospheric laser doppler instrument. *Doppler lidar working group report, ES1A SP-1112. European Space Agency, Darmstadt, Germany.*

Bielli, S., H. Douville, and B. Pohl, 2010: Understanding the west african monsoon variability and its remote effects: an illustration of the grid point nudging methodology. *Climate Dynamics*, **35 (1)**, 159–174.

Blumen, W., 1972: Geostrophic adjustment. *Reviews of Geophysics*, **10 (2)**, 485–528.

Bonavita, M., L. Isaksen, and E. Hólm, 2012: On the use of eda background error variances in the ecmwf 4d-var. *Quarterly journal of the royal meteorological society*, **138 (667)**, 1540–1559.

Bormann, N., S. Saarinen, G. Kelly, and J.-N. Thépaut, 2003: The spatial structure of observation errors in atmospheric motion vectors from geostationary satellite data. *Monthly Weather Review*, **131 (4)**, 706–718.

Borne, M., P. Knippertz, M. Weissmann, A. Martin, M. Rennie, and A. Cress, 2023: Impact of aeolus wind lidar observations on the representation of the west african monsoon circulation in the ecmwf and dwd forecasting systems. *Quarterly Journal of the Royal Meteorological Society.*

Borne, M., P. Knippertz, M. Weissmann, B. Witschas, C. Flamant, R. Rios-Berrios, and P. Veals, 2024: Validation of aeolus l2b products over the tropical atlantic using radiosondes. *Atmospheric Measurement Techniques*, **17 (2)**, 561–581.

Bouttier, F., and G. Kelly, 2001: Observing-system experiments in the ecmwf 4d-var data assimilation system. *Quarterly Journal of the Royal Meteorological Society*, **127 (574)**, 1469–1488.

Brammer, A., and C. D. Thorncroft, 2015: Variability and evolution of african easterly wave structures and their relationship with tropical cyclogenesis over the eastern atlantic. *Monthly Weather Review*, **143 (12)**, 4975–4995.

Burpee, R. W., 1972: The origin and structure of easterly waves in the lower troposphere of north africa. *Journal of the Atmospheric Sciences*, **29 (1)**, 77–90.

Carter, T. S., and Coauthors, 2021: Investigating carbonaceous aerosol and its absorption properties from fires in the western united states (we-can) and southern africa (oracles and clarify). *Journal of Geophysical Research: Atmospheres*, **126 (15)**, e2021JD034 984.

Castanheira, J. M., and C. A. Marques, 2015: Convectively coupled equatorial-wave diagnosis using three-dimensional normal modes. *Quarterly Journal of the Royal Meteorological Society*, **141 (692)**, 2776–2792.

Chanin, M.-L., A. Garnier, A. Hauchecorne, and J. Porteneuve, 1989: A doppler lidar for measuring winds in the middle atmosphere. *Geophysical research letters*, **16 (11)**, 1273–1276.

Charney, J. G., and M. E. Stern, 1962: On the stability of internal baroclinic jets in a rotating atmosphere. *Journal of Atmospheric Sciences*, **19 (2)**, 159–172.

Chen, S., R. Cao, Y. Xie, Y. Zhang, W. Tan, H. Chen, P. Guo, and P. Zhao, 2021: Study of the seasonal variation in aeolus wind product performance over china using era5 and radiosonde data. *Atmospheric Chemistry and Physics*, **21 (15)**, 11 489–11 504.

Cheng, Y.-M., C. D. Thorncroft, and G. N. Kiladis, 2019: Two contrasting african easterly wave behaviors. *Journal of the Atmospheric Sciences*, **76 (6)**, 1753–1768.

Cook, K. H., 1999: Generation of the african easterly jet and its role in determining west african precipitation. *Journal of climate*, **12 (5)**, 1165–1184.

Courtier, P., J.-N. Thépaut, and A. Hollingsworth, 1994: A strategy for operational implementation of 4d-var, using an incremental approach. *Quarterly Journal of the Royal Meteorological Society*, **120 (519)**, 1367–1387.

Courtier, P., and Coauthors, 1998: The ecmwf implementation of three-dimensional variational assimilation (3d-var). i: Formulation. *Quarterly Journal of the Royal Meteorological Society*, **124 (550)**, 1783–1807.

Cress, A., and W. Wergen, 2001: Impact of profile observations on the german weather service's nwp system. *Meteorologische Zeitschrift*, **10 (2)**, 91–101.

Dabas, A., M. Denneulin, P. Flamant, C. Loth, A. Garnier, and A. Dolfi-Bouteyre, 2008: Correcting winds measured with a rayleigh doppler lidar from pressure and temperature effects. *Tellus A: Dynamic Meteorology and Oceanography*, **60 (2)**, 206–215.

de F. Forster, P. M., and K. P. Shine, 1997: Radiative forcing and temperature trends from stratospheric ozone changes. *Journal of Geophysical Research: Atmospheres*, **102 (D9)**, 10 841–10 855.

de Kloe, J., A. Stoffelen, D. Tan, E. Andersson, M. Rennie, A. Dabas, P. Poli, and D. Huber, 2020: Adm-aeolus level-2b/2c processor input/output data definitions interface control document. Tech. rep., AED-SD-ECMWF-L2B-037.

Derrien, M., B. Farki, L. Harang, H. LeGleau, A. Noyalet, D. Pochic, and A. Sairouni, 1993: Automatic cloud detection applied to noaa-11/avhrr imagery. *Remote Sensing of Environment*, **46 (3)**, 246–267.

Derrien, M., and H. Le Gléau, 2005: Msg/seviri cloud mask and type from safnwc. *International Journal of Remote Sensing*, **26 (21)**, 4707–4732.

Desroziers, G., L. Berre, B. Chapnik, and P. Poli, 2005: Diagnosis of observation, background and analysis-error statistics in observation space. *Quarterly Journal of the Royal Meteorological Society: A journal of the atmospheric sciences, applied meteorology and physical oceanography*, **131 (613)**, 3385–3396.

Dias, J., and G. N. Kiladis, 2014: Influence of the basic state zonal flow on convectively coupled equatorial waves. *Geophysical Research Letters*, **41 (19)**, 6904–6913.

Dirksen, R., M. Sommer, F. Immler, D. Hurst, R. Kivi, and H. Vömel, 2014: Reference quality upper-air measurements: Gruan data processing for the vaisala rs92 radiosonde. *Atmospheric Measurement Techniques*, **7 (12)**, 4463–4490.

Dolfi-Bouteyre, A., 2008: Correcting winds measured with a rayleigh doppler lidar from pressure and temperature effects.

Dunion, J. P., and C. S. Marron, 2008: A reexamination of the jordan mean tropical sounding based on awareness of the saharan air layer: Results from 2002. *Journal of Climate*, **21 (20)**, 5242–5253.

ESA, 1999: Atmospheric dynamics mission. European Space Agency Paris.

Ferrett, S., G.-Y. Yang, S. J. Woolnough, J. Methven, K. Hodges, and C. E. Holloway, 2020: Linking extreme precipitation in southeast asia to equatorial waves. *Quarterly Journal of the Royal Meteorological Society*, **146 (727)**, 665–684.

Fink, A., D. Vincent, and V. Ermert, 2006: Rainfall types in the west african sudanian zone during the summer monsoon 2002. *Monthly weather review*, **134 (8)**, 2143–2164.

Fink, A. H., and A. Reiner, 2003: Spatiotemporal variability of the relation between african easterly waves and west african squall lines in 1998 and 1999. *Journal of Geophysical Research: Atmospheres*, **108 (D11)**.

Fink, A. H., and Coauthors, 2011: Operational meteorology in west africa: observational networks, weather analysis and forecasting. *Atmospheric Science Letters*, **12 (1)**, 135–141.

Fisher, M., 2003: Background error covariance modelling. *Seminar on Recent Development in Data Assimilation for Atmosphere and Ocean*, Shinfield Park, Reading, 45–63.

Flemming, J., and Coauthors, 2015: Tropospheric chemistry in the integrated forecasting system of ecmwf. *Geoscientific model development*, **8 (4)**, 975–1003.

Flesia, C., and C. L. Korb, 1999: Theory of the double-edge molecular technique for doppler lidar wind measurement. *Applied Optics*, **38 (3)**, 432–440.

Folger, K., and M. Weissmann, 2014: Height correction of atmospheric motion vectors using satellite lidar observations from calipso. *Journal of Applied Meteorology and Climatology*, **53 (7)**, 1809–1819.

Forster, P. M. d. F., and K. Shine, 2002: Assessing the climate impact of trends in stratospheric water vapor. *Geophysical research letters*, **29 (6)**, 10–1.

Gaetani, M., B. Pohl, H. Douville, and B. Fontaine, 2011: West african monsoon influence on the summer euro-atlantic circulation. *Geophysical Research Letters*, **38 (9)**.

Garnier, A., and M. Chanin, 1992: Description of a doppler rayleigh lidar for measuring winds in the middle atmosphere. *Applied Physics B*, **55 (1)**, 35–40.

Garrett, K., H. Liu, K. Ide, R. N. Hoffman, and K. E. Lukens, 2022: Optimization and impact assessment of aeolus hlos wind assimilation in noaa's global forecast system. *Quarterly Journal of the Royal Meteorological Society*, **148 (747)**, 2703–2716.

Gaspari, G., and S. E. Cohn, 1999: Construction of correlation functions in two and three dimensions. *Quarterly Journal of the Royal Meteorological Society*, **125 (554)**, 723–757.

Gehne, M., and R. Kleeman, 2012: Spectral analysis of tropical atmospheric dynamical variables using a linear shallow-water modal decomposition. *Journal of the atmospheric sciences*, **69 (7)**, 2300–2316.

George, G., G. Halloran, S. Kumar, S. I. Rani, M. Bushair, B. P. Jangid, J. P. George, and A. Maycock, 2021: Impact of aeolus horizontal line of sight wind observations in a global nwp system. *Atmospheric Research*, **261**, 105 742.

George, J. E., and W. M. Gray, 1976: Tropical cyclone motion and surrounding parameter relationships. *Journal of Applied Meteorology (1962-1982)*, 1252–1264.

Gill, A. E., 1980: Some simple solutions for heat-induced tropical circulation. *Quarterly Journal of the Royal Meteorological Society*, **106 (449)**, 447–462.

Gneiting, T., A. E. Raftery, A. H. Westveld, and T. Goldman, 2005: Calibrated probabilistic forecasting using ensemble model output statistics and minimum crps estimation. *Monthly Weather Review*, **133 (5)**, 1098–1118.

Guo, J., and Coauthors, 2021: First comparison of wind observations from esa's satellite mission aeolus and ground-based radar wind profiler network of china. *Atmospheric Chemistry and Physics*, **21 (4)**, 2945–2958.

Haiden, T., M. Janousek, F. Vitart, Z. Ben-Bouallegue, L. Ferranti, C. Prates, and D. Richardson, 2021: Evaluation of ecmwf forecasts, including the 2020 upgrade. **(880)**, doi:10.21957/6njp8byz4.

Harnisch, F., M. Weissmann, C. Cardinali, and M. Wirth, 2011: Experimental assimilation of dial water vapour observations in the ecmwf global model. *Quarterly Journal of the Royal Meteorological Society*, **137 (659)**, 1532–1546, doi:https://doi.org/10.1002/qj.851, https://rmets.onlinelibrary.wiley.com/doi/pdf/10.1002/qj.851.

Haslett, S. L., and Coauthors, 2019: Remote biomass burning dominates southern west african air pollution during the monsoon. *Atmospheric Chemistry and Physics*, **19 (24)**, 15 217–15 234.

Hersbach, H., and Coauthors, 2020: The era5 global reanalysis. *Quarterly Journal of the Royal Meteorological Society*, **146 (730)**, 1999–2049.

Holland, G. J., 1983: Angular momentum transports in tropical cyclones. *Quarterly Journal of the Royal Meteorological Society*, **109 (459)**, 187–209.

Hollingsworth, A., D. Shaw, P. Lönnberg, L. Illari, K. Arpe, and A. Simmons, 1986: Monitoring of observation and analysis quality by a data assimilation system. *Monthly Weather Review*, **114 (5)**, 861–879.

Horányi, A., C. Cardinali, M. Rennie, and L. Isaksen, 2015: The assimilation of horizontal line-of-sight wind information into the ecmwf data assimilation and forecasting system. part ii: The impact of degraded wind observations. *Quarterly Journal of the Royal Meteorological Society*, **141 (689)**, 1233–1243.

Huffman, G. J., D. T. Bolvin, D. Braithwaite, K. Hsu, R. Joyce, P. Xie, and S.-H. Yoo, 2015: Nasa global precipitation measurement (gpm) integrated multi-satellite retrievals for gpm (imerg). *Algorithm Theoretical Basis Document (ATBD) Version*, **4**, 26.

Huijnen, V., and Coauthors, 2019: Quantifying uncertainties due to chemistry modelling–evaluation of tropospheric composition simulations in the cams model (cycle 43r1). *Geoscientific Model Development*, **12 (4)**, 1725–1752.

Hung, M.-P., J.-L. Lin, W. Wang, D. Kim, T. Shinoda, and S. J. Weaver, 2013: Mjo and convectively coupled equatorial waves simulated by cmip5 climate models. *Journal of Climate*, **26 (17)**, 6185–6214.

Hunt, B. R., E. J. Kostelich, and I. Szunyogh, 2007: Efficient data assimilation for spatiotemporal chaos: A local ensemble transform kalman filter. *Physica D: Nonlinear Phenomena*, **230 (1-2)**, 112–126.

Iglewicz, B., and D. C. Hoaglin, 1993: *How to detect and handle outliers*, Vol. 16. Asq Press.

Ingmann, P., and A. Straume, 2016: Adm-aeolus mission requirements document. *Centre ESRaT*.

Inness, A., and Coauthors, 2019: The cams reanalysis of atmospheric composition. *Atmospheric Chemistry and Physics*, **19 (6)**, 3515–3556.

Iwai, H., M. Aoki, M. Oshiro, and S. Ishii, 2021: Validation of aeolus level 2b wind products using wind profilers, ground-based doppler wind lidars, and radiosondes in japan. *Atmospheric Measurement Techniques*, **14 (11)**, 7255–7275.

Janiga, M. A., C. J. Schreck III, J. A. Ridout, M. Flatau, N. P. Barton, E. J. Metzger, and C. A. Reynolds, 2018: Subseasonal forecasts of convectively coupled equatorial waves and the mjo: Activity and predictive skill. *Monthly Weather Review*, **146 (8)**, 2337–2360.

Janiga, M. A., and C. D. Thorncroft, 2016: The influence of african easterly waves on convection over tropical africa and the east atlantic. *Monthly Weather Review*, **144 (1)**, 171–192.

Jarraud, M., 2008: Guide to meteorological instruments and methods of observation (wmo-no. 8). *World Meteorological Organisation: Geneva, Switzerland*, **29**.

Johnson, R. H., T. M. Rickenbach, S. A. Rutledge, P. E. Ciesielski, and W. H. Schubert, 1999: Trimodal characteristics of tropical convection. *Journal of climate*, **12 (8)**, 2397–2418.

Judt, F., 2018: Insights into atmospheric predictability through global convection-permitting model simulations. *Journal of the Atmospheric Sciences*, **75 (5)**, 1477–1497.

Judt, F., 2020: Atmospheric predictability of the tropics, middle latitudes, and polar regions explored through global storm-resolving simulations. *Journal of the Atmospheric Sciences*, **77 (1)**, 257–276.

Jung, H., and P. Knippertz, 2023: Link between the time-space behavior of rainfall and 3d dynamical structures of equatorial waves in global convection-permitting simulations. *Geophysical Research Letters*, **50 (2)**, e2022GL100 973.

Kalapureddy, M., M. Lothon, B. Campistron, F. Lohou, and F. Saïd, 2010: Wind profiler analysis of the african easterly jet in relation with the boundary layer and the saharan heat-low. *Quarterly Journal of the Royal Meteorological Society*, **136 (S1)**, 77–91.

Kalthoff, N., and Coauthors, 2018: An overview of the diurnal cycle of the atmospheric boundary layer during the west african monsoon season: results from the 2016 observational campaign. *Atmospheric Chemistry and Physics*, **18 (4)**, 2913–2928.

Kamga, A. F., S. Fongang, and A. Viltard, 2000: Systematic errors of the ecmwf operational model over tropical africa. *Monthly Weather Review*, **128 (6)**, 1949–1959.

Kamsu-Tamo, P., S. Janicot, D. Monkam, and A. Lenouo, 2014: Convection activity over the guinean coast and central africa during northern spring from synoptic to intra-seasonal timescales. *Climate dynamics*, **43 (12)**, 3377–3401.

Kelly, G., T. McNally, J. Thépaut, and M. Szyndel, 2004: Oses of all main data types in the ecmwf operation system. *Proc. Third WMO Workshop on the Impact of Various Observing Systems on Numerical Weather Prediction*, 63–94.

Kikuchi, K., G. N. Kiladis, J. Dias, and T. Nasuno, 2018: Convectively coupled equatorial waves within the mjo during cindy/dynamo: Slow kelvin waves as building blocks. *Climate Dynamics*, **50**, 4211–4230.

Kiladis, G. N., M. C. Wheeler, P. T. Haertel, K. H. Straub, and P. E. Roundy, 2009: Convectively coupled equatorial waves. *Reviews of Geophysics*, **47 (2)**.

Knippertz, P., A. H. Fink, R. Schuster, J. Trentmann, J. M. Schrage, and C. Yorke, 2011: Ultra-low clouds over the southern west african monsoon region. *Geophysical research letters*, **38 (21)**.

Knippertz, P., and Coauthors, 2017: A meteorological and chemical overview of the dacciwa field campaign in west africa in june–july 2016. *Atmospheric Chemistry and Physics*, **17 (17)**, 10 893–10 918.

Knippertz, P., and Coauthors, 2022: The intricacies of identifying equatorial waves. *Quarterly Journal of the Royal Meteorological Society*, **148 (747)**, 2814–2852.

Kovacic, D. A., M. B. David, L. E. Gentry, K. M. Starks, and R. A. Cooke, 2000: Effectiveness of constructed wetlands in reducing nitrogen and phosphorus export from agricultural tile drainage. Tech. rep., Wiley Online Library.

Krisch, I., and Coauthors, 2020: Data quality of aeolus wind measurements. *Geophysical Research Abstracts*.

Krishnamurthy, P., K. Lewis, and R. Choularton, 2014: A methodological framework for rapidly assessing the impacts of climate risk on national-level food security through a vulnerability index. *Global Environmental Change*, **25**, 121–132.

Krishnamurti, T., and C. Kishtawal, 2000: A pronounced continental-scale diurnal mode of the asian summer monsoon. *Monthly weather review*, **128 (2)**, 462–473.

Laroche, S., and J. St-James, 2022: Impact of the aeolus level-2b horizontal line-of-sight winds in the environment and climate change canada global forecast system. *Quarterly Journal of the Royal Meteorological Society*, **148 (745)**, 2047–2062.

Le Dimet, F.-X., and O. Talagrand, 1986: Variational algorithms for analysis and assimilation of meteorological observations: theoretical aspects. *Tellus A: Dynamic Meteorology and Oceanography*, **38 (2)**, 97–110.

Lélé, M. I., and L. M. Leslie, 2016: Intraseasonal variability of low-level moisture transport over west africa. *Climate Dynamics*, **47 (11)**, 3575–3591.

Lemburg, A., J. Bader, and M. Claussen, 2019: Sahel rainfall–tropical easterly jet relationship on synoptic to intraseasonal time scales. *Monthly Weather Review*, **147 (5)**, 1733–1752.

Levin, E., and Coauthors, 2010: Biomass burning smoke aerosol properties measured during fire laboratory at missoula experiments (flame). *Journal of Geophysical Research: Atmospheres*, **115 (D18)**.

Li, Y., and S. N. Stechmann, 2020: Predictability of tropical rainfall and waves: Estimates from observational data. *Quarterly Journal of the Royal Meteorological Society*, **146 (729)**, 1668–1684.

Lilly, D. K., 1972: Numerical simulation studies of two-dimensional turbulence: I. models of statistically steady turbulence. *Geophysical Fluid Dynamics*, **3 (4)**, 289–319.

Lin, J.-L., and Coauthors, 2006: Tropical intraseasonal variability in 14 ipcc ar4 climate models. part i: Convective signals. *Journal of climate*, **19 (12)**, 2665–2690.

London Economics Space Team, 2022: Aeolus value of information study. https://londoneconomics.co.uk/wp-content/uploads/2022/08/LE-ESA-FR-Final-Report-Aeolus-FINALS2C01072022.pdf.

Lorenc, A., R. Graham, and I. Dharssi, 1992: *Preparation for the use of Doppler wind lidar information in meteorological data assimilation systems.* Great Britain, Meteorological Office.

Lorenz, E. N., 1969: The predictability of a flow which possesses many scales of motion. *Tellus*, **21 (3)**, 289–307.

Lux, O., C. Lemmerz, F. Weiler, U. Marksteiner, B. Witschas, S. Rahm, A. Geiß, and O. Reitebuch, 2020: Intercomparison of wind observations from the european space agency's aeolus satellite mission and the aladin airborne demonstrator. *Atmospheric Measurement Techniques*, **13 (4)**, 2075–2097.

Lux, O., C. Lemmerz, F. Weiler, U. Marksteiner, B. Witschas, S. Rahm, A. Schäfler, and O. Reitebuch, 2018: Airborne wind lidar observations over the north atlantic in 2016 for the pre-launch validation of the satellite mission aeolus. *Atmospheric Measurement Techniques*, **11 (6)**, 3297–3322.

Lux, O., and Coauthors, 2022a: Quality control and error assessment of the aeolus l2b wind results from the joint aeolus tropical atlantic campaign. *Atmospheric Measurement Techniques*, **15 (21)**, 6467–6488.

Lux, O., and Coauthors, 2022b: Retrieval improvements for the aladin airborne demonstrator in support of the aeolus wind product validation. *Atmospheric Measurement Techniques*, **15 (5)**, 1303–1331.

Madden, R. A., and P. R. Julian, 1971: Detection of a 40–50 day oscillation in the zonal wind in the tropical pacific. *Journal of Atmospheric Sciences*, **28 (5)**, 702–708.

Magnusson, L., 2017: Diagnostic methods for understanding the origin of forecast errors. *Quarterly Journal of the Royal Meteorological Society*, **143 (706)**, 2129–2142.

Maloney, E. D., and D. L. Hartmann, 2001: The sensitivity of intraseasonal variability in the ncar ccm3 to changes in convective parameterization. *Journal of Climate*, **14 (9)**, 2015–2034.

Mapes, B., S. Tulich, T. Nasuno, and M. Satoh, 2008: Predictability aspects of global aqua-planet simulations with explicit convection. . *2* , **86**, 175–185.

Mapes, B. E., and R. A. Houze Jr, 1993: Cloud clusters and superclusters over the oceanic warm pool. *Monthly Weather Review*, **121 (5)**, 1398–1416.

Marksteiner, U., C. Lemmerz, O. Lux, S. Rahm, A. Schäfler, B. Witschas, and O. Reitebuch, 2018: Calibrations and wind observations of an airborne direct-detection wind lidar supporting esa's aeolus mission. *Remote Sensing*, **10 (12)**, 2056.

Marseille, G., and A. Stoffelen, 2003: Simulation of wind profiles from a space-borne doppler wind lidar. *Quarterly Journal of the Royal Meteorological Society: A journal of the atmospheric sciences, applied meteorology and physical oceanography*, **129 (594)**, 3079–3098.

Marseille, G.-J., A. Stoffelen, and J. Barkmeijer, 2008: Impact assessment of prospective spaceborne doppler wind lidar observation scenarios. *Tellus A: Dynamic Meteorology and Oceanography*, **60 (2)**, 234–248.

Martin, A., M. Weissmann, and A. Cress, 2023: Investigation of links between dynamical scenarios and particularly high impact of aeolus on numerical weather prediction (nwp) forecasts. *Weather and Climate Dynamics*, **4 (1)**, 249–264.

Martin, A., M. Weissmann, O. Reitebuch, M. Rennie, A. Geiß, and A. Cress, 2021: Validation of aeolus winds using radiosonde observations and numerical weather prediction model equivalents. *Atmospheric Measurement Techniques*, **14 (3)**, 2167–2183.

Martin, C., and I. Suhr, 2021: Ncar/eol atmospheric sounding processing environment (aspen) software, version 3.4. 3.

Masutani, M., and Coauthors, 2010: Observing system simulation experiments at the national centers for environmental prediction. *Journal of Geophysical Research: Atmospheres*, **115 (D7)**.

Mathon, V., H. Laurent, and T. Lebel, 2002: Mesoscale convective system rainfall in the sahel. *Journal of applied meteorology*, **41 (11)**, 1081–1092.

Matsuno, T., 1966: Quasi-geostrophic motions in the equatorial area. *Journal of the Meteorological Society of Japan. Ser. II*, **44 (1)**, 25–43.

McKay, J. A., 2002: Assessment of a multibeam fizeau wedge interferometer for doppler wind lidar. *Applied optics*, **41 (9)**, 1760–1767.

Miyoshi, T., and S. Yamane, 2007: Local ensemble transform kalman filtering with an agcm at a t159/l48 resolution. *Monthly Weather Review*, **135 (11)**, 3841–3861.

Mohan, T., and T. Rao, 2016: Differences in the mean wind and its diurnal variation between wet and dry spells of the monsoon over southeast india. *Journal of Geophysical Research: Atmospheres*, **121 (12)**, 6993–7006.

Mohr, K. I., and C. D. Thorncroft, 2006: Intense convective systems in west africa and their relationship to the african easterly jet. *Quarterly Journal of the Royal*

Meteorological Society: A journal of the atmospheric sciences, applied meteorology and physical oceanography, **132 (614)**, 163–176.

Morcrette, J.-J., and Coauthors, 2009: Aerosol analysis and forecast in the european centre for medium-range weather forecasts integrated forecast system: Forward modeling. *Journal of Geophysical Research: Atmospheres*, **114 (D6)**.

Morss, R. E., C. Snyder, and R. Rotunno, 2009: Spectra, spatial scales, and predictability in a quasigeostrophic model. *Journal of the atmospheric sciences*, **66 (10)**, 3115–3130.

Naderi, F. M., M. H. Freilich, and D. Long, 1991: Spaceborne radar measurement of wind velocity over the ocean-an overview of the nscat scatterometer system. *Proceedings of the IEEE*, **79 (6)**, 850–866.

Nelder, J. A., and R. Mead, 1965: A simplex method for function minimization. *The computer journal*, **7 (4)**, 308–313.

Nicholson, S. E., 2009: A revised picture of the structure of the "monsoon" and land itcz over west africa. *Climate Dynamics*, **32 (7)**, 1155–1171.

Nicholson, S. E., and J. P. Grist, 2003: The seasonal evolution of the atmospheric circulation over west africa and equatorial africa. *Journal of climate*, **16 (7)**, 1013–1030.

Nychka, D., and J. L. Anderson, 2010: Data assimilation. *Handbook of spatial statistics*, 477–492.

Palmer, T., A. Döring, and G. Seregin, 2014: The real butterfly effect. *Nonlinearity*, **27 (9)**, R123.

Pante, G., and P. Knippertz, 2019: Resolving sahelian thunderstorms improves midlatitude weather forecasts. *Nature communications*, **10 (1)**, 1–9.

Park, Y.-Y., R. Buizza, and M. Leutbecher, 2008: Tigge: Preliminary results on comparing and combining ensembles. *Quarterly Journal of the Royal Meteorological Society: A journal of the atmospheric sciences, applied meteorology and physical oceanography*, **134 (637)**, 2029–2050.

Parker, D., and Coauthors, 2005a: The diurnal cycle of the west african monsoon circulation. *Quarterly Journal of the Royal Meteorological Society: A journal of the atmospheric sciences, applied meteorology and physical oceanography*, **131 (611)**, 2839–2860.

Parker, D. J., C. D. Thorncroft, R. R. Burton, and A. Diongue-Niang, 2005b: Analysis of the african easterly jet, using aircraft observations from the jet2000 experiment. *Quarterly Journal of the Royal Meteorological Society: A journal of the atmospheric sciences, applied meteorology and physical oceanography*, **131 (608)**, 1461–1482.

Parker, D. J., and Coauthors, 2008: The amma radiosonde program and its implications for the future of atmospheric monitoring over africa. *Bulletin of the American Meteorological Society*, **89 (7)**, 1015–1028.

Parrish, D. F., and J. C. Derber, 1992: The national meteorological center's spectral statistical-interpolation analysis system. *Monthly Weather Review*, **120 (8)**, 1747–1763.

Poan, D. E., J.-P. Lafore, R. Roehrig, and F. Couvreux, 2015: Internal processes within the african easterly wave system. *Quarterly Journal of the Royal Meteorological Society*, **141 (689)**, 1121–1136.

Portabella, M., and A. Stoffelen, 2009: On scatterometer ocean stress. *Journal of Atmospheric and Oceanic Technology*, **26 (2)**, 368–382.

Pourret, V., M. Šavli, J.-F. Mahfouf, D. Raspaud, A. Doerenbecher, H. Bénichou, and C. Payan, 2022: Operational assimilation of aeolus winds in the météo-france global nwp model arpege. *Quarterly Journal of the Royal Meteorological Society*, **148 (747)**, 2652–2671.

Pu, Z., L. Zhang, and G. D. Emmitt, 2010: Impact of airborne doppler wind lidar profiles on numerical simulations of a tropical cyclone. *Geophysical research letters*, **37 (5)**.

Raicich, F., N. Pinardi, and A. Navarra, 2003: Teleconnections between indian monsoon and sahel rainfall and the mediterranean. *International Journal of Climatology: A Journal of the Royal Meteorological Society*, **23 (2)**, 173–186.

Ratynski, M., S. Khaykin, A. Hauchecorne, R. Wing, J.-P. Cammas, Y. Hello, and P. Keckhut, 2022: Validation of aeolus wind profiles using ground-based lidar and radiosonde observations at la réunion island and the observatoire de haute provence. *EGUsphere*, 1–33.

Reid, J., R. Koppmann, T. Eck, and D. Eleuterio, 2005: A review of biomass burning emissions part ii: intensive physical properties of biomass burning particles. *Atmospheric Chemistry and Physics*, **5 (3)**, 799–825.

Reitebuch, O., 2012: The spaceborne wind lidar mission adm-aeolus. *Atmospheric Physics*, Springer, 815–827.

Reitebuch, O., C. Lemmerz, E. Nagel, U. Paffrath, Y. Durand, M. Endemann, F. Fabre, and M. Chaloupy, 2009: The airborne demonstrator for the direct-detection doppler wind lidar aladin on adm-aeolus. part i: Instrument design and comparison to satellite instrument. *Journal of Atmospheric and Oceanic Technology*, **26 (12)**, 2501–2515.

Reitebuch, O., U. Paffrath, D. Huber, and I. Leike, 2006: Algorithm theoretical baseline document atbd: Adm-aeolus level 1b products. Tech. rep., AE-RP-DLR-L1B-001.

Reitebuch, O., and Coauthors, 2018: Aeolus end-to-end simulator and wind retrieval algorithms up to level 1b. *EPJ Web of Conferences*, EDP Sciences, Vol. 176, 02010.

Reitebuch, O., and Coauthors, 2019: Initial assessment of the performance of the first wind lidar in space on aeolus. *EPJ Web of Conferences*, Vol. 237, 1–4.

Reitebuch, O., and Coauthors, 2020: Assessment of the aeolus performance and bias correction-results from the aeolus disc.

Rémy, S., and Coauthors, 2019: Description and evaluation of the tropospheric aerosol scheme in the european centre for medium-range weather forecasts (ecmwf) integrated forecasting system (ifs-aer, cycle 45r1). *Geoscientific Model Development*, **12 (11)**, 4627–4659.

Rennie, A. M. H., Healy, 2022: Aeolus positive impact on forecasts with the second reprocessed dataset. URL https://www.ecmwf.int/en/newsletter/173/earth-system-science/aeolus-positive-impact-forecasts-second-reprocessed-dataset.

Rennie, M., and L. Isaksen, 2020: The nwp impact of aeolus level-2b winds at ecmwf. Tech. rep., ECMWF Technical Memo 864, Shinfield Park, Reading, UK, https://doi.org/10 . . . .

Rennie, M., D. Tan, E. Andersson, P. Poli, A. Dabas, J. De Kloe, G.-J. Marseille, and A. Stoffelen, 2020: Aeolus level-2b algorithm theoretical basis document-mathematical description of the aeolus level-2b processor.

Rennie, M. P., L. Isaksen, F. Weiler, J. de Kloe, T. Kanitz, and O. Reitebuch, 2021: The impact of aeolus wind retrievals on ecmwf global weather forecasts. *Quarterly Journal of the Royal Meteorological Society*, **147 (740)**, 3555–3586.

Reynolds, C., K. D. Williams, and A. Zadra, 2020: Wgne systematic error survey results summary. *100th American Meteorological Society Annual Meeting*, AMS.

Rios-Berrios, R., and Coauthors, 2023: Observing the diurnal cycle of coastal rainfall over western puerto rico in collaboration with university of puerto rico students. *Bulletin of the American Meteorological Society*, **104 (1)**, E305–E324.

Rotunno, R., and C. Snyder, 2008: A generalization of lorenz's model for the predictability of flows with many scales of motion. *Journal of the Atmospheric Sciences*, **65 (3)**, 1063–1076.

Roundy, P. E., 2018: A wave-number frequency wavelet analysis of convectively coupled equatorial waves and the mjo over the indian ocean. *Quarterly Journal of the Royal Meteorological Society*, **144 (711)**, 333–343.

Sandbhor, S., and N. Chaphalkar, 2019: Impact of outlier detection on neural networks based property value prediction. *Information systems design and intelligent applications*, Springer, 481–495.

Sasaki, Y., 1955: A fundamental study of the numerical prediction based on the variational principle. *Journal of the Meteorological Society of Japan. Ser. II*, **33 (6)**, 262–275.

Sasaki, Y., 1958: An objective analysis based on the variational method. *Journal of the Meteorological Society of Japan. Ser. II*, **36 (3)**, 77–88.

Saunders, R. W., and K. T. Kriebel, 1988: An improved method for detecting clear sky and cloudy radiances from avhrr data. *International Journal of Remote Sensing*, **9 (1)**, 123–150.

Schillinger, M., D. Morancais, F. Fabre, and A. J. Culoma, 2003: Aladin: the lidar instrument for the aeolus mission. *Sensors, Systems, and Next-Generation Satellites VI*, SPIE, Vol. 4881, 40–51.

Schindler, M., M. Weissmann, A. Schäfler, and G. Radnoti, 2020: The impact of dropsonde and extra radiosonde observations during nawdex in autumn 2016. *Monthly Weather Review*, **148 (2)**, 809 – 824, doi:10.1175/MWR-D-19-0126.1.

Schlueter, A., A. H. Fink, and P. Knippertz, 2019a: A systematic comparison of tropical waves over northern africa. part ii: Dynamics and thermodynamics. *Journal of Climate*, **32 (9)**, 2605–2625.

Schlueter, A., A. H. Fink, P. Knippertz, and P. Vogel, 2019b: A systematic comparison of tropical waves over northern africa. part i: Influence on rainfall. *Journal of Climate*, **32 (5)**, 1501–1523.

Schraff, C., H. Reich, A. Rhodin, A. Schomburg, K. Stephan, A. Periáñez, and R. Potthast, 2016: Kilometre-scale ensemble data assimilation for the cosmo model (kenda). *Quarterly Journal of the Royal Meteorological Society*, **142 (696)**, 1453–1472.

Schrage, J. M., and A. H. Fink, 2012: Nocturnal continental low-level stratus over tropical west africa: Observations and possible mechanisms controlling its onset. *Monthly Weather Review*, **140 (6)**, 1794–1809.

Selz, T., 2019: Estimating the intrinsic limit of predictability using a stochastic convection scheme. *Journal of the Atmospheric Sciences*, **76 (3)**, 757–765.

Sénégas, J., H. Wackernagel, W. Rosenthal, and T. Wolf, 2001: Error covariance modeling in sequential data assimilation. *Stochastic environmental research and risk assessment*, **15**, 65–86.

Senior, C. A., and Coauthors, 2021: Convection-permitting regional climate change simulations for understanding future climate and informing decision-making in africa. *Bulletin of the American Meteorological Society*, **102 (6)**, E1206–E1223.

Song, H.-J., J. Kwun, I.-H. Kwon, J.-H. Ha, J.-H. Kang, S. Lee, H.-W. Chun, and S. Lim, 2017: The impact of the nonlinear balance equation on a 3d-var cycle during an australian-winter month as compared with the regressed wind–mass balance. *Quarterly Journal of the Royal Meteorological Society*, **143 (705)**, 2036–2049.

Song, X., and G. J. Zhang, 2018: The roles of convection parameterization in the formation of double itcz syndrome in the ncar cesm: I. atmospheric processes. *Journal of Advances in Modeling Earth Systems*, **10 (3)**, 842–866.

Stoffelen, A., and G.-J. Marseille, 1998: Study on the utility of a doppler wind lidar for numerical weather prediction and climate. *CONTRACTOR REPORT-EUROPEAN SPACE AGENCY CR P.*

Stoffelen, A., G.-J. Marseille, F. Bouttier, D. Vasiljevic, S. De Haan, and C. Cardinali, 2006: Adm-aeolus doppler wind lidar observing system simulation experiment. *Quarterly Journal of the Royal Meteorological Society: A journal of the atmospheric sciences, applied meteorology and physical oceanography*, **132 (619)**, 1927–1947.

Stoffelen, A., and Coauthors, 2005: The atmospheric dynamics mission for global wind field measurement. *Bulletin of the American Meteorological Society*, **86 (1)**, 73–88.

Stowe, L. L., P. A. Davis, and E. P. McClain, 1999: Scientific basis and initial evaluation of the clavr-1 global clear/cloud classification algorithm for the advanced very high resolution radiometer. *Journal of atmospheric and oceanic technology*, **16 (6)**, 656–681.

Straub, K. H., P. T. Haertel, and G. N. Kiladis, 2010: An analysis of convectively coupled kelvin waves in 20 wcrp cmip3 global coupled climate models. *Journal of climate*, **23 (11)**, 3031–3056.

Straume, A.-G., and Coauthors, 2020: Esa's space-based doppler wind lidar mission aeolus–first wind and aerosol product assessment results. *EPJ Web of Conferences*, EDP Sciences, Vol. 237, 01007.

Sun, Y. Q., and F. Zhang, 2016: Intrinsic versus practical limits of atmospheric predictability and the significance of the butterfly effect. *Journal of the Atmospheric Sciences*, **73 (3)**, 1419–1438.

Takayabu, Y. N., 1994: Large-scale cloud disturbances associated with equatorial waves part i: Spectral features of the cloud disturbances. *Journal of the Meteorological Society of Japan. Ser. II*, **72 (3)**, 433–449.

Takayabu, Y. N., and T. Nitta, 1993: 3-5 day-period disturbances coupled with convection over the tropical pacific ocean. *Journal of the Meteorological Society of Japan. Ser. II*, **71 (2)**, 221–246.

Tan, D. G., E. Andersson, M. Fisher, and L. Isaksen, 2007: Observing-system impact assessment using a data assimilation ensemble technique: application to the adm–aeolus wind profiling mission. *Quarterly Journal of the Royal Meteorological Society: A journal of the atmospheric sciences, applied meteorology and physical oceanography*, **133 (623)**, 381–390.

Tan, D. G., and Coauthors, 2008: The adm-aeolus wind retrieval algorithms. *Tellus A: Dynamic Meteorology and Oceanography*, **60 (2)**, 191–205.

Thorncroft, C., and M. Blackburn, 1999: Maintenance of the african easterly jet. *Quarterly Journal of the Royal Meteorological Society*, **125 (555)**, 763–786.

Tompkins, A., C. Cardinali, J.-J. Morcrette, and M. Rodwell, 2005a: Influence of aerosol climatology on forecasts of the african easterly jet. *Geophysical research letters*, **32 (10)**.

Tompkins, A., A. Diongue-Niang, D. Parker, and C. Thorncroft, 2005b: The african easterly jet in the ecmwf integrated forecast system: 4d-var analysis. *Quarterly Journal of the Royal Meteorological Society: A journal of the atmospheric sciences, applied meteorology and physical oceanography*, **131 (611)**, 2861–2885.

Tripathy, S. S., R. K. Saxena, and P. K. Gupta, 2013: Comparison of statistical methods for outlier detection in proficiency testing data on analysis of lead in aqueous solution. *American Journal of Theoretical and Applied Statistics*, **2 (6)**, 233–242.

van der Linden, R., P. Knippertz, A. H. Fink, B. Ingleby, M. Maranan, and A. Benedetti, 2020: The influence of dacciwa radiosonde data on the quality of ecmwf analyses and forecasts over southern west africa. *Quarterly Journal of the Royal Meteorological Society*, **146 (729)**, 1719–1739.

Velden, C. S., and K. M. Bedka, 2009: Identifying the uncertainty in determining satellite-derived atmospheric motion vector height attribution. *Journal of Applied Meteorology and Climatology*, **48 (3)**, 450–463.

Vogel, P., P. Knippertz, A. H. Fink, A. Schlueter, and T. Gneiting, 2018: Skill of global raw and postprocessed ensemble predictions of rainfall over northern tropical africa. *Weather and Forecasting*, **33 (2)**, 369–388.

Vogel, P., P. Knippertz, T. Gneiting, A. H. Fink, M. Klar, and A. Schlueter, 2021: Statistical forecasts for the occurrence of precipitation outperform global models over northern tropical africa. *Geophysical Research Letters*, **48 (3)**, e2020GL091 022.

Walz, E.-M., M. Maranan, R. van der Linden, A. H. Fink, and P. Knippertz, 2021: An imerg-based optimal extended probabilistic climatology (epc) as a benchmark ensemble forecast for precipitation in the tropics and subtropics. *Weather and Forecasting*, **36 (4)**, 1561–1573.

Wang, W., and M. E. Schlesinger, 1999: The dependence on convection parameterization of the tropical intraseasonal oscillation simulated by the uiuc 11-layer atmospheric gcm. *Journal of Climate*, **12 (5)**, 1423–1457.

Weiler, F., M. Rennie, T. Kanitz, L. Isaksen, E. Checa, J. de Kloe, N. Okunde, and O. Reitebuch, 2021a: Correction of wind bias for the lidar on board aeolus using telescope temperatures. *Atmospheric Measurement Techniques*, **14 (11)**, 7167–7185.

Weiler, F., and Coauthors, 2020: Characterization of dark current signal measurements of the accds used on-board the aeolus satellite. *Atmospheric Measurement Techniques Discussions*, 1–39.

Weiler, F., and Coauthors, 2021b: Characterization of dark current signal measurements of the accds used on board the aeolus satellite. *Atmospheric Measurement Techniques*, **14 (7)**, 5153–5177.

Weissmann, M., R. Busen, A. Dörnbrack, S. Rahm, and O. Reitebuch, 2005a: Targeted observations with an airborne wind lidar. *Journal of Atmospheric and Oceanic Technology*, **22 (11)**, 1706–1719.

Weissmann, M., R. Busen, A. Dörnbrack, S. Rahm, and O. Reitebuch, 2005b: Targeted observations with an airborne wind lidar. *Journal of Atmospheric and Oceanic Technology*, **22 (11)**, 1706 – 1719, doi:10.1175/JTECH1801.1.

Weissmann, M., and C. Cardinali, 2007: Impact of airborne doppler lidar observations on ecmwf forecasts. *Quarterly Journal of the Royal Meteorological Society: A journal of the atmospheric sciences, applied meteorology and physical oceanography*, **133 (622)**, 107–116.

Weissmann, M., R. H. Langland, C. Cardinali, P. M. Pauley, and S. Rahm, 2012: Influence of airborne doppler wind lidar profiles near typhoon sinlaku on ecmwf and nogaps forecasts. *Quarterly Journal of the Royal Meteorological Society*, **138 (662)**, 118–130, doi:https://doi.org/10.1002/qj.896, https://rmets.onlinelibrary.wiley.com/doi/pdf/10.1002/qj.896.

Weissmann, M., and Coauthors, 2011: The influence of assimilating dropsonde data on typhoon track and midlatitude forecasts. *Monthly Weather Review*, **139 (3)**, 908 – 920, doi:10.1175/2010MWR3377.1.

Wernham, D., A. Heliere, G. Mason, and A. G. Straume, 2021: Aeolus-2 mission pre-development status. *2021 IEEE International Geoscience and Remote Sensing Symposium IGARSS*, IEEE, 767–770.

Wheeler, M., and G. N. Kiladis, 1999: Convectively coupled equatorial waves: Analysis of clouds and temperature in the wavenumber–frequency domain. *Journal of the Atmospheric Sciences*, **56 (3)**, 374–399.

Wheeler, M., and K. M. Weickmann, 2001: Real-time monitoring and prediction of modes of coherent synoptic to intraseasonal tropical variability. *Monthly Weather Review*, **129 (11)**, 2677–2694.

Witschas, B., C. Lemmerz, A. Geiß, O. Lux, U. Marksteiner, S. Rahm, O. Reitebuch, and F. Weiler, 2020: First validation of aeolus wind observations by airborne doppler wind lidar measurements. *Atmospheric Measurement Techniques*, **13 (5)**, 2381–2396.

Witschas, B., C. Lemmerz, and O. Reitebuch, 2012: Horizontal lidar measurements for the proof of spontaneous rayleigh–brillouin scattering in the atmosphere. *Applied Optics*, **51 (25)**, 6207–6219.

Witschas, B., and Coauthors, 2022a: Spectral performance analysis of the aeolus fabry–pérot and fizeau interferometers during the first years of operation. *Atmospheric Measurement Techniques*, **15 (5)**, 1465–1489.

Witschas, B., and Coauthors, 2022b: Validation of the aeolus l2b wind product with airborne wind lidar measurements in the polar north atlantic region and in the tropics. *Atmospheric Measurement Techniques*, **15 (23)**, 7049–7070.

WMO, G., 1996: Guide to meteorological instruments and methods of observation.

Yang, G.-Y., S. Ferrett, S. Woolnough, J. Methven, and C. Holloway, 2021: Real-time identification of equatorial waves and evaluation of waves in global forecasts. *Weather and Forecasting*, **36 (1)**, 171–193.

Yang, G.-Y., B. Hoskins, and J. Slingo, 2003: Convectively coupled equatorial waves: A new methodology for identifying wave structures in observational data. *Journal of the atmospheric sciences*, **60 (14)**, 1637–1654.

Yasunaga, K., and B. Mapes, 2012a: Differences between more divergent and more rotational types of convectively coupled equatorial waves. part i: Space–time spectral analyses. *Journal of the atmospheric sciences*, **69 (1)**, 3–16.

Yasunaga, K., and B. Mapes, 2012b: Differences between more divergent and more rotational types of convectively coupled equatorial waves. part ii: Composite analysis based on space–time filtering. *Journal of the atmospheric sciences*, **69 (1)**, 17–34.

Yasunaga, K., and B. Mapes, 2012c: Differences between more divergent and more rotational types of convectively coupled equatorial waves. part ii: Composite analysis based on space–time filtering. *Journal of the atmospheric sciences*, **69 (1)**, 17–34.

Ying, Y., and F. Zhang, 2017: Practical and intrinsic predictability of multiscale weather and convectively coupled equatorial waves during the active phase of an mjo. *Journal of the Atmospheric Sciences*, **74 (11)**, 3771–3785.

Žagar, N., 2004: Assimilation of equatorial waves by line-of-sight wind observations. *Journal of the atmospheric sciences*, **61 (15)**, 1877–1893.

Žagar, N., 2017: A global perspective of the limits of prediction skill of nwp models. *Tellus A: Dynamic Meteorology and Oceanography*, **69 (1)**, 1317 573.

Žagar, N., M. Rennie, and L. Isaksen, 2021: Uncertainties in kelvin waves in ecmwf analyses and forecasts: Insights from aeolus observing system experiments. *Geophysical Research Letters*, **48 (22)**, e2021GL094 716.

Žagar, N., A. Stoffelen, G.-J. Marseille, C. Accadia, and P. Schlüssel, 2008: Impact assessment of simulated doppler wind lidars with a multivariate variational assimilation in the tropics. *Monthly weather review*, **136 (7)**, 2443–2460.

Žagar, N., J. Tribbia, J. Anderson, and K. Raeder, 2009: Uncertainties of estimates of inertia–gravity energy in the atmosphere. part ii: Large-scale equatorial waves. *Monthly weather review*, **137 (11)**, 3858–3873.

Zängl, G., D. Reinert, P. Rípodas, and M. Baldauf, 2015: The icon (icosahedral non-hydrostatic) modelling framework of dwd and mpi-m: Description of the non-hydrostatic dynamical core. *Quarterly Journal of the Royal Meteorological Society*, **141 (687)**, 563–579.

Zapotocny, T. H., W. P. Menzel, J. P. Nelson III, and J. A. Jung, 2002: An impact study of five remotely sensed and five in situ data types in the eta data assimilation system. *Weather and forecasting*, **17 (2)**, 263–285.

Zhang, F., N. Bei, R. Rotunno, C. Snyder, and C. C. Epifanio, 2007: Mesoscale predictability of moist baroclinic waves: Convection-permitting experiments and multistage error growth dynamics. *Journal of the Atmospheric Sciences*, **64 (10)**, 3579–3594.

Zhang, F., C. Snyder, and R. Rotunno, 2003: Effects of moist convection on mesoscale predictability. *Journal of the Atmospheric Sciences*, **60 (9)**, 1173–1185.

Zhang, Y., W. B. Rossow, A. A. Lacis, V. Oinas, and M. I. Mishchenko, 2004: Calculation of radiative fluxes from the surface to top of atmosphere based on isccp and other global data sets: Refinements of the radiative transfer model and the input data. *Journal of Geophysical Research: Atmospheres*, **109 (D19)**.

Zhou, X., and B. Wang, 2007: Transition from an eastern pacific upper-level mixed rossby-gravity wave to a western pacific tropical cyclone. *Geophysical research letters*, **34 (24)**.

Zhu, H., M. C. Wheeler, A. H. Sobel, and D. Hudson, 2014: Seamless precipitation prediction skill in the tropics and extratropics from a global model. *Monthly Weather Review*, **142 (4)**, 1556–1569.

Zuidema, P., J. Redemann, J. Haywood, R. Wood, S. Piketh, M. Hipondoka, and P. Formenti, 2016: Smoke and clouds above the southeast atlantic: Upcoming field campaigns probe absorbing aerosol's impact on climate. *Bulletin of the American Meteorological Society*, **97 (7)**, 1131–1135.

Zuo, H., C. B. Hasager, I. Karagali, A. Stoffelen, G.-J. Marseille, and J. De Kloe, 2022: Evaluation of aeolus l2b wind product with wind profiling radar measurements and numerical weather prediction model equivalents over australia. *Atmospheric Measurement Techniques*, **15 (13)**, 4107–4124.